2

TECHNIQUES FOR IMAGING SMALL IMPEDANCE CHANGES IN THE HUMAN HEAD DUE TO NEURONAL DEPOLARISATION

In Collaboration with

University College London

A thesis submitted to Middlesex University in partial fulfilment of the requirements for the degree of

Doctor of Philosophy

Gershon Mawutor Ahadzi

School of Health and Social Sciences

Middlesex University

2006

TABLE OF CONTENTS

List of figures vii
List of tables xiii
List of abbreviations xv
List of symbols xvii
Acknowledgments xviii
Declaration xix
Abstract 1
Chapter 1 3
Introduction and Review 3
1.1 Motivation 3
1.2 Overview 4
1.2.1 Origin of brain signals 4
1.2.2 Bioelectric and biomagnetic signals 9
1.2.3 How does current flow through the brain? 10
1.2.4 Brain Imaging Systems 13
1.2.5 Integrated Imaging Systems and their applications 36
1.2.6 Electrical properties of tissue 38
1.2.7 Resistance changes in the brain and their visibility using EIT 42
1.2.8 Ionic changes and cell swelling during neuronal activity 48
1.2.9 Current injection and voltage measurement 51
1.2.10 Electrode Protocols 56
1.3 Scope of Work 60
1.4 Summary 60
1.5 Objective of research 61
Chapter 2 63
Modelling and the Forward Problem in EIT 63

2.1. Modelling in EIT 63
2.1.1. 2-D models 63
2.1.2. 3-D models 65
2.1.3. Models of the head 65
2.1.4. Modelling in EEG 68
2.1.5. Anisotropy 70
2.2. The forward problem 70
2.3. Mathematical formulation 72
2.4. Uniqueness, ill-posedness and ill-condition 74
2.5. Volume Source in a Homogeneous Volume Conductor 75
2.6. Volume Source in an Inhomogeneous Volume Conductor 76
2.7. Quasistatic Conditions 78
2.8. Summary 78
Chapter 3 80
Neuromagnetic Field Strength Outside The Human Head Due To Impedance Changes From Neuronal Depolarisation 80
3.1 Introduction 80
3.1.1 Background 80
3.1.2 Purpose of study 82
3.1.3 Proposed Imaging Sensor 83
3.1.4 Design 84
3.2 Methods 85
3.2.1 Volume Conductor Model 85
3.2.2 The source model 86
3.2.3 Current Injection 87
3.3 Mathematical Principles 88
3.3.1 Current Density Estimation 88
3.3.2 Magnetic Field Estimation 89

3.4 Simulation 91
3.5 Results 93
3.5.1 Estimated Magnetic Field 93
3.5.2 Variation of magnetic field 96
3.6 Discussion 98
3.6.1 Summary of results 98
3.6.2 Technical issues 98
3.6.3 Would the changes be detectable with current MEG technology? 100
3.6.4 Does this modelling suggest an advantage over EEG recording? 101
Chapter 4 103
Modelling Of Electrode Pairs For Optimal Current Density Estimation In The Visual Cortex And Optimal Voltage Change Measurement 103
4.1 Introduction 103
4.1.1 Background 103
4.1.2 Purpose of study 106
4.1.3 Design 106
4.2 Method 107
4.2.1 The Meshes 107
4.2.2 The source model 109
4.2.3 Current injection and electrode model 110
4.3 Mathematical principles 111
4.3.1 Simulations and Analysis 113
4.3.2 Experimental validation 115
4.4 Results 117
4.4.1 Baseline surface potential 117
4.4.2 Simulated and experimental homogeneous sphere 117
4.4.3 Simulated and experimental three layer head tank 118
4.4.4 Simulated Changes in surface potential 118

4.4.5 Three layer head 118
4.4.6 Four layer head 119
4.4.7 Current density 120
4.4.8 Validation by human Experiment 122
4.4.9 Best Recording electrodes 123
4.5 Discussion 124
4.5.1 Summary 124
4.5.2 Technical Issues 124
Chapter 5 130
Effect of variations in skull conductivity, shape and size of V1 on current density distribution in the brain and baseline surface potential 130
5.1 Introduction 130
5.1.1 Purpose 131
5.1.2 Background 132
5.1.3 Design 137
5.2 Method 141
5.2.1 Head Model 141
5.2.2 Creation of a 3D electrode protocol file 144
5.3 Results 147
5.3.1 Percentage change in current density 147
5.3.2 Percentage change in current density 156
5.3.3 Baseline boundary voltages and changes 156
5.3.4 Changes in boundary voltages for different local conductivity changes 164
5.3.5 Non uniformity ratio 164
5.3.6 Multiple current injection 167
5.4 Discussion 169
5.5 Conclusion 170
Chapter 6 172

magnetic field estimation of the realistic head using eidors 172
6.1 Introduction 172
6.1.1 Purpose 174
6.1.2 Design 174
6.2 Method 175
6.2.1 Volume conductor and source models 175
6.2.2 The electrode protocol 177
6.2.3 The simulation 178
6.3 Results 179
6.3.1 Baseline magnetic fields 179
6.3.2 Percentage Changes in magnetic field 181
6.4 Discussion 188
6.5 Is there any advantage 190
6.6 Observations 191
Chapter 7 193
conclusions and suggestions for future work 193
7.1 Summary of work done 193
7.1.1 Research question 195
7.1.2 Review 195
7.1.3 Multi-modality 196
7.1.4 Optimal electrode protocol 198
7.1.5 Effect of conductivities on surface potential changes 200
7.1.6 Effect of conductivities off-scalp magnetic field changes 201
7.2 Suggestions 201
7.2.1 Methods of increasing current density in the brain 201
7.2.2 Development of accurate forward problem 202
7.2.3 Best optimal current pattern using distinguishability approach 204
Appendix A 209

Geselowitz' Sensitivity Theorem.....209
Appendix B.....211
Spectral noise density.....211
References.....213

List of figures

Figure 1-1: The human brain 4
Figure 1-2: The structure of a typical neurone 5
Figure 1-3: Resting potential curve 6
Figure 1-4: The action potential of a nerve fibre 8
Figure 1-5: A subject in a typical magnetoencephalogram (NTF 275) 24
Figure 1-6: Magnetic Fields 25
Figure 1-7 Magnes 3600 248 MEG Channels 26
Figure 1-8: Principles of SQUID operation 29
Figure 1-10: SQUID sensor electronics 31
Figure 1-11: Flux Transformers a: an axial first order gradiometer which measures $\frac{\partial B_z}{\partial z}$ (approximately Bz at the lower loop) b: second order series axial gradiometer 32
Figure 1-12: Systems already integrated are shown with thick lines, the dotted is currently under study 37
Figure 1.13. The flow of externally applied current inside and outside an axon and across its membrane (a) during the resting state and (b) during depolarisation. More current flows through the intracellular space during depolarisation (Liston, 2003) 47
Figure 1.14: Mechanisms of impedance change within the brain (Tidswell et al., 2001) 50
Figure 1.15: Neighbouring method of impedance data collection. The first four voltage measurements for the set of 13 measurements are shown. B shows another set of 13 measurements, which is obtained by changing the current feeding electrodes. 52
Figure 1.16: Opposite method of impedance data collection 53
Figure 1.17: Cross method of impedance data collection. The four different steps of this approach are illustrated in A through D 54
Figure 1.18: Adaptive method of impedance data collection 55
Figure 1.19: The international 10-20 system seen from the left side of the head (A) and B above the head. A - Ear lobe, C - central, Pg - nasopharyngeal, P - parietal, F -

frontal, Fp - frontal polar, O - occipital. In (C) is the location and nomenclature of the intermediate 10% electrodes, as standardised by the American Electroencephalographic Society. 56

Figure 1.20: Positions of electrodes. Each black spot represents an electrode. The black label gives the electrode code in the 10-20 system, the red number is the electrode reference number used in this work. 59

Figure 3-1: EIT system for current injection 83

Figure 3-2: (a) An approximation of the realistic head to a fourshell sphere model showing points of current injection E1 and E2. R, C, and L are the locations of typical SQUID sensors for the measurement of the magnetic field. The gray region Ωp is a collection of nodes indicating a region in the brain where the neurons are firing and the conductivity is σ'. The conductivity at other regions within the volume Ω is σ. (b) The EEG 10-20-system showing the relationship between the location of an electrode and the underlying area of cerebral cortex. 85

Figure 3-3: Predicted change in resistivity versus frequency during neuronal depolarisation 87

Figure 3-4: The depolarised region is denoted by Ω_p whereas the remaining volume is labelled Ω_u. The entire volume conductor is represented by Ω. The point at which the magnetic field is estimated is B. The position vectors of the source (node) and point of measurement are respectively $r_{o\alpha}$ and r_α respectively from a fixed origin O. The distance between the source and P is $|\vec{r}_\alpha - \vec{r}_{o\alpha}|$. J_α denotes the current density at a node.$\alpha \in \{i, j, k\}$ 89

Figure 3-5: Fractional magnetic field change during evoked response with respect to position for homogeneous sphere fine mesh model The x-axis denotes the distance of the centre of the depolarised region from the centre of the head. 96

Figure 3-6: Fractional magnetic field change from baseline with respect to position for fourshell fine mesh model. The x-axis denotes the distance of the centre of the depolarised region from the centre of the head. 97

Figure 3-7: A MatLab interpolated SURF plot of current density on an 80x80 grid (A m^{-2}) in the plane of two bipolar electrodes applying 1μA on the surface of a) a homogenous sphere of conductivity σbrain and b) a 4-shell sphere. The x- and y-axes are pixel numbers (Liston, 2003).....100

Figure 4.2: A - The brain region showing the primary visual cortex as Brodmann area 17 and B shows the modelled realistic head with V1 using FEM.....109

Figure 4.4: Illustration of EIT acquisition principle: small current injected through a pair of electrodes, and the surface potential (V) measured via another pair. This process is repeated for different injection-measurement combinations.....114

Figure 4.5A: The homogeneous spherical tank phantom, shown for clarity without the presence of the shell to represent the skull. The protruding leads are the connections to various positions.....116

Figure 4.5B: The head shaped tank phantom shown with the two halves separated and a human skull inside.....116

Figure 4.6. Mean current density in V1 for an injected current through electrodes 29 and 30 paired with other electrodes. The horizontal axis refers to the number assigned to each electrode as modelled.....121

Figure 4.7 Comparison between measured base voltages on human and simulated base voltages from 4 shell realistic mesh (skull conductivity 17.5mS/m). The Blue is injection pair 1 (23-30) and red is injection pair 2 (27-29).....122

Figure 5.1: The three selected morphologies of the primary visual cortex a) inclined b) elongated c) blob.....139

Figure 5.2: The element faces on the surfaces of the four parts of the full, layered head mesh a) the scalp, b) the skull, c) the CSF and d) the brain region. The scalp region contains 10,078 nodes, the skull region 6,325 nodes, the CSF region 2,064 nodes and the brain region 6,702 nodes.....142

Figure 5.3: The nodal clouds describing a) the head-shaped mesh with skull compartment, b) the fourshell mesh and c) the full, layered head mesh. The different tissues are colour-coded as shown in the key....143
Figure 5.5a. Plot of current density and percentage change in mean current density in V1 as a function of skull conductivity for morphology 1, for volumes 1 and 2 of the primary visual cortex....148
Figure 5.5b. Plot of current density and percentage change in mean current density in V1 as a function of skull conductivity for morphology 1, for volumes 3 and 4 of the primary visual cortex....149
Figure 5.6a. Plot of current density and percentage change in mean current density in V1 as a function of skull conductivity for morphology 2, for volumes 1 and 2 of the primary visual cortex....151
Figure 5.6b. Plot of current density and percentage change in mean current density in V1 as a function of skull conductivity for morphology 2, for volumes 3 and 4 of the primary visual cortex....152
Figure 5.7a. Plot of current density and percentage change in mean current density in V1 as a function of skull conductivity for morphology 3, for volumes 1 and 2 of the primary visual cortex....154
Figure 5.7b. Plot of current density and percentage change in mean current density in V1 as a function of skull conductivity for morphology 3, for volumes 3 and 4 of the primary visual cortex....155
Figure 5.8a Plot of baseline boundary voltages for different conductivities with respect to index of measurement electrode pairs for morphology 1 for sizes 1 and 2....158
Figure 5.8b Plot of baseline boundary voltages for different conductivities with respect to index of measurement electrode pairs for morphology 1 for sizes 3 and 4....159
Figure 5.9a Plot of baseline boundary voltages for different conductivities with respect to index of measurement electrode pairs for morphology 2 for sizes 1 and 2....160

Figure 5.9b Plot of baseline boundary voltages for different conductivities with respect to index of measurement electrode pairs for morphology 2 for sizes 3 and 4.....161
Figure 5.10a Plot of baseline boundary voltages for different conductivities with respect to index of measurement electrode pairs for morphology 3 for sizes 1 and 2.....162
Figure 5.10b Plot of baseline boundary voltages for different conductivities with respect to index of measurement electrode pairs for morphology 3 for sizes 3 and 4.....163
Figure 5.11a. Non-uniformity ratio plots for different electrode combinations for a fixed conductivity of 17.5 mSm^{-1} 166
Figure 5.11b Non-uniformity ratio plots for different electrode combinations with variation over skull conductivity 166
Figure 5.12a: Mean current density in V1 for independent current injection pairs as a function of conductivity 167
Figure 5.12b. Mean current density in V1 for multiple current injection where the injected currents are 100 μA each and using morphology 1.....168
Figure 6-1: The homogeneous and head spherefine head models. The homogeneous head model has 24,734 nodes whereas the spherefine has 36,000 nodes.....176
Figure 6-2: The fourshell head model with 42,093 nodes. The conductivity values of the different shells (scalp, skull, cerebrospinal fluid, and brain) are as specified in table 4.1, section 4.2.1 176
Figure 6-3: The red-circles (o) denote electrode positions for current injection whereas the blue crosses (+) are 1-cm radially away from points of current injection where the Squids are located for estimating the baseline magnetic field. The green points (*) are the sensor locations L, C and R (used in chapter 3) Both axes have units in meters 177
Figure 6.4: Baseline magnetic field for fourshell head model. The horizontal axis refers to the location of the SQUIDs position.....179
Figure 6.5: Baseline magnetic field for realistic head model. The horizontal axis refers to the location of the SQUIDs position.....180

Figure 6.7: Realistic head percentage changes in magnetic field from baseline as a function of position of SQUIDs, for morphology 1 and sizes 3 and 4 183
Figure 6.8: Realistic head percentage changes in magnetic field from baseline as a function of position of SQUIDs, for morphology 2 and sizes 1 and 2 184
Figure 6.9: Realistic head percentage changes in magnetic field from baseline as a function of position of SQUIDs, for morphology 2 and sizes 3 and 4 185
Figure 6.10: Realistic head percentage changes in magnetic field from baseline as a function of position of SQUIDs, for morphology 3 and sizes 1 and 2 186
Figure 6.11: Realistic head percentage changes in magnetic field from baseline as a function of position of SQUIDs, for morphology 3 and sizes 3 and 4 187
Figure B-1: Spectral noise density for a SQUID as a function of frequency. Source(MEG-EEG Centerat Pitié-Salpêtrière Hospital, 2000) 211

List of tables

Table 1-1: Reported values for the resistivity of grey matter 39
Table 3-1: Baseline magnetic field for fine mesh 94
Table 3- 2: Maximum magnetic field change from baseline field strength for fine mesh 94
Table 3-3: Maximum percentage change from baseline magnetic field for fine mesh 94
Table 3-4: Baseline magnetic field for medium mesh 95
Table 3- 5: Maximum magnetic field change from baseline field strength for medium mesh 95
Table 3.6: Maximum percentage change from baseline magnetic field for medium mesh 95
Table 4.1: Conductivity values of the different layers of the head (Oostendorp and Debelke, 2000) 108
Table 4.2: Listed are the three meshes, the number of nodes and elements and the ratio of largest-to-smallest element size in each head shape. This ratio is a measure of their quality and a smaller value is desirable 108
Table 4.3: Comparison between simulated and experimental baseline voltages for homogeneous spherical tank 117
Table 4.4: Comparison between simulated and experimental baseline voltages for three-layer head tank (latex tank) for the best pairs of electrodes 118
Table 4.5: Best pairs for recording surface potential and injecting current for the 3 layer head 119
Table 4.6: Best pairs for recording surface potential and injecting current for the 4 layer head 120
Table 5.1: Specific conductivity of bone. (n.a : not applicable) 133
Table 5.2: Computed volumes of the left and right hemisphere of V1 together with the total mean volume 140

Table 5.3: Listed are the three meshes used in this chapter, the number of nodes and elements in each and the ratio of largest-to-smallest element size in each, a measure of their quality. A smaller value is desirable 143
Table 5.4 Computed percentage change in mean current density for a 1% local change V1 over variations in skull conductivity and volume of V1 156
Table 5.6: Percentage change in boundary voltages with respect to local conductivity and skull conductivity 164
Table 6.1 Range of baseline magnetic fields across SQUID sensor locations for two types of current injections protocol: (DMO - Diametrically Opposed and BCE Best Current Injection Electrodes) 181
Table 6.5 Computed percentage change baseline magnetic field for a 0.6% local change inV1 over SQUID locations 189
Table 6.6 Computed percentage change baseline magnetic field for a 1% local change inV1 over SQUID locations 189
Table 6.7 Computed percentage change baseline magnetic field for a 1.6% local change inV1 over SQUID locations 189

List of abbreviations

ACT	Applied Current Tomography
BCE	Best Current-injection Electrode
BEM	Boundary Element Method
BOLD	Blood Oxygenation Level Dependent
BREIT	BOLD-Related Electrical Impedance Tomography
CAP	Compound Action Potential
CAT	Computerised Axial Tomography
CBV	Cerebral Blood Flow
CSF	Cerebrospinal Fluid
CT	Computed Tomography
DC (dc)	Direct Current
DOM	Diametrically Opposed Method
EcoG	Electrocortigogram
EEG	Electroencephalography
EIDORS	Electrical Impedance and Diffuse Optical Reconstruction Software
EIT	Electrical Impedance Tomography
EITS	Electrical Impedance Tomographic Spectroscopy
EP	Evoked Potential
FEM	Finite Element Method
fMRI	functional Magnetic Resonance Imaging
Hb	Hemoglobin
HbO_2	Oxygenated Hemoglobin
I-DEAS	Integrated Design and Analysis Software
IEG	Immediate-Early Gene
IPT	Industrial Process Tomography
MaTOAST	Matlab Time-resolved Optical Absorption and Scattering Tomography
MEG	Magnetoencephalography
MCS	Multiple Current Source

MRI	Magnetic Resonance Imaging
NIRS	Near Infra Red Spectroscopy
NURBS	Non-Uniform Rational B-Spline
PET	Positron Emission Tomography
RNA	Ribonucleic Acid
rCBF	regional Cerebral Blood Flow
SCS	Single Current Source
SEP	Somatosensory Evoked Response
SPM	Statistical Parametric Mapping
SQUIDS	Superconducting QUantum Interference Devices
SPECT	Single Photon Emission Computerised Tomography
SVD	Singular Value Decomposition
SVS	Single Voltage Source
TOAST	Time-resolved Optical Absorption and Scattering Tomography
VEP	Visual Evoked Potential
V1	Primary Visual Cortex

List of symbols

σ	Conductivity
$\mathbf{E}$	Electric Field
ϕ	Electric Potential
$\mathbf{H}$	Magnetic Field
$\mathbf{J}$	Current Density
V	Voltage
$\mathbf{A}$	Sensitivity Matrix
Z	Impedance
I	Current
Ψ,Φ	Electric Potential
M	Number of Measurements
N	Number of Pixels/Nodes
S	Support Matrix
v	elemental volume
$\mathbf{r}$	Position Vector
r	Radial Position

Acknowledgments

I wish to express my sincere appreciation to my Director of Studies, Professor Richard H. Bayford, host supervisor Dr David S. Holder and co-supervisor Dr Robert Ettinger for their indefatigable effort in directing me to complete this study. I am very much indebted to them for their professional guidance.

Special thanks to my colleagues Dr Adam Liston from whom I had a lot of encouragement at the initial stage of the project; Ori Gilad, who tutored and made proud of using MatLab as my everyday programming tool. Lior Horesh, I say a big thank you for assisting me to understand the lengths of codes in the forward solution.

To God be the Glory!

Sponsors: University of Ghana, Legon-Accra, Ghana

Declaration

I carried the research work presented in this thesis under the supervision of **Prof. Richard Bayford**, the Director of Studies together with my external supervisors **Dr David Holder** (Medical Physics and Bioengineering Department, University College London) and **Dr Robert Ettinger** (School of Computing Science, Middlesex University). The laboratory and experimental validation work reported was done partly at the Clinical Neurophysiology Department of University College London Hospitals and the Medical Physics and Bioengineering Department, **University College London**.

Many members of the EIT group both past and present in one way or the other contributed tremendously to this research work. The experimental section was done in collaboration with **Ori Gilad** who is also a PhD student working on experimental set ups for human studies, which could be used to verify some of my predictions from the models I developed. **Adam Gibson** – development of an analytical homogenous head model for a conduction sphere, and **Adam Liston** who developed the fourshell head model which were used extensively in the first part of this research work. **Andrew Bagshaw** helped me in the initial modification of and debugging the 3D MaTOAST code.

The realistic head model meshes were by courtesy of **Andrew Tizzard** and **Richard Bayford**. I used MatLab to develop and implement codes for the simulation. However, a number of functions and modules were adopted from EIDORS with the singular help of **Lior Horesh**.

Refereed Paper as a Result of this work[1]

Ahadzi, G. M., Liston, A. D., Bayford, R. H., & Holder, D. S. 2004, "Neuromagnetic field strength outside the human head due to impedance changes from neuronal depolarization", Physiol. Meas., vol. 25, no. 1, pp. 365-378.

[1] This is enclosed in an envelope attached to the back of this thesis

Conference Papers & Posters as a Result of this work

1. Ahadzi, G. & Bayford RH 2005, "Current density distribution in the brain and baseline scalp potential - How are they influenced by variations in skull and local conductivity, shape and size of V1?" Poster Presentation - Inauguration and opening of Biomedical Laboratory Centre, Middlesex University.

2. Ahadzi, G. & Bayford, R. 2005, "Are there any changes in the mean current density in the visual cortex due to variations in the conductivity of the human skull?" Abstract of Research in Practice, Institute of Social & Health Research, School of Health & Social Sciences, Middlesex University, London, June 24 2005, pp.10.

3. Ahadzi, G. & Bayford, R. 2006, "Is magnetic recording of EIT the holy grail of imaging small and fast impedance changes in the human brain?" Abstract of Research in Practice, Institute of Social & Health Research, School of Health & Social Sciences, Middlesex University, London, June 23 2006, pp.15

4. Ahadzi, G., Gilad, O., Horesh, L., Bayford, R., & Holder, D. 2004, "An EIT electrode protocol for obtaining optimal current density in the primary visual cortex", Proceedings of the XII Intern.Conf.Electrical Bio-Impedance and EIT, Gdansk, Poland, vol. II, pp. 621-624.

5. Ahadzi, G., Liston, A., Bayford, R., & Holder, D. 2003, "Would SQUID measurement of magnetic fields be a better way to do EIT imaging of fast electrical brain activity?" Proceedings of 4th International Conference on Biomedical Applications of EIT, University of Manchester Institute of Technology, Manchester.

6. Gilad, O., Ahadzi, G., Bayford, R., & Holder, D. 2004, "Near DC conductivity change measurement of fast neuronal activity during human VEP", Proceedings of the XII International Conference Electrical Bio-Impedance and EIT, Gdansk, Poland, vol. I, pp. 279-282.

7. Gilad, O., Ahadzi, G., Bayford, R., & Holder, D. 2004, "Near DC resistivity change measurement of fast neuronal activity during human visual evoked potentials (VEP)", Poster Presentation, Medical Physics & Bioengineering Department, University College London.

8. Gilad, O., Horesh, L., Ahadzi, G., Bayford, R., & Holder, D. 2005, "Could synchronized neuronal activity be imaged using low frequency electrical impedance tomography?" Scientific Abstracts of the 6th International Conference on Biomedical Applications of EIT, Univ.Col.London, June 22 - 24 2005.

9. Gilad, O., Horesh, L., Ahadzi, G., Bayford, R., & Holder, D. 2005, "Towards imaging synchronised neuronal activity using low frequency electrical impedance tomography", Poster Presentation, Medical Physics & Bioengineering Department, University College London.

10. Horesh, L., Bayford, R., Yerworth, R., Tizzard, A., Ahadzi, G., & Holder, D. 2004, "Beyond the linear domain - the way forward in MFEIT image reconstruction of the human head", Proceedings of the XII Intern.Conf.Electrical Bio-Impedance and EIT, Gdansk, Poland, vol. II, pp. 683-686.

Abstract

A new imaging modality is being developed, which may be capable of imaging small impedance changes in the human head due to neuronal depolarization. One way to do this would be by imaging the impedance changes associated with ion channels opening in neuronal membranes in the brain during activity. The results of previous modelling and experimental studies indicated that impedance changes between 0.6%and 1.7% locally in brain grey matter when recorded at DC. This reduces by a further of 10% if measured at the surface of the head, due to distance and the effect of the resistive skull. In principle, this could be measured using Electrical Impedance Tomography (EIT) but it is close to its threshold of detectability.

With the inherent limitation in the use of electrodes, this work proposed two new schemes. The first is a magnetic measurement scheme based on recording the magnetic field with Superconducting Quantum Interference Devices (SQUIDs), used in Magnetoencephalography (MEG) as a result of a non-invasive injection of current into the head. This scheme assumes that the skull does not attenuate the magnetic field. The second scheme takes into consideration that the human skull is irregular in shape, with less and varying conductivity as compared to other head tissues. Therefore, a key issue is to know through which electrodes current can be injected in order to obtain high percentage changes in surface potential when there is local conductivity change in the head. This model will enable the prediction of the current density distribution at specific regions in the brain with respect to the varying skull and local conductivities.

In the magnetic study, the head was modelled as concentric spheres, and realistic head shapes to mimic the scalp, skull, Cerebrospinal Fluid (CSF) and brain using the Finite Element Method (FEM). An impedance change of 1% in a 2cm-radius spherical volume depicting the physiological change in the brain was modelled as the region of depolarisation. The magnetic field, 1 cm away from the scalp, was estimated on injecting a constant current of 100 μA into the head from diametrically opposed electrodes. However, in the second scheme, only the realistic FEM of the head was used, which included a specific region of interest; the primary visual cortex (V1). The simulated physiological change was the variation in conductivity of V1 when neurons were assumed to be firing during a visual evoked response. A near DC current of 100 μA was driven through possible pairs of 31 electrodes using EIT techniques. For a fixed skull conductivity, the resulting surface potentials were calculated when the whole head remained unperturbed, or when the conductivity of V1 changed by 0.6%, 1%, and 1.6%.

The results of the magnetic measurement predicted that standing magnetic field was about 10pT and the field changed by about 3fT (0.03%) on depolarization. For the second scheme, the greatest mean current density through V1 was 0.020 ± 0.005 μAmm^{-2}, and occurred with injection through two electrodes positioned near the occipital cortex. The corresponding maximum change in potential from baseline was 0.02%. Saline tank experiments confirmed the accuracy of the estimated standing potentials. As the noise density in a typical MEG system in the frequency band is about $7fT/\sqrt{Hz}$, it places the change at the limit of detectability due to low signal to noise ratio. This is therefore similar to electrical recording, as in conventional EIT systems, but there may be advantages to MEG in that the magnetic field directly traverses the skull and instrumentation errors from the electrode-skin interface will be obviated. This has enabled the estimation of electrode positions most likely to permit recording of changes in human experiments and suggests that the changes, although tiny, may just be discernible from noise.

Introduction and Review

Chapter 1

INTRODUCTION AND REVIEW

1.1 Motivation

A great deal of scientific research has been carried out over the last few decades to learn more about the functional activities and dysfunction of the human brain. It has been established that electrical interaction between neurones is responsible for the transmission of information in the human brain. Associated with these interactions are changes in ion concentration and hence impedance changes which occur when the brain is functioning or in a state of dysfunction.

There are three main mechanisms that give rise to impedance changes in the human head, namely: cell swelling during conditions such as epilepsy or stroke, cerebral blood volume change during functional activity and neuronal depolarisation. Prior to the commencement of my research, Electrical Impedance Tomography (EIT) reproducible images have been obtained by the University College London Hospitals (UCLH) EIT group which includes: spreading depression (Boone and Holder, 1996b), epilepsy (Rao et al., 1996), evoked activity in animals (Holder et al., 1996b) using cortical electrodes, and preliminary images in humans during evoked responses using scalp electrodes. Currently, there are a number of research projects underway to improve the sensitivity of EIT to detect the small impedance changes of slow blood flow changes. The research utilises the UCLH Mark 1b EIT system, which has adequate performance of imaging impedance changes of 5 – 50% known to occur in the brain during normal activity, epilepsy or stroke. However, work done by Kevin Boone (Boone K. and Holder, 1994) suggested that impedance changes accompanying neuronal depolarisation may be of the order of 1% or less (Boone K., 1995) which is beyond the capabilities of existing EIT systems. There is the need to device new measurement techniques for studying these small impedance changes.

1.2 Overview

The following sections give an overview of the origin of brain signals and its components, the principles and techniques of some of the brain imaging systems used in measuring these signals. The clinical and practical applications of these devices have also been outlined. The electrical properties of tissues: especially their conductivity values have been addressed.

1.2.1 Origin of brain signals

The major components of the nervous system are the brain (Figure 1-1), nerves and muscle. The brain is supplied with information along the sensory or afferent nerves, which are effected by sensations such as heat, touch and pain. The basic component of both brain and nerves is the neurone (Figure 1-2). There are many forms of neurone but all consist of a cell body, dendrites and axon (Brown *et al.*, 1999).

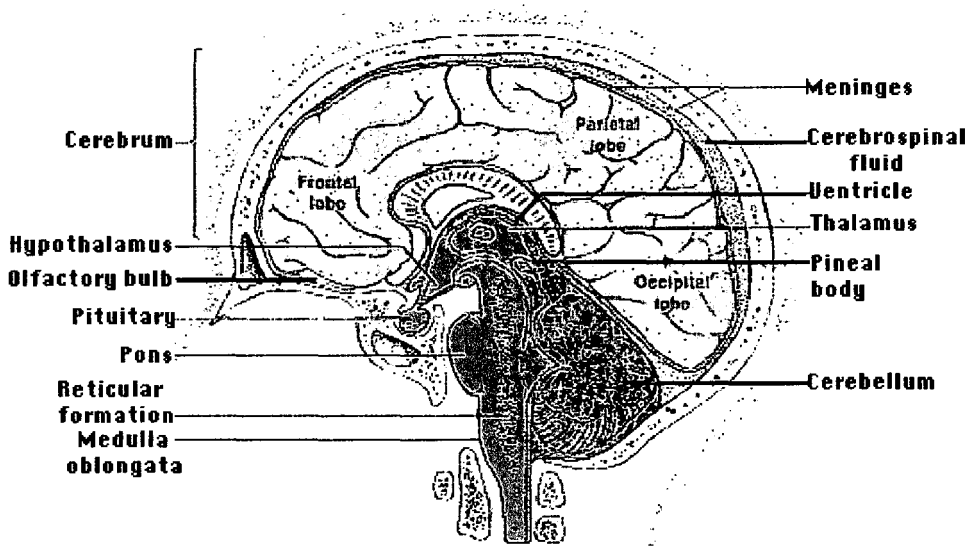

Figure 1-1: The human brain

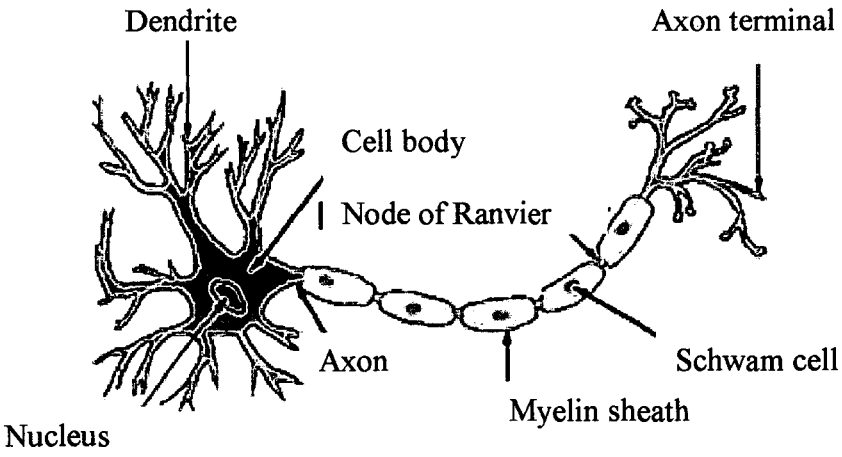

Figure 1-2: The structure of a typical neurone

The dendrites act as the means of information input to the cell, and the axon as the channel for the output information. The axon allows a cell to operate over a long distance, whilst the dendrites enable short-distance interactions with other cells. The cell body of the neurone may be within the brain or within the spinal cord and the nerve axon might supply a muscle or pass impulses up the brain. The brain itself is a collection of neurones which can interact electrically via the dendrites and axons and so can function in a similar manner to an electronic circuit (Brown *et al.*, 1999; Brown *et al.*, 1999).

1.2.1.1 Resting Potential

Neurons are covered with a semi-permeable membrane, with only 5 nm thickness. The membrane is able to selectively absorb and reject ions in the intracellular fluid. The membrane basically acts as an ion pump to maintain a different ion concentration between the intracellular fluid and extracellular fluid. While the sodium ions are continually removed from the intracellular fluid to extracellular fluid, the potassium ions are absorbed from the

extracellular fluid in order to maintain an equilibrium condition. Due to the difference in the ion concentrations inside and outside, the cell membrane become polarized.

In equilibrium, the interior of the cell is observed to be 70 mV negative with respect to the outside of the cell. This is close to the equilibrium potential for potassium ions K^+, for which the neurons have a relatively high permeability (Ganong, 1987). The mentioned potential is called the resting potential (figure 1-3).

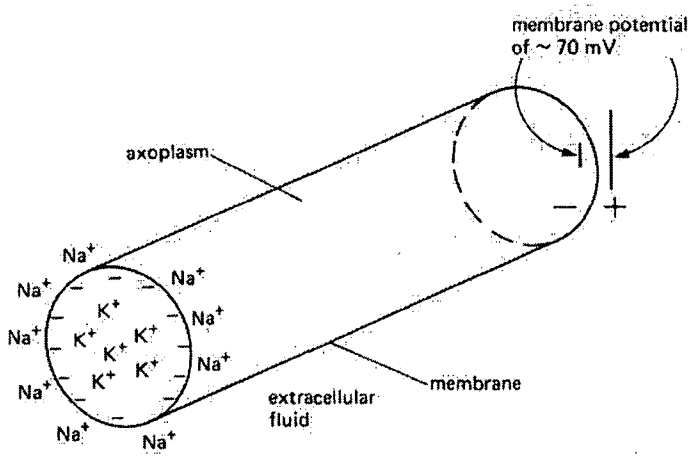

Figure 1-3: Resting potential curve
(adapted from Options in Physics: Medical Physics (Pope, 1984))

1.2.1.2 Excitatory and Inhibitory Synapses

A neuron receives inputs from a large number of neurons via its synaptic connections. Nerve signals arriving at the presynaptic cell membrane cause chemical transmitters to be released into the synaptic cleft. These chemical transmitters diffuse across the gap and join to the postsynaptic membrane of the receptor site. The membrane of the postsynaptic cell gathers the chemical transmitters. This cause either a decrease or an increase in the efficiency of the local sodium and potassium pumps depending on the type of the chemicals released into the synaptic cleft. While the synapses, whose activation decreases the efficiency of the pumps,

cause depolarisation of the resting potential, the effects of the synapses, which increase the efficiency of pumps, result in hyperpolarisation. The first kind of synapses encouraging depolarisation is called excitatory and the others discouraging it are called inhibitory synapses. If the decrease in the polarization is adequate to exceed a threshold then the post-synaptic neuron fires.

1.2.1.3 Action Potential

When a nerve cell, for example is stimulated, the cell membrane suddenly becomes permeable to Na^+ ions, which then move into the axoplasm from their higher concentration area outside (see figure 1-4). The increase in positive charge inside the cell leads to a change in the membrane potential from about -70 mV to 0 mV (depolarisation) and further to about +40 mV (reverse polarisation). Almost immediately, the membrane becomes impermeable to Na^+ ions and permeable to K^+ ions, which consequently leave their high concentration area inside the fibre and move out, thereby restoring the original membrane potential of -70 mV, (repolarisation). The Na^+ and K^+ ions are re-exchanged later during a slower recovery period.

The arrival of impulses to excitatory synapses adds to the depolarisation of soma, while inhibitory effect tends to cancel out the depolarising effect of excitatory impulse. In general, although the depolarisation due to a single synapse is not enough to fire the neuron, if some other areas of the membrane are depolarised at the same time by the arrival of nerve impulses through other synapses, it may be adequate to exceed the threshold and fire.

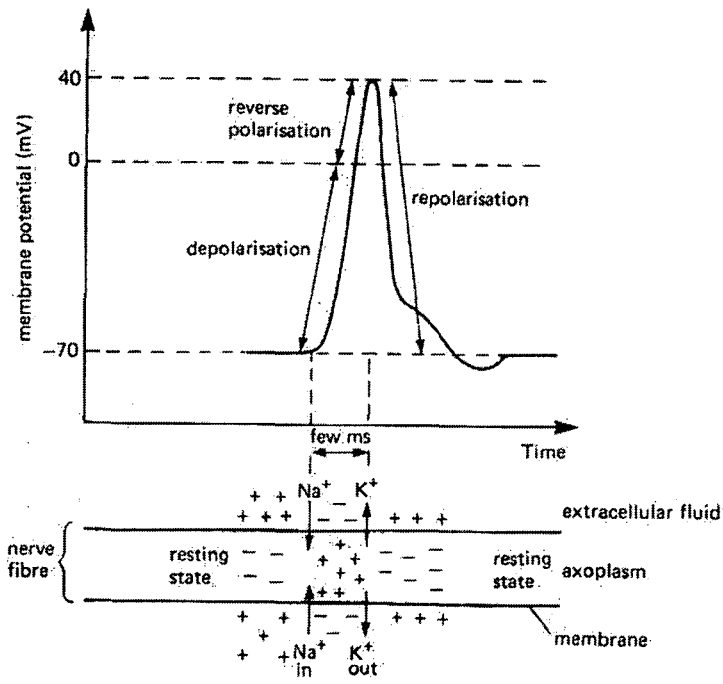

Figure 1-4: The action potential of a nerve fibre
(adapted from Options in Physics: Medical Physics (Pope, 1984))

The excitatory effects result in interruption of the regular ion transportation through the cell membrane, so that the ionic concentrations immediately begin to equalize as ions diffuse through the membrane. If the depolarisation is large enough, the membrane potential eventually collapses, and for a short period of time the internal potential becomes positive. The action potential is the name of this brief reversal in the potential, which results in an electric current flowing from the region at action potential to an adjacent region with a resting potential. This current causes the potential of the next resting region to change, so the effect propagates in this manner along the membrane wall.

1.2.1.4 Refractory Period

Once an action potential has passed a given point, it is incapable of being re-excited for a while called refractory period. Because the depolarised parts of the neuron are in a state of recovery and cannot immediately become active again, the pulse of electrical activity always propagates in only forward direction. When the cell is excited, the permeability for certain ions changes, which allows mainly sodium to travel freely through the membrane. The potential of the cell then rises to positive values. After a short period of time, the permeability returns normal and the flow of potassium restores the resting potential. The moving ions then give rise to a current within the cell, which can be described by a current dipole. The current dipole then generates currents in the surrounding tissues, the so-called volume currents (Karp et al., 1981).

1.2.2 Bioelectric and biomagnetic signals

A biopotential is a potential generated inside the body and generally arises from salt concentration differences across cell membranes. These so-called membrane potentials are exhibited by nerve, muscle and gland cells. Although all living cell membranes pass water, the solute transmitted depends on the state and type of membrane.

As explained in the previous section, neural tissue generates electric potentials within the body and these potentials give rise to electric currents in the tissue, which may be referred to as bioelectric signals. The bioelectric signals give rise to electrical signals, which tend to give rise to magnetic fields. For example, such biomagnetic fields from the heart were first recorded as recently as 1963 by Baule and McFee (Brown et al., 1999). The biomagnetic data measured are used to determine the location of the electric source inside the body that produces the magnetic field and for signal analysis. One can determine the location and the strength of focal sources (e.g. a single current dipole) or the distribution and strength of extended sources (e.g. a current density distribution) (Mosher *et al.*, 1999) .

The bioelectric signals can be recorded using an electroencephalogram (EEG) whereas the non-invasive technique for localising and characterising the electrical activity of the central nervous system by measuring the associated biomagnetic signals is a magnetoencephalogram (MEG). Hans Berger was the first to measure small potential differences at the scalp in 1924, and Brener et al. were the first to present biomagnetic measurements of visually evoked (Brenner et al., 1975). Since then, these types of measurements have been used for fundamental and clinical brain research (Wieringa H.J., 1993).

When electrically active tissue produces a bioelectric field, it simultaneously produces a biomagnetic field. Thus the origin of both the bioelectric and biomagnetic signals is the bioelectric activity of the tissue. Magnetic detection of the bioelectric activity introduces both technical and bioelectromagnetic differences compared to the electric method. One important technical advantage of the magnetic method is that biomagnetic signals may be detected without attaching electrodes to the skin. Furthermore, superconducting SQUID detectors are capable of detecting direct currents. On the other hand, biomagnetic technology needs, especially in brain studies, very expensive instrumentation and a magnetically shielded room. Their cost is at least 25 times that of electroencephalography (EEG) instrumentation (Wikswo et al., 1993). Bioelectromagnetic differences include differences in the information contents of the electric and magnetic signals and in the abilities of these methods to concentrate their measurement sensitivity or to localize electric sources.

1.2.3 How does current flow through the brain?

When an alternating current is applied to the head, the current is transferred between the electrodes by movements of free ions. As usual, this current will tend to take the path of least electrical resistance. When it enters the scalp tissue, it encounters a large resistance from the presence of the skull and so the majority of the current will pass through the scalp. This has been demonstrated experimentally inside a saline filled tank, which contained a real human skull, and in which the current was applied at electrodes in the 'scalp layer', outside the skull and current density measured within the skull (Rush and Driscoll, 1968). Their work

demonstrated that approximately half the current applied in polar-drive from scalp electrodes entered the cranial cavity. Similar results have been obtained in live, anaesthetised rabbits, in which scalp electrodes apply a current to the rabbit's head inside an MRI scanner; the MRI detects the magnetic component of the electrical current in two orthogonal directions, from which the current density can be calculated in each part of the head (Joy and Lebedeev, 1999). Joy and Lebedeev's work demonstrated that 15% of the applied current entered the brain. Some of the differences between the rabbit and human skull experiments probably arise from different sizes and shapes, and the method of detecting current in a live animal, compared to a saline filled sank. However, if these results apply to EIT in the human head, then these studies provide limits on the size of attenuation of impedance changes due to the skull of a factor of between 2 to 7 (Joy and Lebedeev, 1999).

Once inside the skull, the CSF will provide a shunt path to the current due to its lower resistivity compared to brain, which are, respectively, 65 Ωcm and 390 Ωcm (Geddes and Baker, 1967; Ranck, 1963). However, as the CSF has a low volume compared to the brain, a significant proportion of current will be conducted through the brain. Once the current is in the brain, the current will be distributed through several anatomical compartments: the neuronal and glial cells, the extracellular space and the blood volume. Estimates of the size of these spaces in humans are unknown, although the cerebral blood volume (CBV) fraction has been non-invasively measured with PET in normal volunteers. The CBV varies between 1.9 to 3.5 ml/100g, and 2-3.5% of the brain volume. In rabbits, the blood volume has been demonstrated to contribute to 10% of the impedance of the brain (VanHarreveld and Ochs, 1956), by an experiment in which blood was drained from the rabbit and replaced with a more conductive solution of 0.9% saline. Estimates of the extracellular space (ECS) in humans have to be derived from animal studies, in which invasive tests can be performed. Such measurements of the ECS, measured by dye dilution techniques in rats, demonstrate that it comprises 12-18% of the brain volume. The resistivity of the ECS can be estimated from measurements of the ion concentration of the ECS in the exposed cat sensorimotor cortex (Dietzel and Heinemann, 1982), which contains 146 mmol Na^+, 149 mmol Cl^- and 3 mmol K^+ ions. These results imply that the resistivity of the ECS is similar to 0.9% saline (140mmol

NaCl) which has a resistivity of 51 Ωcm at body temperature (Geddes and Baker, 1967). The final two compartments, the neurons and glial cells, comprise the remaining 80% of the volume of the brain.

The relative size and contribution to the resistivity of the brain of these cells has been calculated on measurements of the impedance of rabbit cortex (Ranck, 1963) in which the estimated volumes of the neuronal and glial cells were calculated to be 40% each of the cortex volume. In the same analysis, in which the resistivity of rabbit cortex was measured at 240 Ωcm at 50 kHz (Ranck, 1963). Ranck calculated that the path of a low frequency current in the brain would be predominantly through the large volume low resistivity glial cells, as well as the lower resistivity extracellular fluid space and blood volume. This is because although the blood and ECS have a lower resistivity than glial cells, they have less conductive volume, and therefore bulk current flow would be through the glial cells. The reason that glial cells conduct current is that they are permeable to potassium and chloride ions (Lux et al., 1986), unlike the neuronal cells which have a highly insulating membrane which is only permeable to ions during depolarisation with the action potential or during cell energy failure. This explains why in healthy brain, there is only a small amount of current that will conduct through the intra-cellular space of the neuronal cells due to their high membrane resistance. Some conduction does occur through neuronal cells, due to those nerves which are aligned with the direction of current flow; in this scenario the surface area of the cell membranes "seen" by the current is very large, and despite a high resistivity, the resistance to current is low.

Changes in impedance would therefore be expected from changes in blood volume, neuronal cell size, and the size and concentration of ions within the extracellular current. Such changes may arise directly from the neuronal activity, for example during sensory stimulation or during epilepsy, or the impedance changes may arise from the vascular changes of blood flow and blood volume that are a secondary consequence of neural activity. The physiology of these changes will be briefly considered later in section 1.2.7.

1.2.4 Brain Imaging Systems

Several techniques have evolved in the last seventy years after Hans Berger's measurement, which allow non-invasive diagnosis of brain conditions. The most widespread of these techniques has been EEG for continuous monitoring of cortical function. In the last twenty years, anatomical imaging techniques such as Computer Tomography (CT) and Magnetic Resonance Imaging (MRI) have become accepted into clinical practice (Gibson, 2000). More recently, functional MRI and Positron Emission Tomography (PET) have been developed for imaging functional activity (Gibson, 2000).

The aforementioned techniques, whilst undoubtedly revolutionizing neurology and improving the diagnosis of brain disorders, invariably require large, expensive and immobile equipment. EEG is portable but does not as yet offer clinically useful images and is sensitive only to activity in the brain (Gibson, 2000). There remains a niche for small, low cost, and portable brain imaging system, which could be used at the bed- or cot-side in hospitals and even in ambulances and remote areas.

To improve upon the limitations of those techniques, Holder (1987) suggested that EIT might provide such a system. However, the techniques developed for EIT are still at the research stage and have not yet been adopted as an established medical imaging modality.

1.2.4.1 Electrical Impedance Tomography

Electrical Impedance Tomography (EIT) is an imaging modality that estimates the electrical properties at the interior of an object from measurements made on its surface. Typically, currents are injected into the object through electrodes placed on its surface, and the resulting voltages are measured. In other words, this technique can be classified as injected-EIT (Rigaud and Morucci, 1996) as the probing current is applied to the volume conductor via surface electrodes. Alternatively, coils can also be placed around the object for current generation. Such approach can be classified as induced-EIT (Freeston and Tozer, 1995). In either case, the

sensitivity of peripheral voltage measurements to conductivity perturbations is position dependent and poor for inner region (Birgul et al., 2003).

In this thesis, injected-EIT technique was used where an appropriate set of current patterns, with each pattern specifying the value of the current for each electrode, was applied to the object. A reconstruction algorithm uses knowledge of the applied current patterns and the measured electrode voltages to solve the inverse problem, computing the electrical conductivity and permittivity distributions in the object. This inverse problem is significantly more difficult than that for a modality such as X-ray computed tomography where the photon paths are essentially straight lines. In EIT, the current flow is determined by the impedance distribution within the object. Additionally, the problem is ill-posed (detailed explanation in section 2.3), meaning that large changes in impedance at the interior of the object can result in only small voltage changes at the surface.

1.2.4.1.1 Categories of EIT systems

EIT systems can be categorised in several ways, which are static, dynamic and multi-frequency imaging systems.

1.2.4.1.2 Static EIT

Static, otherwise known as absolute system is one, which usually produces an image of the absolute value of either the resistivity or conductivity or impedivity of tissue. This type of image is not easy to produce, largely because of the difficulties in taking body shape into account. This approach is suited to the breast as it can be deformed around a fixed array of electrodes, and therefore a similar electrode and breast model used in the reconstruction algorithm. However, this approach is less suited for non-deformable parts of the body such as the head and chest, in which it is difficult to apply electrodes in a symmetrical ring, and in addition it is difficult to record the three-dimensional position of the electrodes with such accuracy. Whilst some images have been produced either by applying current patterns, the

images produced are as yet difficult to interpret and the associated systems are not commercially available for clinical use (Giffiths et al., 1992; Jossinet and Trillaud, 1992). In this category, current is applied through many electrodes in a trigonometric pattern designed to maximize sensitivity throughout the object. Examples of this are the ACT or ACT3 systems at the Rensselaer Polytechnic Institute in the USA (Saulnier and Blue, 2001).

1.2.4.1.3 Dynamic EIT

A dynamic system is one, which only attempts to image changes in resistivity or impedivity. This is rather a simpler task than producing static image because the shape of the body has a much smaller effect on the image. A dynamic imaging system collects data over time in order to observe relative changes in impedance. The main reason for imaging dynamic impedance changes is to eliminate or reduce reconstruction errors that occur due to differences between the mathematical reconstruction model of the object and the actual object imaged. The commonest errors that exist between the model and the object imaged are the impedance of the electrode skin interface, the difference in shape between the object and the reconstruction model, and errors in electrode position (Barber and Brown, 1988). To reduce these errors impedance changes are reconstructed with reference to a baseline condition: if the electrode placement errors in the baseline images and the impedance change images are the same, then these errors cancel if only *impedance change* is imaged (Barber and Brown, 1988). Although the dynamic imaging approach minimises reconstruction errors, it does limit the application of EIT as it can only be used in conditions in which an impedance change occurs over the short time course of the experiment. The reason that a short time course is required is due to the phenomenon of electrode drift, in which the impedance of the electrode/skin interfaces changes with time. Over short periods of a few minutes, this drift is either negligible or is approximately linear and can be corrected, however longer intervals produce larger, non-linear changes which will result in reconstruction errors. An example of this is the Sheffield Mark 1 system (Barber and Seagar, 1987).

1.2.4.1.4 Multi-frequency EIT

The purpose of multi-frequency EIT is to measure the changes in electrical conductivity with frequency, which occurs in biological tissues. This technique uses the different impedance characteristics of tissues at different measurement frequencies and therefore an impedance contrast at different frequencies (Gabriel et al. 1996). An example of such a contrast would be the difference between cerebro-spinal fluid (CSF) and the grey matter of the brain. As the CSF is an acellular, ionic solution, it can be considered a pure resistance, so that its impedance is identical and equal to the resistance for all frequencies of applied current. However, the grey matter, which has a cellular structure, has a higher impedance at low frequencies than at high frequencies (Ranck, 1963). This difference arises due to the high capacitance of the cell membrane. The impedance of a capacitor, C, is given by

$$\mathbf{Z} = \frac{1}{j\omega C}$$

where ω is the frequency of the applied current. The complex number, j, indicates that the impedance of a capacitor will cause the phase of the voltage across the capacitor to lag behind the phase of the applied current by π. At low frequency currents, the impedance is high, and at high frequency currents the impedance is low. This frequency difference can theoretically be exploited to provide a contrast in the impedance images obtained at different frequencies, and provide a means of identifying different tissues in multifrequency EIT image. Some EIT work has now taken advantage of the different frequency responses of tissues to perform difference imaging between different frequencies (Kerner and Hartov, 2001; Kerner and Hartov, 2002). This technique, if successful in brain impedance imaging, has the potential to image longstanding changes in the brain, such as tumours, cysts and stroke.

However, systematic measurement errors arise due to changes in the response of the data-collection system with frequency, and these must be quantified before the accuracy of tissue measurements can be known. A major cause of systematic errors is stray capacitance in the 'front end' stages of the electronics. The problem is that if the errors are not exactly the same

for all drive/receive combinations, the error background on the image will be non-uniform giving rise to spurious features which can be confused with true, localized changes in the tissues. Such errors can readily be observed by forming dual-frequency images (one frequency referenced against another) of an object whose conductive properties do not change with frequency, such as a tank of saline solution (Schlappa et al., 2000). An example of this system is the Sheffield Mk3.5, which uses eight electrodes and an adjacent drive/receive electrode data acquisition protocol to deliver packets of summed sine waves at frequencies between 2kHz and 1.6MHz (Wilson et al., 2001).

1.2.4.2 EIT systems at UCLH

There are three EIT systems being used by the UCLH-EIT group. These are the HP-EIT, UCLH Mark 1b, and UCLH Mark 2.

1.2.4.2.1 HP-EIT

Tidswell and Gibson (Tidswell and Gibson, 2001) published human images by using HP 4284A Impedance Analyser (Hewlett Packard http://www.hewlettpackard.com). This was modified in order to switch through different combinations of 4-terminal impedance measurements using 31 electrodes placed on the head. In a 4-terminal impedance measurement, two drive electrodes deliver current while the potential difference is measured between the other measure electrodes. Current was delivered at 50 kHz with a magnitude of between 1 and 2.5 mA using combinations of electrodes that were diametrically opposed to one another.

1.2.4.2.2 UCLH Mark 1b

The UCLH Mark 1b system can address up to 64 electrodes independently and employs a single 4-terminal impedance-measuring circuit and cross point switches, which can be controlled using software installed on a laptop. The electrodes are connected from the scalp to a head-box the size of a videocassette, which is worn by the subject. This, in turn, is connected by a 10m-ribbon cable to a base box, the size of a video recorder, which works at 18 single frequencies that can be chosen over the frequency band between 77Hz and 225 Hz (Yerworth *et al.*, 2002). The long lead allows the patient to be ambulatory and the size of the equipment allows the system to be portable.

The magnitude of the impedance is measured using a synchronous-demodulation voltage sensing circuit. Since signal phase is dependent on the positions of the drive and measure electrodes, and on the characteristics of the object under study, a phase shift is selected as optimal for each measurement combination so that demodulation occurs in-phase with the signal. Gain is also selected in order that the digitized voltage represents a sizeable proportion of the full range and digitization noise is minimized on the receive side. More than 600 hundred measurements can be made every second. The protocol used presently requires 258 measurements to be made during acquisition of one image. This takes just over 0.4s.

1.2.4.2.3 UCLH Mark 2 – EITS of the Human Brain

A new multi-frequency EIT design had been developed at UCL, which adapted the Sheffield Mark 3.5 system for use with up to 64 electrodes (Yerworth *et al.*, 2002). Cross point switches were added to a single current/receive module, on this system, in order to allow selection from any combination of 32 available electrodes and to produce what is known as the UCL Mark 2 system. The system was successful in producing multi-frequency images of cylinders of banana with diameter 10% the diameter of a saline-filled spherical tank.

1.2.4.3 Inherent Difficulties in EIT

Despite EIT being non-invasive, inexpensive, portable and potentially highly informative medical imaging modality, there are several factors which limit its performance, and stand in the way of its adoption as a clinically standalone and viable technique (Frerichs, 2000; Holder, 2001; Morucci and Rigaud, 1996). These limitations may be classified into two main groups as physical and mathematical. While the physical limitations could be addressed to some extent by improvements in instrumentation, the mathematical limitations are fundamental. Any attempts to mitigate them in the reconstruction procedure involve various and often undesirable performance compromises. Consequently, these two classes of limitations are coupled in a fundamental way such that an attempt to mitigate the second by modifying the acquisition often aggravates the first.

1.2.4.3.1 Physical limitations

Most of the physical limitations are directly related to the electrode-body interface. They rather include variability and poor reproducibility of imaging inner-body organs and tissues, which are attributed to problems associated with the electrode placement and the electrode-tissue impedance (Rigaud and Morucci, 1996; Kolehmainen et al., 1997; Baysal and Eyuboglu, 2000). These are a source of uncertainty and noise in the EIT measurements. In spite of improvements in instrumentation over the years, the reconstruction of the admittance or conductance distribution image is performed, therefore, in a noisy low signal-to-noise ratio (SNR) environment (Boone and Holder, 1996a; Rigaud and Morucci, 1996).

1.2.4.3.2 *Mathematical limitations*

The mathematical limitations are associated with the inverse problem of determining the admittance or conductance distribution $\sigma(x,y,z)$ in the imaged object Ω from boundary measurements of current i_e and voltages v_e. Assuming probing at all points of the boundary $\partial\Omega$, this inverse problem is ill-posed due to instability such that a small error in the

measurement produces arbitrarily large errors in the reconstruction of $\sigma(x,y,z)$ (Levy et al., 2002). Even though stability can be restored by sufficiently restricting the class of admissible $\sigma(x,y,z)$ to for example smooth $\sigma(x,y,z)$, these results use very high spatial frequencies in the imposed boundary conditions, which are impractical with a finite electrode system.

In practice, currents are applied and the voltages measured using a finite number N_e of discrete electrodes. It is only possible to determine a finite number $d = \frac{1}{2}N_e(N_e - 1)$ of degrees of freedom (DOF) in $\sigma(x,y,z)$. Irrespective of the measurement noise level, this results in images with resolution limited to no more than $N_t = d$ independent resolution cells. Hence, increasing the number of image resolution cells calls for many small, closely spaced electrodes. This requires reduced electrode area, thus increasing the electrode-skin impedance, with associated increase in skin current density, noise, and errors.

An attempt to increase the resolution will also be hampered in a more fundamental way, which is related to the continuous version of the problem. Even if the number of pixels, N_t in the image is low enough to guarantee a unique solution for a discretized version of the problem is ill posed, the finer the discretization, the more severe the ill conditioning.

The problem of ill conditioning is closely related to a high sensitivity of the measured data at the boundary surface to changes of the impedances in areas near the body surface, while there is low sensitivity to changes of impedances in areas deep within the body (Yorkey et al., 1987; Woo et al., 1993). A look at the Jacobian J, reveals that large singular values of it are attributed to the impedances near the body surface while the small singular values are attributed to impedances deep within the body. The upshot of this is that while acceptable resolution may be achieved near the surface of the object, high-resolution reconstruction of the internal structure near its centre, which is often of the greatest interest, is immensely difficult (Levy et al., 2002). The noisy measurements and the poor conditioning of the problem, combined with its nonlinearity, present a challenge to reconstruction algorithms. Although significant

progress in various aspects of reconstruction algorithms and optimal current excitation has been made over the years, the noise and conditioning problems remain the fundamental difficulties (Levy et al., 2002).

With the inherent difficulty of sensing admittance information in the interior of the object using boundary voltage information, a number of researchers proposed a number of solutions by using different imaging techniques.

1.2.4.4 Clinical Uses of EIT

Biological tissues have a wide range of resistivities. This implies that good tissue contrast can be obtained in EIT imaging. Sudhakar Bhar has identified thirteen major areas where EIT can be used for clinical applications at low cost and without any known hazard. EIT has been used in a number of applications, where in some, only the resistive component of the impedance is estimated and the technique is called Electrical Resistance Tomography (ERT). This is typically used for geological applications. In other cases, only the reactive component of the impedance is estimated and the technique is known as Capacitive Tomography. Its application includes imaging of multiphase fluid flow in the process industry.

Another application of EIT is imaging of the human body where EIT has the desirable property of not requiring exposure to ionising radiation. This property, combined with relatively low cost of EIT instrumentation, makes it attractive for continuous monitoring of patients (Bayford *et al.*, 1995). Among the possible medical applications for EIT are monitoring for lung problems, such as accumulating fluid or collapsed lung, non-invasive monitoring of heart function and blood flow, monitoring for internal bleeding, screening for breast cancer, studying emptying of the stomach and pelvic fluid accumulation as a result of pelvic pain. Other applications of EIT are quantifying severity of pre-menstrual syndrome by determining the boundary between dead and living tissue, measuring local internal temperature changes associated with hyperthermia treatments or cryosurgery, and improving electrocardiograms and electroencephalograms (Webster, 1990).

The other areas where EIT is also applicable are in apnea monitoring, stomach emptying, and bladder volume. It can also be used to monitor total body water (TBW) and body fat, fracture healing and impedance changes in the head that constitute brain imaging. The potential applications of EIT in imaging brain function include normal activity or neurological conditions such as stroke or epilepsy (Webster, 1990).

1.2.4.5 Induced-current electrical impedance tomography (ic-EIT)

In induced-current electrical impedance tomography (ic-EIT), electrical currents are induced in the region to be investigated by time varying currents in coils external to the region, and the resulting potential differences between adjacent peripheral electrodes are measured. The coil is moved to different positions, or several; somewhat differently positioned such coils are used to generate independent excitations. Electrodes similar to those in EIT pick up the electric potentials that develop on the boundary of the object due to the currents induced in the object by the magnetic field. The method of ic-EIT is excitation by magnetic and the pickup is electric. Compared with the injected current method, these measured voltages, together with knowledge of the current distribution in the region, are used to determine the distribution of conductivity within the region.

Freeston and Tozer (1995) used this method coupled with an algorithm based on sensitivity matrix to image distribution of conductivity in a 2D phantom. They observed that the use of induced currents has a number of features, which make it a possible alternative to injected currents in some applications (Freeston and Tozer, 1995). These features are as follows:

1 The currents in the region to be studied are not limited by the current density at the electrodes, and therefore it is possible to use larger current densities with a corresponding increase in signal to noise ratio

2 The electrodes on the periphery of the region are used only to sense the voltage, and not the current drive, and hence the electronics close to the electrodes can be designed for this one function. In some injection systems, separate electrode sets are used for the

current drive and voltage measurements, but this increases the number of cables linking the target and instrumentation, and the number of electrode attachment

3 Increasing the number of external coils can increase the number of independent measurements, and the number of electrodes does not limit this. In principle, it is possible to manipulate the distribution of current within the region being investigated to interrogate a particular part of the region in detail.

This method is reported to allow better control of currents in the centre of the object and, therefore, improved imaging in this region (Levy et al., 2002). This has been supported by an analysis of the distinguishability of an isotropic concentric homogeneity (Eyuboglu et al., 2000; Levy et al., 2002).

In spite of these advantageous features, one practical difficulty with the induced system is that the time varying magnetic field will induce electromotive force (emf) in the measuring circuits and so cause spurious results. However, it is possible to reduce the error signals to acceptable levels by careful attention to the location of the cabling between the target and instrumentation(Tozer *et al.*, 1992; Tozer, 1992). Levy et al., also observed that the resolution offered by this method is limited, at least in part owing to the difficulty of synthesizing a large number of independent measurements by the external coil (Levy *et al.*, 2002).

1.2.4.6 Magnetoencephalography (MEG)

The purpose of brain imaging is to map the internal structure of the brain and to localise areas of dysfunction using non-invasive measuring techniques. MEG (Figure 1-5) is a non-invasive technique for localising and characterising the electrical activity of the central nervous system by measuring the associated magnetic fields emanating from the brain.

Figure 1-5: A subject in a typical magnetoencephalogram (NTF 275)

The longitudinal neuronal current flow generates an associated magnetic field. Though, this magnetic field is very weak to order of femto Tesla, it can be detected by SQUIDs (Hamalainen et al., 1993). Figure 1-6 shows that the fluctuations in the earth's magnetic field, or the magnetic disturbances from electrical appliances, power cables and traffic are of the order many times higher than neuro-magnetic signals generated by the brain.

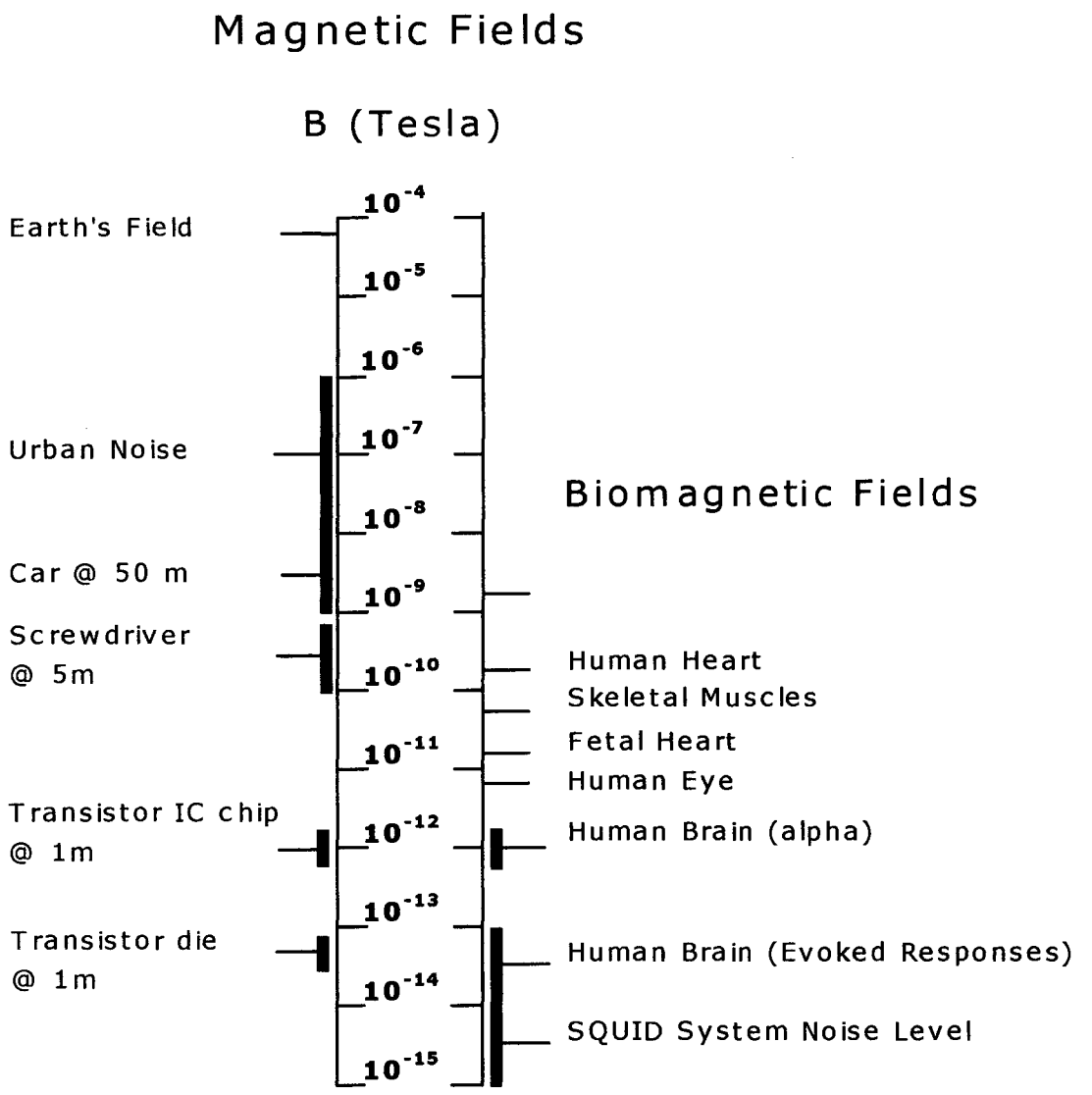

Figure 1-6: Magnetic Fields

In biomagnetic measurements, two kinds of detectors are used. These are axial and planar gradiometers. Two kinds of measurement systems are used in the most advanced MEG experiments. Clinical-type measurements are made with a whole-head mapping system, which has a very large number of channels (more than 100) in a helmet-like dewar (Figure 1-7)

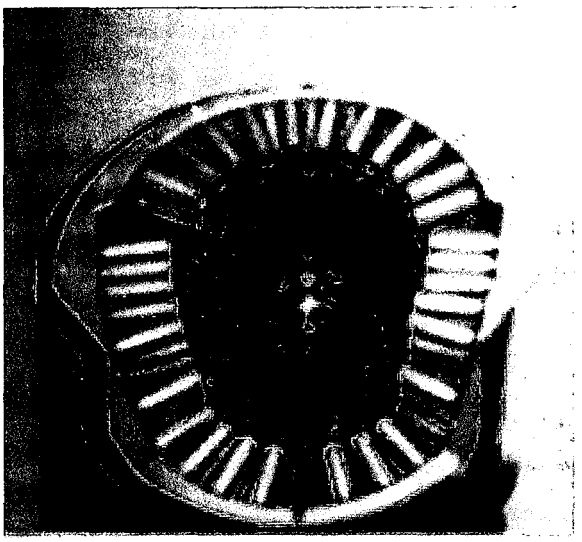

Figure 1-7 Magnes 3600 248 MEG Channels

Regardless of whether the detectors in the whole-head system are axial or planar gradiometers, differences between signals from adjoining channels are usually calculated during signal analysis (Malmivuo *et al.*, 1997). Another important MEG instrument design is the micro-SQUID, in which the detector coil is situated in vacuum space allowing measurements at very small measurement distances, being down to 1.5 mm from the scalp. The coil radius is approximately 1 to 2 mm. Such a device has only a few channels and it can be used only in a limited region of the head at a time (Malmivuo *et al.*, 1997).

A third possible MEG system, which is being developed, is the electric potential probes. These are electrometer-based sensors, which combine remarkable sensitivity with extremely high input impedance. These sensors have been demonstrated to need only modest electrostatic shielding even at the highest levels of sensitivity. They can operate under room temperature and do not need cryogenic conditions as in SQUIDs (Harland et al., 2001).

Biological events generate magnetic signals that can be measured at the skin surface. Some of the first measurements of biomagnetic activity were cantered on measuring magnetic signals being given off by the heart muscle. It is possible to have cranial recordings of biomagnetic

activity. In principle, whenever there is a voltage change due to ionic flow through a neuron cell's membrane, it generates an electrical signal, which in turn generates a magnetic signal. Therefore, magnetic signal (MEG) is generated by the same kinds of neuronal changes that generate EEG and Evoked Response Potentials (ERPs) (Hamalainen et al., 1993).

1.2.4.6.1 Similarities between ERP and MEG

Both Evoked Response Potential (ERP) and MEG are fairly direct measures of Central Nervous System (CNS) activity that underlies cognitive processing, and can provide high spatial resolution because they have a high temporal sampling rate. They seem to be measuring the same kind of cognitive events and therefore, presumably are measuring the same dipole sources, and can be combined with MRI to provide an estimate of source localization.

1.2.4.6.2 Advantages of MEG over ERPs

The biggest advantage that MEG has over ERP is that the tissue that they pass through in the brain does not distort the generated magnetic fields. However, electrical currents are distorted because the primary current, which is generated by the cognitive process that we wish to study, can cause secondary currents, which are not associated with neuron activity, but they look like primary (cellular generated) currents. When the electrical activity is measured at the scalp, it is the effect of measuring both primary and secondary currents. Electrical currents are also distorted because the brain and skull tissues are not uniform in their conductive properties. The tissue itself distorts the signal. These problems make it very difficult in determining where in the head the electrical signal is coming from (the inverse problem) (Griffiths *et al.*, 1992).

1.2.4.6.3 Disadvantages of MEG

MEG equipment is very expensive, large and cumbersome to use. The signal to noise ratio is much worse than for ERPs, and brain magnetic fields are often a billion times or more smaller than the background magnetic noise (figure 1-6).

1.2.4.6.4 Measuring MEG

Three necessary tools are needed for MEG research, namely: a magnetically shielded room, SQUID and Gradiometers. The only way to measure the tiny magnetic fields generated by the neurons of the brain (which measure around a few hundred fTesla) is to measure the fields using a SQUID and reduce the background noise as much as possible. In order to reduce background magnetic "noise" the process should be carried out in a magnetic shielded room and more gradiometers are used to reduce noise. Basically, the gradiometer selectively cancels out distant magnetic signals and the number of gradiometers acts something like the number of electrodes in ERPs.

1.2.4.6.5 Applications of MEG

MEG has been used for several clinical applications, providing information on diseases of the brain and helping to plan appropriate treatment. The most typical applications are epilepsy treatment, location of lesions and tumours and preparation for neurosurgery.

1.2.4.7 The SQUID

The SQUID is the bedrock of MEG. This is a highly sensitive magnetic sensor, which can detect magnetic fields less than one fifty millionth (1/50,000,000) of terrestrial magnetism. SQUID utilizes the quantum effect of superconductivity and is more than three orders higher in sensitivity than conventional magnetic sensors.

1.2.4.7.1 Principles of SQUID Operation

A SQUID is made of a superconducting thin film using photolithography to create parallel Josephson junctions as shown in Figure 1-8. When the bias current, I_b, is applied to the SQUID, voltage across the SQUID is zero if the current is less than critical current.

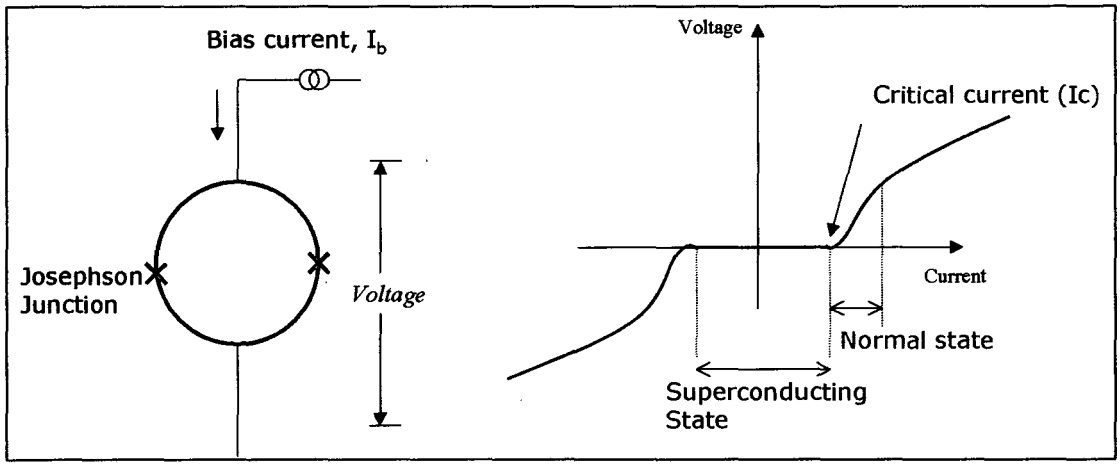

Figure 1-8: Principles of SQUID operation

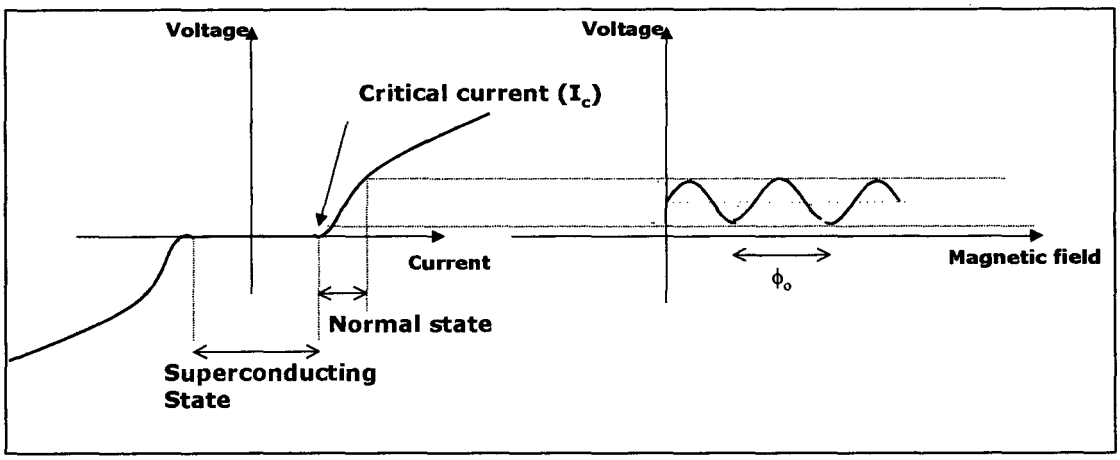

Figure 1-9: Flux Quantisation

When the bias current exceeds critical current, I_c, the SQUID turns to the normal state and voltage is produced. When a flux is introduced into the SQUID loop, the critical current decreases.

When the bias current is fixed at a slightly higher value than the critical current and an external magnetic field is applied, the voltage will change in a periodic wave in accordance with the flux quantisation as shown in Figure 1-9. In other words, the voltage is periodic with changing flux (Swithenby SJ, 1980; Tesche and Clarke, 1977). The magnetic field can be measured by monitoring the change in voltage.

1.2.4.7.2 Scheme of Control Detection Electronics of SQUID

Usually, the SQUID is used as a zero-detector, that is the flux in the SQUID is kept constant by compensating the change in the magnetic flux by coupling it back through an integrator (Clarke, 1977).

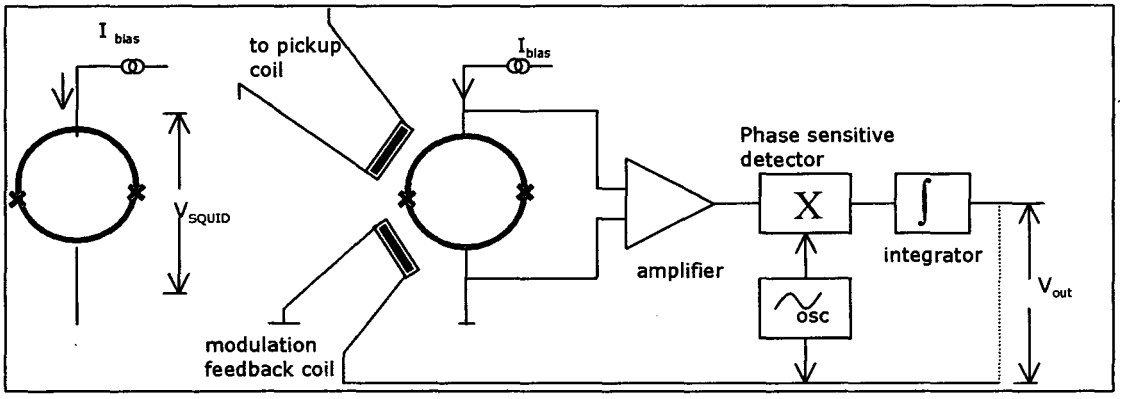

Figure 1-10: SQUID sensor electronics

The output of the integrator is a measure for the change in the magnetic flux. Usually, the SQUID is operated in a flux-locked loop, whereby a modulation frequency is applied. Phase sensitive detection is used to retrieve the output voltage of the SQUID as shown in Figure 1-10.

1.2.4.8 Flux Transformers

The flux is fed into the SQUID by means of a flux transformer to reduce interference. There are many forms of such flux transformers depending on their ability to reduce external magnetic fields. Their arrangement consists of pick-up coils and a signal coil, which are inductively coupled to the SQUID. The magnetic signals from the brain are extremely weak as compared with ambient magnetic field variations (see Figure 1-6). A SQUID is very sensitive to magnetic field changes and so it must be shielded. Typical values for magnetic fields

produced by power wiring and equipment in a modern building are 5 x 10^5 pT at 50/60 Hz (Brown et al., 1999). Thus rejection of outside disturbances is of paramount importance.

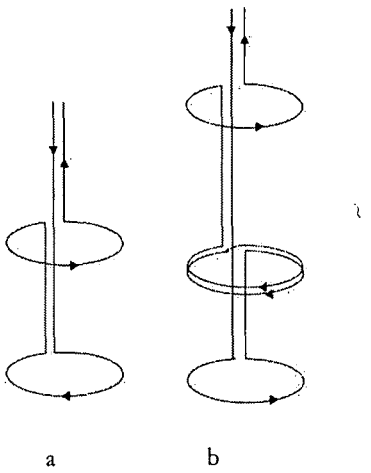

Figure 1-11: Flux Transformers a: an axial first order gradiometer which measures $\frac{\partial B_z}{\partial z}$ (approximately Bz at the lower loop) b: second order series axial gradiometer

Significant noise is caused, for example, by fluctuations in the earth's geomagnetic filed, by moving vehicles and elevators, radio, television, and microwave transmitters, and by the omnipresent power-line fields. The electrical activity of the heart also generates a field, which on the chest is two to three orders of magnitude larger than the signals from the brain outside the head.

The sensitivity of the SQUID measuring system to external magnetic noise is greatly reduced by the proper design of the flux transformer, a device normally used for bringing the magnetic field signal to the SQUID. For example, an axial first order gradiometer consists of pickup (lower) coil and a compensation coil, which are identical in area and connected in series but wound in opposition (Figure 1-11a). This system of coils is insensitive to spatially uniform changes in the background field, but responds to inhomogeneous changes. Therefore, if the signal of interest arises near the lower coil, it will cause a much greater change of field in the

pickup coil, thus producing a net change in the output. In effect, the lower loop picks up the signal, while the upper compensates for variations in the background field. Gradiometers, thus make the measuring device particularly sensitive to nearby sources (Carelli et al., 1983). The flux transformers are, just like the SQUIDs, superconducting, which means that they must be immersed in liquid helium, which has a temperature of 4.2 K.

Figure 1-11(b) shows a second-order axial gradiometer in which two first-order gradiometers are connected together in opposition so that the detection coil is insensitive to both homogeneous fields and uniform field gradients. This arrangement further improves the cancellation of magnetic fields generated by distant sources. A shortfall of higher order gradiometers is that to avoid reduction of the signal energy coupled to the SQUID the height of the coil may become practically long.

1.2.4.9 Electroencephalography (EEG)

Electrophysiological methods have been used to study brain function, over milliseconds, of individual neurons. Their depolarisation, or "firing", is well understood, as is the integration of signals on their cell projections, dendrites, from the synapses of neighbouring neurons. A neuron abhors vacuum and brain function depends on the spatial and temporal synchrony of large populations of neurons.

Local behaviour of many neurons has been studied using depth electrodes but the electrical signature of neuronal activity can also be detected on the surface of the cortex (an electrocortigogram, ECoG) or with scalp electrodes (an electroencephalogram). EEG, which is the most widespread monitoring technique, measures voltage, changes on the scalp providing information about the electrical activity of neurons near the surface of the cortex. EEG can be used to study a subject's response to visual, auditory or somatosensory (touch and movement) stimulation, or to detect abnormal activity associated with epilepsy or encephalitis.

The magnitude of the signal depends not only on the number and location but also the geometry of the synchronously firing neurons, since it is possible for many arrangements to generate currents so that their associated potential distributions cancel. Therefore, EEG is sensitive to the dendritic currents of active pyramidal neurons, oriented parallel to each other so that their potential distributions do not cancel. Temporal resolution is high and data are normally collected at a sampling rate of around 250Hz, sufficient to describe a 70ms interictal spike, common in epilepsy, with over 17 data points. However, while EEG successfully localises active areas of cortex close to the skull, localisation of deep activity is less reliable. EEG is non-invasive and safe. It is also inexpensive and widely used as a clinical tool. It is, however, difficult to detect signals from neurons deeper in the brain, and spatial resolution is poor.

EEG can be used as a parametric or an imaging tool in the estimation of EEG sources in the brain (Baillet and Mosher, 2001). In the former, also called inverse dipole modelling, it is assumed that the electrical activity in the cortex can be represented by a few equivalent dipole sources. The number, localization, magnitude and orientation of these are estimated, iteratively, until the calculated potential distribution matches best the measured voltages at the scalp electrodes. As an imaging tool, dipoles are assigned to each tessellated element on the cortical surface and are oriented perpendicular to that as are the pyramidal sources. Only the amplitudes are unknown and these are varied again until the calculated potential distribution best matches the data. For parametric modelling, since the activity in the cortex is distributed, it can be that a single dipole cannot adequately represent an active section of cortex or that the dipole that does so exists outside the head! It is also found that the more dipoles a model guesses, the less successful it is. For source imaging, the number of unknowns is two orders of magnitude higher than the number of electrodes so the problem is severely underdetermined and though mathematically difficult but solvable. Associated also with neuronal depolarisation are metabolic demands, met in the active area, by increased regional cerebral blood flow (rCBF). Several techniques rely on the change in tissue characteristics caused by this increase and are listed briefly in the next section.

1.2.4.10 Positron Emission Tomography

Positron Emission Tomography (PET) can be used to image blood flow or metabolism, closely coupled to neural activity (Jueptner and Weiller, 1995) and has been a great aid to cognitive neuroscience (Fox and Raichle, 1984; Raichle, 1998). For perfusion studies, the source of positrons could be emission by the injected radiopharmaceutical $H_2{}^{15}O$, which can be easily produced and which has a half-life of about two minutes, enabling many repeat experiments in the same subject. Also used are the radionuclides Carbon-11, Nitrogen-13, and Fluorine-18. Pairs of photons produced by annihilation are emitted at 180° to each other so that the site of the event can be deduced from the timing and location of their detection. The theoretical limit of spatial resolution of this technique is 2-3mm because this is the distance the emitted positron travels before it is annihilated. However, in practice, the technique has a resolution of about 6-mm.

1.2.4.11 Single Photon Emission Computer Tomography (SPECT)

Similar to PET, SPECT acquires information on the concentration of radionuclides introduced to the patient's body. However, because only a single photon is emitted, a collimator is required in order to know the direction from whence the photon came. Where PET might employ 500 detectors, only 3 collimators might be used in SPECT. Detection efficiency is greatly reduced and, consequentially, so too are sensitivity and resolution (about 7mm) (Wirestam *et al.*, 2000). However, SPECT can be performed at approximately one-third the cost of PET due to the nature of SPECT instrumentation and the availability of the appropriate nucleotides such as Xe-133 (Wirestam *et al.*, 2000).

1.2.4.12 Functional Magnetic Resonance Imaging (fMRI)

The dynamic version of MRI is functional MRI. This relies, once again on paramagnetic contrasts within the brain. Here the source of contrast is not the variation of anatomical tissue but of rCBF, changes in which can be detected either by paramagnetic labelling of blood entering the brain or by blood deoxygenation contrast since HbO_2 is paramagnetic and Hb is not (Jezzard and Turner, 1996). The latter is known as the blood oxygenation level dependent or BOLD signal. fMRI has led the way in examination of cognitive function, along with PET but it is fMRI that is the main tool for research imaging of normal brain function. It is a non-invasive technique, which has high sensitivity and a spatial resolution of about 1 mm (Wirestam *et al.*, 2000). Its temporal resolution, seconds, is adequate to record rCBF changes which occur over several seconds. The disadvantages of fMRI are its expense and its requirement of a dedicated, shielded room - it is estimated that image acquisition from one subject costs £600 (Malmivuo *et al.*, 1997).

1.2.5 Integrated Imaging Systems and their applications

For a better understanding of the functioning of the brain, imaging modalities should be able to localise sources of electric and magnetic activity with a reasonable spatial resolution and an excellent temporal resolution. It has been realised that a single imaging modality is either efficient in terms of temporal resolution or spatial resolution. Many multidisciplinary research groups, during the past few years have tried to combine imaging modalities in order to improve upon image qualities. Figure 1-12 gives an indication about some of the modalities that have been integrated.

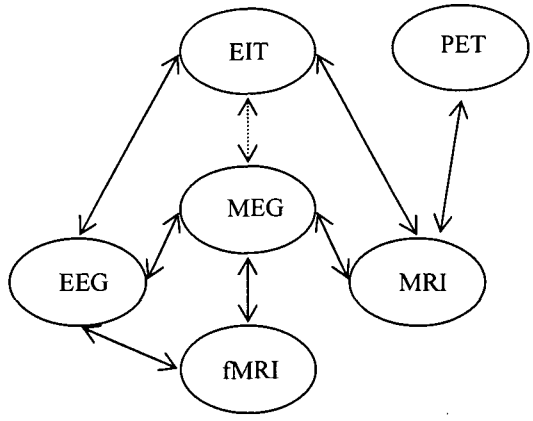

Figure 1-12: Systems already integrated are shown with thick lines, the dotted is currently under study.

Walter et al. in 1992 have demonstrated the merging of PET data with MRI and MEG data (Walter et al., 1992). They localised sources from magnetic responses due to voluntary movement of the right foot, right thumb, right index finger and right cheek. Wieringa, J.H. in 1993, integrated MRI with MEG and EEG (Wieringa H.J., 1993). Wieringa constructed an algorithm to automatically establish a transformation from PET coordinates to MRI coordinates, and to display the PET data in colour in a transparent way over the MRI scan.

The UCLH group has been studying the feasibility of integrating MEG and EIT. The author of this thesis carried out this integration study, as EIT has a limitation when it comes to imaging small impedance changes in the head due to neuronal depolarization. It has also been found out that for dipole localization, using EEG only is inadequate, and so Boone et al. combined EEG and EIT in order to improve upon dipole localization (Boone K. and Holder, 1994).

Magnetic resonance–electrical impedance tomography (MR–EIT) was first proposed in 1992. In this study, a new imaging modality for high-resolution conductivity imaging is proposed. Both, the surface potentials and magnetic fields produced by the probing current are measured. Surface potentials are measured by using conventional electrical impedance tomography techniques and using magnetic resonance imaging techniques performs high-resolution magnetic field measurements. The conductivity distribution is reconstructed

iteratively, to minimize the difference between the current densities calculated based on the potential measurements and the magnetic field measurements. The proposed technique was tested on simulated data with or without simulated noise and it has been shown that absolute conductivity images with high resolution can be reconstructed (Zida Ider et al., 2003).

1.2.6 Electrical properties of tissue

The validation of measured values in this thesis depended largely on the realistic models of the conductive behaviour of the head at both microscopic and macroscopic levels. The impedance of living tissue has resistive and reactive components because of the presence of fatty cell membranes. For this reason, it is more difficult to pass current through it at lower frequencies than at high frequencies. At low frequencies, flow is generally restricted to the extracellular space but as frequency is increased, current begins to bypass the membranes and enter the cells themselves, resulting in a resistivity decrease. In the following, the reactive component is neglected and we may speak in terms of frequency-dependent resistivity rather than the complex impedivity.

Below are documented the many measured, macroscopic values of resistivity for each of the tissues present, the brain, CSF, skull and scalp.

1.2.6.1 The brain

It is difficult to compare the measurements made of the resistivity of cerebral cortex because they have been made using different electrode configurations and current frequencies. Ranck (Ranck, 1963) measured the resistivity of rabbit cerebral cortex to be 3.21 ± 0.45 Ωm at 5 Hz and 2.3 ± 0.37 Ωm at 5 kHz. He used two pairs of electrodes, one to deliver current and one to measure a potential difference between two points in the tissue. This is a four-terminal measurement, which avoids the effects of electrode polarization at low frequencies and can be taken to give a reliable result. In rats (Ranck, 1966), he determined cortical resistivity to be

around 2.5 Ωm using a similar method. VanHarreveld (VanHarreveld and Ochs, 1956) found it to be 2.30 - 2.85 Ωm by making measurements with two electrodes at 1 kHz on the surface of rabbit cortex and then comparing them with measurements on the surface of a block of agar of brain dimensions. Later he found the resistivity of rabbit's cortical tissue to be 2.08 ±0.06 Ωm at 1Hz using two depth electrodes, one deeper than the other along a line perpendicular to the surface of the cortex (VanHarreveld and Murphy, 1963). Freygang and Landau (Freygang and Laundau, 1955) used the four-electrode method and found cortical resistivity to be 2.22 ± 0.09 Ωm using pulses of constant current lasting between 0.3 ms and 0.7 ms. It is difficult to determine to which frequency this measurement equates because the membrane time constant, $\tau = RC$, for neurons is of order milliseconds so it is unlikely that the voltage induced by the constant current reached steady state while the pulse endured. A summary of the above results is given in Table 1-1.

Source	Animal	Resistivity (Ωm)	Technique	Measurement Frequency (Hz)
(Freygang and Landau 1955)	Cat	2.22 ± 0.09	4-electrode	
(VanHarreveld and Ochs 1956)	Rabbit	2.30 - 2.85	2-electrode	1000
(VanHarreveld and Murphy, 1963)	Rabbit	2.08 ± 0.06	2-electrode	1000
(Ranck, 1963)	Rabbit	3.21 ± 0.45	4-electrode	5
(Ranck, 1963)	Rabbit	2.30 ± 0.37	4-electrode	5000
(Ranck, 1963)	Rat	2.5	4-electrode	1.5 - 3000

Table 1-1: Reported values for the resistivity of grey matter

White matter has a resistivity several times higher than grey and, in addition, is highly anisotropic. Using the 0.3 - 0.7 ms pulse technique, the resistivity of cat white matter was found to be approximately 3.44 Ωm, almost double that of grey (Freygang and Laundau, 1955). Van Harreveld (1963) found the resistivity of rabbit white matter to be over 4 times that of grey. In their review, Geddes and Baker (1967) report values, averaged over low-frequency, body

temperature measurements on rabbits and cats, of 2.84 Ωm and 6.82 Ωm for the resistivity of grey and white matter respectively. In addition to this, they also report the ratio of transverse to longitudinal resistivities of this fibrous tissue range between 5.7 and 9.4.

1.2.6.2 The Cerebro Spinal Fluid (CSF)

The resistivity of CSF is 0.56 Ωm, as measured most recently by Baumann (1997) at body temperature. CSF is perhaps the most easily measured of the constituents of the head listed here.

1.2.6.3 The skull

Resistivity values for the skull range from 18 Ωm at 1MHz on freshly excised human bone tissue (Hemingway and McLendon, 1932) to approximately 90 Ωm for excised rat femur at 10kHz (Kosterich and Foster, 1983). Law (Law, 1993a) reported large variations in skull resistivity from site to site. Four-terminal measurements, made at 100Hz, revealed resistivities between 13.6 Ωm at a suture line and 214 Ωm at compact bone. The overall average was 75.6 ± 41.0 Ωm.

Assuming that dry skull is, effectively, an insulator, Rush and Driscoll (Rush and Driscoll, 1968) found its effective resistivity, when soaked with a conducting fluid, to be 80 times that of the fluid. If the fluid were to be CSF, the skull resistivity would be 45 Ωm. More recently, it has been suggested that the contrast between skull resistivity and that of brain was much less than was previously implemented in models (Oostendorp and Debelke, 2000). Specifically, a mathematical model of the head, used by Rush and Driscoll (Rush and Driscoll, 1969), and others subsequently, assumed a ratio of 1/80 between brain and skull resistivity. Rather, Oostendorp et al. (2000) suggest, this should be modelled as the contrast between CSF and skull. Their 100Hz - 10kHz measurement of 66.7 ± 13.0 Ωm (2000) is, respectively, about 14 and 120 times greater than the resistivity values reported above for brain and CSF, and it is very similar to that of Law.

The anisotropy of bone is well demonstrated by the results of Saha and Williams (Saha and Williams, 1992) who made measurements at 100kHz on the tibia bone to find the axial, circumferential and radial mean resistivities to be 16, 158 and 215 Ωm.

1.2.6.4 The scalp

Only a single measurement of conductivity of scalp has been generally cited (Burger and Milaan, 1994) but researchers often use a value of 2.27 Ωm as the average of skin and muscle.

1.2.6.5 The blood

Whole blood consists of erythrocytes (containing haemoglobin) and other cells in plasma. The erythrocytes have shapes resembling doughnut with an outer diameter of about 10 μm. Plasma forms the liquid part containing electrolytes and large organic electrically charged molecules. Lysed erythrocytes are disrupted cells with their intracellular material (haemoglobin) discharged into the liquid. The electrical properties of whole blood and lysed blood are naturally different. The resistivity of human blood is dependent on the amount of haematocrit (the percent of whole blood that is comprised of red blood cells). The haematocrit is a measure of both the number of red blood cells and the size of red blood cells. Resistivities of between 1.3 and 1.7 Ωm were measured by Rosenthal (Rosenthal and Tobias, 1948) for 37°C blood at normal levels (~ 40%) of haematocrit.

1.2.7 Resistance changes in the brain and their visibility using EIT

There are three categories of resistance changes in the brain that may be imaged using EIT, large, medium and small. In the subsections, which follow are brief looks at the theory of the changes, and a review of investigations made by the EIT community.

1.2.7.1 Large -Pathological resistance changes

Large resistance changes occur over seconds, minutes or hours due to cell swelling, or ischaemia. Here, metabolic demands are not met, due to the prolonged, repetitive activity during epilepsy, for example, or due to an interruption of the supply of oxygen-carrying blood, as in stroke (Lux, Heinemann et al. 1986). This results in anoxic depolarization. As a consequence, the active pumps fail to maintain the correct balance of ions inside and outside the neurons (homeostasis), and osmosis occurs (Hansen and Olsen 1980). This reduces the amount of extracellular space in the ischaemic region and increases its resistivity.

1.2.7.2 Neonatal intraventricular haemorrhage (IVH) and hypoxia-ischaemia

There is a high risk of intraventricular haemorrhage (IVH) in a neonate; however, an early diagnosis can lead to improved treatment. When blood displaces CSF, there is approximately a three-fold resistivity increase, which should be detectable using EIT. Another cause of disabling or fatal brain injury is hypoxia-ischaemia, caused by the lack of oxygen or blood to the brain at birth. Of great use in neonatal care would be a cotside system, such as EIT, that imaged the head continuously.

Neonatal imaging has mainly been confined to studies of the lungs (Brown, Primhak et al. 2002). However, some preliminary images were presented by Murphy et al. (1987), and numerous evoked response experiments have been performed on neonates by this group, though none have yet been published (Tidswell and Gibson, 2001).

1.2.7.3 Stroke

In treatment of stroke, it is important to know what type of stroke has occurred, ischaemic or haemorrhagic in order to know which drug to administer. For ischaemic stroke, blood is not reaching the damaged area to deliver the oxygen required for metabolism, resulting in apoptosis, a process of cell death. In this case, if a blood clot is causing the blockage, it is necessary to administer a thrombolitic drug to break it down, although the effectiveness of these drugs is greatly reduced after the first 3 hours. It would be extremely undesirable to administer such drugs if the stroke were to be haemorrhagic. EIT is a technique that could provide immediate and continuous bedside monitoring of stroke patients and would not require the expense and inconvenience of MRI.

Resistance increases of 15-60% were obtained by a 50kHz measurements on the cortical surface of anaesthetized rats with induced ischaemia (Holder 1993). Scalp measurements returned changes 5-10 times less than this, suggesting that it would be possible to image changes in resistivity caused by ischaemic stroke. These measurements were relative to a baseline, however, since baseline images cannot be acquired from a stroke patient it is thought that EITS (Brown and Primhak, 2002) will be a more appropriate technique for proper stroke diagnosis. Work is in progress at UCL to develop a multi-frequency system to produce static, tissue contrast images of stroke (Horesh et al., 2004).

1.2.7.4 Epilepsy

Focal epilepsy is a functional abnormality often related to a structural abnormality like a lesion, and an individual's seizure always originates from the same cerebral focus. For patients with intractable epilepsy, surgery is required to remove that part of the brain and accurate localisation of the epileptic focus is crucial before surgical excision. As mentioned above, the repetitive activity due to a focal seizure can cause local ischaemia, detectable using EIT (Lux, Heinemann et al. 1986). Continuous monitoring is necessary because the occurrence of seizures is so unpredictable, therefore EIT may be better suited than fMRI for localization of epileptic foci. At present, EEG inverse dipole modelling is used for such a purpose. Patients

have their epilepsy-suppressing medication suspended for a week prior to surgery, during which time they are monitored with EEG in order to gain as much electrical information as possible during seizure activity. This technique is quite successful for localisation of superficial foci but less so for foci situated deeper in the brain. For these, EEG electrodes are often implanted deep in the brain, a process, which can cause irreversible damage. EIT may provide a more powerful, as well as less invasive, alternative for their localisation.

Previous work with EIT involved the placement of electrodes on the exposed cortex of anaesthetised rabbits. This showed the magnitude of the conductivity changes during an induced epileptic seizure to be about 10% (Holder, Rao et al. 1996; Rao, Gibson et al. 1997; Rao 2000). Studies are being carried out at present using scalp EIT electrodes in addition to EEG electrodes to collect data from presurgical patients in the telemetry ward at King's Hospital (Brown and Primhak, 2002; Liston, 2003). Interpretable images have been obtained ictally, or during a seizure, from several subjects but none has been published as of yet.

1.2.7.5 Spreading depression and migraine

Cortical Spreading Depression (CSD) was first reported by Leâo (1944) and takes the form of a wave-front of intense electroencephalographic (EEG) activity, which travels at about 3mm min^{-1}. In the wake of this is left a depression of EEG activity, as cell swelling occurs, and a DC potential shift as the extracellular ionic content changes (Hansen and Olsen 1980). The propagation of the wave-front is thought to be caused by the passive diffusion of excitatory neurotransmitting substances ahead of the active region (Bures, Buresova et al. 1974). Study of the speed of propagation of the auras experienced by sufferers of migraine has suggested that the mechanisms for this may be similar to those for CSD but this yet to be confirmed (Welch, Barkley et al. 1337).

An accompanying resistivity increase occurs as a result of the cell swelling. At 1.6kHz this has been measured as a 100% change (Hoffman, Clarck et al. 1973) and as 40% at 50kHz (Ranck 1964). In experiments carried out by the UCLH-EIT group, Boone (1994; 1995) initiated an

episode electrically in 6 anaesthetized and paralyzed rabbits and, upon cortical measurement using a ring of 16 electrodes, observed resistivity increases in reconstructed APT images of 5-20%, moving at 2-5mm/min. Most recently, Yoon (1999) measured a conductivity decrease at 100kHz of 5%, with a latency of 30-60s, followed by a change of 34% with a latency of 200-300s.

1.2.7.6 Medium, functional changes – slow

Medium-sized resistance changes occur over a time course of seconds as a result of changes in rCBF during normal brain activity. Since blood is about 4 times less resistive than the cortex, it is expected that an rCBF increase will produce a resistance decrease in a reconstructed EIT image and that it is possible, therefore, to image brain function using EIT. Although there are already perfectly good techniques for imaging the metabolic response due to brain function, efforts towards this end in impedance tomography are very worthwhile as a means to test algorithms and hardware by comparison of images with the "expected" results obtained by fMRI and PET.

Cardio-synchronous EIT (McArdle and Brown, 1993; Brown and Primhak, 2002) was used to observe conductivity changes of magnitude 0.2% in the adult human head, related to the cardiac cycle after 500 cycles were averaged. EIT images have also been obtained using a ring of 16 electrodes on the cortical surface of anaesthetized rabbits during intense photic stimulation in both eyes (Holder, Rao et al. 1996). Resistance decreases of 4.5 ±2.7% were observed in the appropriate cortical areas with a time course similar to the stimulation. More recently human evoked response experiments have been carried out by the UCL group (Gibson 2000; Tidswell, Gibson et al. 2001b). Although surface resistance measurements generally changed in magnitude by 0.5-1% during stimulation, there was a large variability in changes observed in the reconstructed images. Only 19 out of 52 recordings returned changes localised in the "expected" cortical region due to changes in surface measurements.

1.2.7.7 Small, functional changes – fast

The change of resistive properties in individual neurons underlies all neural activity. When a neuron depolarises, ion channels open in the cell membrane and its resistance decreases over tens of milliseconds (Cole and Curtis 1939; Araki and Terzuolo 1962). Therefore it is easier for current to flow inside the neurons during depolarisation than during the resting state, as is shown diagrammatically in Figure 1.13. Qualitatively, therefore, we expect the resistance of the tissue containing depolarising neurons to decrease while the extra ion channels remain open. When the activity of a population of neurons displays spatial and temporal coherence, as in normal brain function, there is therefore an accompanying resistivity change in the active tissue as a whole. This lasts for tens of milliseconds, the length of the signal on an EEG trace accompanying an evoked potential EEG successfully localizes electrically active areas of cortex close to the skull with sufficient temporal resolution to distinguish neural events tens of seconds apart. But, as mentioned above, localization of deeper activity is less reliable. fMRI and PET may be used to generate images of activity with a high spatial resolution throughout the brain but their temporal resolution is only sufficient to observe metabolic consequences of neuronal depolarization (Boone and Holder, 1995; Liston *et al.*, 2001). It would be of great use to cognitive studies if an imaging technique combine the spatial and temporal resolution of fMRI/PET and EEG respectively to map neuronal activity itself, rather than its consequences. A technique such as EIT has the capability of measuring with sufficient time-resolution to do so if it can attain the sensitivity required to detect the small changes associated with neuronal depolarization (Boone and Holder 1995). Boone predicted a resistance decrease of about 0.01% measured on the surface of the scalp (Boone 1995) and that the maximal resistance change associated with neuronal depolarization occurs when measurement is made at DC.

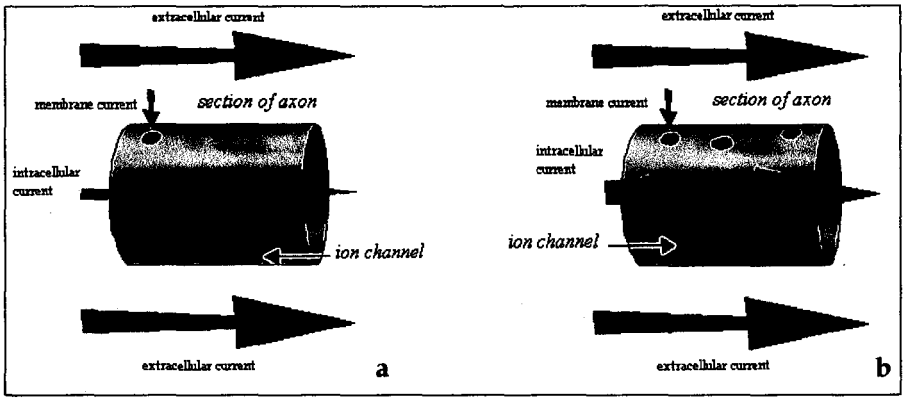

Figure 1.13. The flow of externally applied current inside and outside an axon and across its membrane (a) during the resting state and (b) during depolarisation. More current flows through the intracellular space during depolarisation (Liston, 2003)

Klivington and Galambos (Klivington and Galambos 1968) reported localised cortical resistance changes of 0.005% at 10kHz, during auditory evoked responses in cat. They used a sharpened, intracranial wire electrode and a platinum plate electrode resting on the adjacent cortical surface. This means that over half the total sensitivity was to a 1-mm layer of tissue surrounding the wire electrode, where current density was maximal. This is a volume similar to that containing the evoked, neuronal activity. Therefore, the method was very sensitive to localised changes in resistivity, directly comparable with the measured changes in resistance. Freygang and Landau (Freygang and Landau 1955) used the four-electrode method described in section 1.2.9.1 to measure a decrease of 3.1%±0.8% due to direct electrical stimulation on the surface of the cortex. Boone measured resistance changes of -0.01% to -0.03% due to evoked responses in rabbit brains (Boone 1995). He stimulated the median nerve, injected a square wave of constant current between electrodes 1-3mm apart and measured voltage between electrodes 9mm apart. All electrodes were on the surface of the cortex.

1.2.8 Ionic changes and cell swelling during neuronal activity

The simplified explanation of the action potential, illustrates the mechanism by which changes of intra- and extracellular ion concentration and cell swelling may occur as a result of neuronal activity. These changes have been measured experimentally. The reduction of extracellular fluid volume by 30 % was calculated to be due to two major mechanisms: 1) Neuronal cell swelling: due to increased intraneuronal osmolarity from the breakdown of ATP into smaller molecules by increased ATPase activity, which acts to draw in water from the extra-cellular space. Neuronal cell swelling accounts for approximately 8 % of the ECF volume reduction, 2) Glial cell swelling: the extracellular potassium ion concentration increased from 3 to 12 mmol as a result of enhanced neuronal activity and as glial cells are freely permeable to potassium, K^+ ions diffuse down a concentration gradient into the glial cells and are released into the extra-cellular fluid space in areas of low neuronal activity and low potassium concentration. This sets up a current along the glial cells, transmitted in the extracellular fluid by a chloride ion current to the area of potassium release and a sodium ion current to the area of glial potassium entry. Because the sodium ions only partially replace the potassium and chloride ions which leave the extracellular space within the neuronally active area, there is a reduction in osmolarity and a subsequent diffusion of water into the higher osmolarity glial cells (Lux *et al.* 1986): the glial cells swell and the size of the extracellular space decreases.

In a nutshell, these changes: i) increase cell swelling at the site of increased neuronal activity and reduce extra-cellular fluid volume and ii) decrease cell size and increase extra-cellular fluid volume in surrounding areas of lower neuronal activity. The net effect of a 30% decrease of ECF volume and a 10 % increase in osmolarity will be to increase impedance at the neuronally active area Figure 1.14. A smaller impedance decrease is expected in the surrounding less active area where potassium and water are redistributed into the extracellular space.

As Lux et al.'s work was been performed in animals under extremes of neuronal activity, i.e. epilepsy or electrical stimulation of cortical slices, so the cell swelling measured was not

necessarily applicable to physiological ranges of neuronal activity such as those produced by evoked responses. However it was conceivable that repetitive neuronal stimulation from evoked responses would result in similar ionic and cell swelling changes of epilepsy, but to a lesser degree.

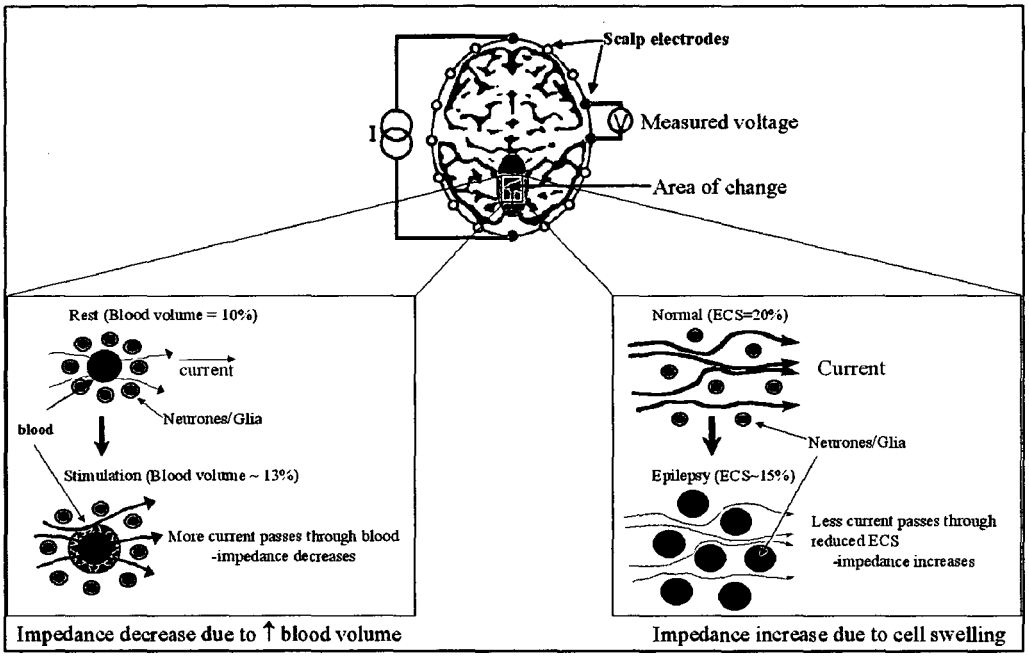

Figure 1.14: Mechanisms of impedance change within the brain (Tidswell et al., 2001)

Left figure: Impedance decrease due to increased blood volume. This diagram represents the neuronal cells in green, with a blood vessel in the centre of the cells. During physiological activity, a signal is sent to the blood vessels which increases blood flow and blood volume to that cortical area (Malonek *et al.* 1997). As blood has a lower resistivity than the surrounding brain (150 Ωcm and 350 Ωcm, respectively), the increase in the lower resistivity volume of blood will allow more current to flow through that area of tissue and decrease the bulk impedance of that volume of cortex. **Right figure: Impedance increase due to cell swelling.** In this figure, the cells are represented in green (top), and expand during cell swelling (blue - bottom). During normal function, the size of the conductive extra-cellular space (ECS) is 20% of the brain volume. During epilepsy, moderate cell swelling occurs as water and ions enter the glial cells and the neurones (Lux *et al.* 1986), and the volume of the low resistivity ECS is reduced. This increases the bulk impedance of that area of cortex. Larger changes of cell swelling are seen during ischaemia and spreading depression, which cause much larger increases in brain impedance (Holder 1992; Boone *et al.* 1994).

1.2.9 Current injection and voltage measurement

1.2.9.1 Methods of Current Injection

There are two distinct ways of data collection in EIT, namely the two-electrode and four-electrode methods. In the two-electrode method, voltages are measured from the same electrodes through which the current has been injected. With the four-electrode method, current is injected through some electrodes and voltages measured from the other electrodes. This method minimizes error in voltage measurement due to the contact impedances that are present in the two-electrode method. The four-electrode type can be classified into four main groups, namely: neighbouring, opposite, cross methods and adaptive (Isaacson et al., 1992).

1.2.9.2 Neighbouring Method

For the *neighbouring* method (Figure 1.15), current is injected through two adjacent electrodes and voltage measured from all other pairs. The current is first applied through electrodes 1 and 2. The current density is, of course, highest between these electrodes and it decreases rapidly as a function of distance. The surface potential is then measured successively with electrode pairs 3-4, 4-5,...,15-16. From these 13 surface potential measurements, the first four measurements are illustrated in Figure 1.15, which are all independent. Each of these is assumed to represent the impedance between the equipotential lines intersecting the measurement electrodes.

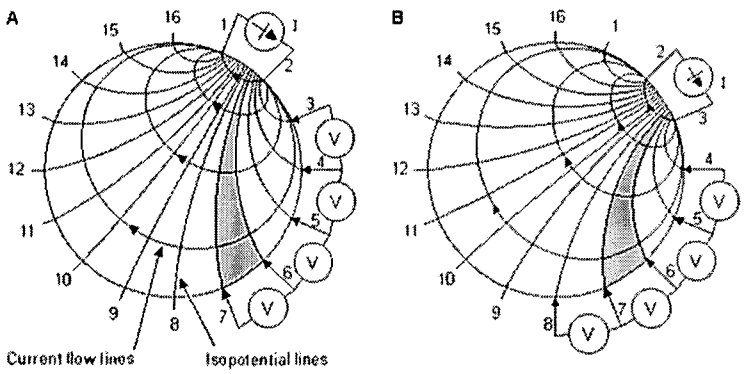

Figure 1.15: Neighbouring method of impedance data collection. The first four voltage measurements for the set of 13 measurements are shown. B shows another set of 13 measurements, which is obtained by changing the current feeding electrodes.

This is indicated with shading for the voltage measurement between electrodes 6 and 7. The next set of 13 surface potential measurements is obtained by driving the current through electrodes 2-3 (Figure 1.15 B).

In general, with n electrodes, there are $n(n-3)$ possible voltage measurements. However, only one half of these are independent due to reciprocity theorem, which states that reversing the voltage measurement and current injection electrodes would give an identical trans-impedance. It produces a non-uniform current density since most of the injected current travels near the boundary. It reduces sensitivity of the voltage measurements to resistivities that take place at the centre of the object.

1.2.9.3 Opposite Method

The opposite method (Figure 1.16), which produces a more uniform current distribution hence a good sensititvity, is another alternative impedance measurement (Hua *et al.*, 1993). With this approach, current is injected through two diametrically opposed electrodes (16 –8) and the electrode adjacent to the current injecting electrode is used as the voltage reference. Voltage is measured from all other electrodes except the current injection electrodes, yielding 13 voltage measurements. The first four are illustrated in Figure 1.16A. The next set of 13

measurements is obtained by selecting electrodes 1 and 9 for current injection as shown in Figure 1.16B. When *n* electrodes are used, there are *½n(n-3)* data points.

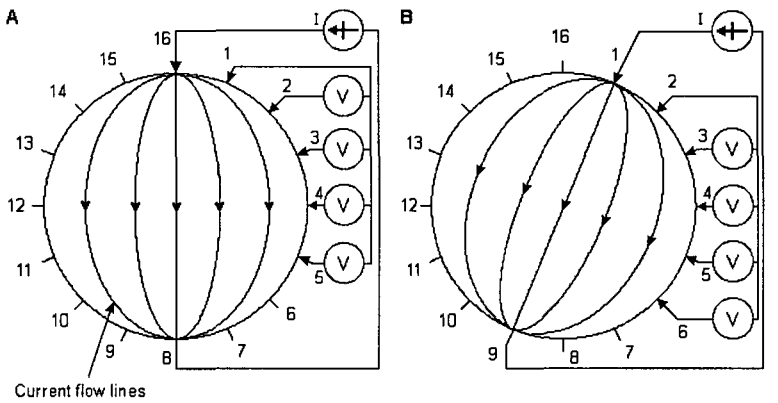

Figure 1.16: Opposite method of impedance data collection

1.2.9.4 The Cross Method

A more uniform current is obtainable when the current is injected between a pair of more distant electrodes (Hua *et al.*, 1993). This approach, known as the cross method (Figure 1.17), one electrode is made a current reference and the current source is applied successfully to the other electrodes. For instance electrodes 16 and 1, are first selected for current and voltage reference electrodes respectively. The other current electrode, electrode 2 is first used. The voltage is measured successively for all other 13 electrodes with electrode 1 as reference. Current is then driven through electrode 4 and the voltage is measured successively for all 13 electrodes with electrode 1 as a reference (Figure 1.17A).

This is repeated using electrodes 6, 8, ..., 14 as in figure 1.17B, C, D.

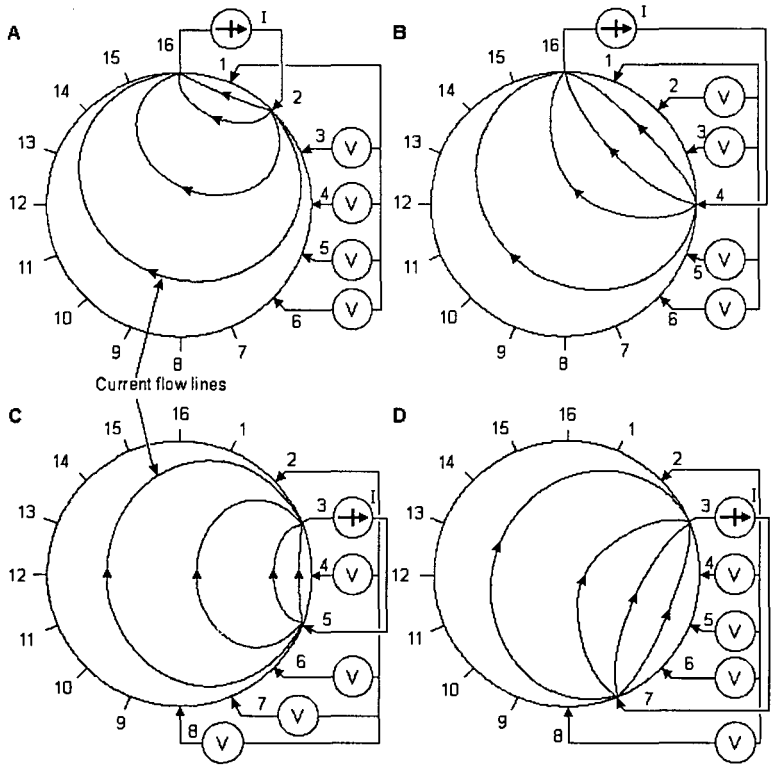

Figure 1.17: Cross method of impedance data collection. The four different steps of this approach are illustrated in A through D

1.2.9.5 The Adaptive Method

The last in the series, the adaptive has been proposed by Gisser, Isaacson, and Newell in 1987 (Hua *et al.*, 1993) where current is injected through all electrodes (Figure 1.18). As current flows through all electrodes simultaneously, as many independent current generators are needed as are electrodes used. The voltages are measured with respect to a single grounded electrode. For n number of electrodes, the number of voltage measurements for a certain current distribution is (n-1). The desired current distribution is then rotated one electrode increment. Thus ½n different current distributions are obtained, yielding ½n(n-1) independent voltage measurements.

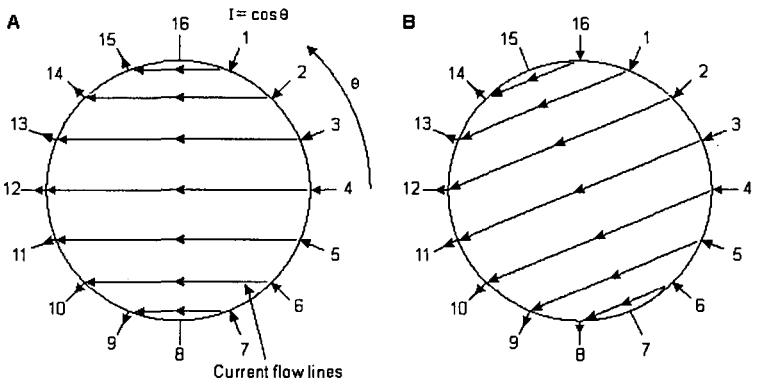

Figure 1.18: Adaptive method of impedance data collection

1.2.9.6 Mixed Method

In this work, 31 electrodes were defined for the current injection and all possible combinations of these electrodes were explored. The electrodes were paired for current injection combining all the four methods described above. This approach aims at looking at good sensitivity in some predefined regions. The electrode arrangement was divided into two groups namely front and back. The front ones consisted of electrodes 1, 2, 3,...,18: and the back ones were 19, 20, 21,...,31. All electrodes were paired and by using reciprocity theorem, there were in all 465 possible current injection patterns (½n(n - 1)).

1.2.10 Electrode Protocols

In this section, we find some of the electrode protocols that have been in use and the one applicable to EIT at present.

1.2.10.1 EEG Lead Systems

The internationally standardized 10-20 system is usually employed to record spontaneous EEG. In this system, twenty-one (21) electrodes are located on the surface of the scalp, as shown in Figure 1.19A and 1.19B.

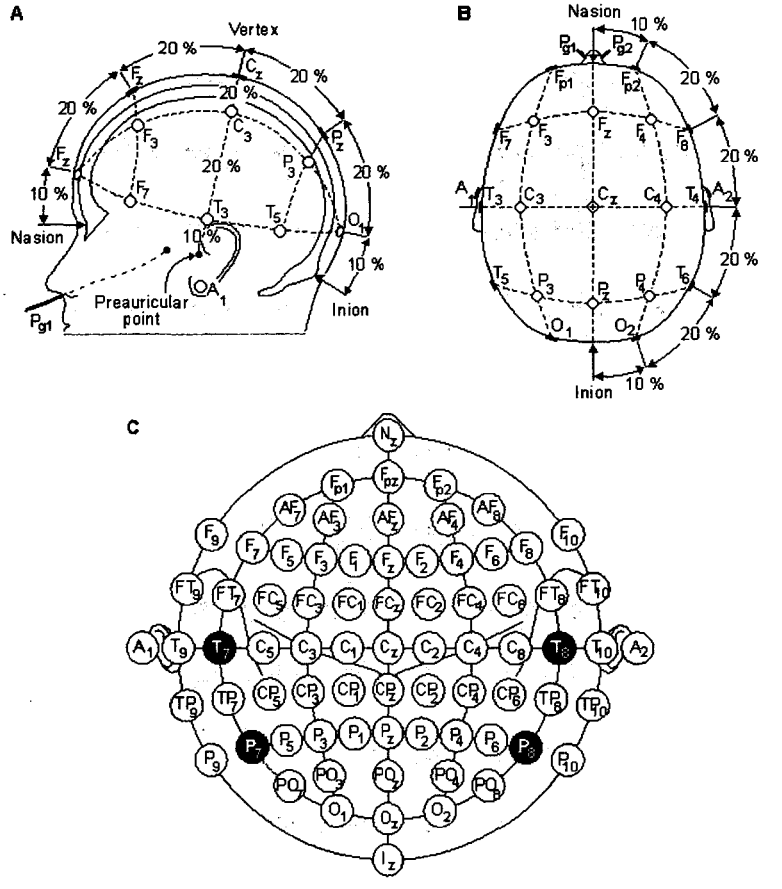

Figure 1.19: The international 10-20 system seen from the left side of the head (A) and B above the head. A - Ear lobe, C - central, Pg - nasopharyngeal, P - parietal, F - frontal, Fp - frontal polar, O - occipital. In (C) is the location and nomenclature of the intermediate 10% electrodes, as standardised by the American Electroencephalographic Society.

The positions are determined as follows: The reference points are the nasion, which is the delve at the top of the nose, level with the eyes; and inion, which is the bony lump at the base of the skull on the midline at the back of the head. From these points, the skull perimeters are measured in the transverse and median planes. Electrode locations are determined by dividing these perimeters into 10% and 20% intervals. Three other electrodes are placed on each side equidistant from the neighbouring points as seen in Figure 1.19B (Cooper et al., 1969; Jasper, 1958).

1.2.10.2 American Encephalographic Society (AES) System

In addition to the 21 electrodes of the international 10-20 system, intermediate 10% electrode positions are also used. The locations and nomenclature of these electrodes are standardised by the AES (Figure 1.19C). In this recommendation, four electrodes have different names as compared to the 10-20 system; these are T7, T8, P7 and P8. These electrodes are drawn in black with text being in white.

1.2.10.3 Queens Square System

Besides the international 10-20 and AES systems, many other electrode systems exist for recording electric potentials on the scalp. The Queen Square System of electrode placement has been proposed as a standard in recording the pattern of evoked potentials in clinical tests (Blumhardt *et al.*, 1977). Bipolar or unipolar electrodes can be used in the EEG measurement. In the first method the potential difference between a pair of electrodes is measured. In the latter method, the potential of each electrode is compared either to a neutral electrode or to the average of all electrodes.

1.2.10.4 EIT Electrode System

The number of electrodes and their positions are the two most important factors affecting image quality. The number of electrodes limits the number of independent measurements, which are available which, in turn limits the resolution, which may be obtained in the final image. The electrodes should be positioned so as to maximize the measured impedance change, so as to optimize the sensitivity.

Work has been done by the UCLH group regarding electrode arrangements (Gibson, 2000), which were tested in saline-filled hemispherical tank (Tidswell et al., 2001). Using 31 electrodes arranged in three rings (of 16, 8 and 8 electrodes) provided good image quality in the (x, y) plane but poor resolution in the z-direction due to under sampling, even if 672 measurements were taken. Better spatial sampling was achieved with electrodes evenly spaced over the whole head. The internationally recognized 10-20 system (Cooper et al., 1969) of electrode placement for EEG defines the location of 21 electrodes from anatomical features and is designed to cover the scalp evenly. Images obtained using these electrode positions were, however, unable to localize an object. It appeared that 21 electrodes did not provide sufficient information to reconstruct accurate images.

More information was provided by adding 10 more electrodes to those of the 10-20 system (Figure 1.20). Eight of the additional electrodes (8, 9, 10, 11, 19, 20, 21, 22) were placed between the standard electrodes and two more (28 and 30) were placed lower down on the head to improve sampling in the z-direction and around the visual cortex (Gibson A.P., 2000a). This has been the electrode protocol used throughout the thesis.

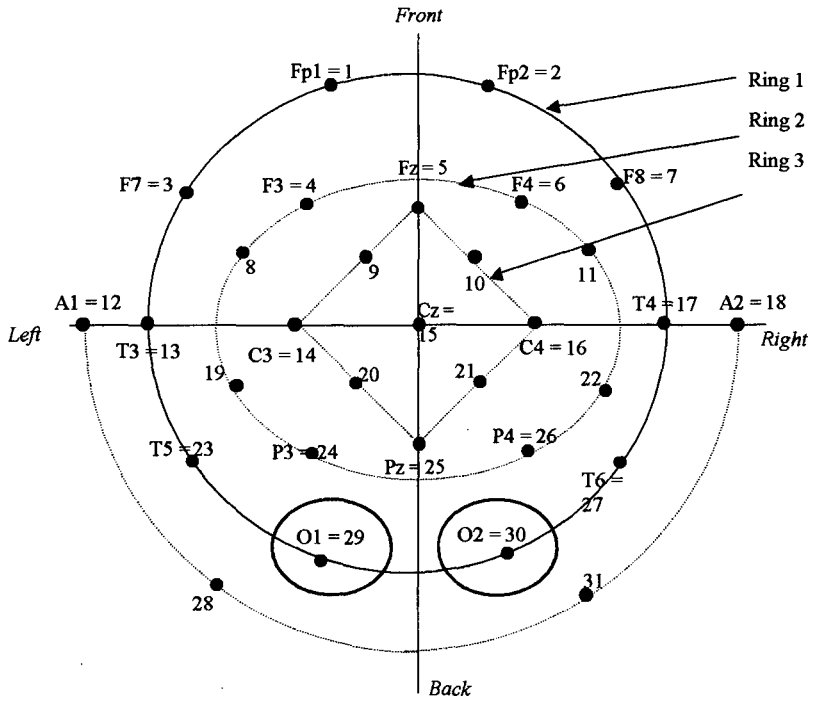

Figure 1.20: Positions of electrodes. Each black spot represents an electrode. The black label gives the electrode code in the 10-20 system, the red number is the electrode reference number used in this work.

1.3 Scope of Work

In the next chapter (chapter two) is a review of some of the modelling methods used in EIT in general. In addition, the essential theory in formulating the forward problem in EIT has also been discussed. In chapter three, work done on the study of the integration of EIT with MEG for enhanced brain imaging has been presented. The proposed physical model together with the background mathematics has been enumerated. Besides, the different head models and methodology used in acquiring the results are explained in details. Presented in chapter four is, work done in estimating the current density in the primary visual cortex, "EIT electrode protocol for obtaining optimal current density in the brain". The validation of baseline voltages using the proposed protocol electrodes was presented in this fourth chapter as well. Chapter five deals with the effect of realistic geometry of the human head, the shape and size of the primary visual cortex, and the variation in the skull conductivity on the mean current density in the brain and changes in boundary voltages. The effect of variations in local conductivity changes has also been analysed. In chapter six, is a comparison between the magnetic field strength using spherical and realistic head models. In addition, the effect that the local conductivity changes have on magnetic field outside the head has also been studied. The last chapter, seven gives a summary of the work done, discussions, conclusions, and suggestions for future work.

1.4 Summary

This chapter provided an overview of the origin of brain signal and how they could be detected using a number of imaging techniques. The techniques relevant to this work are EIT and SQUIDs. Their development and contribution, experimental and physiological evidence by which EIT should be able to detect impedance in the human head has been reviewed. Methods of current injection and electrode protocols used in EIT were also reviewed. In addition, current methods of establishing functional information about the human brain have been reviewed, which support the hypothesis that impedance changes occur in the human brain during a variety of physiological and pathological conditions.

1.5 Objective of research

The primary objective of my research is to explore some new techniques for imaging small and fast impedance changes in the head due to neuronal depolarisation. This includes using Finite Element Method in developing accurate and realistic solutions to the forward problem in EIT. The research question is whether magnetic detection of brain activity could yield measurable changes in magnetic field as compared to changes in the electrical method. In the next chapter is an outline of the essential models and mathematical formulations that are used in EIT.

Modelling and Forward Problem in EIT

Chapter 2

MODELLING AND THE FORWARD PROBLEM IN EIT

This chapter gives a description of the models that have been used in all aspects of EIT, for estimation brain activities or reconstruction of brain images. This will incorporate examples from EIT and EEG modelling, 3-D and 2-D models and the effects on them due to the layered nature of the head. A brief account is also given on the mathematical derivations of the forward solution in EIT using Maxwell's equations.

2.1. Modelling in EIT

2.1.1. 2-D models

2.1.1.1. General reconstruction

Section 1.2.4.4 describes the use of EIT for many applications in medical imaging. The ultimate aim of EIT is to reconstruct images based on boundary voltage measurements consistent with current patterns used. Before this could be achieved there it is important to estimate what is known as the Jacobian. However, to generate this Jacobian for image reconstruction, it is necessary to calculate gradients of the potential ($\nabla\Phi$ and $\nabla\Psi$), knowing something about the pattern of current being applied (Appendix A) and making assumptions about the shape of the object under consideration and about its internal conductivity distribution σ.

In many cases of image reconstruction of thoracic or gastrointestinal images, electrodes were arranged in a plane and a 2-D model was used to approximate the internal fields when a single plane of electrode was used for measurement. This was done using analytical and FEM models of a circular conductor (Avis, 1993; Avis and Barber, 1994; Metherall and Barber, 1996; Patterson and Zhang, 2001), and of a plane conductor with a more realistic boundary shape (Borsvic and McLeod, 2001; Jain and Isaacson, 1997). The latter was found to reduce

distortions markedly when data was obtained from a non-circular boundary. The 2-D model was extended to 2½-D in reconstruction of data from a cylindrical tank, assuming axial uniformity (Jerbi and Lionheart, 2000) where stacked slices were assumed to be circular, uniform conductors. Results showed improvements over strictly 2-D methods. 2-D circular models have also been used in general to reconstruct breast images (Kerner and Paulsen, 2002)although they suggest that a 3-D approach is needed to increase sensitivity to deep lesions.

2.1.1.2. Models of the head

2-D models have also been used in the reconstruction of brain images. Boone used the Sheffied backprojection algorithm (Barber and Seagar, 1987) to reconstruct images of spreading depression in the rabbit cortex (Boone and Holder, 1994b). This assumed that the resisitivity distribution was initially homogeneous and 2-dimensional, as is the cortex of the rabbit brain. Bayford used a 2-D algorithm based on backprojection for reconstruction of data from a 2-D phantom with a circular, Plaster of Paris ring to simulate the presence of a skull (Bayford *et al.*, 1995). Gibson *et al.* (2000) suggested a 2-D circular FEM solution to model impedance changes in the center of the neonatal head and their resultant boundary voltage changes, but did not actually perform any reconstructions with this model. The problem of stroke detection and monitoring was approached by Clay and Ferree (Clay and Ferree, 2002) using a circular FEM with four concentric regions representing brain, CSF, skull and scalp, as did Gibson *et al.*. Images were reconstructed using an iterative approach and high correlation was shown between simulated and reconstructed impedance changes.

Pidcock *et al.* presented a formulation of rectangular, circular and elliptic analytic and semi-analytic solutions for the problem of EIT, including, in each case, the presence of layers (Pidcock et al., 1994a). No reports have been made of the models' implementation.

2.1.2. 3-D models

2.1.2.1. General reconstruction

Since current is not confined to 2-dimensions in a 3-D object, it is more appropriate to employ 3-D models in a reconstruction algorithm for such medical applications as have been described above. Pidcock *et al.* also presented a formulation of cubic, cylindrical and spherical analytic and semi-analytic solutions for the 3-D problem of EIT, and, as for the 2-D case, included in each case, the presence of layers (Pidcock et al., 1994b) but, again, no reports were made of the models' implementation.

Analytical and FEM-based 3-D models have been applied for imaging resistivity perturbations in cylindrical simulations and phantoms (Kleinermann and Avis, 2001; Vauhkonen and Vauhkonen, 2000) and static and dynamic images have been obtained of the human thorax during respiration (Saulnier and Blue, 2001) using several planes of electrodes. Blue concluded from his results that, for a system with a given number of channels, it is best to divide the electrodes among several planes rather than increasing resolution in a single plane by placing all of them in a dense ring. In the latter case, he reports a larger artefact than in the former due to impedance perturbations occurring outside image plane. Kleinermann reported, from inspection of singular values, that the 3-D reconstruction algorithm appeared to be better conditioned than the 2-D algorithm. He also modelled an elliptical cylinder but reconstructed images were not presented.

2.1.3. Models of the head

There are several examples of 3-D models used to reconstruct EIT images of the head. The analytical models approximate the head as a sphere only and FEM models as a sphere or a realistic, head-shaped geometry.

2.1.2.1. Spherical and homogeneous models

Our group at UCL has previously produced images of resistance changes in hemispherical and head-shaped phantoms and in the head, during brain function, using a 3D analytical forward solution for a homogeneous sphere (Gibson, 2000; Tidswell and Gibson, 2001). Both these studies showed that, in the presence of a real or simulated resistive skull, the homogeneous algorithm reconstructed impedance changes too centrally, suggesting the need to take the skull into account in future algorithms. In the head-shaped tank, a 12% resistance change was localized with an error of 6-25mm without the presence of the skull and 19.6-36mm with the skull in place. In the hemispherical tank, the mean value for peak impedance change inside a simulated skull was 34% that of the change without the presence of the skull and the localization error (with skull) was 6.5-20.3mm. Localisation accuracy was similar for reconstructions from tanks with and without the simulated skull when a radial correction factor of 1.6 was introduced.

A perturbation approach was employed by Morruci *et al.* (Morucci and Granie, 2006; Morucci and Granie, 1995) to reconstruct an off-centre perturbation in an otherwise homogeneous sphere. A direct sensitivity matrix was produced, using BEM, for a square grid describing the upper hemisphere and 40 electrodes arranged in rings from its equator to its apex.

2.1.2.2. Spherical and inhomogeneous models

There are two examples of the use of analytical, layered sphere models in the literature. The solution for potential was derived by Ferree *et al.* (Ferree et al., 2000) for injection of current I through point electrodes on a four-shell sphere in order to estimate the regional head tissue conductivities *in vivo*. A similar method was employed by Goncalves *et al.* (Goncalves and de Munck, 2002; Goncalves and de Munck, 2000) in order to better specify regional head conductivities when solving for the EEG problem, but their analytical model included only three layers. Neither paper reported reconstruction of images.

Another spherical model of the head was produced by Towers *et al.* (Towers and McCann, 2000). They used the Ansoft Maxwell FEM package to solve for one hemisphere of a sphere consisting of 4 concentric shell layers, scalp, skull, CSF and brain with a ring of 16 scalp electrodes attached around its equator. They did not produce images but showed the requirements of voltage measurement sensitivity to be 100-120 dB in order to detect changes in rCBF and those due to application of a carotid clamp. They also compared their results with those from a 2-D model, which indicated sensitivity requirements 15 dB less severe than did the 3-D model.

2.1.2.3. Realistic geometry and inhomogeneity

A FEM model of a 4-compartment, realistically-shaped head was used by Gibson (Gibson, 2000) in a truncated SVD algorithm to reconstruct images from tank data and human evoked responses. In neither case were reconstructions significantly better than when an analytical spherical model was used, but he suggested that errors in the mesh may have substantially reduced the accuracy of the FEM-generated sensitivity matrices and hence reduced the benefits of including realistic geometry and inhomogeneity in the forward model. Images were reconstructed iteratively by Polydorides and Lionheart (Polydorides and Lionheart, 2001) from simulation of a visual evoked response using a similar FEM model on an improved mesh with 5 compartments and electrodes arranged in a ring.

In a further study, the change in transfer impedance was studied for a 30-40% impedance change due to a $10cm^3$ central oedema, as simulated by a FEM model with realistic head geometry, including 13 different tissues and using hexahedral elements (Bonovas and Kyriacou, 2001). However, no images were presented using this technique. A solution for current flow through a realistically shaped head was reported by Bayford *et al.* (2001), using *integrated design engineering analysis software (IDEAS).* A full sensitivity matrix was not built, however, and no images were reconstructed.

2.1.4. Modelling in EEG

The problem of dipole modelling in EEG is similar to that in EIT because it is necessary to calculate distributions of potential and of electric field inside the head. The non-sphericity and inhomogeneity of the head present similar problems. Three- and four-shell models are often used in source localisation from measured EEGs (Rush and Driscoll, 1969; Mosher *et al.*, 1999; Cuffin and Schomer, 2001; Ary and Klein, 1981; Yvert and Bertrand, 1997). Mostly, multi-shell models have included three shells only, neglecting the CSF, which is expected to shunt some of the injected current. In the past, spherical models have been compared with non-spherical models and homogeneous with non-homogeneous. Some of the results of these comparisons follow:

2.1.4.1. The effect of shells

(Ary and Klein, 1981)) quantified the difference between analytical solutions for potential generated by a dipole in 1) a homogenous sphere with conductivity that of brain and 2) a system of three concentric shells, brain, skull and scalp, each with appropriate conductivity. The latter suggested that a radial correction factor of about 1.6 could compensate for the presence of the skull and the resultant localization error when a homogenous model is used.

2.1.4.2. The effect of geometry in the presence of shells

Many researchers have compared the use of spherical and non-spherical models for localizing dipoles within non-spherical objects. Simulation studies, such as that by Roth (Roth and Balish, 1993), showed average and maximum localization errors of 19.7mm and 40mm when dipoles were simulated in the frontal and temporal lobes of a realistic BEM model and reconstructed using a 3-shell sphere mode. Yvert (Yvert and Bertrand, 1997) performed a similar calculation for 2000 simulations of dipoles at random positions on the segmented cortical surface of a realistically-shaped, 3-shell BEM model. Localization errors for inverse calculations with a spherical model were reported to be 5-6mm in the upper part of the head

and 15-25mm in the lower part. Cuffin (Cuffin and Schomer, 2001) investigated two features of non-spherical geometry in the head, the general boundary shape and the brainpan, which is the very non-spherical surface at the bottom of the brain cavity. Inverse calculations were performed using an analytical 3-sphere model and data was generated using 3-shell, non-spherical BEM models with and without a brainpan. It was found that the maximum localization errors were approximately 10mm in the former (with brainpan) and 20mm in the latter (without brainpan).

The same author reported localization studies of 177 dipole sources created by injecting current into depth electrodes implanted into the brains of 13 human subjects. Using a 3-layered sphere model for the inverse calculation, the best average localization that could be achieved was 10mm. In a similar study, (Krings and Chiappa, 1999) used a 4-shell spherical head model to localize 11 dipoles in only 2 subjects. Localization errors were 17mm and 13mm using 21 electrodes and 41 electrodes respectively, when a proportionality correction factor was applied to correct for non-spherical head shape. Errors were 23mm and 17mm when the factor was not applied. In the latter study, electrodes were implanted and anchored with metal skull screws. In the former, anchors were non-conductive.

In order to study the effect of realistic geometry in correct physiological localization of the source associated with somatosensory evoked potentials (SEPs), Kristeva-Feige *et al.* (Kristeva-Feige and Grimm, 1997) performed 9 daily replications of a right median nerve stimulation experiment on one healthy subject. A 3-shell spherical model and a 3-compartment realistically shaped BEM model were used for the inverse calculations and both located the dipole sources, correctly, within the postcentral gyrus when results were projected onto the individual's MRI and compared with an fMRI image during the same stimulation protocol.

2.1.5. Anisotropy

A further problem in both EIT and EEG is that the tissue inside the head is highly anisotropic, in which case, it is possible that no isotropic conductivity distribution could accurately predict the measured data (Lionheart, 1998). Data measured from a real-skull phantom head was reconstructed by (Baillet and Mosher, 2001), who suggested that full, anisotropic realistic head FEM models were necessary, rather than spherical models to fit the data with a reasonable level of residual variance. They suggested that an analytical spherical model, while not as good as the detailed FEM and BEM models, produced better results than the simpler FEM and BEM models with realistic geometries but less conductivity constraints.

In order to include anisotropy information in a FEM model of the head, conductivity tensor data could be provided by diffusion-weighted tensor MRI. Haueisen et al. (Haueisen and Tuch, 2002) found a minor influence of anisotropy on source localization but a major influence on source strength estimation when tissue anisotropy was considered in localization using computer-simulated data. The effect of anisotropy is not investigated in this thesis.

2.2. The forward problem

One of the main methods used to solve the forward problem uses a simplified computer model of the object and the electrode positions on its boundary. For each impedance measurement made on the object, a sensitivity coefficient is calculated for each pixel in the EIT image, which determines the size of the voltage change which would be measured at that electrode combination for a change in conductivity at that pixel (Geselowitz, 1971).

Another method of solving the forward problem is to use an analytical technique, in which a simplified geometric representation of the object is used. In the first part of this thesis, the forward model which represents the head is a sphere of uniform conductivity (Gibson 2000). The advantage of this technique is that it is relatively straightforward to implement in a computer program, for simple geometric models of the object. Even information about

different tissue layers can be incorporated in the model to improve its accuracy (Liston *et al.*, 2002). However, the disadvantage of the analytical technique is that it cannot be used to implement complex geometric shapes, such as the shape of the head, holes in the head - such as eye sockets, nor can it incorporate information about tissue anisotropy: the different electrical properties that a tissue has to a current applied in different directions.

For more complex and more realistic information to be incorporated into the forward model, computer simulations of the object need to be used. Examples of these are finite element method (FEM), or the computationally less demanding boundary element method (BEM). The advantage of such models is that they can be constructed from real images of the head, obtained by either MRI or CT (Bayford *et al.*, 2001a), to incorporate realistic shape information. In addition they can also include information about the tissue layers in the head, such as the scalp, skull, CSF and brain. Once this information is incorporated, each tissue component can be given a resistivity value, obtained from impedance measurements of that tissue published in the literature. The FEM can be used to calculate the field produced throughout the model upon current injection, and from this a sensitivity matrix can be generated which relates the sensitivity of each voltage measurement to a conductivity change at each location in the model. These locations are analogous to the pixel positions in the final EIT image slices. Once the sensitivity matrix is calculated for all the boundary impedance measurements, it can then be inverted to obtain the EIT images from the scalp voltage changes. The disadvantage of the FEM solution is that it is difficult to implement for a complex head-shape. Initial attempts (Gibson 2000) used a FEM with elements of different geometric shapes that produced large errors in the forward solution. Subsequent work has used a variety of software packages to create a finer FEM model, with more elements, in order to reduce these errors. This has required the use of a variety of commercially available software packages, and software developed within UCL in order to create and solve the FEM, respectively.

2.3. Mathematical formulation

In any EIT reconstruction problem, there is always the need to construct a physical model for observations known as the forward model. In connection with this, equations must be derived relating the measured voltages, injected currents and conductivity distributions. Using Maxwell's equations of electromagnetism as a starting point (Hamalainen et al., 1993), the equation for this physical model can be derived. In all EIT models used, the equation governing the interior of the body is the same but the boundary conditions differ. Maxwell's equations in inhomogeneous media can be written in the form

$$\nabla \times \vec{E} = \frac{\partial \vec{B}}{\partial t} \text{ (Faraday's law of induction)} \tag{2.1}$$

$$\nabla \cdot \vec{E} = \frac{\rho}{\varepsilon_r \varepsilon_o} \text{ (Gauss' law of electricity)}$$

$$\nabla \times \vec{H} = \vec{J} + \frac{\partial \vec{D}}{\partial t} \text{ (Ampere's law)} \tag{2.2}$$

$$\nabla \cdot \vec{B} = 0 \text{ (Gauss' law for magnetism)}$$

where E is electric field, B magnetic induction, H magnetic field, D electric displacement, and J current density.

Assuming the injected currents are time-harmonic with frequency ω, the electric and magnetic fields are of the form

$$\begin{aligned} \vec{E} &= \tilde{E} e^{i\omega t} \\ \vec{B} &= \tilde{B} e^{i\omega t} \end{aligned} \tag{2.3}$$

In linear isotropic media the following relations are valid:

$$\vec{D} = \varepsilon\vec{E}$$
$$\vec{B} = \mu\vec{H} \qquad (2.4)$$
$$\vec{J} = \sigma\vec{E}$$

where ε, μ, and σ are respectively the permittivity, permeability and conductivity of the medium. In EIT, the tissues are usually approximated as isotropic even if the muscle is highly anisotropic (Geddes and Baker, 1967). Using the relations in (2.4), the equations in (2.1) and (2.2) can be expressed in the form

$$\nabla \times \vec{E} = -i\omega\mu\vec{H} \qquad (2.5)$$

$$\nabla \times \vec{H} = \vec{J} + i\omega\varepsilon\vec{E} \qquad (2.6)$$

In EIT, as in any other bioelectric phenomena, there are current sources (Malmivuo and Plonsey, 1995) that are here denoted with J^s. Therefore, the current density is divided into two components $\vec{J} = \vec{J}^o + \vec{J}^s$, where $J^o = \sigma\vec{E}$ is the so called ohmic current. Consequently, the equations (2.5) and (2.6) can be expressed as

$$\nabla \times \vec{E} = -i\omega\mu\vec{H} \qquad (2.7)$$

$$\nabla \times \vec{H} = (\sigma + i\omega\varepsilon)\vec{E} + \vec{J}^s \qquad (2.8)$$

The electric field in terms of the electric potential can be expressed as

$$\vec{E} = -\nabla\phi \qquad (2.9)$$

Combining Gauss' law and equation (2.9) gives the Poisson's equation:

$$\nabla^2\phi = -\frac{\rho}{\varepsilon_r\varepsilon_o} \qquad (2.10)$$

and if there are no free charges, $\rho = 0$, the Poisson's equation reduces to Laplace's equation as

$$\nabla^2\phi = 0 \qquad (2.11)$$

This partial differential equation has an infinite number of solutions, each giving a distribution of ϕ. To limit these solutions, boundary conditions can be applied which specify the value of

certain parameters at the surface. These may be either: Dirichlet conditions, in which the potential at the surface is specified ($\phi = v_i$ under electrode i,); Neumann conditions, in which the current density crossing the boundary is specified ($\sigma\nabla\phi.\mathbf{n} = j_i$ under electrode i and $\sigma\nabla\phi.\mathbf{n} = 0$ elsewhere) ; or mixed conditions, which are a combination of Dirichlet and Neumann conditions.

Throughout this thesis, the concern is with known current injection $\boldsymbol{j}$ so, when this is defined, it is possible to solve the Neumann problem to find ϕ and hence v_i. In practice, a finite number of electrodes are used, giving a finite number N of possible voltage measurements. These can form a vector $\mathbf{V}=[v_1, v_2, \ldots, v_N]$ which can be related to the conductivity distribution σ by a matrix $\mathbf{A}_\sigma$.

$$\mathbf{A}_\sigma\sigma = \mathbf{V} \tag{2.12}$$

This is the formulation of the forward problem and the inverse problem requires recovery of σ knowing $\mathbf{V}$. Because $\mathbf{A}_\sigma$ is dependent on σ, the matrix equation (2.12) can be said to represent a system of non-linear differential equations whose solution is σ. For the same reason, the inverse problem is also non-linear.

2.4. Uniqueness, ill-posedness and ill-condition

A solution to equation 2.12 is unique when no other solution for σ returns the same value of $\mathbf{V}$. The most intuitive question to ask is whether it is possible in EIT that more than one conductivity distribution could produce the same boundary voltage measurements $\mathbf{V}$ within their precision? The answer is yes. If measurements were made to infinite precision and the entire object surface was sampled continuously, the solution would be unique. However, there is loss of information in the imaging process since data are discretely sampled and noisy and a large variation of resistivity may only produce a small variation in the discrete measurements.

Therefore, the problem is ill-posed. It is also ill-conditioned, since small oscillations in the solution, i.e. noise in **V**, can produce large, wild oscillations in the solution for σ. The measured data can suggest a set of approximate solutions for conductivity and it is wise to apply additional constraints from the physics of the problem. Regularisation methods and a priori information (the detailed description of these are beyond the scope of this thesis) can be utilized as a means to compensate for loss of information in order to reduce the solutions set.

2.5. Volume Source in a Homogeneous Volume Conductor

The non-conservative current that arises from the bioelectric activity of nerve and muscle cells due to the conversion of energy from chemical to electric form is known as the impressed current density $J^i(x,y,z,t)$. The individual elements of this bioelectric source behave as electric current dipoles. Hence J^i equals the volume dipole moment density of the source which is zero everywhere outside the region of active cells (Plonsey, 1969). If the volume conductor is infinite and homogeneous and the conductivity is σ, the primary sources J^i establish an electric field E and a conduction current σE. As a result, the total current density (Geselowitz, 1967) is given by:

$$\vec{J} = \vec{J}^i + \sigma\vec{E} \tag{2.13}$$

The quantity σE is often referred to as the return current. This current is necessary to avoid build-up of charges due to the source current. Because the electric field E is quasistatic, it can be expressed at each instant of time as the negative gradient of a scalar potential ϕ, and Equation 2.13 may be rewritten as

$$\vec{J} = \vec{J}^i + \sigma\vec{E} \tag{2.14}$$

Since the tissue capacitance is negligible (quasistatic conditions), charges redistribute themselves in a negligibly short time in response to any source change. Since the divergence of J evaluates the rate of change of the charge density with respect to time, and since the charge density must be zero, the divergence of J is necessarily zero. (We refer to the total current J as

being solenoidal, or forming closed lines of current flow.) Therefore, Equation 2.13 reduces to Poisson's equation:

$$\nabla \cdot \vec{J}^{i} = \nabla \cdot \sigma \nabla \Phi + \nabla \cdot \vec{J} = \sigma \nabla^2 \Phi + \nabla \cdot \vec{J} \tag{2.15}$$

Equation 2.14 is a partial differential equation satisfied by Φin which $\nabla.J^i$ is the source function (or forcing function). The solution of Equation 2.15 for the scalar function $\sigma\Phi$ for a region that is uniform and infinite in extent (Stratton, 1941) is:

$$4\pi\sigma\Phi = -\int \vec{J}^{i} \cdot \nabla\left(\frac{1}{r} dv\right) \tag{2.16}$$

2.6. Volume Source in an Inhomogeneous Volume Conductor

In Section 2.3 it was assumed that the medium is uniform (i.e., infinite and homogeneous). Such an assumption allowed the use of simple expressions that are valid only for uniform homogeneous media of infinite extent. However, even an in vitro preparation that is reasonably homogeneous is nevertheless bounded by air, and hence globally inhomogeneous. One can take such inhomogeneities into account by adding additional terms to the solution. In this section we consider inhomogeneities by approximating the volume conductor by a collection of regions, each one of which is homogeneous, resistive, and isotropic, where the current density J^i is linearly related to the electric field intensity E (Schwan and Kay, 1956). Such inhomogeneities can be taken into account while at the same time retaining the results obtained in the previous section (which were based on the assumption of uniformity).

An inhomogeneous volume conductor can be divided into a finite number of homogeneous regions, each with a boundary S_j. On these boundaries both the electric potential Φ and the normal component of the current density must be continuous:

$$\Phi'(S_j) = \Phi''(S_j) \tag{2.17}$$

$$\sigma' \nabla \Phi'(S_j) \cdot \bar{n}_j = \sigma'' \nabla \Phi''(S_j) \cdot \bar{n}_j \tag{2.18}$$

where the primed and double-primed notations represent the opposite sides of the boundary and n_j is directed from the primed region to the double-primed one.

If dv is a volume element, and $\Psi$and ϕ are two scalar functions that are mathematically well behaved in each (homogeneous) region, it follows from Green's theorem (Smyth, 1968) that

$$\begin{aligned} &\sum_j \iint_{s_j} \left[\sigma_j' \left(\Psi' \nabla \Phi' - \Phi' \nabla \Psi'\right) - \sigma_j'' \left(\Psi'' \nabla \Phi'' - \Phi'' \nabla \Psi''\right)\right] \cdot d\bar{S}_j \\ &= \sum_j \int_{v_j} \left(\Psi \nabla \cdot \sigma_j \nabla \Phi - \Phi \nabla \cdot \sigma_j \nabla \Psi\right) dv_j \end{aligned} \tag{2.19}$$

If we make the choice of $\Psi = 1/r$, where r is the distance from an arbitrary field point to the element of volume or area in the integration, and ϕ is the electric potential, and substitute Equations 2.15, 2.17, and 2.18 into Equation 2.8, then we obtain the following useful result (Geselowitz, 1967):

$$4\pi\sigma \Phi(r) = \int_v \bar{J}^i \cdot \nabla\left(\frac{1}{r}\right) dv + \sum_j \int_{s_j} \left(\sigma_j'' - \sigma_j'\right) \Phi \nabla\left(\frac{1}{r}\right) \cdot d\bar{S}_j \tag{2.20}$$

This equation evaluates the electric potential anywhere within an inhomogeneous volume conductor containing internal volume sources.

The purpose of measuring bioelectric signals is to measure their source, not the properties of the volume conductor with the aid of the source inside it. Therefore, the clinical measurement systems of bioelectric events should be designed so that the contribution of the second term in Equation 2.20 is as small as possible.

2.7. Quasistatic Conditions

In the description of the volume conductor constituted by the human body, the capacitive component of tissue impedance is negligible in the frequency band of internal bioelectric events, according to the experimental evidence of Schwan and Kay (1957). They showed that the volume conductor currents were essentially conduction currents and required only specification of the tissue resistivity. The electromagnetic propagation effect can also be neglected (Geselowitz, 1963). This condition implies that time-varying bioelectric currents and voltages in the human body can be examined in the conventional quasistatic limit (Plonsey and Hepper, 1967). That is, all currents and fields behave, at any instant, as if they were stationary. The description of the fields resulting from applied current sources is based on the understanding that the medium is resistive only, and that the phase of the time variation can be ignored (i.e., all fields vary synchronously).

2.8. Summary

Some of the essential models and theories used in EIT have been outlined in this chapter. Their applications in this work start with the first ever attempt to use EIT/MEG (SQUIDs), as multi-modality and this would be addressed in the next chapter.

Neuromagnetic Field Strength

Chapter 3

NEUROMAGNETIC FIELD STRENGTH OUTSIDE THE HUMAN HEAD DUE TO IMPEDANCE CHANGES FROM NEURONAL DEPOLARISATION

3.1 Introduction

3.1.1 Background

The UCLH EIT Research Group, which the author is part of, focuses on the application of Electrical Impedance Tomography (EIT) for imaging impedance changes in the human head. With this technique, currents are applied to the volume using electrodes and the resulting voltages on the electrodes are measured. The internal distribution of conductivity changes is computed based on this boundary measurement. There are three main mechanisms that give rise to these impedance changes, namely; cell swelling during conditions such as epilepsy or stroke (Gamache et al., 1975; Hossman, 1971), cerebral blood volume change during functional activity (Hansen and Olsen, 1980) and neuronal depolarisation. Reproducible EIT images related to the first two mechanisms have been obtained during epilepsy (Holder et al., 1996a), stroke , spreading depression and evoked activity in animals using cortical electrodes (Bagshaw et al., 2003). Preliminary images of these have recently been obtained in humans during evoked responses (Tidswell et al., 2001)using scalp electrodes. In contrast, the imaging of neuronal depolarisation is still at the theoretical stage because the magnitude of the changes is much less than those due to blood flow or cell swelling, and is at the limit of detectability of present EIT systems.

This study concerns a new method that could be used to image the last mechanism – impedance changes during neuronal depolarisation, which may be classified as a fast brain activity (Rao et al., 1996). During neuronal depolarisation, ion channels open in the dendritic membrane causing its resistance to decrease over tens of milliseconds (Araki and Terzuolo,

1962; Cole and Hodgkin, 1939). It is therefore easier for current to flow inside the neurons during neuronal depolarisation than during the resting state. Hence, qualitatively, we expect the resistance of the tissue containing depolarisation neurons to decrease while the extra ion channels remain open. A model of resistance change in the human cortex during neuronal depolarisation estimated that there is a resistivity decrease of 0.4 - 1.6% in cerebral cortex, which corresponds to a peak change 0.04 - 0.16% when recorded on the scalp (Liston, 2003). This model suggested that the resistance changes are maximal at dc.

Other imaging modalities of electrical brain activity include Electroencephalography (EEG), Positron Emission Tomography (PET), and functional Magnetic Resonance Imaging (fMRI). EEG has excellent temporal resolution but a poor spatial resolution, especially for changes deep within the brain. PET and fMRI have good spatial resolution, of several millimetres, but a time resolution that is only sufficient to measure the metabolic changes associated with neuronal activity, occurring over a few seconds. During human brain activity, similar blood flow changes have been detected using PET and fMRI.

Another imaging technique, capable of imaging brain function due to electrical activity, is Magnetoencephalography (MEG). This is a non-invasive technique for localizing and characterizing the electrical activity of the central nervous system by measuring the associated magnetic fields emanating from the brain. Evoked responses and spontaneous brain activity are two major processes which may be studied by means of MEG (Hamalainen, 1992; Hamalainen, 1992). Studies show that the typical magnetic field outside the head evoked by external stimulation has an amplitude of 50 - 500 fT (Hamalainen et al., 1993) which is on the order of 10^{-9} of the static geomagnetic field of the earth. The measurement of the weak fields can be obtained using Superconducting Quantum Interference Devices (SQUIDs). These have noise levels below $7fT/\sqrt{Hz}$ (Brown et al., 1999), and become unpredictable when the operating frequency is near dc. In view of this, the magnetic field measurement devices have to be extremely sensitive, and external magnetic noise is attenuated.

Electrophysiological methods like MEG and EEG provide measures that reflect neural ensemble activity in the millisecond time scale. Estimating the locations of the brain sources of MEG and EEG activity, however, is problematic due to the nonuniqueness of the solutions (Ahlfors *et al.*, 1999). Combining haemodynamic and electrophysiological information holds promise for imaging patterns of human brain activity in both space and time (Ahlfors *et al.*, 1999). It would be of great use if an imaging technique combines the level of spatial resolution they demonstrate with the temporal resolution of electrophysiological methods in order to map neuronal activity itself, rather than its consequences. EIT could offer this possibility. An advantage of MEG over EIT is that the presence of skull does not attenuate the magnetic field measured by MEG. This is because electrical potentials measured on the scalp are often strongly influenced by various inhomogeneities in the head, making accurate determination of the activated area (Hamalainen et al., 1993). The other advantage is that the problem of contact impedance due to electrodes in EIT measurements is eliminated in the case of MEG.

In principle, the advantage of using SQUIDs and injecting known dc currents in EIT could be combined. The present study explored this possibility by simulating the magnetic field that would be generated by fast electrical brain activity when a maximum allowable constant current of 100 μA is injected. The injected current is based on square wave pulses (Anling, 2000) and below the threshold current for stimulating brain tissue.

3.1.2 Purpose of study

The purpose of this study is to combine EIT and MEG system, as a new multi-modality system in imaging small impedance changes due to neuronal depolarization. Voltage measurements of neuronal activity are prone to low signal to noise ratio due electrode impedance and resisitivity of the skull. An alternative approach is to determine whether measurement of magnetic fields with SQUIDs would be superior as the skull does not attenuate magnetic fileds. To resolve this, some specific issues were modelled: (i) the magnitude of the standing magnetic field due to injection of a current, and whether this falls within the sensitivity of SQUIDs and (ii) the relative size of the magnetic field change during neuronal activity.

3.1.3 Proposed Imaging Sensor

The proposed sensor would be an EIT system (Figure 3-1) for injecting current and instead of measuring the surface potential; SQUID sensors would replace the electrodes measuring the potential V.

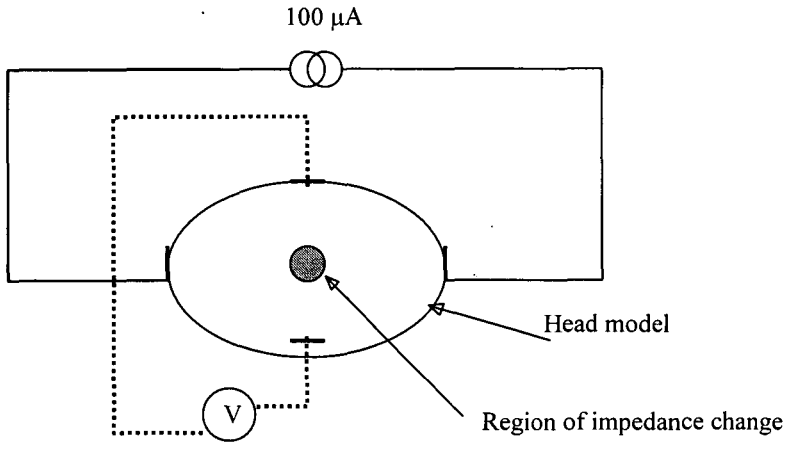

Figure 3-1: EIT system for current injection

I proposed using SQUIDs to measure the magnetic field due to the impedance change in the head due to neuronal depolarisation, as they are capable of detecting very tiny magnetic fields in the order of femto Tesla. A SQUID is made up of a superconducting thin film using photolithography to create parallel Josephson junctions. When a bias current, I_b, is applied to the SQUID, voltage through it is zero if the current is less than critical current. When the bias current originating from the pick up coils exceeds critical current, I_c, the SQUID turns to the normal state and voltage is produced. This voltage will change in a periodic wave in accordance with the flux quantization.

3.1.4 Design

Simulation was performed using a computer model in which the head was simulated either as a spherical Finite Element Model which was homogeneous or had four shells representing scalp, skull, CSF and brain. The physiological situation modelled was that of visual evoked responses in which there is neuronal activity in the visual cortex in response to binocular viewing of a checkerboard. The conductivity change was estimated from a biophysical model of the impedance change during evoked responses, which estimated it to be a 1% decrease (Liston, 2003) and a typical volume for this change was taken as a 2 cm radius sphere of brain. The resulting change in magnetic field was calculated when this volume changed conductivity at different points along the entire anteroposterior axis of the head, therefore simulating impedance changes that might occur for evoked activity in any cortical or subcortical structure.

A good measure of detectability of the neuromagnetic signals is its signal to noise ratio (SNR). The SNR is a measure of how the signal from the head compares to other background signals. In order to calculate the SNR, the simulated signal strengths were compared with the spectral noise density of a typical dc SQUID system which is $7fT/\sqrt{Hz}$ (Figure B-1 (Appendix B)) in a broad frequency band of 1 - 100 Hz. As detailed in section 3.1.1, beyond these frequencies the noise level is unpredictable and becomes significantly higher (Internet Communication, 2002).

3.2 Methods

3.2.1 Volume Conductor Model

Two head models were considered. The first, modelled the head as a four-shell sphere (Figure 3-2(a)) depicting the head to be made up of the brain, cerebrospinal fluid (CSF), skull and scalp. Respectively, each layer had conductivities of 0.25, 1.79, 0.018 and 0.44 Sm^{-1} (Geddes and Baker, 1967) and were inhomogeneous and anisotropic (Liston, 2003). The outer radii of the brain, CSF, skull and scalp were 8.0, 8.2, 8.7,and 9.2 cm respectively.

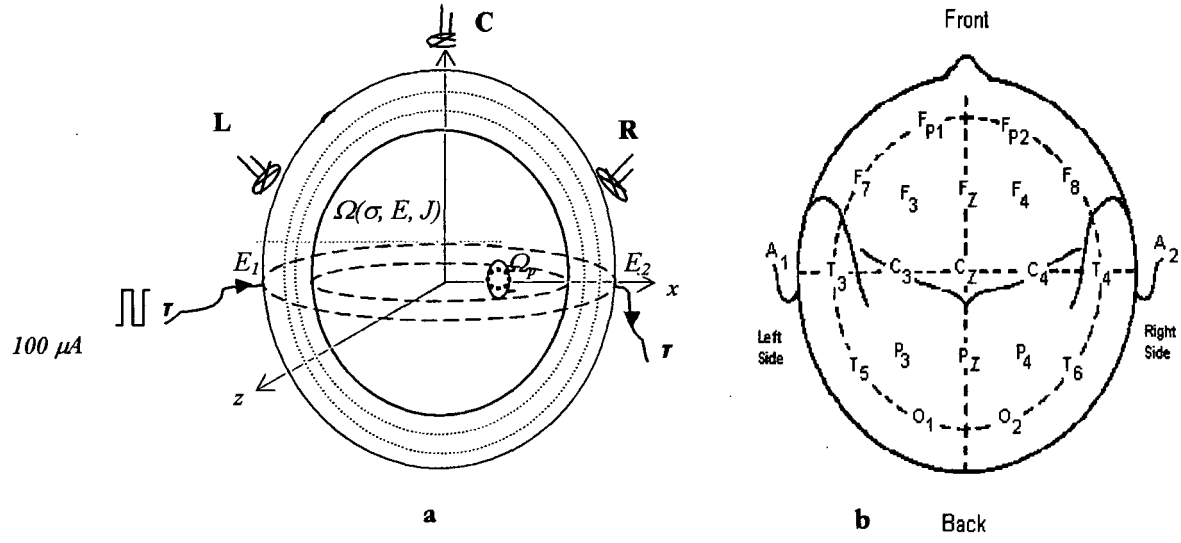

Figure 3-2: (a) An approximation of the realistic head to a fourshell sphere model showing points of current injection E1 and E2. R, C, and L are the locations of typical SQUID sensors for the measurement of the magnetic field. The gray region Ωp is a collection of nodes indicating a region in the brain where the neurons are firing and the conductivity is σ'. The conductivity at other regions within the volume Ω is σ. (b) The EEG 10-20-system showing the relationship between the location of an electrode and the underlying area of cerebral cortex.

The second head model was a homogenous and isotropic sphere with a brain and outer radius of the scalp as 8.0 and 10 cm respectively. This model did not take into account the presence of the skull and cerebrospinal fluid.

A FEM mesh was generated using a software package known as IDEAS; an industry standard meshing software (Bayford *et al.*, 2001b) to model the head as a simple homogeneous sphere or four concentric spheres. Two different mesh densities, one with over 44,000 and the other 27,000 four-node tetrahedron elements were developed for the fourshell model. The spherically homogeneous model contained two mesh densities of 42,093 and 24,734 four-node tetrahedral elements. These two different mesh densities were included to ensure the accuracy of the expected results. All layers were modelled as purely resistive and the meshes were then used to estimate the current density by using a program developed in MATLAB 6.1 based on the TOAST suite of forward solver programmes developed originally for optical tomography (Arridge et al., 2000). This program estimates the current density by applying the theory detailed in sections 2.3 and 2.4.

3.2.2 The source model

The relative size of the source was based on physiological changes that occur in the visual cortex during evoked potential recordings. Based on the mean volume of the primary visual cortex, V1, in humans, which are 5692 and 5119 mm^3 for the right and left hemispheres respectively (Andrews et al., 1997), this region was modelled as a sphere of radius 11 mm, in the posterior occipital lobe. To obtain a significant change in the magnetic field when there is brain activity, the source was then modelled to be slightly bigger than this known primary visual area. It was modelled as a 2 cm radius sphere using realistic FEM, which will predict the effect on the magnetic field change during brain activity.

3.2.3 Current Injection

Biophysical modelling has indicated that changes in cerebral impedance during neuronal activity are largest with applied current below 10 Hz (Figure 3-3), (Boone K., 1995) as the mechanism is that current only enters the intracellular space when ion channels open during neuronal depolarization. If higher applied frequencies are employed, current enters the intracellular space at rest as well, by traversing the capacitance of the neuronal membrane; there is then a much smaller change when ion channels in the membrane open. This model has been demonstrated experimentally (Liston, 2003) on crab nerve showing maximal impedance changes occurring at low frequencies.

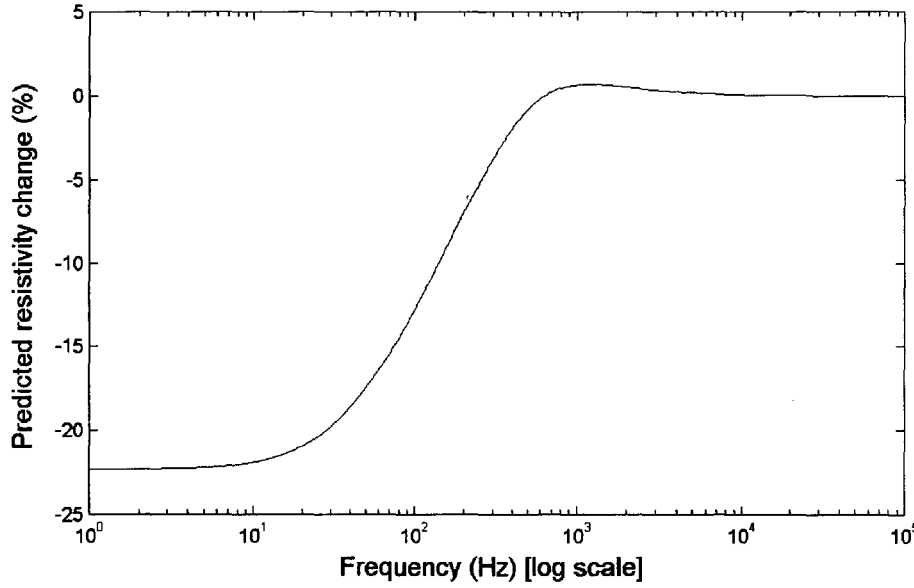

Figure 3-3: Predicted change in resistivity versus frequency during neuronal depolarisation

The injected current was chosen to be near dc (8 Hz) for maximal impedance change during neuronal depolarization. In addition, at this frequency, the effect of electromagnetic induction that may give rise to creation of eddy currents will be negligible. For medical applications and safety implications, a maximum allowable current of 100 μA (Anling, 2000) was injected. A

simplified electrode model (point electrode) was simulated by assuming that the injected current was a continuous function by totally ignoring the effects of the electrodes.

3.3 Mathematical Principles

3.1.1 Current Density Estimation

If current passes through a conductive object, there will be a distribution of potential ϕ throughout the object, which is dependent on the distribution of conductivity, σ. If the distribution of conductivity is known and the sources and sinks are on the surface, the induced potential within the object can be predicted using Laplace's equation

$$\nabla \cdot (\sigma \nabla \phi) = 0 \tag{3.1}$$

The potential, ϕ, is a non-linear function of conductivity. Analytical solutions to this equation have been found for only simple resistivity distributions (Boone K., 1995). We therefore performed the modelling with a finite element mesh, using a linear approximation for each cell (Woo et al., 1993)

In this work, since the current is being applied at near dc, the propagation of the low frequency electromagnetic field is virtually free of the feedback action from eddy currents. The current density distribution is defined by the potential gradient and the specific conductivity σ of the different regions

$$\vec{\mathbf{J}} = -\sigma \nabla \phi \tag{3.2}$$

3.1.2 Magnetic Field Estimation

With reference to a fixed origin, the magnetic field at a point B, due to a current density $\vec{J}$ in an element $d\tau$, at a point $\vec{r}$ from P, is, according to the law of Biot-Savart (Sarvas, 1987),

$$\mathbf{B}(\vec{r}) = \frac{\mu_o}{4\pi} \vec{J} \times \frac{\vec{r}}{|\vec{r}|^3} d\vec{\tau} \tag{3.3}$$

where μ_o is permeability of free space.

For simplicity we have a 3D representation of the entire volume conductor, Ω, as shown in Figure 3-4. The volume whose the conductivity remained constant was represented by Ω_u and the depolarised region by Ω_p. It was further assumed further that the number of nodes in the non-depolarised region was N_u and that of the depolarised region was N_p. The total number of nodes in the entire volume is therefore $N_t = N_u + N_p$.

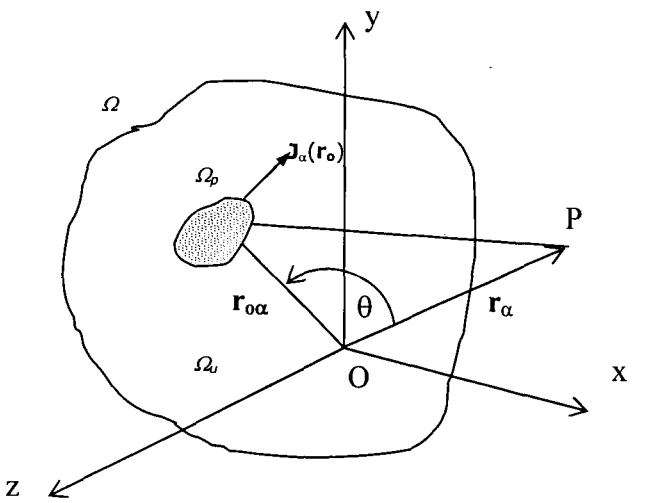

Figure 3-4: The depolarised region is denoted by Ω_p whereas the remaining volume is labelled Ω_u. The entire volume conductor is represented by Ω. The point at which the magnetic field is estimated is B. The position vectors of the source (node) and point of measurement are respectively $r_{o\alpha}$ and r_α respectively from a fixed origin O. The distance between the source and P is $|\vec{r}_\alpha - \vec{r}_{o\alpha}|$. J_α denotes the current density at a node.$\alpha \in \{i, j, k\}$

By using Biot-Savart law, the magnetic field at the point P due to the i^{th} node in the region Ω_u is given by

$$B^u(\vec{r}_{oi}) = \frac{\mu_o}{4\pi}\vec{J}_i \times \frac{(\vec{r}_i - \vec{r}_{oi})}{|\vec{r}_i - \vec{r}_{oi}|^3} d\vec{\tau}_i \tag{3.4}$$

and that due to the j^{th} node in the region Ω_p can be found as

$$B^p(\vec{r}_{oj}) = \frac{\mu_o}{4\pi}\vec{J}_j \times \frac{(\vec{r}_j - \vec{r}_{oj})}{|\vec{r}_j - \vec{r}_{oj}|^3} d\vec{\tau}_j \tag{3.5}$$

Without any perturbation, the magnetic field due to the k^{th} node in the volume Ω at point P is given by

$$B^b(\vec{r}_{ok}) = \frac{\mu_o}{4\pi}\vec{J}_k \times \frac{(\vec{r}_k - \vec{r}_{ok})}{|\vec{r}_k - \vec{r}_{ok}|^3} d\vec{\tau}_k \tag{3.6}$$

In order to obtain the contribution of all nodes at the point of measurement of the magnetic field when part of the brain is depolarised (perturbed), the vector sum resulting from equations 3.4 and 3.5, can be computed as

$$B_p = \sqrt{\left(\sum_{j=1}^{N_u} B_{jx}^u + \sum_{i=1}^{N_p} B_{ix}^p\right)^2 + \left(\sum_{j=1}^{N_u} B_{jy}^u + \sum_{i=1}^{N_p} B_{iy}^p\right)^2 + \left(\sum_{j=1}^{N_u} B_{jz}^u + \sum_{i=1}^{N_p} B_{iz}^p\right)^2} \tag{3.7}$$

If B_b represents the baseline magnetic field (the unperturbed magnetic field) at the point P when the conductivity of the whole brain region remains unchanged then this field, and based on equation 3.6 can be computed as

$$B_b = \sqrt{\left(\sum_{k=1}^{N_t} B_{kx}\right)^2 + \left(\sum_{k=1}^{N_t} B_{ky}\right)^2 + \left(\sum_{k=1}^{N_t} B_{kz}\right)^2} \tag{3.8}$$

In this research, the interest was in the change in magnetic field from baseline as a result of the 1% change in impedance during neuronal depolarization. This could be computed as the

relative change in magnetic field, ΔB, by taking the difference between the perturbed and unperturbed magnetic fields such that

$$\Delta B = B_p - B_b \tag{3.9}$$

3.4 Simulation

The two head models (section 3.2.1) and the defined region of perturbation (section 3.2.2) were implemented in the simulation of the forward models developed in the previous section. For each head model, the simulation was done in two parts. The first part simulated the lower baseline magnetic field, B_b, of the head when the conductivity remained unchanged. The second part simulated the magnetic field, B_p, of the whole head when the conductivity of only the predefined volume within it changed by 1%. To estimate the magnetic field due to this small change in conductivity, the simulation was repeated fifteen times by varying the centre of the perturbed volume in the range $(-8 < x < 8)$ cm in steps of 1 cm laterally from the right (T4) to the left (T3) temporal lobe (Figure 3-2(b)). The points of measurement of the magnetic field were chosen at locations C (0, 11, 0) near Cz, R (4, 4, 9.3) near C4, and L (-4, 4, 9.3) near C3 which were located about 1 cm away from the scalp. R and L were closer to the region where the current density we expected to be higher and the region of perturbation was closest. With this arrangement, one may obtain the strongest magnetic field at these points as the source or region of perturbation is closest. This will be the best-case scenario. The location C was located 11 cm from the centre of the brain where the current density was not as strong as the periphery. To maximize the sensitivity at the centre of the brain, a diametrically opposing current injection pattern was chosen; such that the current was injected through the left temporal (T3) and collected it at the right temporal (T4) lobe.

All measurement-related estimations were carried out in a Cartesian coordinate system with units in centimetres (Figure 3-2(a)). The z-axis runs through the pre-auricular points from right to left, and the x-axis runs perpendicular towards the nasion, thus the y-axis points to the

top of the head. A program written in MATLAB was used for modelling the dc injection at the selected electrodes and estimation of the current density distribution within the volume. It also defined and modified the conductivity of the perturbed region and hence the computation of the magnetic field at the chosen locations.

3.5 Results

In the design, two head models were generated with two different mesh densities. The head models with the higher mesh densities were referred to as fine meshes, and those with lower mesh densities as medium meshes. Thus, there were the fourshell fine and medium meshes for the fourshell head model, and then sphere fine and medium meshes for the homogeneous head model.

3.5.1 Estimated Magnetic Field

3.5.1.1 Fine Mesh

For the fine mesh, the standing magnetic field was 30 – 37 pT for the homogeneous sphere model and about one third of this for the four-shell sphere (Table 3-1). The change in magnetic field was greatest when the volume of conductivity change was near the edge of the head (Figure 3-5 & 3-6) and so near to the points of current injection, for all three sensors. The peak change (which actually corresponded to when the change in conductivity was at the edge for all 3 cases, but at one edge for L and the other edge for R) was 1.2 - 3.1 fT (Table 3-2), which corresponded to a proportional change of 0.004 - 0.029% (Table 3-3). The proportional change in the four-shell model was about four to five times greater than that of the homogeneous model.

	Baseline magnetic field (pT) at point		
Type of Head Model	C	R	L
Homogeneous Sphere	30.6	36.5	36.6
Four-shell Sphere	9.9	10.5	10.6

Table 3-1: Baseline magnetic field for fine mesh

	Maximum field change from baseline magnetic field (fT) at		
Type of Head Model	C	R	L
Homogeneous Sphere	1.2	2.2	2.6
Four-shell Sphere	1.6	3.1	2.7

Table 3- 2: Maximum magnetic field change from baseline field strength for fine mesh

	Maximum percentage change from baseline magnetic field (%) at		
Type of Head Model	C	R	L
Homogeneous Sphere	0.004	0.006	0.007
Four-shell Sphere	0.016	0.029	0.026

Table 3-3: Maximum percentage change from baseline magnetic field for fine mesh

3.5.1.2 Medium Mesh

For the medium mesh, the standing fields and absolute field changes were approximately double those calculated with the fine mesh, but the proportional changes were very similar, being four to five times greater again with the four shell model (Tables 4 - 6).

	Baseline magnetic field (pT) at point		
Type of Head Model	**C**	**R**	**L**
Homogeneous Sphere	47.3	55.5	55.6
Four-shell Sphere	15.9	16.8	16.8

Table 3-4: Baseline magnetic field for medium mesh

	Maximum field change from baseline magnetic field (fT) at		
Type of Head Model	**C**	**R**	**L**
Homogeneous Sphere	1.9	4.4	3.9
Four-shell Sphere	2.9	5.2	4.9

Table 3- 5: Maximum magnetic field change from baseline field strength for medium mesh

	Maximum percentage change from baseline magnetic field (%) at		
Type of Head Model	**C**	**R**	**L**
Homogeneous Sphere	0.004	0.008	0.007
Four-shell Sphere	0.018	0.031	0.029

Table 3.6: Maximum percentage change from baseline magnetic field for medium mesh

3.5.2 Variation of magnetic field

With reference to the four-shell fine mesh, the change in magnetic field as detected by the central sensor (C) varied from a minimum of 0.001% for location of impedance change in the centre to a maximum of 0.02% at the edge of the head. The right and left sensors detected a maximum change of about 0.036% for the nearest region of conductivity change and about 0.011% for the farthest region of change. They both recorded a minimum change of 0.001% just as the central sensor (Figure 3-5).

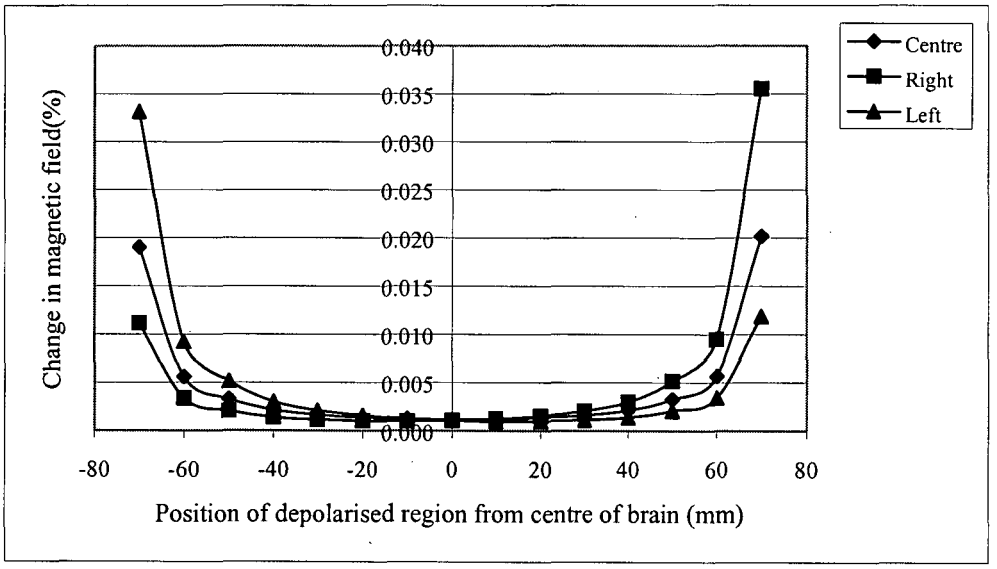

Figure 3-5: Fractional magnetic field change during evoked response with respect to position for homogeneous sphere fine mesh model The x-axis denotes the distance of the centre of the depolarised region from the centre of the head.

For the homogeneous fine mesh, all three sensors recorded a minimum change of 0.001% at the centre of the head and about 0.004% to 0.011% at the edges (Figure 3-6).

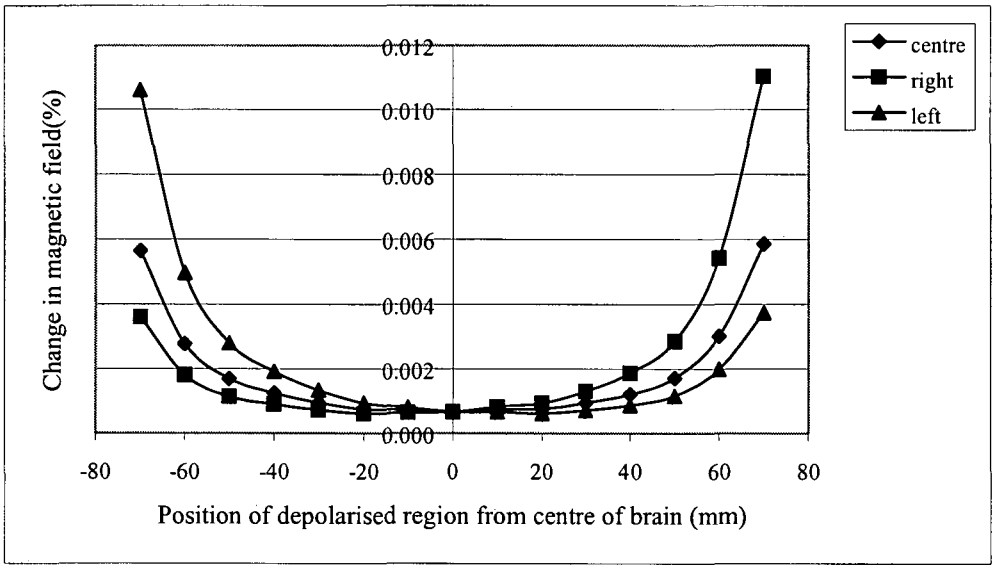

Figure 3-6: Fractional magnetic field change from baseline with respect to position for fourshell fine mesh model. The x-axis denotes the distance of the centre of the depolarised region from the centre of the head.

3.6 Discussion

3.6.1 Summary of results

In order to validate the procedure for this study, symmetrical measurements were done over a broad anatomical range, by using a fourshell and homogeneous model, and a fine or medium mesh. The results were in broad agreement and in a way to support the belief that the results were not contaminated by numerical errors which may arise in the use of numerical methods like FEM. The standing fields were of the order of 10 pT, and the proportional changes were about four orders of magnitude smaller, in the region of a few fT. The changes were greatest when the volume with changed conductivity was at the edges of the head, and near the points of current injection.

3.6.2 Technical issues

The percentage changes in magnetic field from baseline values for the two different meshes were similar but the calculated baseline magnetic field for the homogeneous model was about three times that of the fourshell. This appears reasonable as in the fourshell model the skull's resistance would cause a potential drop in the brain region as compared to the homogeneous model. In FEM, a finer mesh typically would result into a more accurate and convergent solution. The latter could be used to explain why the calculated fields for the fine meshes were relatively smaller than those of the medium meshes.

For all meshes and head models, the baseline magnetic field seen by sensor C confirmed the relatively longer distance the conductivity change was from it as compared to sensors R and L (Tables 3-1 and 3-4). They in turn had measured almost the same magnitude of baseline magnetic field as they were placed symmetrically. There was at most 0.5 fT difference between the change measured by the sensors R and L, though they were symmetric to each other. This difference might be attributed to non-symmetry in the meshes and partially due to rounding errors.

To validate the results, they were compared with an analytical solution obtained from previous work done in the UCLH-EIT group, (Liston *et al.*, 2002) based on the different head models, conductivity parameters and dimensions used in our numerical solution. The current density, J(r) was found analytically by evaluating the electric field E(r) at each node and multiplying each nodal value by the conductivity of the medium in which that node existed. Nodes on the boundary between two media were considered to belong to the inner medium. The analytical current density data was then utilized in computing the magnetic field at the three locations as done in the numerical solution. The analytical baseline magnetic fields obtained were of the order of 10 pT whereas the best-case (when the conductivity change was near the edge) magnetic field change from baseline was of the order of a few fT. These values compared well with those obtained for the numerical solution.

As the strength of magnetic field at a point is dependent upon current density of the source and the source's distance from that point, for each model, the mean magnitude of current density was then found only for the region defined as brain. Plots showed that far less current entered the brain in the fourshell than in the homogeneous case (Figure 3-7). The mean current density in the diametric plane across the head was 5.0×10^{-4} Am^{-2} and 9.0×10^{-5} Am^{-2} in the homogeneous and four-layered concentric spheres, respectively. Its maximum value was 1.1×10^{-3} Am^{-2} and 1.9×10^{-4} Am^{-2} for the two spheres respectively. These values may be explained because the skull was resistive in the fourshell model and this is consistent with the finding that the magnetic field estimated for the homogeneous sphere was greater than that of the fourshell.

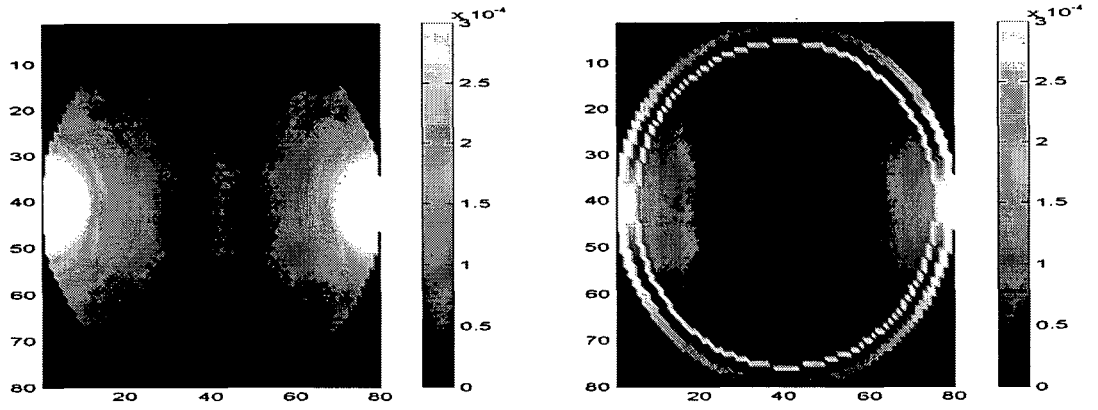

Figure 3-7: A MatLab interpolated SURF plot of current density on an 80x80 grid (A m^{-2}) in the plane of two bipolar electrodes applying 1μA on the surface of a) a homogenous sphere of conductivity σbrain and b) a 4-shell sphere. The x- and y-axes are pixel numbers (Liston, 2003).

3.6.3 Would the changes be detectable with current MEG technology?

The dynamic range of neuromag 122 dc SQUID (4D Neuroimaging, San Diego, USA) for example is ±200 pT. The standing magnetic field for head models considered in this study was estimated to be in the range 10 to 40 pT. For the best approximation to the head, the obtained field was about 10 pT. Since these results were within the dynamic range of the neuromag, we should be able to use SQUIDs to detect the standing magnetic field of the head without saturation. However, there is the question of how sensitive the SQUIDs are in measuring changes from baseline magnetic field. The estimated change from baseline magnetic field was about 3fT, which is at least two times lower than the spectral noise density of 7 fT in neuromag 122 at a frequency band of 1 - 10 Hz (Figure B-1 (Appendix B)). With averaging, this may be detectable, but will be at the lower limit of sensitivity.

Although no physical measurements were undertaken with the proposed system, to validate the results further it is possible to compare them with some known brain activities measured with MEG systems. Evoked and spontaneous magnetic fields measured on the scalp (measurement distance 2 - 4 cm away from the current source) by MEG are respectively of the

order of 10 pT and 0.1 pT (Bodurka and Bandettini, 2002). These signal strengths are over 10 times stronger than the predicted noise level of 7 fT. We also compared our results with some of the conventional physiological events that are recorded using MEG, such as alpha rhythms. Alpha rhythm currents are obtained in a narrow frequency band of 8 to 13 Hz. Magnetic fields produced by alpha-rhythm fields several centimetres outside the scalp has been predicted theoretically as 7×10^{-10} gauss, that is 0.07 pT (Cohen, 1968). The signals recorded have a SNR better than the threshold of 3 dB.

3.6.4 Does this modelling suggest an advantage over EEG recording?

A mathematical model of resistance change (Liston, 2003) suggested a change with scalp electrode recording as about 0.01% at near dc. EEG gives a similar result, and does not show the possible advantage we might have suspected with MEG being insensitive to the skull. As MEG is much more costly and technically difficult, and the possibility of saturating amplifiers, there is no evident advantage in terms of signal to noise ratio. However, it could be advantageous in terms of signal quality and this could only be determined in the future by experimental evaluation.

Electrode Pairs for Optimal Current Density

Chapter 4

MODELLING OF ELECTRODE PAIRS FOR OPTIMAL CURRENT DENSITY ESTIMATION IN THE VISUAL CORTEX AND OPTIMAL VOLTAGE CHANGE MEASUREMENT

4.1 Introduction

4.1.1 Background

With an injected current into an electrically conducting object such as the human head, it induces surface potentials, current densities, and magnetic flux density distributions. Generally, these distributions are determined according to the geometry, electrode configuration, and the conductivity changes and distributions (internal electrical properties) of the subject. A literature review revealed that three mechanisms were identified as the cause of impedance change in the human head (Section 1.1). These changes could be classified as slow or fast (Gilad *et al.*, 2004a).

The electrical resistivity of the cell membrane decreases during neuronal depolarisation, thus allowing external current to flow more freely through the cell (Cole and Curtis, 1939). These changes last tens of milliseconds (Araki and Terzuolo, 1962; Cole and Hodgkin, 1939) -fast impedance change- and are expected to occur at frequencies below 100Hz. This is related to membrane capacitance, which limits current from flowing into the cell at low frequencies whereas at high frequencies the current can flow through the membrane regardless of the state of ion channels (Boone, 1995; Liston, 2003). For example, when the activity of a population of neurons displays spatial and temporal coherence such as in visual evoked response, it will be accompanied with resistivity change of the active tissue as a whole.

The UCLH-EIT group used EIT to obtain reproducible images of slow impedance changes with scalp electrodes (Boone and Holder, 1996a; Holder et al., 1996b; Rao et al., 1996; Tidswell et al., 2001). Currently, there are a number of research projects underway to improve

the sensitivity of EIT to detect fast impedance changes (Gilad *et al.*, 2004a). Previous work (Boone and Holder, 1994a) suggested that impedance changes accompanying neuronal depolarisation may be of the order of 0.06 - 1.7% locally at frequencies below 100 Hz (Boone and Holder, 1994a). However, imaging of these changes is beyond the capabilities of existing EIT systems.

A recent study using EIT to measure fast impedance changes, based on a mathematical model, suggested that the impedance change when measured locally in the brain was about 1% and reduced by a factor of 10 (0.1%) when measured on the scalp (Liston, 2003). Once again, this was due to shunting of the current through the scalp instead of flowing through the high resistive skull. On the other hand, as electrodes are placed on the scalp to collect the surface potential, the effect of contact impedance between skin and electrodes limits the accuracy of the measurement of surface potential.

Other methods have been used in attempt to image fast impedance changes. Recently, a new imaging system was proposed which combined EIT and Superconducting Quantum Interference Devices (SQUIDs) in an attempt to minimise the problem of contact impedance (Ahadzi et al., 2004a). A mathematical model, which consisted of the head and modelled as a homogeneous sphere or four-shell to represent the volume conductor in 3D using FEM, was used to validate this system. With an injected near DC current of 100 μA, the baseline magnetic field was about 10 pT. The change from baseline due to a 1% change in brain region as big as a 2-cm radius sphere along the left and right temporal lobe was 3fT (Ahadzi *et al.*, 2004a). The estimated signal to noise ratio (SNR) in a frequency band of 1 - 100 Hz revealed that the magnetic field change due to the simulated physiological changes was below detectability by a typical MEG system which has spectral noise density of $7fT/\sqrt{Hz}$.

As the human skull is irregular in shape and less conductive, a key issue is to locate electrodes positions through which current can be injected. This will enable the development of a model, which could predict the current density distribution at specific regions in the brain. The solution to this issue is essential in Electrical Impedance Tomography systems since a good

knowledge of the current distribution could allow the detection of smaller conductivity changes. In addition, it will enable us to know how much current to inject in order to constrain current densities from exceeding the threshold values which may excite certain parts of the brain tissue.

The brain region, whose conductivity change is of interest in this section, is the primary visual cortex area. During visual evoked stimulation, ninety percent (90%) of the activity takes place in the primary visual cortex (Chiappa, 1990). In humans, the primary visual cortex is located nearly entirely on the medial surface of the occipital lobe, with approximately two-thirds of primary visual cortex (V1) lying within the walls of the calcarine sulcus.

This chapter presents the study, which addressed the electrode configuration that could be suitable for obtaining optimal current densities and surface potential with respect to fast impedance changes, which are due to visual evoked responses in the primary visual cortex. The result of this work has already been used in UCLH-EIT group to estimate the fast resistivity changes in humans during visual evoked potential (Gilad *et al.*, 2004b; Gilad *et al.*, 2004a; Gilad *et al.*, 2005b).

4.1.2 Purpose of study

The purpose of this work was to model current flow through the head in low frequency impedance measurement of neuronal depolarization. The experimental paradigm selected was the full field visual evoked responses with impedance measurement using scalp electrodes. The expected change in conductivity was set to 1%, which was the middle value of the conductivity changes in the human cortex accompanying neuronal depolarization. By doing so, the proposed application would be validated, and suggest optimal ways to perform planned human recordings.

The specific questions to be answered were:

1) How large are the standing potentials on the scalp?
2) How large are the proposed changes?
3) What is the peak current density in the brain for current injection of the limit allowed for permissible auxiliary current under safety regulations - 100 μA? The reason for this was that if this were well below the current level at which the brain would be stimulated, if necessary, the current applied could be increased in order to improve the signal-to-noise ratio.
4) Which electrode combinations are the most sensitive to achieve the above three objectives?

Finally, tank measurements of the standing surface potentials were done in order to validate the mesh predictions empirically.

4.1.3 Design

In order to achieve the above objectives, a FEM was used to model the head to be a homogeneous sphere or a realistic three or four layer shapes. The homogeneous sphere and realistic three layer head models were used to test the accuracy of the numerical modelling by estimating the baseline surface potential only when current was injected through some pairs of electrodes. To validate the numerical modelling, two tank experiments were performed,

namely: the spherical tank (simulated as homogeneous sphere) and latex tank (simulated as a realistic three layer head) by physically injecting current through some selected electrodes and measuring the baseline surface potential.

For the changes in baseline potential due to change in conductivity in V1, only the three and four layer head shapes were used. The current injection was simulated through various pairs of electrodes and the current densities in V1 and surface potentials were numerically calculated for an assumed or no activity in V1. The experimental and the modelling results were then compared. In addition, the current densities obtained by our modelling were compared with various values from literature reviews specifying current density thresholds for stimulating brain tissues or changing its activation in order to allow us (UCLH-EIT group) to estimate the current level limit that could be used for our (UCLH-EIT group) human EIT measurements.

4.2 Method

4.2.1 The Meshes

Unlike in chapter 3 where two head shapes were used, in this chapter, three head geometries were considered for the finite element modelling. These were a homogeneous head-shape (homogeneous-head), the same head-shape containing a human skull (skull-head) and that of a full, layered human head containing brain, CSF, skull and scalp (full-head). However, this first model was used in the previous chapter to investigate the magnetic field measurements due to impedance changes in the head during neuronal depolarisation (Ahadzi *et al.*, 2004a). The other head shapes were realistic models, which contained a cavity to represent the air space behind the nose. An industry FEM software package, I-DEAS (Bayford *et al.*, 2001a), was used to generate these meshes describing realistic head geometry with linear, tetrahedral elements. A solid model was used to generate surfaces of the scalp, skull, CSF and brain to produce the head shaped meshes (Bayford *et al.*, 2001a). For the full head with four layers, the scalp region contained 10,078 nodes, skull region 6,325 nodes, CSF region 2,064 nodes, and brain region 6,702 nodes

The different conductivities of the layers of the head used in this work are summarized in Table 4.1, whereas Table 4.2 shows the number of nodes and elements for each head model used.

Layer of head	Conductivity (Sm^{-1})
Scalp	0.440
Skull	0.018
CSF	1.790
Brain	0.250

Table 4.1: Conductivity values of the different layers of the head (Oostendorp and Debelke, 2000)

Head Shape Type	Number of nodes	Number of elements	Ratio of largest to smallest element
Homogeneous head	22,420	106,825	49
Head-Shape with Skull	16,983	87,850	2,050
Full Head with 4 layers	25,169	136,442	1,605

Table 4.2: Listed are the three meshes, the number of nodes and elements and the ratio of largest-to-smallest element size in each head shape. This ratio is a measure of their quality and a smaller value is desirable

4.2.2 The source model

The primary visual cortex (Brodmann area 17) (figure 4.2A) was modelled as the correlated size variations in human visual cortex, but excluding lateral geniculate nucleus and optic tract.

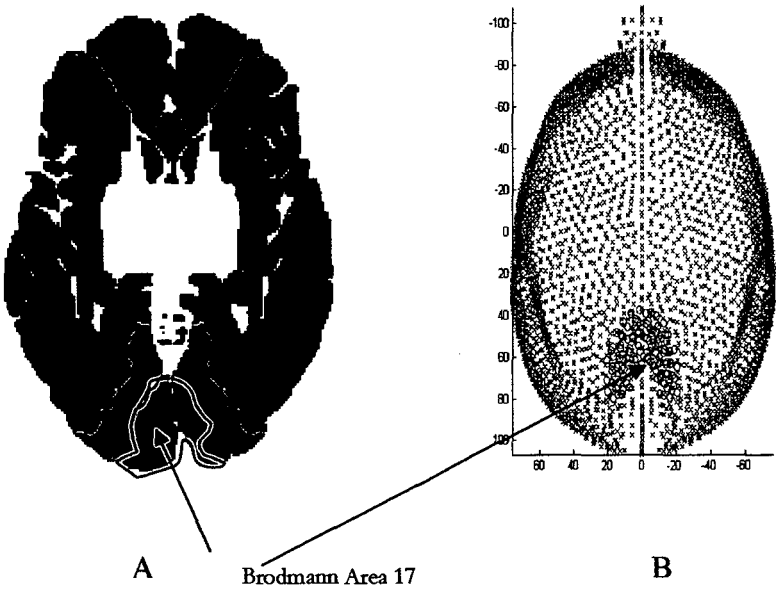

Figure 4.2: A - The brain region showing the primary visual cortex as Brodmann area 17 and B shows the modelled realistic head with V1 using FEM

The mean volumes of the left and right hemispheres of the visual cortex were respectively 5,119 and 5,692 mm^3. An inter-individual variation was detected when V1 volume measurements were combined for corresponding hemispheres of 14 brains (range 7,769 - 14,213 mm^3) with the mean total volume of about 10,770 mm^3 (Andrews et al, 1997). With these figures, V1 was modelled using FEM in the form of two overlapping ellipsoids to depict the shape of it as a strawberry (figure 4.2B), and the total volume was 10, 811 mm^3.

4.2.3 Current injection and electrode model

Biophysical modelling has indicated that changes in cerebral impedance during neuronal activity are largest with applied current below 10Hz (Boone K., 1995) as the mechanism is that current only enters the intracellular space when ion channels open during neuronal depolarisation. If currents of higher frequencies are applied, current enters the intracellular space at rest as well, by traversing the capacitance of the neuronal membrane; there is then a much smaller change when ion channels in the membrane open. This model has been demonstrated experimentally (Liston *et al.*, 2001) on crab nerve showing maximal impedance changes occurring at low frequencies. We chose the injected current to be near dc (8 Hz) for maximal impedance change during neuronal depolarisation. In addition, at this frequency the effect of electromagnetic induction that may give rise to creation of eddy currents will be negligible.

For medical applications and safety implications, a maximum allowable current of 100μA (Anling, 2000) was injected, and through surface electrodes, which are typically used during normal EEG activity measurements. In the human experiments (not presented in this paper), the electrodes used are the Ag-AgCl disc, 9 mm in diameter with radially varying recession cone starting 1.5 mm from the circumference (6 mm diameter) into a depth of 3 mm. For the numerical analysis, this empty cone, usually filled with conductive jell when applied on human skin was modelled as a simplified model of the EEG electrode as a uniformly distributed current across a flat 9 mm diameter disc.

4.3 Mathematical principles

In a linear isotropic medium, the current density $\vec{J}$, and the electric field $\vec{E}$ are related by the approximation

$$\vec{J} \approx \gamma\vec{E} \approx (\sigma + i\omega\varepsilon)\vec{E} \tag{4.1}$$

where σ is the electrical conductivity, ε the electrical permittivity and γ the complex admittivity of the medium. If there are no current sources in the interior of the volume and the electric field does not change with time, then

$$\nabla \cdot \vec{J} = 0 \tag{4.2}$$

Substituting (4.1) into (4.2) leads to

$$\nabla \cdot \gamma\vec{E} = 0 \tag{4.3}$$

The Laplacian elliptic partial differential equation resulting from this is

$$\nabla \cdot (\gamma \nabla u) = 0 \tag{4.4}$$

The mixed (Dirichlet and Neumann) boundary conditions accompanying the Laplacian equation (4.4) are formally known as the electrode model. This model is superior to the previously used continuum, shun and gap models due to its better resemblance to the physical systems.

The associated current density underneath the surface of the electrodes is then

$$\gamma \frac{\partial u}{\partial v} = \vec{J} \tag{4.5}$$

and it is zero elsewhere.

In addition, for each of the electrodes, the integral of the current density over the whole electrode surface, s, is equal to the total amount of current I_l flowing to or from that electrode,

$$\int_{E_l} \gamma \frac{\partial u}{\partial v} ds = I_l \qquad l = 1, \ldots, L \tag{4.6}$$

where L is the number of electrodes in the system. The value of potential V_l measured on electrode l is equal to the sum of the potential on the boundary surface underneath that electrode and the potential drop across the electrode's contact impedance z_l in ohms per square meter is

$$u + z_l \gamma \frac{\partial u}{\partial v} = V_l \tag{4.7}$$

For this study, we assumed the conductivity of V1 to be σ_o when there is no visual activity (unperturbed state) and σ_1 when there is visual stimulation (perturbed state). Let $V_l(\sigma_o, j)$ be the estimated unperturbed surface potential between two pairs of electrodes when current density j is applied to another pair of electrodes, and $V_l(\sigma_1, j)$ be the estimated perturbed surface potential. The change in surface potential when there is or no activity in V1 is estimated as $\Delta V = V_l(\sigma_1, j) - V_l(\sigma_o, j)$ and the estimated percentage change is

$$\frac{\Delta V}{V_l(\sigma_o, j)} \times 100 \tag{4.8}$$

The change in the measured voltage between two points a and b depends only on the perturbation of the $\nabla\phi$ term of the electric field

$$\Delta v_{ab} = -\int_a^b \Delta(\nabla\phi) \cdot d\mathbf{l} \tag{4.9}$$

The solution for the potential ϕ within a given conductivity distribution can be obtained numerically by using FEM. With the FEM, we assumed there are N_t and N_v number of nodes in the entire volume and V1 respectively, and represented the absolute current density at each node in V1 due to an independent current injection pair l as J_{il}. The statistical mean current density in V1 due to the l^{th} current injection pair is computed as

$$\bar{J}_l = \frac{1}{N_k} \sum_{k=1}^{N_v} J_{il} \tag{4.10}$$

$l = 1, 2, \ldots$,number independent of combinations, and $k = 1, 2, \ldots, N_v$.

4.3.1 Simulations and Analysis

The homogeneous sphere and the two realistic heads were simulated in turn. The position vectors of all current injecting and recording electrodes were defined as the electrode protocol likewise those of the nodes and elements of the three head models. The positions of the electrodes were based on the EEG 10-20 electrode configuration (figure 1.16) with an additional 10 electrodes forming the EIT electrode system (Gibson, 2000). Electrodes 29 and 30 are nearest the occipital cortex (figure 1.16), the region of the head where the conductivity changes are being simulated. A near DC current of 100μA was simulated as being driven through all possible pairs of 31 electrodes using EIT techniques and the surface potential numerically calculated. Secondly, the surface potential was computed when the brain is unperturbed or as a result of an assumed physiological change of 1% being variation in conductivity of V1 when neurons are firing during a visual evoked response.

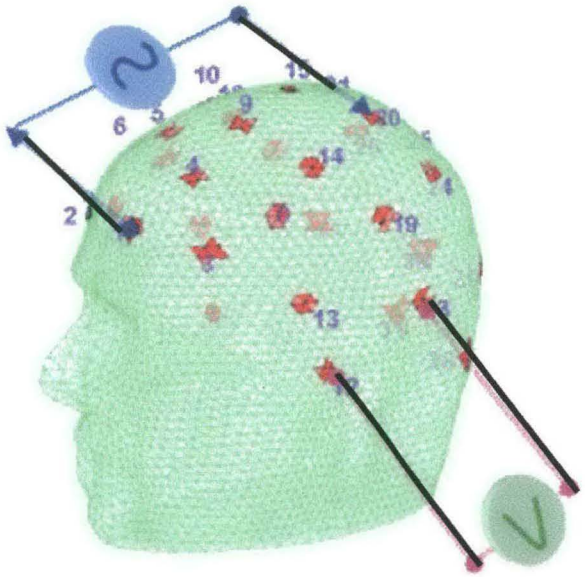

Figure 4.4: Illustration of EIT acquisition principle: small current injected through a pair of electrodes, and the surface potential (V) measured via another pair. This process is repeated for different injection-measurement combinations

For the three head shapes, a total of 465 unique current injections were simulated with 4,000 scalp recordings. For each unique current injection pair, the mean, median, maximum and minimum current densities within V1 were computed whereas for each recording pair the baseline or the change in surface potential was estimated. One of the goals of this work was to know the highest change so it could be measured easily in the first instance. Secondly, there is the need to have a high baseline voltage to increase the signal to noise ratio. To achieve these, 1) the top 10% of electrodes pairs that gave the highest mean current density (J_{mv}) in V1, and 2) those with the maximum surface potential change, V_{mv}, due to 1% change in conductivity in V1 were selected.

4.3.2 Experimental validation

To validate the FEM predictions in terms of the baseline surface potential, the measurements were performed experimentally by using a homogenous spherical tank filled with 0.2% saline (figure 4.5A) with radius 10 cm similar to the FEM model of the homogeneous sphere, and then latex tank (figure 4.5B) for the three layer realistic head. The latter is a three layer realistic tank mimicking scalp, skull, and brain and CSF. It employed a real and dry human skull with resistivity of $0.005Sm^{-1}$ ($208.0 \pm 2.1\ \Omega m$) (Tidswell and Gibson, 2001), and 0.2% saline, so that the conductivities of the scalp, CSF and brain were all equal and similar to that of brain. A current of 100 μA at 8 Hz was physically injected using some selected electrodes and only the baseline surface potential recorded for the two phantoms as there isn't any a phantom for producing the changes yet. The measurements were taken under room temperature of 18°C. Another experiment was performed using the spherical tank to validate the simulated results by considering the baseline potentials for all possible pairs of current injection electrodes.

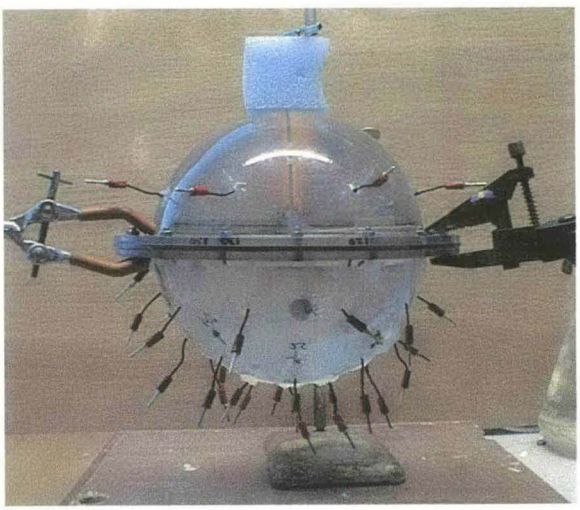

Figure 4.5A: The homogeneous spherical tank phantom, shown for clarity without the presence of the shell to represent the skull. The protruding leads are the connections to various positions

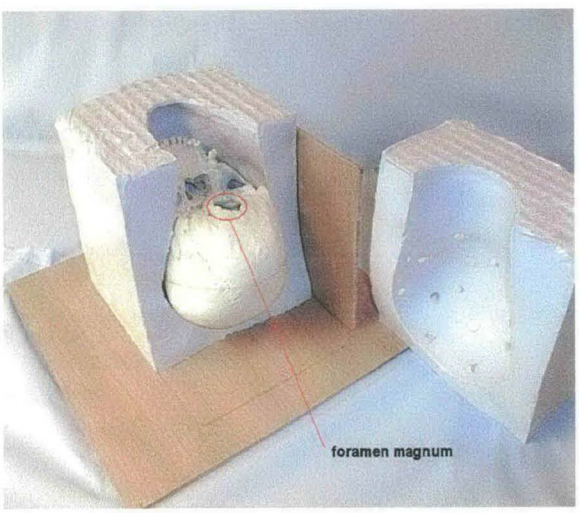

Figure 4.5B: The head shaped tank phantom shown with the two halves separated and a human skull inside

4.4 Results

To reflect the purpose of this study, the results which were obtained numerically or by experimental validation are presented in the following fashion: baseline surface potential, changes in baseline surface potential, current density values, and best electrodes.

4.4.1 Baseline surface potential

In the sub-sections that follow, the results for the estimated (simulated) and experimental baseline surface potentials for the homogeneous sphere and the three layer realistic head are presented. These were based on the top 10% of the electrode pairs that gave the highest baseline surface potential.

4.4.2 Simulated and experimental homogeneous sphere

For the best pairs of recording or injection electrodes, the estimated (S) baseline voltages for the model and experimental (E) baseline surface potential for the homogeneous spherical tank were very close (Table 4.3). The absolute difference between these two values was in the range 0.009 - 0.048 mV and constituted a maximum error of 14%.

Best electrode pairs				**Baseline Voltage (mV)**		**Change (S vs E) (%)**
Drive pair		**Recording pair**		**Simulated (S)**	**Experimental (E)** (±0.001 μV)	
1	30	7	17	0.235	0.244	4
2	29	7	17	0.359	0.340	5
7	23	27	30	0.233	0.237	2
17	13	27	30	0.351	0.399	14
27	3	29	23	0.233	0.248	6

Table 4.3: Comparison between simulated and experimental baseline voltages for homogeneous spherical tank.

4.4.3 *Simulated and experimental three layer head tank*

The percentage difference between the estimated baseline voltages for the model and experimental for the three layer head was in the range 14 - 53 % (Table 4.4). With any pair of electrodes, the baseline voltage recordings are of the same order of magnitude.

Best electrode pairs				**Baseline Voltage (mV)**		**Change (S vs E) (%)**
Drive pair		**Recording pair**		**Simulated (S)**	**Experimental (E)** (±0.001 μV)	
23	31	30	29	-0.436	-0.517	16
27	28	30	29	0.370	0.538	31
22	23	30	29	0.234	0.303	23
23	30	28	31	-0.424	-0.491	14
24	27	30	29	-0.315	-0.477	34
27	23	30	29	0.287	0.454	37
17	30	29	23	0.119	0.251	53

Table 4.4: Comparison between simulated and experimental baseline voltages for three-layer head tank (latex tank) for the best pairs of electrodes

4.4.4 *Simulated Changes in surface potential*

In the following sub-sections, are presentations of the results of the estimated and change in baseline surface potential when there is no change or change in conductivity of V1 respectively for the three and four layer heads. These were based on the top 10% electrode combinations that produced the maximum change in surface potential.

4.4.5 *Three layer head*

Using both the highest mean current density (J_{mv}) and maximum surface potential change (V_{mv}) for the three layer head, the baseline voltages recorded were between -0.4 and 0.1 mV (Table 4.5). The change from baseline due to conductivity change of 1% in V1 was in the

range 0.018 - 0.071 μV (Table 4.5). The mean estimated change (+/- standard error (SE)) for the best pairs was (0.021 ± 0.003)%.

Best electrode pairs				Estimated Voltage		Percentage Voltage Change
Drive pair		Recording pair		Baseline (B) [mV]	Change (C) [μV]	
23	31	30	29	-0.436	0.071	0.016
27	28	30	29	0.370	0.064	0.017
22	23	30	29	0.234	0.063	0.027
23	30	28	31	-0.424	0.062	0.015
24	27	30	29	-0.315	0.062	0.019
27	23	30	29	0.287	0.061	0.021
17	30	29	23	0.119	0.044	0.037
22	27	30	29	-0.115	0.018	0.016

Table 4.5: Best pairs for recording surface potential and injecting current for the 3 layer head

4.4.6 Four layer head

For the realistic head shape tank, the best injection and recording electrodes gave a baseline voltage change in the range -0.4 to 0.2 mV (Table 4.6). The estimated voltage change due to 1% change in conductivity was in the range 0.02 - 0.03 μV. The mean estimated percentage change (+/- SE) for the best pairs was (0.009 ± 0.001)%.

Best electrode pairs				Estimated Voltage		Percentage Voltage Change
Drive pair		Recording pair		Baseline (B) [mV]	Change (C) [μV]	
23	30	31	28	-0.444	0.030	0.007
24	27	30	29	-0.305	0.028	0.009
27	23	31	28	0.266	0.026	0.009
19	27	30	29	-0.270	0.026	0.010
29	27	28	31	-0.250	0.026	0.010
19	30	28	31	-0.367	0.025	0.007
22	23	30	29	0.213	0.024	0.011

Table 4.6: Best pairs for recording surface potential and injecting current for the 4 layer head

4.4.7 Current density

From the 465 unique current injections, the injection pairs, which gave the highest mean current density in V1 when there is or no conductivity change, were looked at. A current injection through electrodes 29 and 30 (which are the electrodes nearest the primary visual cortex) paired with other electrodes produced higher mean current densities in V1. The mean values of these combinations were plotted as in figure 4.6.

The greatest mean current density in VI was 0.024 μAmm^{-2}, and occurred for two injection electrode pairs namely 30 - 17 and 30 - 23. Electrode pairs, which recorded the minimum mean current density of 0.014 μAmm^{-2}, were 29 - 19 and 29 - 20. The recorded mean current density (mean ± SE) in V1 for various injection electrodes was 0.020 ± 0.005 μAmm^{-2}.

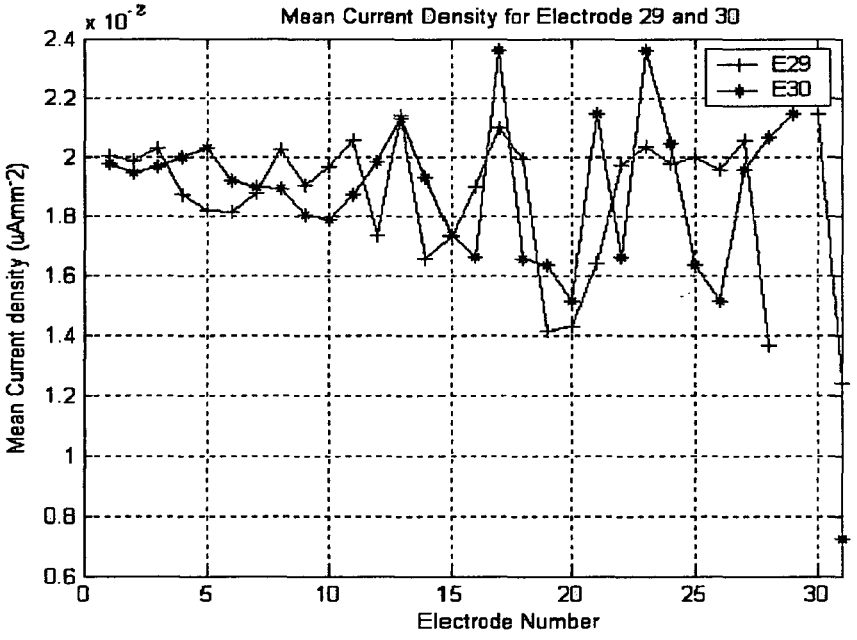

Figure 4.6. Mean current density in V1 for an injected current through electrodes 29 and 30 paired with other electrodes. The horizontal axis refers to the number assigned to each electrode as modelled.

4.4.8 Validation by human Experiment

Figure 4.7 is fitted linear curves for 20 blocks of data (taken from 7 subjects, two injection pairs (23-30 and 27-29) and some repeated sessions). The measured voltages were linearly normalized according to the current level used as if it was all done with 100μA (as in the modelling). The predicted voltages were estimated from the realistic fourshell model, whereas the measured was derived from the human experiment.

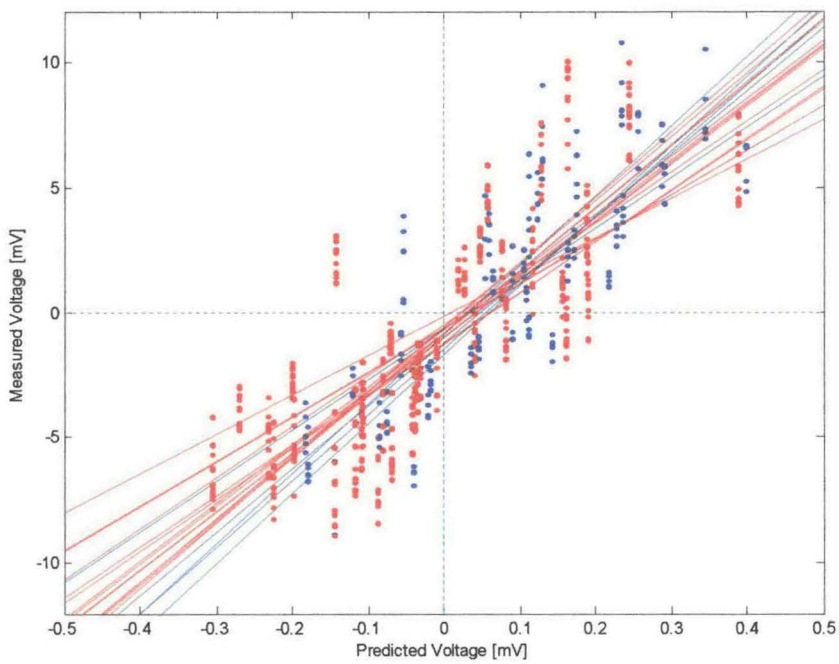

Figure 4.7 Comparison between measured base voltages on human and simulated base voltages from 4 shell realistic mesh (skull conductivity 17.5mS/m). The Blue is injection pair 1 (23-30) and red is injection pair 2 (27-29).

The slopes are between 15 and 27 and the offset is quite low. This suggests that the voltages are multiplied by the slope factor and not shifted by extra constant voltage. The roughly linear placement of the data point suggests that there is some grain of agreement between the model and the experiment. This can be refined further by taking the real positions of the electrodes at individual case and generate a position file for the simulation. This is because the

placement of the electrodes on the head was attempted to be symmetric and equally spaced around the visual cortex and was not following strictly the MK1B protocol.

4.4.9 Best Recording electrodes

For the homogenous head shape, the simulated estimations indicated that the maximum surface potential was recorded using electrode 7 and 17, when current was injected through electrode pair 2 and 29 (Table 4.3). On the other hand, the experimental results showed that the greatest surface potential was recorded using electrode pair 27 and 30 when current was injected through electrodes 17 and 13 (Table 4.3). For the three layer head, the electrode pairs that recorded the maximum change in baseline voltage of 0.071μV due to a 1% change in conductivity in V1 was 30 and 29 when current was injected through electrode pair 23 and 31. The biggest percentage change in surface potential (0.04%) recorded was by electrode pair 29 and 23 when current was injected through electrode pair 17 and 30 (Table 4.4). In the case of the four layer head, electrode pair 30 and 29 recorded the greatest surface potential change when the injection pair was 24 and 27 (Table 4.5). However, electrode pair 30 and 29 recorded the greatest percentage change in surface potential, with the current injection through electrodes 22 and 23.

For all three cases of head geometry (homogeneous sphere, three layer head and four layer head) used, the maximum voltage changes occurred when at least one of the recording pairs was near the occipital cortex that is electrode 29 (O1) or 30 (O2) (Table 4.3 – 4.5) and when the injection pairs were across the occipital cortex.

4.5 Discussion

4.5.1 Summary

With an injected current of 100 μA, the corresponding absolute baseline surface potential was in the range 100 - 400 μV with 0.02% as the maximum change from baseline with a resistivity change of 1% in V1. There was a variation of 1 to 14% difference between the baseline voltages simulated and those measured for the homogeneous spherical tank and this confirmed the numerical accuracy of the model not withstanding some numerical errors such as noise. Though the order of magnitude was the same, there was a significant difference (up to 50%) between the simulated voltages and those measured for the latex tank. However, the estimated percentage change in surface potential for the three layer head was 0.02% whereas that of the four layer head was 0.01%. With an injection current of 100 μA, the greatest mean current density through V1 was 0.020 ± 0.005 μAmm^{-2}, and occurred when at least one of the injection electrodes was near the occipital cortex. The best current injection electrodes for optimal current density in V1 were electrodes 23 (T5) and 30 (O2) or when at least one of them was either electrode 29 (O1) or 30. For optimal recording of change in scalp potential, the best electrode pair was 29 and 30 when current was injected through electrodes 23 and 31.

4.5.2 Technical Issues

4.5.2.1 Baseline and changes in surface potential

The baseline surface potential for the simulated and experimental homogeneous spheres appeared to be similar. This similarity was because, the skull was not incorporated, and so there was no shunting effect due to the resistive skull. However, the large percentage error between the baseline surface potential for the experimental and simulated three layer head, could be attributed to the in-homogeneity in mesh, geometry of the head, and possibly rounding errors in the numerical analysis.

For the three layer head, the estimated percentage change in baseline surface potential was 0.02% whereas in the four layer head it was 0.01%. The difference in percentage change in surface potential between these two head shapes could be attributed to the shunting effect of the scalp as it was incorporated in the four layer head but not in the three layer one.

4.5.2.2 Limitations to the current density

The combination of current strength, size of stimulated area and stimulation duration are thought to be relevant parameters that describe stimulation strength and thus control the efficacy of stimulation. The total charge deposited has been formulated mathematically as current strength per unit area. This is because different current intensities or densities will result in different amounts of neuronal de- or hyperpolarisation. The question of whether the injected current could be increased to higher values in order to increase the current density in the brain without stimulating effects is subjective in scope as it depends on the area of the brain in question. Another parameter of importance in achieving stimulation effects - most probably by determining the neuronal population stimulated - is the direction of current flow. This is generally defined by the electrode positions and polarity. This could be clearly seen when electrodes were placed on the heads of two different subjects with different head shapes. In this case, the electrode positions measured would be completely different and would not conform to the predefined electrode positions used for the simulation.

In order to compare the current density values and its effects in any region of the brain, a large number of papers were reviewed on current density and threshold values, which may cause stimulation of brain tissues or increased activity; this in based on the extensive review done by Ranck (Ranck, 1975) and Nitsche (Nitsche *et al.*, 2003) along with others. Nitsche reviewed 17 human and 39 animal studies, which focused on the long lasting effects of Transcranial Direct Current Stimulation (tDCS). The information presented in some of these studies is relevant to our understanding of current density threshold that will cause immediate effects on neuronal firing rate and EP waveform. It is evident that the stimulating threshold current density

depends on the charge deposited on the surface of an electrode, surface area of the electrode, polarity, duration, and distance of a brain tissue from the point of current injection. We have found that there is a wide range of threshold magnitudes obtained by these various researchers.

With regard to modelling, Rattay (Rattay, 1998; Rattay, 1999) modelled the various neuron types of the CNS using compartment model and equivalent electrical network. The theory predicts the influence of electrical and geometrical parameters on the excitation threshold. A 0.1ms stimulating pulse was given from a point source in a homogenous sphere from a distance of 1 to 9 mm from various positions around the neuron and at positive and negative polarities. The current density thresholds obtained were in the range 9 - 338μAmm^{-2} for anodic stimulation and 3 - 707μAmm^{-2} for cathodic stimulation. These values are the current densities at the nerve tissue when current is injected through cochlear implant and not on the scalp. The large range indicates the importance of the geometrical placement of the source relative to the axis of the axon.

Bindman (Bindman et al., 1962; Bindman et al., 1964) studied the immediate and long term effects of currents applied on the exposed pia on rat forepaw. She used current of 3μA on a surface of 12mm^2, with 0.2 ms pulses to obtain evoked potentials. The current density on the scalp was 0.25μAmm^{-2}, and the resulted effect was large changes in the EP shape in both anodal and cathodal stimulation.

Ranck (Ranck, 1975) reviewed thoroughly the literature up to year 1975 and chose 10 studies with the most reliably documented procedure and satisfactory by taking care of four issues: 1) of shock artefact obscuring the response; 2) the elements were proved to be stimulated directly and not synoptically through other element; 3) the anatomy of the recorded cells is known to determine which parts of it are nearest to the stimulating electrodes; 4) the part of the cell the action potential is initiated is known. We are interested in the lower limit for the more sensitive neuron population. The low limit range varied between stimulated structures

but could be summarized to be in the range of 4 to 40μAmm^{-2} when stimulating near myelinated fibres and 6 to 96μAmm^{-2} when stimulating near cell bodies.

For current density threshold in humans, for an electrode size of 35 cm^2 placed near the occipital region Oz vs. Cz, with an injected direct current of 1000μA for 420 - 600 seconds, the current density on the scalp was 0.29μAmm^{-2}. This current density is known to cause long lasting after effects of changing phosphene threshold and contrast sensitivity (Antal *et al.*, 2001; Antal *et al.*, 2002; Antal *et al.*, 2003b; Antal *et al.*, 2003a). Kincses (Kincses et al., 2004) also reported that for an electrode (35 cm^2 in surface area) placed above the prefrontal cortex, with a current of 1000 μA for 600 seconds, the current density on the scalp is 0.29 μAmm^{-2} and this has the effect of 20% improvement of probabilistic classification learning task for anodal stimulation. In another report, (Liebetanz *et al.*, 2002; Matsunaga *et al.*, 2004; Nitsche and Paulus, 2000) with an injected current of 1000 μA on an electrode size of 35 cm^2 placed above the motor cortex for 300, 600 and 4 seconds respectively would produce a current density of 0.29 μAmm^{-2} on the scalp. These authors reported the effect as being 20 - 40 % change in Motor Evoked Potential (MEP) for anodal and cathodal stimulation, 40% increased Somatosensory Evoked Potential (SEP) for anodal stimulation, and 20% increased and decreased MEP for anodal and cathodal stimulation respectively. A contrast between the last example and the previous lies in the location at which the current has been injected and consequently its effect.

In the cases cited, they used long dc stimulation, which probably polarises parts of the brain. This will not occur when an alternating current at low frequency is used. The predicted mean current density in V1 was 0.02 μAmm^{-2} when a current of 100 μA was injected at 8Hz on a surface electrode of size 3 cm^2 near the occipital cortex. However in comparison with the cases cited for Kincses (Kincses et al., 2004) and Antal (Antal *et al.*, 2001), the injected current and surface area of the electrodes are 10 times smaller. If a linear relationship was assumed between current and current density, and if the surface area of the electrodes remained the same and the injected current was increased ten times, it would mean that mean current

density of 0.2 μAmm^{-2} would be obtained in V1. This value comes close to those reported by the authors Liebetanz (Liebetanz *et al.*, 2002), Matsunga et al. (Matsunaga *et al.*, 2004), and Nitche (Nitsche and Paulus, 2000; Nitsche *et al.*, 2003) cited but under different circumstances of long dc stimulation.

4.5.2.3 Best electrodes

The best current injection electrodes for optimal current density in V1 were electrodes 23 (T5) and 30 (O2) or when at least one of them was either electrode 29 (O1) or 30. For optimal recording of change in scalp potential, the best electrode pair was 29 and 30 when current was injected through electrodes 23 and 31. These were electrodes near the occipital cortex and were consistent for three and four layer head models.

To sum up, with respect to our model, saline tank experiments confirmed the accuracy of the estimated standing potentials and this will enable the estimation of electrode positions most likely to permit recording of changes in human experiments and suggests that the changes, although tiny, may just be distinct from noise.

Effect of Variations in Conductivity on Scalp Potential and Current Density

Chapter 5

EFFECT OF VARIATIONS IN SKULL CONDUCTIVITY, SHAPE AND SIZE OF V1 ON CURRENT DENSITY DISTRIBUTION IN THE BRAIN AND BASELINE SURFACE POTENTIAL

5.1 Introduction

In the previous chapter, some electrode pairs were identified for obtaining optimal current density and change in surface potential. However, the investigation was limited to only one skull conductivity value of 17.5 mSm^{-1}, local conductivity change of 1% and fixed shape and size of the primary visual cortex. Individuals have different head shapes and sizes. They also have different skull conductivities and local conductivity changes dependent upon visual perception. This chapter looked at three global parameters, namely conductivity, geometry, and electrode positions. Their effect on the baseline voltages and current distributions in the human brain were investigated. The parameters investigated under conductivity were the changes in local conductivity due to neuronal depolarization, and variation in the conductivity of the skull from person to person. Under geometry, a study was done to find out whether the correlated sizes and shapes of the primary visual cortex have any effect on the estimated baseline surface potentials as well as the current distribution in the brain. The third factor was to study the effect on baseline surface potentials and current distribution due to electrodes positions where current was injected. This factor was previously investigated in chapter three with respect to only a single conductivity value of the skull and one shape and size of the primary visual cortex.

5.1.1 Purpose

The purpose of this piece of work was to investigate the effect of the irregular shape of the skull and its conductivity on how current was distributed in the brain when a known current was injected. An aspect of this study was to find out whether there was any significant change in current density distribution in the primary visual cortex if the conductivity or geometry of the skull changes. An investigation was also made to determine whether the baseline voltages as measured on the surface changes with time, which was functional. Another important aspect was to look at the baseline voltages when there were changes in the local conductivity changes due to neuronal depolarisation.

To answer whether there were any effects on the baseline voltage or current distribution in the brain, the following were proposed:

Just as in chapters three and four, the purpose of this chapter was to model current flow through the head in low frequency impedance measurement of neuronal depolarisation. The physiological paradigm selected was the full field visual evoked responses with impedance measurement using scalp electrodes. However, the expected change in local conductivity was set to three values: 0.6%, 1% and 1.6%, which were subsets of the conductivity changes in the human cortex accompanying neuronal depolarisation based on cable theory and mathematical model (Liston et al., 2001). The EIT paradigm used in this study assumed thirty-one electrodes equally spaced around a realistic head with current injected through some selected pairs of electrode, and the surface potential measured between the remaining electrode pairs (Gibson, 2000).

This work validates the proposed application, and suggests optimal ways (Gilad et al., 2005a) to perform planned human recordings. The specific questions answered were:

1. With a fixed local conductivity change of 1%, how big are the changes in baseline potential on the scalp when there is variability in the skull conductivity?
2. Is there any significant change in how current density is distributed in the brain when the skull conductivity changes?
3. For fixed skull conductivity, what effect does a change in local conductivity have on the changes in boundary voltages and current distribution?
4. What is the relationship between the variation in current density and position of current injection electrodes?
5. If current were injected through multiple electrode pairs, would there be an appreciable increase in the current density?

5.1.2 Background

5.1.2.1 Skull conductivity

The location and strength of a bioelectric source that generates electrical or magnetic activity on or near the surface of the head are crucial for imaging physiological activities of the brain. The strength of the measured generated electrical or magnetic activity is limited by the conductivity of the skull, as it is less conductive than other brain tissues. Due to this low conductivity, only a fraction of the electric activity of the brain permeates the skull and appears distributed over the head surface as the EIT for example. Thus, EIT is greatly affected by the conductivity of the skull and, conversely, source localisation is highly dependent on the assumed value of this conductivity. Hoekema (Hoekema et al., 2003) reported that simulation studies have shown that the depth of the source determined while assuming an incorrect skull conductivity may differ from its actual position by up to two centimetres (Huiskamp et al., 1999).

Presently, available data on bone conductivity are mostly derived from animal material or from post-mortem human material. Studies of the rat femoral bone (Kosterich et al., 1984) show that the conductivity of bone is largely dependent on the conductivity of the fluid content of

bone. The conductivity of the human skull has been measured using post-mortem skulls (Oostendorp and Debelke, 2000; Saha and Williams, 1992) that has been allowed to dry (Saha and Williams, 1992) or had been kept in a freezer (Oostendorp and Debelke, 2000). However, the validity of these measurements may be questioned because of exposure to air, even for a few minutes, may cause drying out and hence decrease the conductivity of bone (Saha et al., 1984).

Oostendorp (Oostendorp and Debelke, 2000) used EIT techniques to measure indirectly skull conductivity where a current was applied to the intact head of a living person and the resulting potentials were measured at 32 positions on the head. The skull conductivity was then calculated from volume conduction computations, where the ratio between the conductivity of the rest of the head was estimated. The reported values of the specific conductivity of the skull summarised in table 5-1 below:

Component	Conductivity (mS/m)	Freq. (Hz)	Temp.	Reference
Human skull (soaked in saline)	1.18 – 7.73	20	n.a	Akhtari et al. (2000)
Human skull (compact – soaked)	4.7 – 7.8	100	n.a	Law (1993)
Human skull (live)	4.87 – 21.4	20	n.a	Akhtari et al. (2000)
Human skull (in vivo)	13	10 - 1000	37	Oostendorp et al. (2000)
Human skull (in vitro)	15	10 - 100K	37	Oostendorp et al. (2000)
Human skull (dry, then soaked)	10 - 28	100	n.a	Law (1993)

Table 5.1: Specific conductivity of bone. (n.a : not applicable)

As the human head has been modelled to consist of brain (white matter and cortex), CSF, skull and scalp, it is essential that an accurate knowledge of these tissue conductivities is known. The accuracy enhances the reduction of errors in calculating the forward solution of the extracranial magnetic fields and electric potentials produced by intracranial sources of activity. The estimation of incorrect values of these tissue conductivities can greatly affect the magnitude of the magnetic fields and electric surface potentials (Okada et al., 1999; Ollikainen et al., 1999).

Law (Law, 1993b) showed that there is a considerable variation in skull conductivity in samples obtained from various regions of human cadaver skull. His study suggested that skull conductivity might be determined by its thickness and structural variations such as sutures and bone formations. Bone thickness varied widely over the skull surface, and the thickest region lay over the occipital plate whereas the thinnest regions were on the side of the head where the temporal bone did not overlap the parietal plate. The mean thickness of the skull was measured to 5.2 ± 0.8 mm (Law, 1993b). Skull resistivity values as measured by Law ranged from 1,360 to 21,400 Ωcm. From the samples taken by Law, the lowest resistivity values were from samples along the bone plug, which contained suture lines. He observed that samples with suture lines had a much lower resistivity than samples without sutures and the highest resistivity was about 3,940 Ωcm. This was about thirty percent lower than the lowest resistivity from the samples without suture lines. This suggests that skull resistivity is altered primarily by the presence of suture lines and cancellous bone. The presence of suture lines may provide a path of least resistance for current, hence decreasing the overall resistivity for a particular region.

The inclusion of skull resistivity or conductivity in the forward model will likely improve spatial resolution by decreasing systematic error due to simplifying assumptions on geometry and resistivity. Rush and Driscoll (1967) have shown that changes in the attenuation ratio between skull and brain layers of three-concentric sphere model can affect the amplitudes

calculated for the scalp. Thus local variations in skull thickness and resistivities would introduce deviations in scalp potential distributions calculated with a uniform layer model.

Gabriel et al. (Gabriel *et al.*, 1996) showed frequency dependence of conductivity for cancellous bone (100 - 10 M Hz) and cortical bone (10 kHz - 1 MHz). The frequency dependence of the conductivities of the individual skull layers in the range 10 - 90 Hz, varied by as much as 14%. This frequency dependence of conductivity causes the volume conductor to act as a low pass filter and may have considerable effect in EEG source localisation (Stinstra and Peters, 1998). In their study, a 20% increase in conductivity resulted in a scalp potential dropping by a factor of 2 in the range 1 - 100 Hz.

The range of resistivity values indicates that these variations are of sufficient significance that they should be considered for incorporation in realistic head models (Pohlmeier et al., 1997). Consequently, recent efforts have been directed at developing models, which more properly reflect the true geometric and conductive properties of the human head.

5.1.2.2 Stimuli used to elicit the VEP

Two general types of visual stimuli are most often used to elicit VEPs, namely unpatterned flashing lights and patterned stimuli, which in clinical laboratories are usually checkerboards. Unpatterned flashing stimuli can be produced with a photostimulator similar to those used in standard EEG recording for photic driving. The intensity, colour, and rate of stimulation of the stimulator can be varied. Pattern stimuli can be presented in three ways. The first, a flashing patterned stimulus, is produced by placing a photostimulator behind a large photographic transparency of black and white checks. However, a flashing pattern stimulus contains two parameters that change simultaneously; there is an abrupt increase in brightness accompanied by the presentation of a pattern. There is an interaction between the brightness increase and pattern change, producing a pattern VEP that is "contaminated" by luminance changes. To avoid luminance contamination of the VEP, a pattern with a constant average luminance can be

presented. This is accomplished in two ways: by pattern onset-offset or by pattern reversal. In pattern onset-offset, the check appear for a discrete amount of time (e.g., 500 msec), and then disappear.

5.1.2.3 Responses to various Stimuli

The VEP waveform depends on the type of stimulus used to generate it. A useful distinction that is made in VEP work is between transient and steady-state VEPs. A transient VEP is produced when the stimulus is presented at a slow temporal rate, whereas a steady-state VEP is produced when the stimulus is presented at a rapid temporal rate. The temporal rate at which VEPs change from transient to steady-state varies depending on a variety of factors, but in general six to eight alterations (or flashes) per second represent the region of change.

5.1.2.4 Current injection and voltage measurement

The method of current injection and voltage measurement, which will be used in chapter, will be consistent with the system described in section 1.2.9.

5.1.2.5 Optimum Electrode Protocol for VEP

There are different schools of thought regarding the optimal electrode location for clinical testing for VEP. In general, the largest amplitude signal is usually obtained 1 to 2 cm above the inion along the midline. Some prefer to use the international EEG 10:20 (Binnie et al., 1996)system for electrode placement and record from an active electrode at Oz, and others have used electrodes located at O1 and O2. It is preferable to use referential electrode configurations, with the occipital electrode referenced to some relatively indifferent place on the head, such as the ear lobe, mastoid, or midfrontal region.

In 2D reconstruction (Bayford *et al.*, 1995), electrodes are placed around the object to be examined. When current is applied to opposite electrodes, a voltage profile exits which is a

maximum at one current electrode and decreases monotonically to the other. This profile is sampled by measuring between all adjacent electrodes. The voltage between any two (non-adjacent) electrodes can then be found by a linear combination of these measurements. This forms a complete set of independent measurements; complete, because the whole voltage profile is sampled, and independent because none of these measurements can be found by a linear combination of the others. In fact, there are two complete sets adjoining the two current electrodes – one around each side of the object. This concept of a complete set of independent measurements taken equally spaced electrodes helped to provide a systematic way to drive a 3D measurement protocol (Tidswell and Gibson, 2001).

5.1.3 Design

5.1.3.1 Modelling of Region of conductivity change

Just as in the previous chapter, the brain region of interest is the primary visual cortex which during VEP, 90% of the activity takes place (Binnie et al., 1996). In humans, the primary visual cortex is located nearly entirely on the dedial surface of the occipital lobe, with approximately 2/3 of V1 lying within the walls of the calcarine sulcus. With reference to the Broadmann area 17, Tailairach System, MRI and PET studies on the area and volume of the primary visual cortex, on the average, the left hemisphere is slightly smaller than the right hemisphere of the visual cortex. This area is modelled based on Andrews et al.'s work (Andrews et al., 1997) on the correlated size variations in human visual cortex, lateral geniculate nucleus and optic tract. On average, the volumes of the left and right hemispheres of the visual cortex are respectively 5,119 and 5,692 mm^3. An inter-individual variation was detected when V1 volume measurements were combined for corresponding hemispheres of 14 brains (range 7,769 – 14,213 mm^3) with the mean total volume of about 10,770 mm^3. The visual cortex was modelled in the form of ellipsoids to depict the shape of it as two strawberry shapes inclined at an angle (morphology 1). The second model was modelled as two strawberry shapes joined together (morphology 2), and third was modelled to represent its shape as strawberry shapes put together (morphology 3).

5.1.3.2 Shapes of V1

Depending on the individual, the primary visual cortexes are of different shapes and sizes or volumes. Three shapes and four sizes were identified and used for this study. The shapes of the primary visual cortex were analyzed as morphologies 1, 2 and 3 as depicted in figure 5.1. Morphology 1 (figure 5.1a) was modelled in the form of 2 strawberry shapes inclined at an angle, whereas morphology 2 (figure 5.1b) looks elongated. The third morphology was modelled like a blob as shown in figure 5.1c.

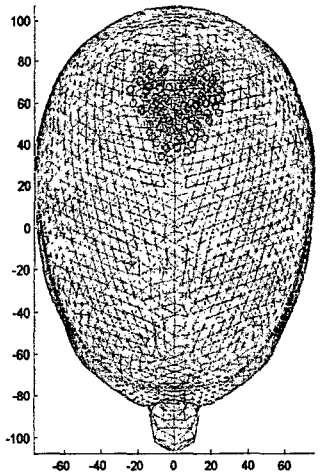

a

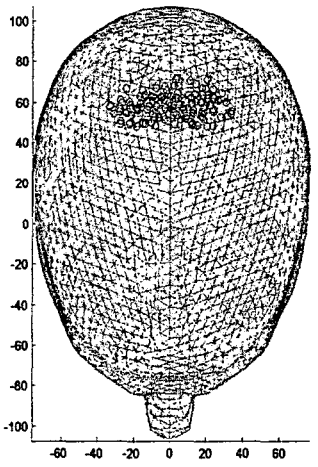

b

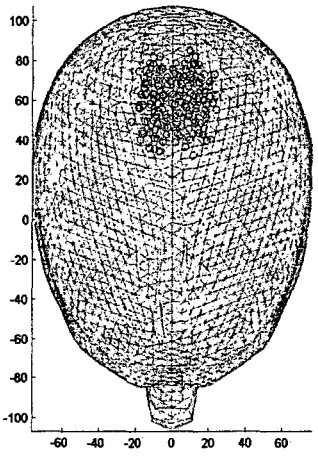

c

Figure 5.1: The three selected morphologies of the primary visual cortex a) inclined b) elongated c) blob

5.1.3.3 Computed volumes of V1

The volumes of the hemisphere (left and right) together with their entire total were calculated (Table 5.2). The volume of V1 according to studies on correlated sizes of the primary visual cortex was in the range 7,769 to 14,213 mm^3 (Andrews et al., 1997). The models took into consideration the maximum volume (size 4) and minimum volume (size 3) and the mean volume (size 2). An extremely small volume (size 1) outside the range was also modelled to see the effect of very small volumes of V1 on the factors under investigation. The volumes of all the hemispheres over each size were the same across the different morphologies chosen.

	Volume of Hemisphere (mm^3)		
Size	**Left**	**Right**	**Total**
1	1,257	1,325	2,582
2	5,127	5,729	10,856
3	4,260	3,204	7,464
4	7,008	7,580	14,588

Table 5.2: Computed volumes of the left and right hemisphere of V1 together with the total mean volume

5.2 Method

To realize the goals of the above objectives, a FEM was employed in modelling the head as a four layer realistic head (Bayford *et al.*, 2001a; Liston, 2003). Current was injected through some selected pairs of electrodes. The current densities in V1 and the surface potentials for an assumed or no activity in V1 were numerically calculated for a fixed local conductivity change of 0.6%, 1% and 1.6%.

5.2.1 Head Model

The head geometry used for meshing was that of a full, layered human head containing brain, CSF, skull and scalp (full-head). The full head model also contained a cavity to represent the air space behind the nose. I-DEAS was used to generate meshes describing realistic head geometry with linear, tetrahedral elements. A solid model (Horesh et al., 2004) was generated by using lofted 2-D non-uniform rational B-spline (NURB) surfaces of the head; skull, CSF and brain produced the head shaped meshes. The NURB outlines were obtained by segmentation of MRI image slices. It was again necessary to partition the geometrical volume, although this was done by a different method than for the spherical meshes.

The surface meshes for the four compartments (full head), described above, are shown in figure 5.2 and nodal clouds, in figure 5.3 colour-coded for tissue type, for the skull-head mesh, the 4-shell sphere mesh and the full, layered head mesh.

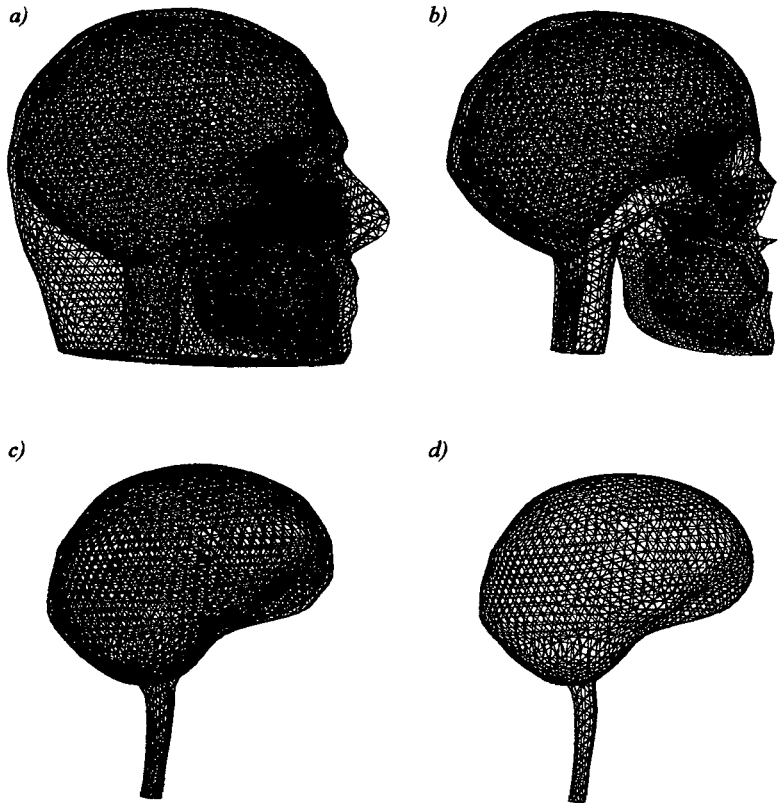

Figure 5.2: The element faces on the surfaces of the four parts of the full, layered head mesh a) the scalp, b) the skull, c) the CSF and d) the brain region. The scalp region contains 10,078 nodes, the skull region 6,325 nodes, the CSF region 2,064 nodes and the brain region 6,702 nodes

The numbers of nodes and elements are listed for each in Table 5-3, along with the ratio of largest-to-smallest element, a measure of mesh quality. Larger values indicate poor mesh quality. The layered meshes of realistic head geometry were poorest but these compared well with the linear and quadratic meshes used by Gibson (2000) (ratios 40,000 and 170,000 respectively).

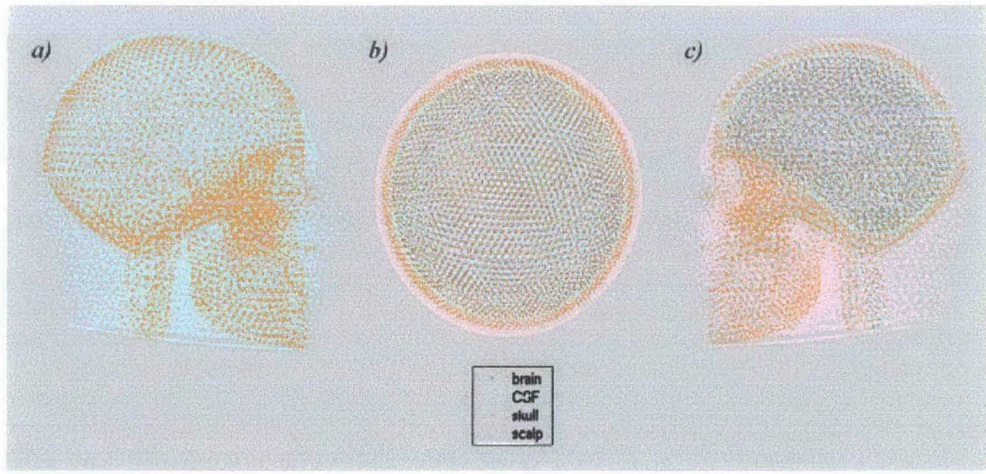

Figure 5.3: The nodal clouds describing a) the head-shaped mesh with skull compartment, b) the fourshell mesh and c) the full, layered head mesh. The different tissues are colour-coded as shown in the key

Head Shape Type	Number of nodes	Number of elements	Ratio of largest-to-smallest element-volume
4-Shell Sphere	22,420	106,825	66
Head-Shape with Skull	16,983	87,850	2,050
Full Head with 4 layers	25,169	136,442	560

Table 5.3: Listed are the three meshes used in this chapter, the number of nodes and elements in each and the ratio of largest-to-smallest element size in each, a measure of their quality. A smaller value is desirable

5.2.2 Creation of a 3D electrode protocol file

The electrode arrangement can be split into two main sections. These are the electrode positions and the order in which those electrodes are used, known as the protocol. Both are stored as text files which are read into the algorithm during the forward model.

5.2.2.1 Electrode positions

The number of electrodes and their positions are the two most important factors affecting image quality. The number of electrodes limits the number of independent measurements, which are available which, in turn limits the resolution, which may be obtained in the final image. The electrodes should be positioned so as to maximize the measured impedance change, so as to optimize the sensitivity.

Work has been done in our group regarding electrode arrangements, which were tested in saline-filled hemispherical tank. Using 32 electrodes arranged in three rings (of 16, 8 and 8 electrodes) provided good image quality in the (x, y) plane but poor resolution in the z-direction due to under sampling, even if 672 measurements were taken. Better spatial sampling was achieved with electrodes evenly spaced over the whole head. The internationally recognized 10-20 system of electrode placement for EEG defines the location of 19 electrodes from anatomical features and is designed to cover the scalp evenly (figure 5.4). Images obtained using these electrode positions were, however, unable to localize an object. It appeared that 19 electrodes did not provide sufficient information to reconstruct accurate images.

More information was provided by adding 12 more electrodes to those of the 10-20 system (see figure 1.16). Eight of the additional electrodes were placed between the standard electrodes and four more were placed lower down on the head to improve sampling in the z-direction and around the visual cortex (Gibson A.P., 2000b).

5.2.2.2 Electrode Protocol

The electrode protocol file gives the order in which the electrodes are used and is simply a list of four electrode impedance measurements. The electrode positions, whilst evenly sampling the head, were effectively randomly spaced from the point of view of organizing the electrode protocol. Despite this, three very approximate rings of electrodes were defined (Figure 1.16).

Current was injected through widely spaced electrodes. With electrodes on the surface of a hemisphere, polar current drive could only be used between electrodes on the equator (ring 1). Additional measurements were made using near-polar current drive between electrodes in ring 2 and between rings 1 and 2. Voltage measurements were made along three lines joining the current injection electrodes. Two were parallel to the equator of the head and the third passed over the apex. These lines were, of course, not straight, but depended on the electrode positions (see figure 1.16). Additional measurements were made between electrodes 12, 28, 31 and 18, which were lower down on the head. Finally, any voltage measurements, which were close to an isopotential line (e.g. current drive between electrodes 2 and 29 and voltage measurement between 28 and 31), were removed from the protocol.

For example, the first current injection was between 1 and 30 (see Figure 3.4), with voltage measurements between electrodes 2-7, 7-17 and 17-27, then 29-23, 23-13 and 13-3 and over the apex by measuring 4-9, 9-15 and 21-26, Finally, the four electrodes at the back of the head - 18-31, 31-28 and 28-12 - were used. In all, the 31 electrodes were used thus giving 465 possible current injection combinations and about 4950 voltage recording pair combinations.

5.2.2.3 The simulation

The parameters varied in this simulation were the skull conducitivity, local percentage change in conductivity, shape and size of V1. These were simulated in turn. The position vectors of all current injecting and recording electrodes were defined as the electrode protocol likewise those of the nodes and elements of the head models. The positions of the electrodes were based on the EEG 10-20 electrode configuration (figure 5.4) with an additional 10 electrodes forming the EIT electrode system (Gibson, 2000).

A near DC current of 100 μA (Lionheart et al., 2001) was simulated through all possible pairs of 31 electrodes using EIT techniques and the surface potential numerically calculated. The mean current density in V1, surface potential, and non-uniformity ratio were numerically calculated. These were repeated for variable skull conductivity, shape and size of V1, and with no local changes. Secondly, the entire simulation was repeated when the brain is perturbed as a result of an assumed local physiological change of 0.6%, 1%, and 1.6% being variation in conductivity of V1 when neurons are firing during a visual evoked response.

5.3 Results

In the sections, which follow, are presentation of the results obtained for the current density distribution and changes due to variations in skull conductivity. Also presented are the boundary voltages together with the changes from baseline.

5.3.1 Percentage change in current density

5.3.1.1 Strawberry shaped V1

The graphs (figure 5.5) mean current density in V1 as function of conductivity for different current injection patterns. The percentage changes with respect to variation in conductivity for different injection patterns are also presented. For all sizes of V1, the highest mean current density was obtained with electrode pair 23 and 30 across the entire skull conductivity variations, and the least mean current density for skull conductivity values less than 0.01 mSm^{-1} was recorded using electrode pair 13 and 17; and for conductivity values greater than 0.01 mSm^{-1} the least mean current density was obtained when current was injected through electrode pairs 2 and 29. In any case the least mean current density was obtained when current was injected through diametrically opposed electrodes.

For size 1, the highest percentage changes across the skull conductivity were obtained when current was injected through the electrodes pairs 12 and 31. However, the least percentage change was estimated when current was injected through electrode pair 2 and 29. For size 2, the greatest percentage changes were obtained when the current was injected through electrode pair 29 and 31; and the least percentage change was obtained when current was injected through electrode pair 23 and 30. However, for sizes 3 and 4, the highest percentage change in mean current density was obtained when current was injected through electrode pairs 2 and 29 and the least was obtained when current was injected through electrode pair 12 and 31.

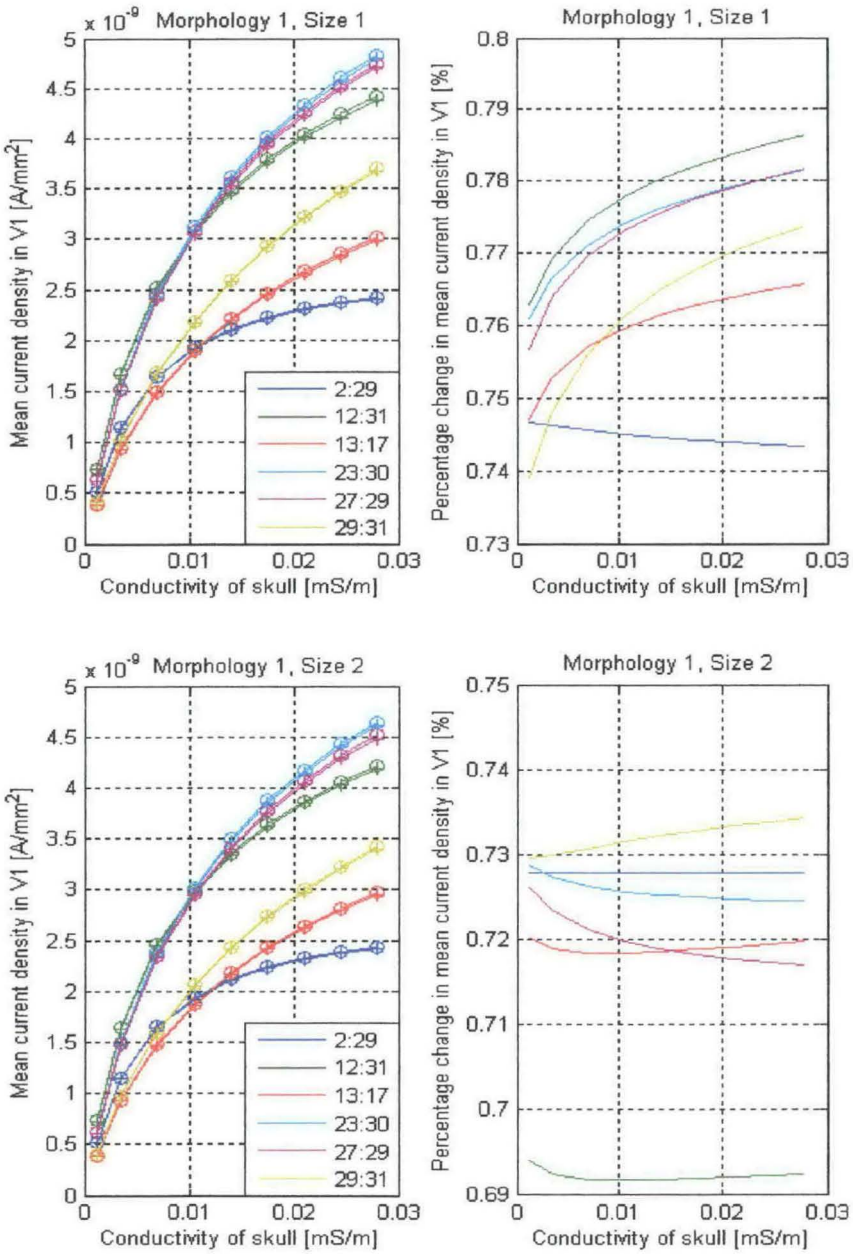

Figure 5.5a. Plot of current density and percentage change in mean current density in V1 as a function of skull conductivity for morphology 1, for volumes 1 and 2 of the primary visual cortex

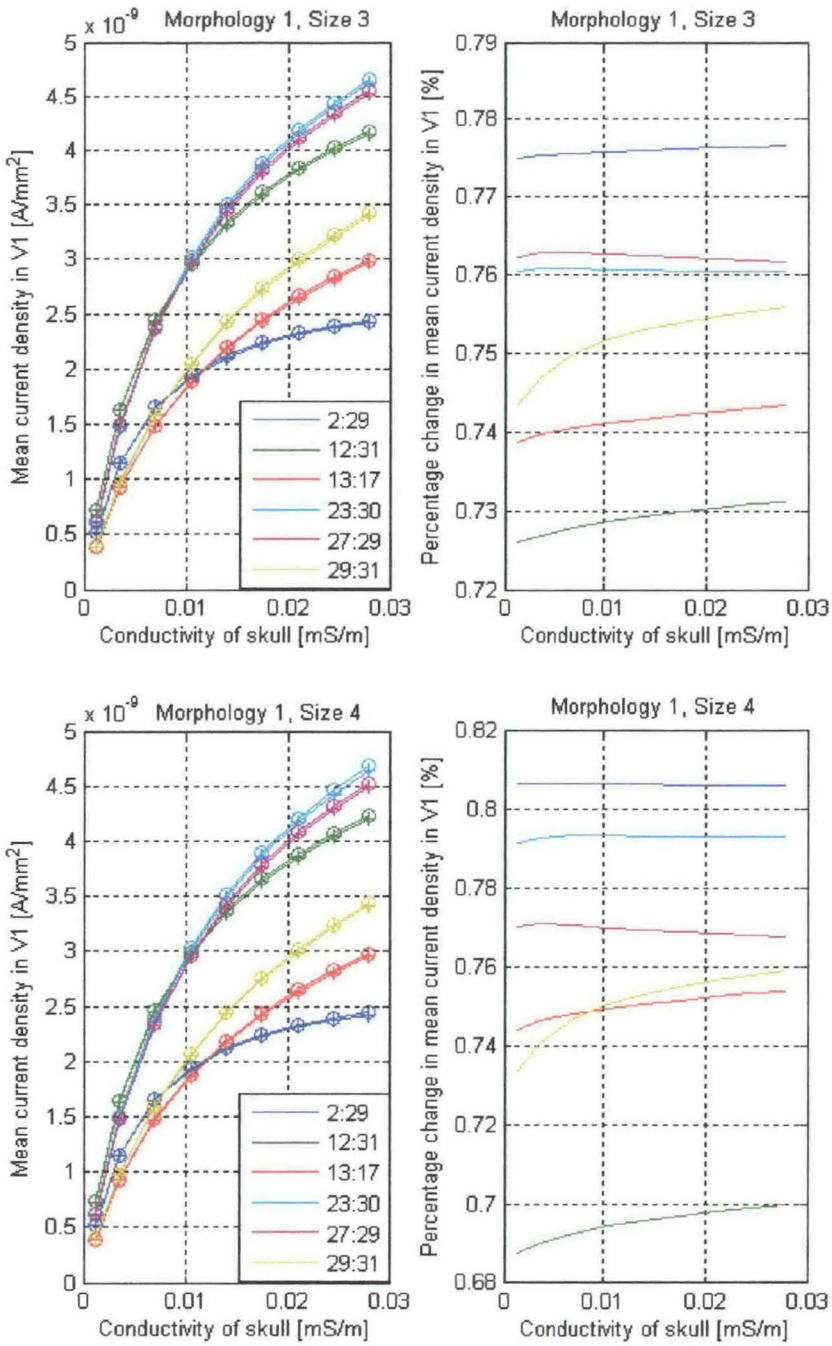

Figure 5.5b. Plot of current density and percentage change in mean current density in V1 as a function of skull conductivity for morphology 1, for volumes 3 and 4 of the primary visual cortex

5.3.1.2 Elongated shaped V1

In this section are plots of mean current density in V1 as a function of skull conductivity for the second morphology (the elongated). The percentage changes with respect to variation in conductivity for different injection patterns are also presented (figure 5.6). For all sizes of V1, the highest mean current density was obtained with electrode pair 23 and 30 across the entire skull conductivity variations, and the least mean current density for skull conductivity values less than 0.01 mSm^{-1} was recorded using electrode pair 13 and 17; and for conductivity values greater than 0.01 mSm^{-1} the least mean current density was obtained when current was injected through electrode pairs 2 and 29. Just as in the first morphology, the least mean current density was obtained when current was injected through diametrically opposed electrodes. In relation to the percentage changes in mean current density across the skull conductivity, for all sizes the highest changes were obtained when current was injected through electrode pair 2 and 29, and the least was obtained with the injection electrodes being 12 and 31.

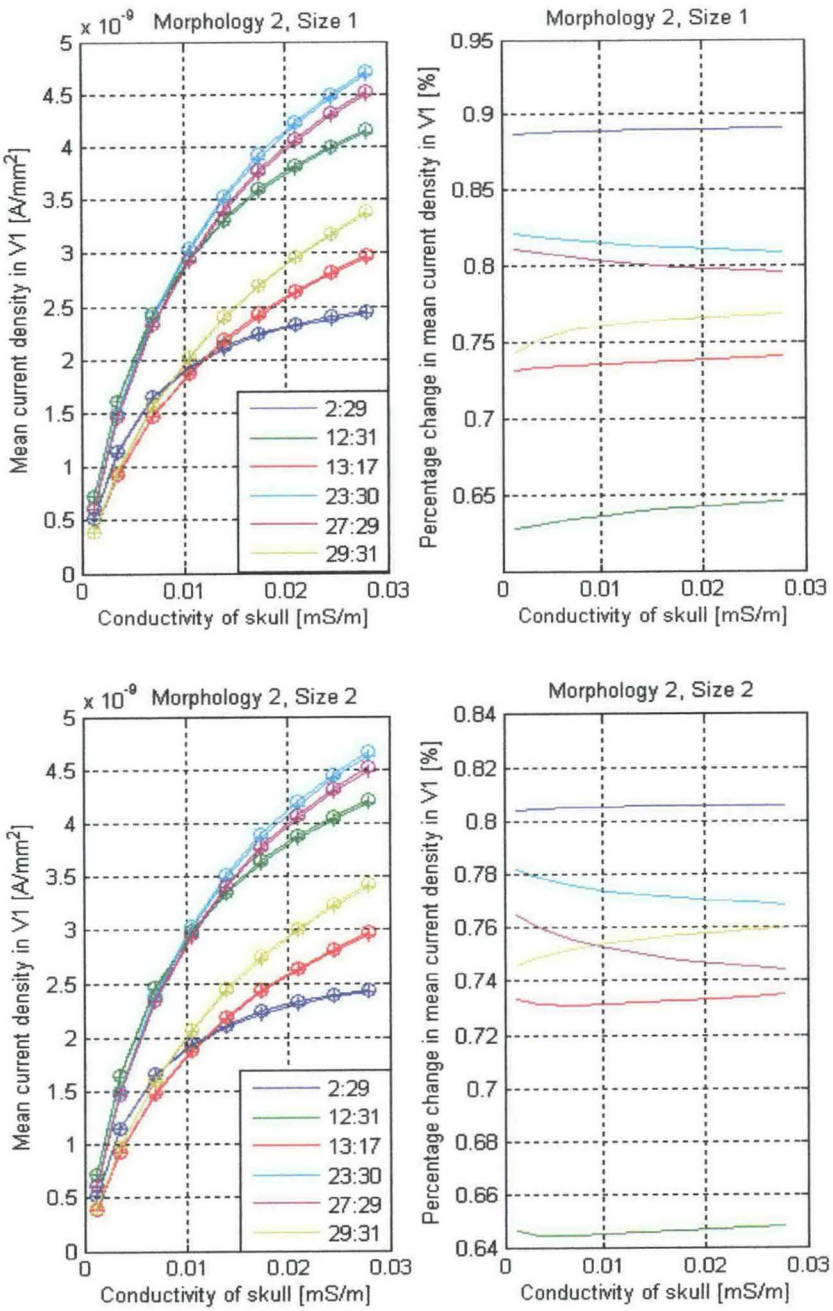

Figure 5.6a. Plot of current density and percentage change in mean current density in V1 as a function of skull conductivity for morphology 2, for volumes 1 and 2 of the primary visual cortex

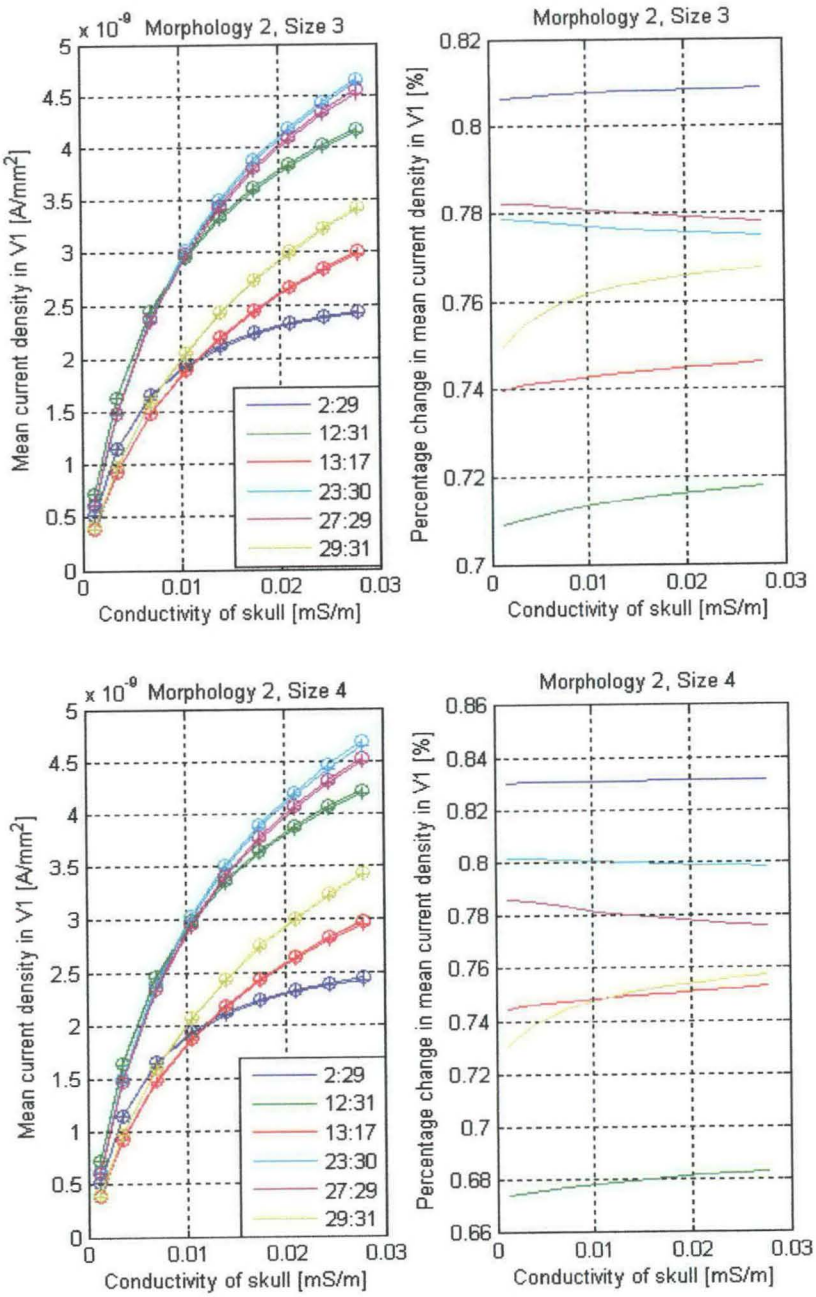

Figure 5.6b. Plot of current density and percentage change in mean current density in V1 as a function of skull conductivity for morphology 2, for volumes 3 and 4 of the primary visual cortex

5.3.1.3 Blob shaped V1

Figure 5.7 shows that the highest mean current density across skull conductivity and size of V1 was obtained when the injection electrodes were 23 and 30 just as it was for the first two morphologies. The least mean current density followed the same pattern as it was for the first two morphologies. However, for size 1, the highest and least changes were obtained when the injection electrode pairs were 12 and 31, and 2 and 29. For size 2, the highest and least percentage changes were obtained when the injection electrodes were 29:30, and 12:31 respectively. But for sizes 3 and 4, the highest mean current density in V1 was associated with electrode pair 2:29 whereas the least was associated with 23:30 (figure 5.7).

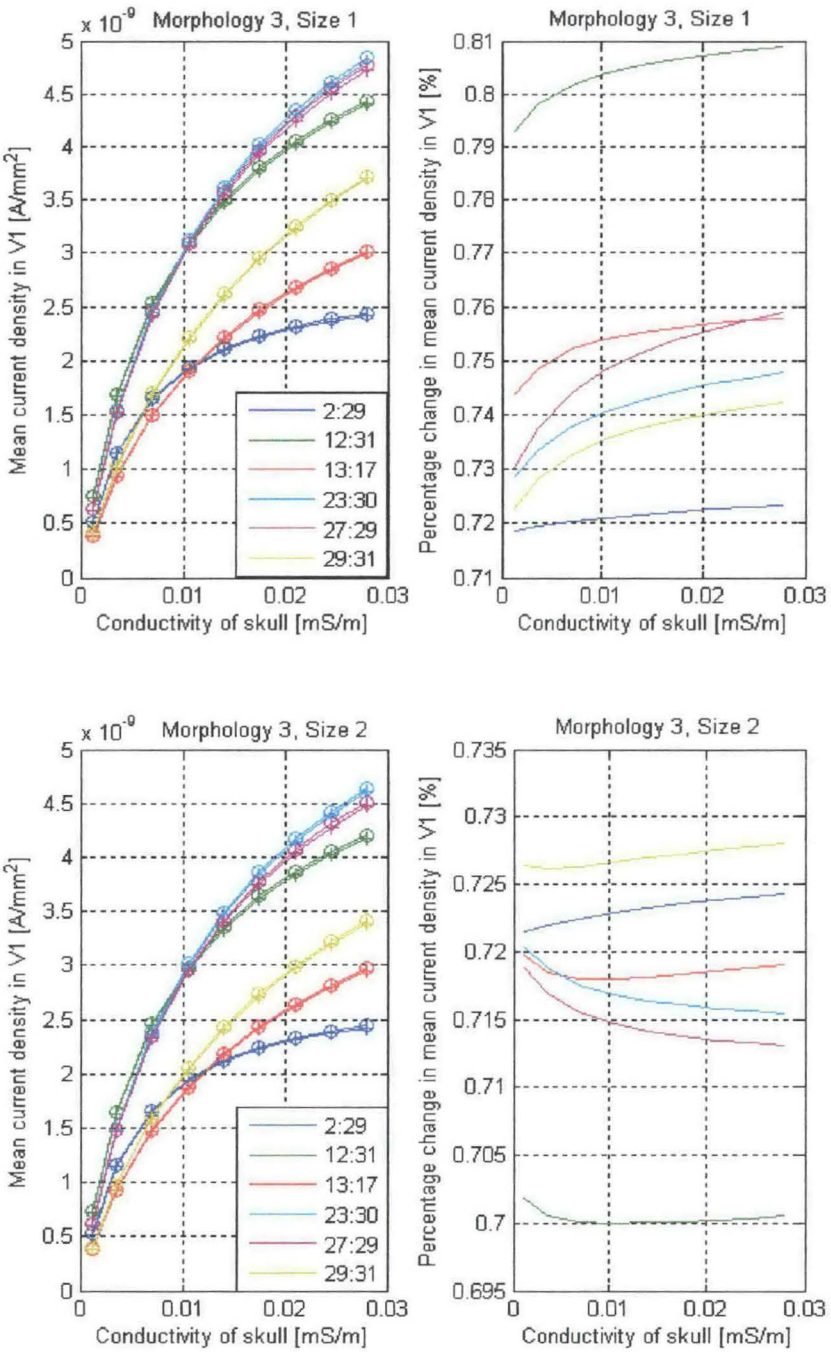

Figure 5.7a. Plot of current density and percentage change in mean current density in V1 as a function of skull conductivity for morphology 3, for volumes 1 and 2 of the primary visual cortex

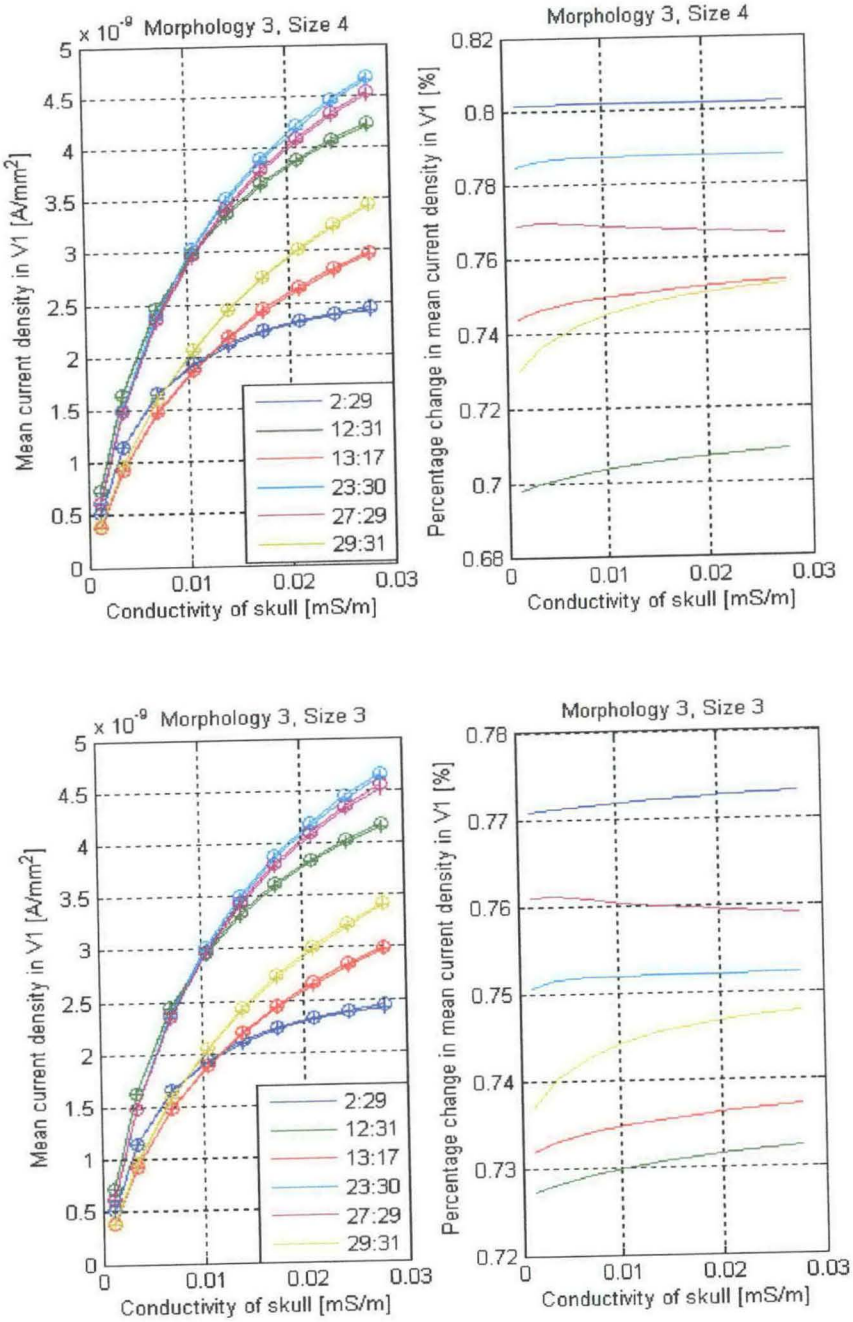

Figure 5.7b. Plot of current density and percentage change in mean current density in V1 as a function of skull conductivity for morphology 3, for volumes 3 and 4 of the primary visual cortex

5.3.2 Percentage change in current density

Table 5.4 gives a summary of the mean current densities in V1 across all conductivities of the skull. Across all sizes of V1, the second morphology has the highest percentage changes (0.85%) in mean current density as compared to the first and third morphologies. On the other hand, it has the least percentage change of 0.63%, thus, the largest range for percentage change in current density. There isn't any much difference in the percentage change for the inclined and blob morphologies, however, the maximum ranges for the percentage changes are 0.12% and 0.10% for the inclined and blob models. All these maximum ranges occurred for the largest volumes (size 4).

	Volume of Morphology (mm^3)		
Size	**1**	**2**	**3**
1	0.74 - 0.79	0.63 - 0.85	0.72 - 0.81
2	0.69 - 0.74	0.64 - 0.80	0.70 - 0.73
3	0.72 - 0.78	0.70 - 0.81	0.73 - 0.77
4	0.69 - 0.81	0.67 - 0.83	0.70 - 0.80

Table 5.4 Computed percentage change in mean current density for a 1% local change V1 over variations in skull conductivity and volume of V1

5.3.3 Baseline boundary voltages and changes

In this section, are the presentations of results of the how the surface potential changes with skull conductivity as seen by the different recording electrodes. The baseline surface potentials for the selected skull conductivities were estimated and plotted in Figures 5.8, 5.9, 5.10 for the strawberry, elongated and blob shaped V1 respectively. The plots also show the percentage changes from baseline surface potential as a result of 1% change in local conductivity.

For all shapes and sizes of V1, the baseline surface potential as estimated by the selected electrodes increase with decreasing skull conductivity and was in the range ±3.0 - ±8.0 mV. The highest percentage changes for the strawberry shaped V1 for the sizes 1, 2, 3 and 4 were respectively 0.1%, 0.04%, 0.03% and 0.05%. The mean percentage changes were 0.01%, 0.005%, 0.002% and 0.005% across the different sizes.

For the elongated shaped V1, the highest percentage changes from baseline were 0.04% for sizes 2 and 3 (about 40% less than size 1 of the strawberry shaped V1), and the 0.07% and 0.05% for sizes 1 and 4 respectively. However, the mean percentage change across all sizes was 0.005% (Figure 5.9). For the last shape of V1, the highest changes were 0.1%, 0.04%, 0.03%, and 0.05% for sizes 1, 2, 3 and 4 respectively. Meanwhile, the mean changes were 0.01% for size 1, and 0.005% for sizes 2, 3, and 4 (Figure 5.10).

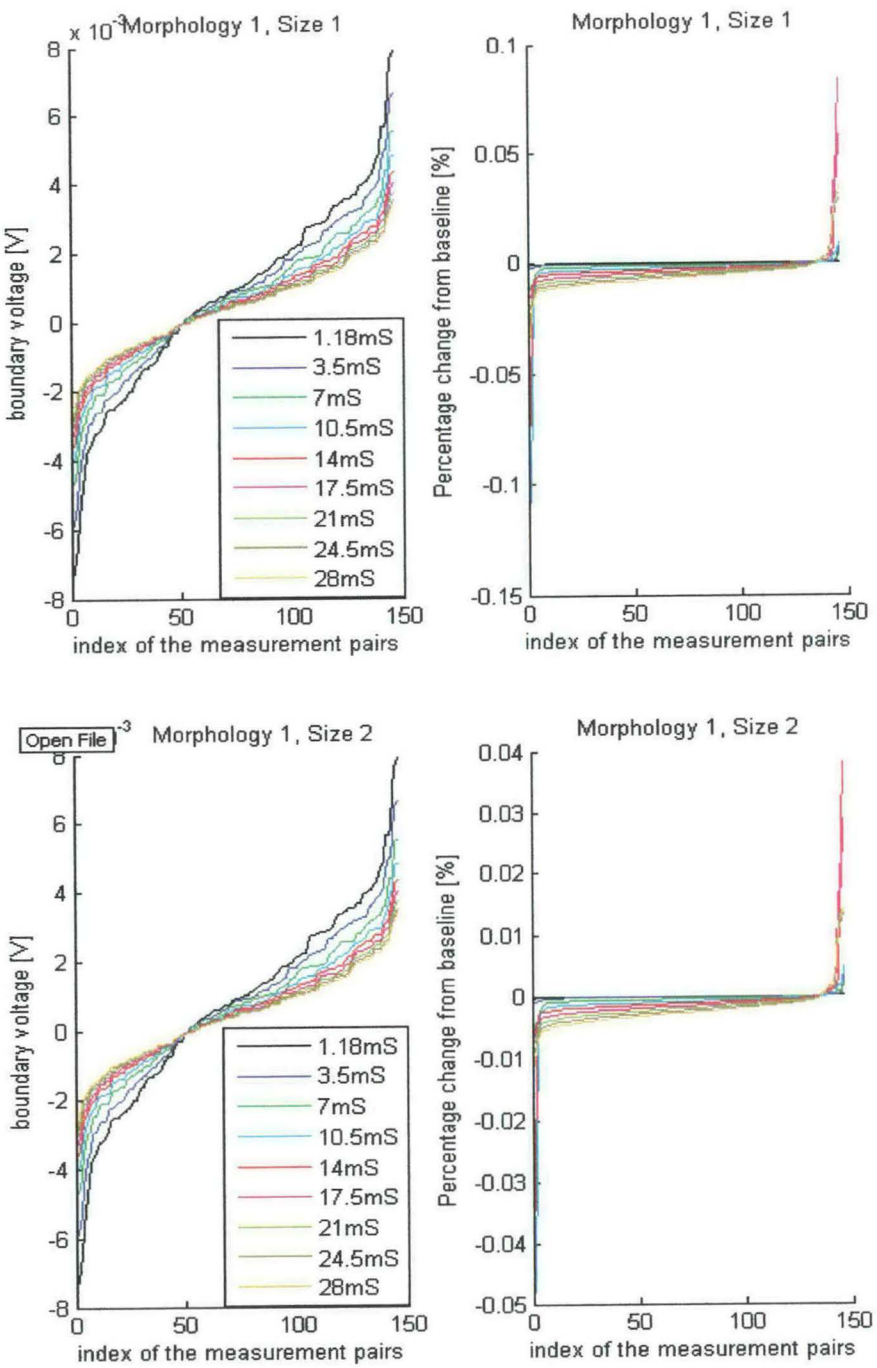

Figure 5.8a Plot of baseline boundary voltages for different conductivities with respect to index of measurement electrode pairs for morphology 1 for sizes 1 and 2

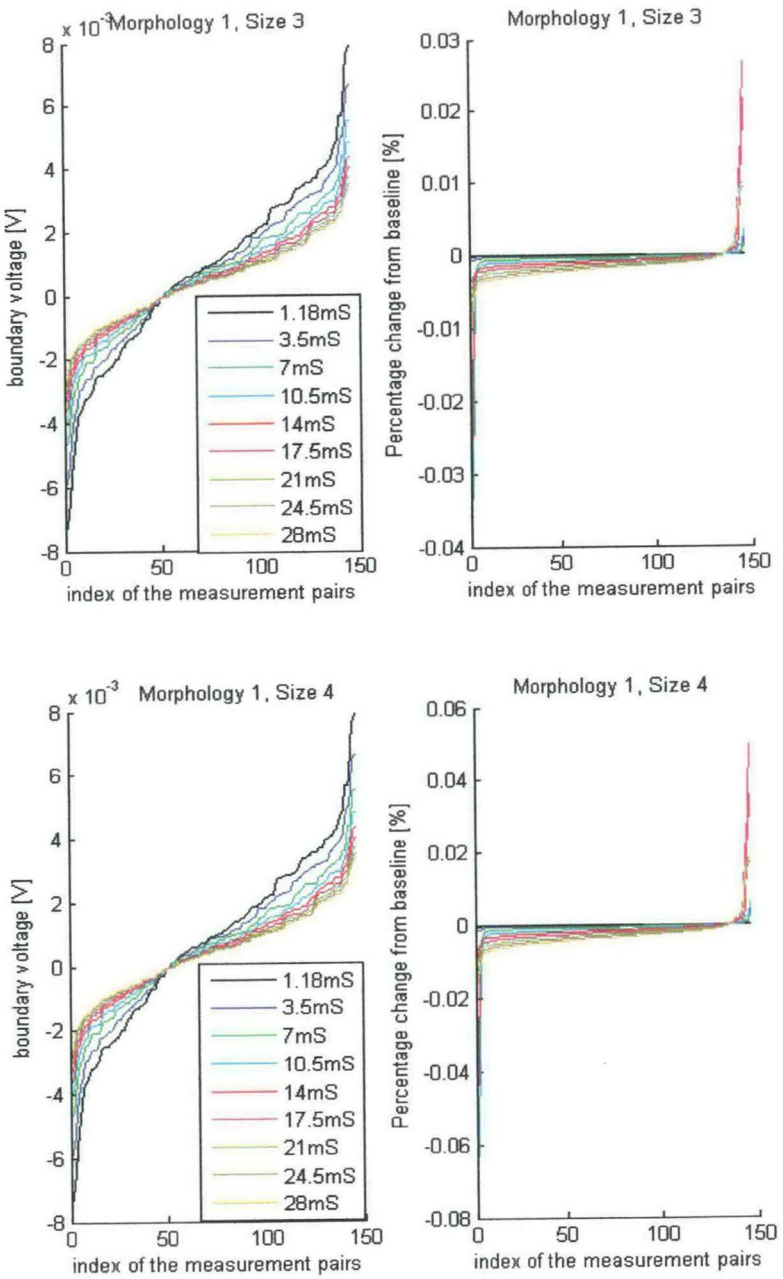

Figure 5.8b Plot of baseline boundary voltages for different conductivities with respect to index of measurement electrode pairs for morphology 1 for sizes 3 and 4

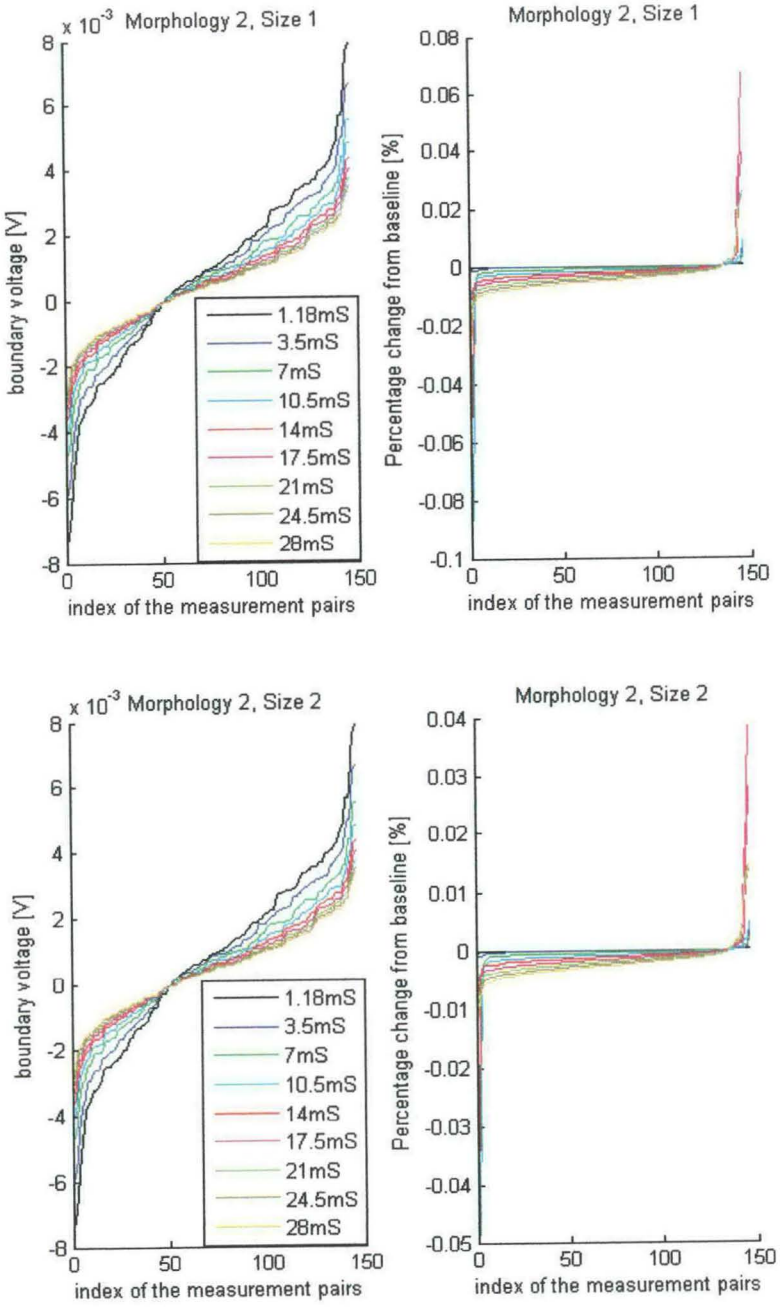

Figure 5.9a Plot of baseline boundary voltages for different conductivities with respect to index of measurement electrode pairs for morphology 2 for sizes 1 and 2

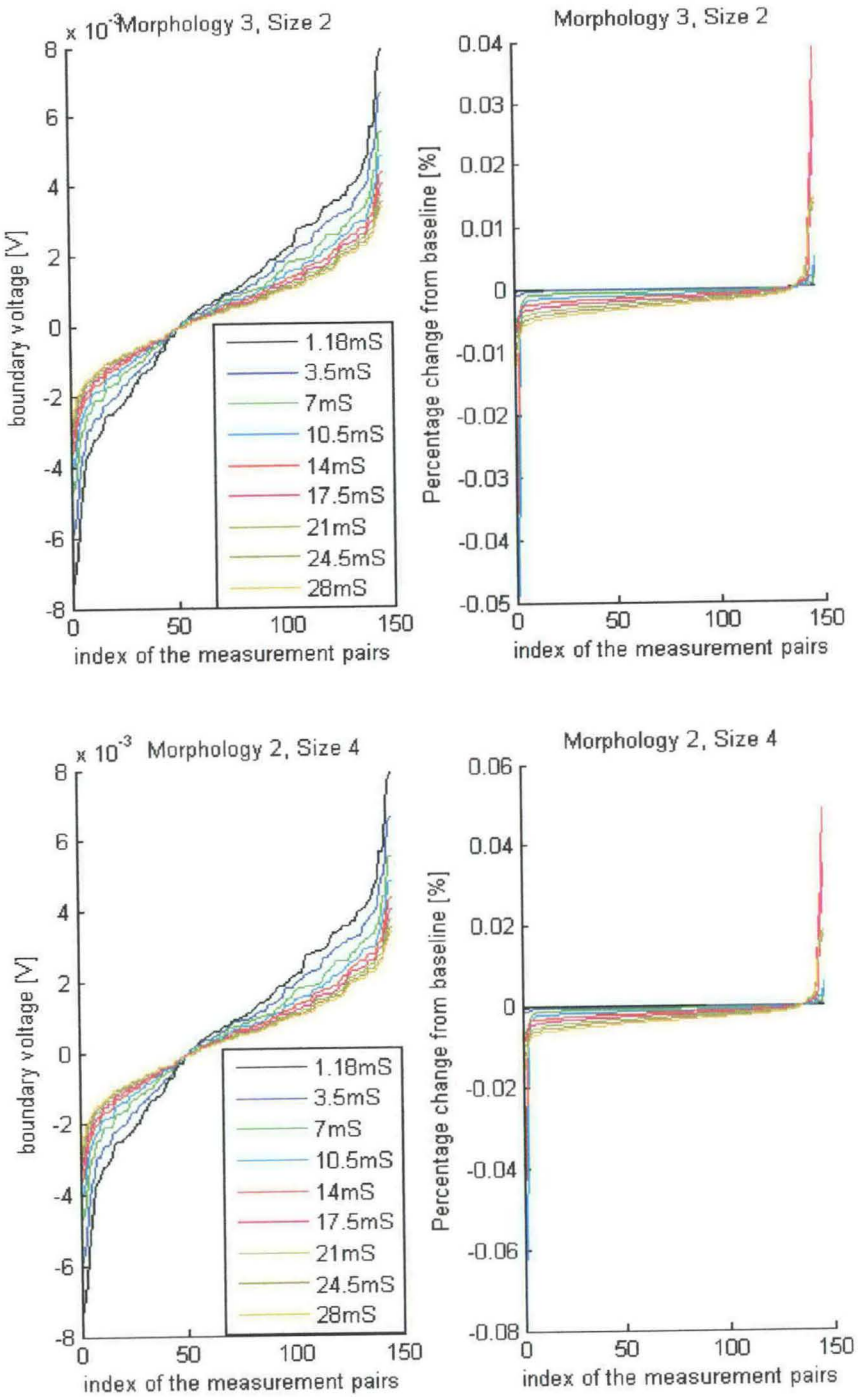

Figure 5.9b Plot of baseline boundary voltages for different conductivities with respect to index of measurement electrode pairs for morphology 2 for sizes 3 and 4

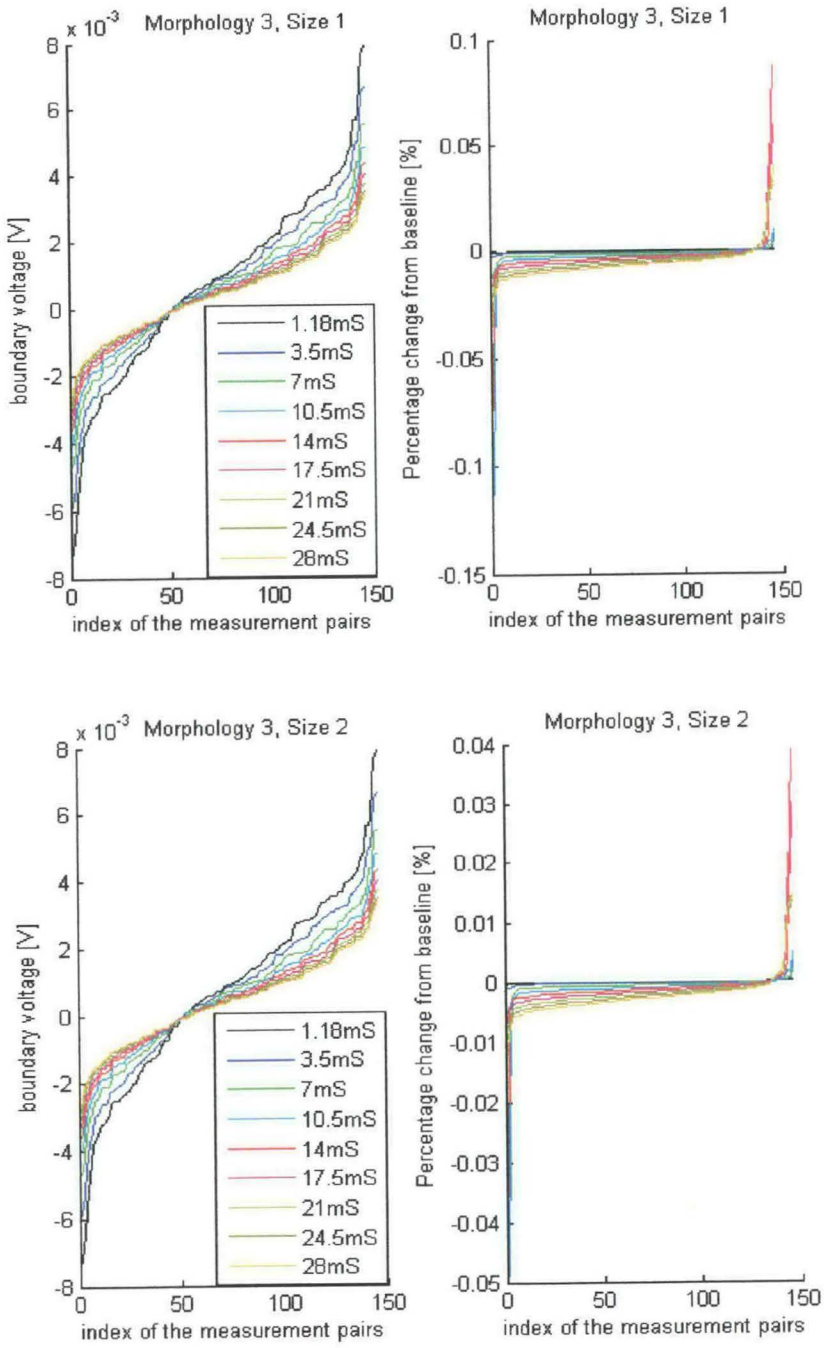

Figure 5.10a Plot of baseline boundary voltages for different conductivities with respect to index of measurement electrode pairs for morphology 3 for sizes 1 and 2

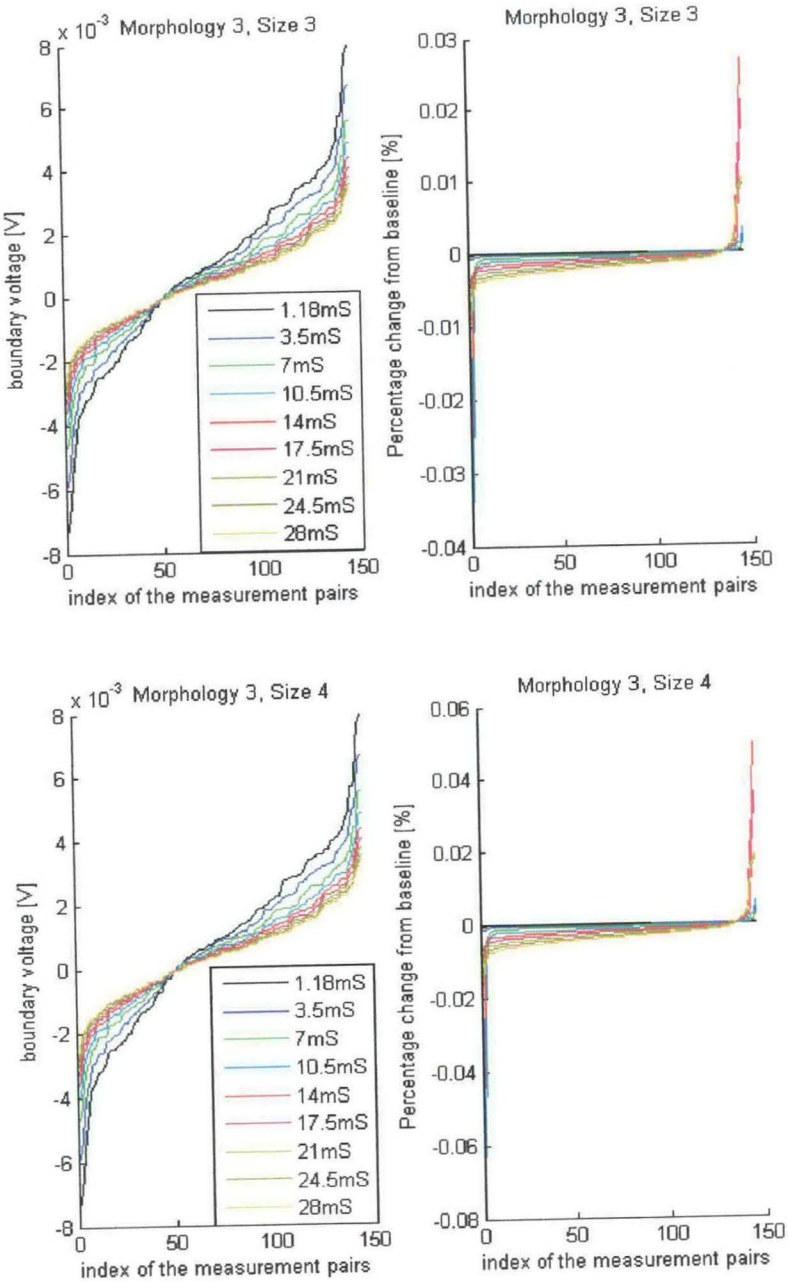

Figure 5.10b Plot of baseline boundary voltages for different conductivities with respect to index of measurement electrode pairs for morphology 3 for sizes 3 and 4

5.3.4 Changes in boundary voltages for different local conductivity changes

Two skull conductivities of 3.5 and 17.5 mSm^{-1}, together with three local percentage changes were selected and the percentage changes in baseline surface potential were estimated. Table 5.6 shows the relationship between percentage changes in surface potential with respect to skull conductivity and percentage change in local conductivity of V1. For fixed skull conductivity, the higher the local change, the higher the percentage changes from baseline surface potential. The table again shows that the higher the skull conductivity, the larger the changes from baseline surface potential. With any local change, the percentage change in baseline surface potential increased by an order of 10 when the skull conductivity changed from 3.5 to 17.5 mSm^{-1}.

	Percentage change in boundary voltage for skull conductivity of	
Local change (%)	**3.5 mSm^{-1}**	**17.5 mSm^{-1}**
0.7	0.0006 - 0.0024	0.005 - 0.020
1	0.0009 - 0.0033	0.006 - 0.030
1.6	0.0014 - 0.0052	0.010 - 0.050

Table 5.6: Percentage change in boundary voltages with respect to local conductivity and skull conductivity

5.3.5 Non uniformity ratio

Non-uniformity ratio is expressed here as the ratio between the maximum J_{max} and minimum J_{min} current densities in the primary visual cortex. The closer the ratio is to unity, the more uniform the distribution of the current density in the region. Figure 5.11a shows a plot of non-uniformity ratio as a function 31 current injection electrodes. Each electrode was paired with all other electrodes for current injection. The non-uniformity ratio was also analysed for some selected injection pairs as shown in the legend of figure 5.11b. This was done as a function of

skull conductivity. The non-uniformity ratio ranged from 1.2 to 10. For figure 5.1b, the non-uniformity ratio increased with increasing skull conductivity. The best uniformity across skull conductivity was for current injection through electrode 2:29 and 13:17, which are diametrically opposed electrodes. The worse distribution was obtained when current was injected through electrode 29:31, 27:29, 23:30, and 12:31.

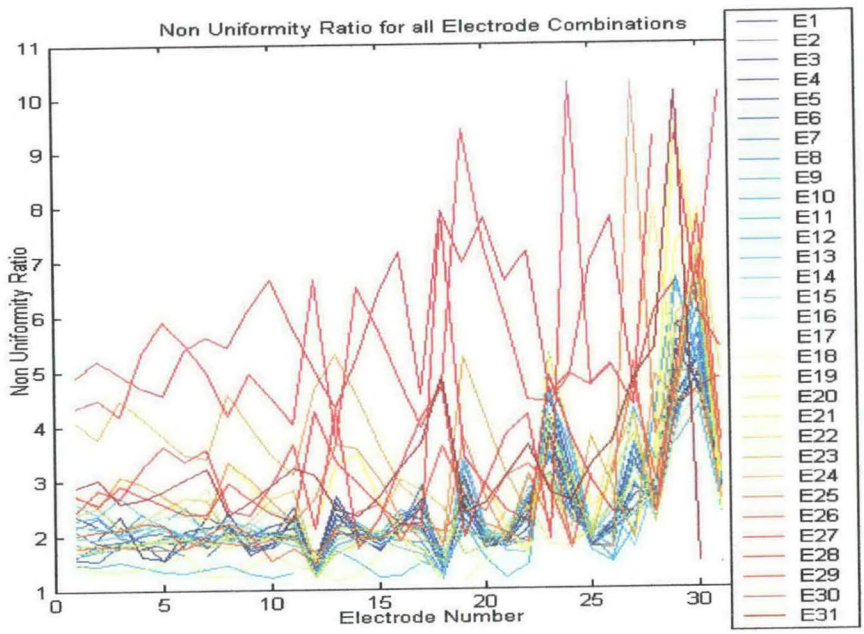

Figure 5.11a. Non-uniformity ratio plots for different electrode combinations for a fixed conductivity of 17.5 mSm^{-1}

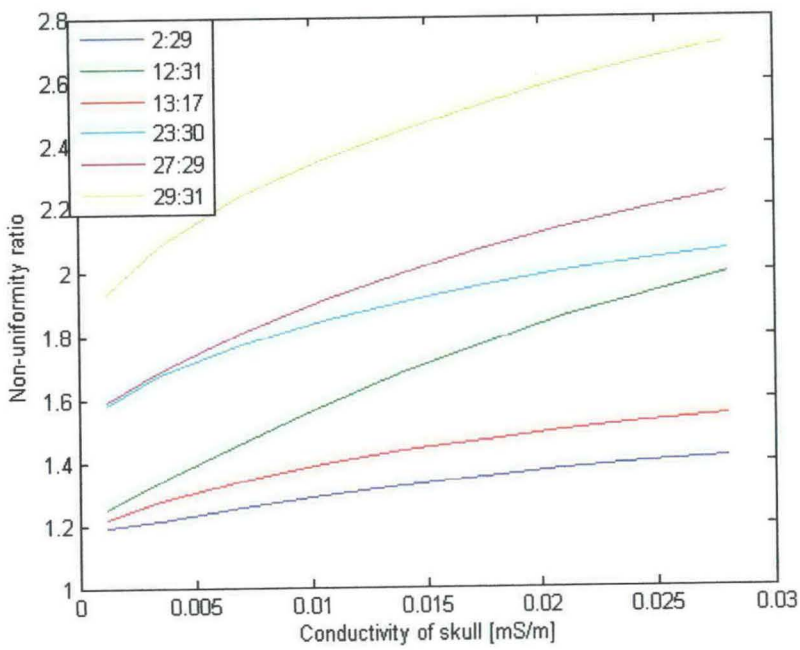

Figure 5.11b Non-uniformity ratio plots for different electrode combinations with variation over skull conductivity

5.3.6 Multiple current injection

Figure 5.12a shows a plot of mean current density in V1 against variations in skull conductivity for four different injections pairs under conditions that there was no perturbation or perturbation in V1. The plot revealed that with or without perturbation, the mean current density increased in V1 when the skull conductivity was increased. The minimum mean for the selected case was 0.4 $nAmm^{-2}$ and the maximum was 4.7 $nAmm^{-2}$. In figure 5.12b, is a plot of the multiple current injection as a function of skull conductivity. The least and greatest current density were 1.6 and 13 $nAmm^{-2}$ respectively, which was about 4 times the those of the single current injection.

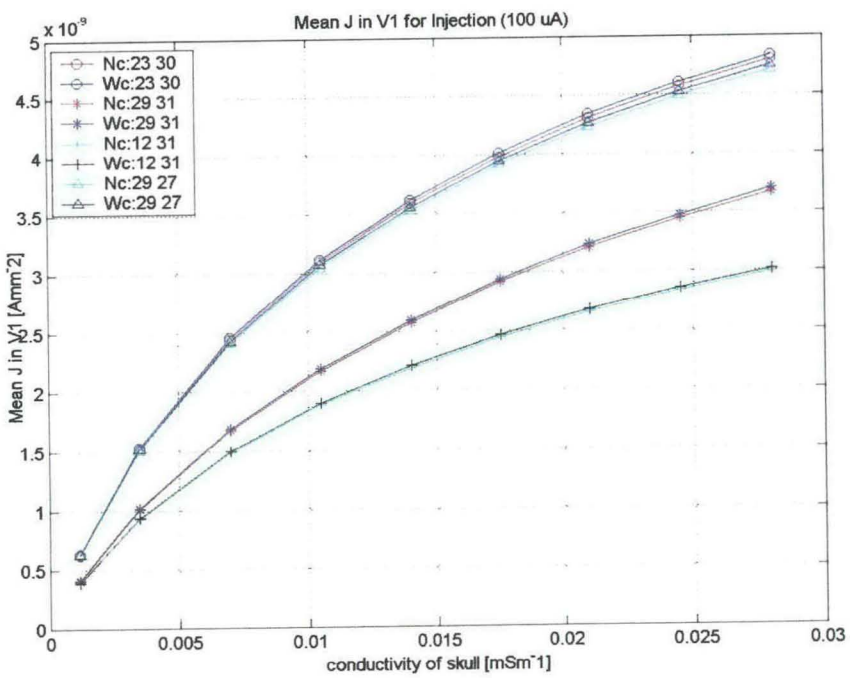

Figure 5.12a: Mean current density in V1 for independent current injection pairs as a function of conductivity

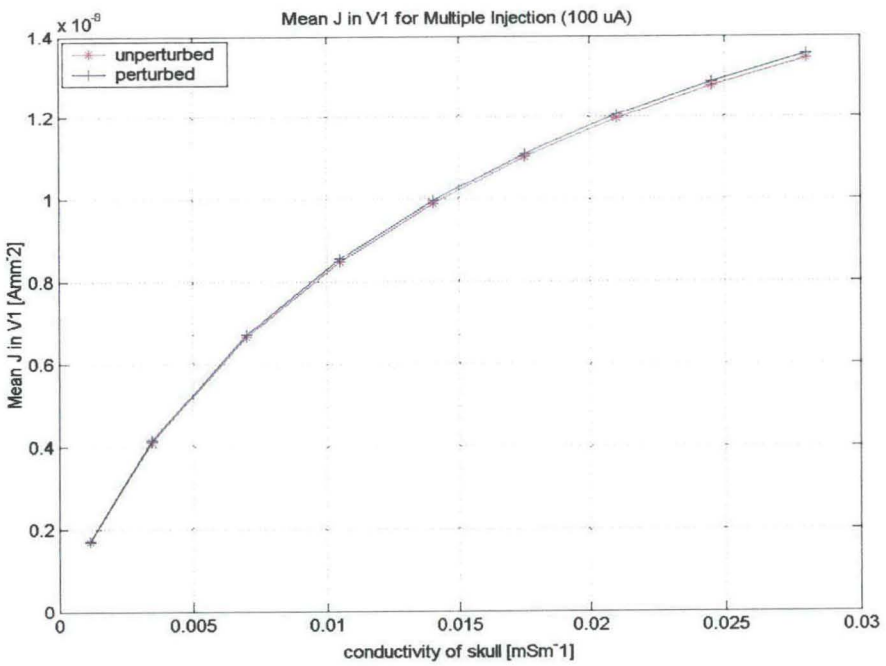

Figure 5.12b. Mean current density in V1 for multiple current injection where the injected currents are 100 μA each and using morphology 1

5.4 Discussion

As expected, the plot of the variation of current density with skull conductivity revealed two important things. First, the magnitude of the mean current density in V1 is not only dependent on the skull conductivity but also on the current injection electrode (I_e) (Figures 5.5 - 5.7) and secondly, the magnitude of J in V1 is neither linearly dependent on skull conductivity nor electrode position. It has also been revealed that the changes in magnitude of the current density in V1 when it remained unperturbed or when there was activity also depended on the size and geometry of V1 (Figure 5.5 - 5.7)

With an increase in skull conductivity, irrespective of the position where the current was injected, the mean J increases monotonically. The reason for this increase is mainly due to the fact that with an increase in skull conductivity the more easily it is for the current to flow through the skull.

It was only one of the morphologies that was examined for the effect of local conductivity changes on mean current density and boundary voltages. For the three selected local conductivity changes, it was observed that an increase in percentage local change gave rise to a higher mean current density as well. This pattern is due to the fact that when the local conductivity increases then there is the tendency for more current to flow through V1, hence a higher current density.

Current injection electrode pairs that were diametrically opposed (2:29, 13:17) tend to give the least mean but higher uniformity ratio in current density in V1. This condition could be attributed to the fact that with diametrically opposed electrodes, the current distribution in V1 is much more uniform just as it is in the brain itself. This least value of the mean current density in V1 for the diametrically opposed electrodes really conforms to the fact that they were far from the region of interest (V1). It has been observed and proven in the previous chapter that for optimal current density in V1, at least one of the injecting electrodes should be close to the primary visual cortex. However, this was investigated for only one value of skull conductivity. It

has now been established that irrespective of the skull conductivity, optimal current density in V1 would be obtained when at least one electrode is near the occipital cortex, for example electrode pairs 29-31, 27-30 and 23-30. However, the distribution of current density is less uniform as compared to those of diametrically opposed electrodes.

With respect to the shape of V1, the elongated had a lower mean current density as compared to the other two shapes (the blob and inclined). However, the mean current density is dependent on the size and shape of V1 (Table 5.4). The larger V1 is, the higher the mean current density in V1, and this is irrespective of the skull conductivity. This is attributed to the larger volume of current density. Meanwhile, changes in baseline voltages remained almost the same irrespective of changes in geometry of V1.

5.5 Conclusion

With a fixed local conductivity change, the estimated baseline surface potential in terms of the skull conductivity did not change much even though the latter changed considerably by over 100%. Secondly, the shapes and sizes of V1 had little effect on the percentage change on the surface potential as well. However, the surface potential decreased with an increase in skull conductivity. On the whole, the biggest surface potential change from baseline was 0.1% and mean across all the measurement was 0.005%. The mean current density in V1 is highly dependent upon the following factors: the skull conductivity in question, local percentage in conductivity of V1 itself and the shape and size of it. Another crucial determinant is the position or electrode pairs through which the current was injected. The greatest mean current density in V1 was obtained when at least one of the injection electrodes was near the occipital cortex. Diametrically opposed electrodes when used to inject current into the head had a uniform distribution of current density in both the brain and region of interest. This work shows that the mean current density could be increased in the brain region by using multiple current injection pattern. It was evident that with the same amount of current injected through four electrode injection pairs, the overall current density increased at most four times.

Magnetic Field Estimation of the Realistic Head Using EIDORS

Chapter 6

MAGNETIC FIELD ESTIMATION OF THE REALISTIC HEAD USING EIDORS

6.1 Introduction

Magnetoencephalography has proven to be very useful in the detection and characterisation of electrical brain activity. The magnetic fields, which are generated by neural activity, can be measured close to the head surface with a high spatial resolution, and the sensor positions relative to the subject's head can precisely be estimated. The magnitude of fast electrical brain activities changes has ever been investigated by modelling and animal studies by the UCLH EIT group. Mathematical modelling, based on cable theory, estimated local resistivity changes near DC to be 3.7% for peripheral nerve bundles and 0.06 -1.7% for the cortex during Evoked Potentials (EP) (Boone, 1995; Liston, 2003). These predictions agreed with measurements done on crab peripheral nerve which showed a change of 0.5 -1.0% (Boone, 1995; Boone and Holder, 1996a; Holder, 1992; Liston *et al.*, 2001) and measurement on the surface of rabbit cortex during median nerve evoked response which showed a change of 0.01-0.03% (Boone, 1995; Boone and Holder, 1995). In order to predict how local changes are translated when measured on the surface of the scalp, Liston (Liston, 2003) initially estimated the boundary changes to drop to 0.006-0.17%.

In 2003, a research was done to determine whether SQUID measurement of magnetic fields could be a better way to do EIT imaging of fast electrical brain activity (Ahadzi et al., 2003). The results of this investigation paved way for the first studies on neuromagnetic field strength estimations due to impedance changes accompanying neuronal depolarization (Ahadzi *et al.*, 2004a). These were by computer modelling and simulation (MATOAST) using FEM to model the head as homogeneous and four concentric spheres. The physiological changes in the brain were assumed to be spherical blobs located at different positions along the line joining the left and right temporal lobes. The magnetic field strengths were estimated at three locations on the head; whilst current was injected through diametrically opposed

electrodes near the left and right temporal lobes. The predictions were that for a 1% change in local conductivity within the brain, the change in baseline magnetic field was up to a maximum of 3fT, which is two times by far smaller than the spectral noise density of 7 fT in neuromag 122 at a frequency band of 1 - 10 Hz (see section 3.6.3).

The potential advantage of using spherical models in solving the forward problem has rather a limited accuracy due to the misinterpretation of the current flow in the brain volume. Standard head models could be a useful compromise between spherical models and the elaborate realistically shaped head models. These standard head models based on magnetic resonance image and model computations for each individual subject may be useful only in case a simpler model fails to solve accurately the forward problems.

Ahadzi (Ahadzi *et al.*, 2004b) then used realistic FEM of the head and solution of the forward problem (EIDORS – (for completeness, EIDORS has a suite, which performs mesh generation, reconstruction and image display) to quantitatively estimate the potential changes on the scalp when a 1% local resistivity change occurred at the visual cortex during VEP. Boundary voltage changes were estimated to be 0.02-0.04% for optimal four terminal resistivity measurements. In the previous chapter, further numeric predictions, in terms of boundary voltages, were made by studying how they were affected by different skull conductivies of the head, local conductivity changes, the shapes and sizes of the primary visual cortex (see chapter five).

These numeric predictions are further refined in the present study in which one is assessing the influence of these variations on the magnetic field strength. For further validation and to compare the accuracy of the modelling work done, EIDORS has been used here to compute the magnetic fields.

6.1.1 Purpose

The purpose of this chapter was to develop a new forward model to estimate the magnetic field strength related to the impedance change by utilising EIDORS. Specific questions to be answered are:

i. What are the magnitudes of the magnetic field for three different head models: the homogeneous, fourshell and realistic head?
ii. Are there any significant differences in the percentage changes from baseline magnetic field due to different shapes and sizes of V1?
iii. How different are these changes as compared to the electrical recordings?
iv. Does the magnetic recordings using SQUIDs offer any advantage over the electrical recordings?

6.1.2 Design

Three FEM model of the head, the homogeneous or spherefine, fourshell and realistic (Bayford et al., 2001a) were generated using a modified version of EIDORS (Polydorides and Lionheart, 2002). The electrode nomenclature would be consistent with the EIT electrode protocol numbering, and the physiological change was assumed to be conductivity variations in the primary visual cortex, which in turn varied in shape and size. Current was injected through three diametrically opposed (DMO) electrodes (13:17, 2:29, and 12:31) and three other pairs of electrodes located at the back of the head (best current injection electrode (BCE) pairs 23:30, 27:30, and 29:31 (sections 1.2.10.4 and 4.5.2.3)). The magnetic field strength would be assessed 1-cm radially away from all electrode positions except those used for the current injection.

6.2 Method

6.2.1 Volume conductor and source models

Four head models, the homogeneous, spherefine, fourshell and realistic head meshes were generated using FEM, and were used as the volume conductors. The homogeneous and spherefine models (figure 6-1) assumed the human head to be spherical in shape and were made up of the brain only and of radius 8 cm. The fourshell model (figure 6-2) had the same dimensions as specified in section 3.2.1. The head geometry used for the realistic head was that of a full, layered human head containing brain, CSF, skull and scalp (full-head as seen in section 5.2.1). The full head model also contained a cavity to represent the air space behind the nose. In all cases EIDORS was used to generate the meshes describing the geometry with linear, tetrahedral elements.

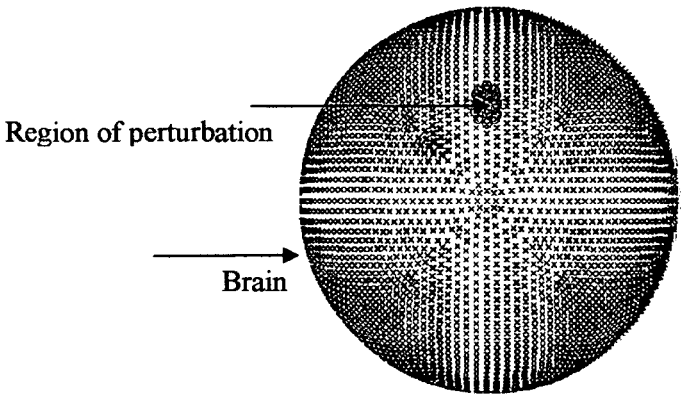

Figure 6-1: The homogeneous and head spherefine head models. The homogeneous head model has 24,734 nodes whereas the spherefine has 36,000 nodes.

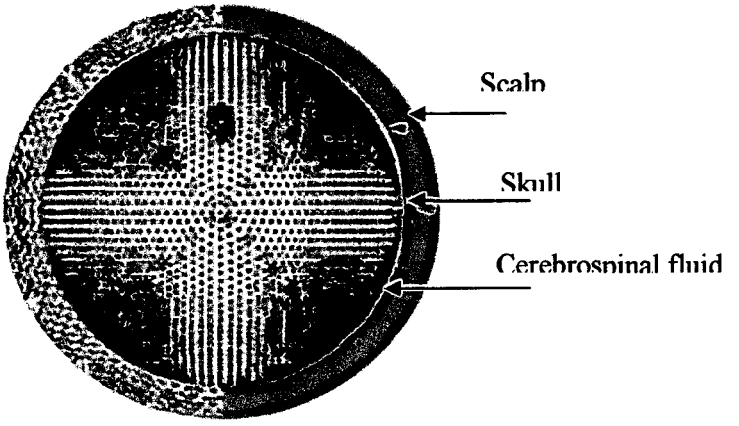

Figure 6-2: The fourshell head model with 42,093 nodes. The conductivity values of the different shells (scalp, skull, cerebrospinal fluid, and brain) are as specified in table 4.1, section 4.2.1

The source models were a spherical blob of radius 2-cm or the primary visual cortex denoting the region of perturbation. The description of the shapes and sizes of V1 used here are as detailed in sections 5.1.3.1 and 5.1.3.3 respectively.

6.2.2 The electrode protocol

There were 31 electrodes and their positions were the same as those depicted in figure 1-16. Thirty-one SQUIDs were used as the magnetic field sensors and were positioned 1-cm radially outward from each electrode position (figure 6-3).

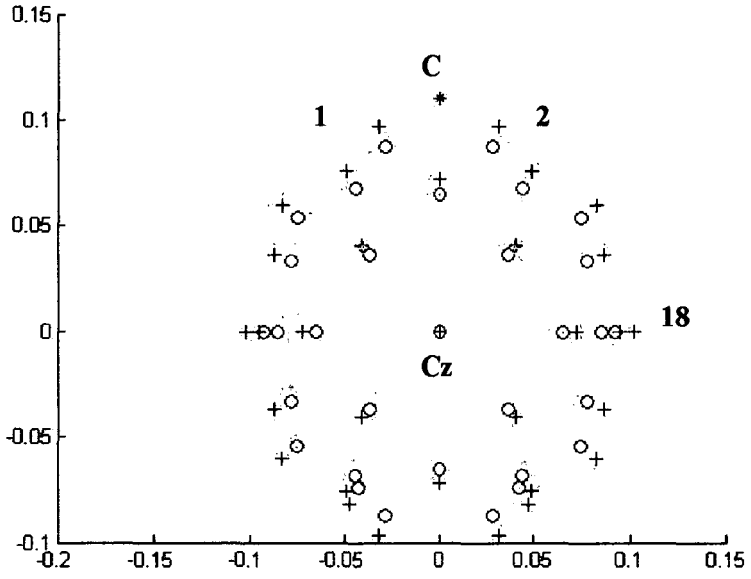

Figure 6-3: The red-circles (o) denote electrode positions for current injection whereas the blue crosses (+) are 1-cm radially away from points of current injection where the Squids are located for estimating the baseline magnetic field. The green points (*) are the sensor locations L, C and R (used in chapter 3) Both axes have units in meters

6.2.3 The simulation

The simulations described in this section were carried out with whole head magnetometer consisting of 31 channels with radial orientations, which were arranged on a hemi-sphere as locations 1 - 31 as seen in figure 6.3. The magnetic fields were computed for various shapes and sizes of the primary visual cortex. No noise was added to the data. A 100 μA constant square wave current was injected through some selected electrodes. EIDORS functions were modified for the purpose of this simulation and were used for the estimation of current distribution at nodes based on Geselowitz sensitivity theorem, within the meshed volume conductors. After extracting the current densities at all nodes, the magnetic field estimation outside the head 1-cm from all the electrode positions except the injection electrodes were obtained using the magnetic potential method.

The actual simulation was performed in two main parts to determine the baseline and perturbed magnetic fields. The baseline magnetic field involved the forward estimation of magnetic field induced at all magnetic field sensor positions outside the head (about 1-cm radially off the head) when the volume conductor was assumed to have constant conductivity without any perturbation. The perturbed field represented the magnetic field outside the head when conductivity changes in the range 0.06 to 1.7% due to neuronal depolarisation causing equivalent impedance change throughout the whole head volume. This perturbed was the resultant magnetic field when the conductivity of the primary visual cortex was locally perturbed by 0.6%, 1.0% and 1.6% due to evoked response.

6.3 Results

6.3.1 Baseline magnetic fields

6.3.1.1 Baseline magnetic field - fourshell and realistic head models

The variation of the baseline magnetic field as a function of the SQUID locations, 1-cm radially outward from current injection electrode are plotted in Figure 6.4. The top figure refers to the magnetic field due to current injection through the diametrically opposed electrodes, whereas the bottom figure refers to the magnetic field due to current injections through electrodes located at the back of the head. The magnitudes of the largest baseline magnetic field were 41 pT and 28 pT for DOM and BCE respectively.

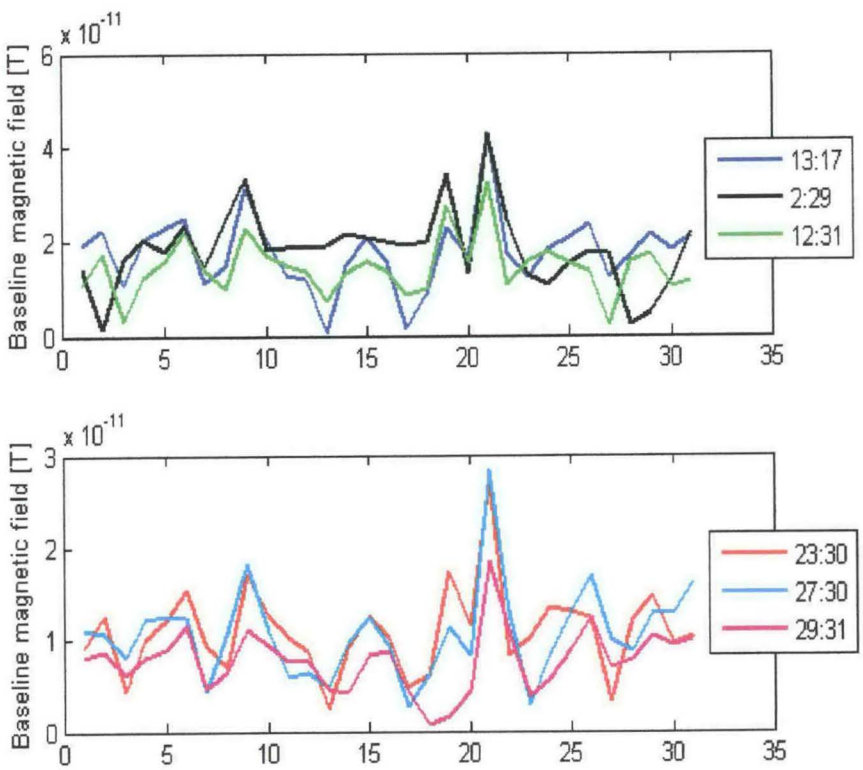

Figure 6.4: Baseline magnetic field for fourshell head model. The horizontal axis refers to the location of the SQUIDs position

The baseline magnetic field variation over SQUIDs locations for the realistic head is plotted in Figure 6.5. The upper figure shows the variation of the magnetic field due to current injection through diametrically opposed electrodes. The bottom figure refers to the variations in magnetic field due to current injection through the electrodes at the back of the head. The biggest magnitudes of the magnetic field were 75 pT and 46 pT respectively for the DOM and BCE.

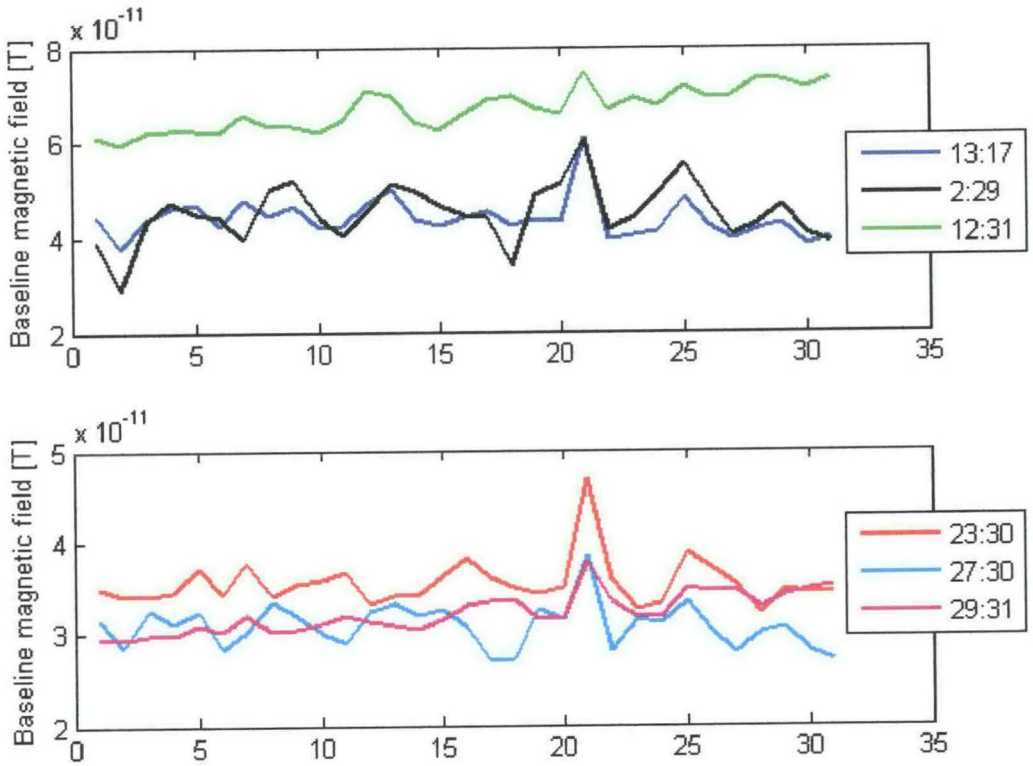

Figure 6.5: Baseline magnetic field for realistic head model. The horizontal axis refers to the location of the SQUIDs position

6.3.1.2 Comparison of magnetic field

The baseline magnetic field for the four-shell model for the current injection protocol selected was in the range of 1 - 42 pT, and that of the realistic head was between 20 - 70 pT. In general, in both cases, the magnetic field due to the injection through diametrically opposed electrodes was slightly higher than that due injection of current through electrodes near the primary visual cortex (Table 6.1).

		Baseline Magnetic field [pT]		
Injection Pairs		**Fourshell**	**Realistic**	**Inj Protocol**
13	17	1 - 74	39 - 60	DMO
2	29	2 - 42	30 - 60	DMO
12	31	3 - 32	60 - 72	DMO
23	30	3 - 37	34 - 47	BCE
27	30	3 - 29	27 - 37	BCE
29	31	1 - 18	30 - 37	BCE

Table 6.1 Range of baseline magnetic fields across SQUID sensor locations for two types of current injections protocol: (DMO - Diametrically Opposed and BCE Best Current Injection Electrodes)

6.3.2 Percentage Changes in magnetic field

Figures 6.6 - 6.8 show the plots of the changes in magnetic field for different morphologies as a function of the locations of the SQUIDs. The injection electrodes that recorded the biggest changes in magnetic field from baseline in descending order were 23:30, 27:30, and 29:31. These were the visual cortex electrodes due to current injection through the diametrically opposed electrodes 13:17, 2:29, and 12:31 and occurred at SQUID locations at the back of the head.

6.3.2.1 Morphology 1

The largest change in magnetic field (0.05%) was recorded for SQUID location near the back of the head and was due to current injection through electrode pair 23:30. This best-case scenario occurred for morphology 1 with size 1 (upper figure of Figure 6.6).

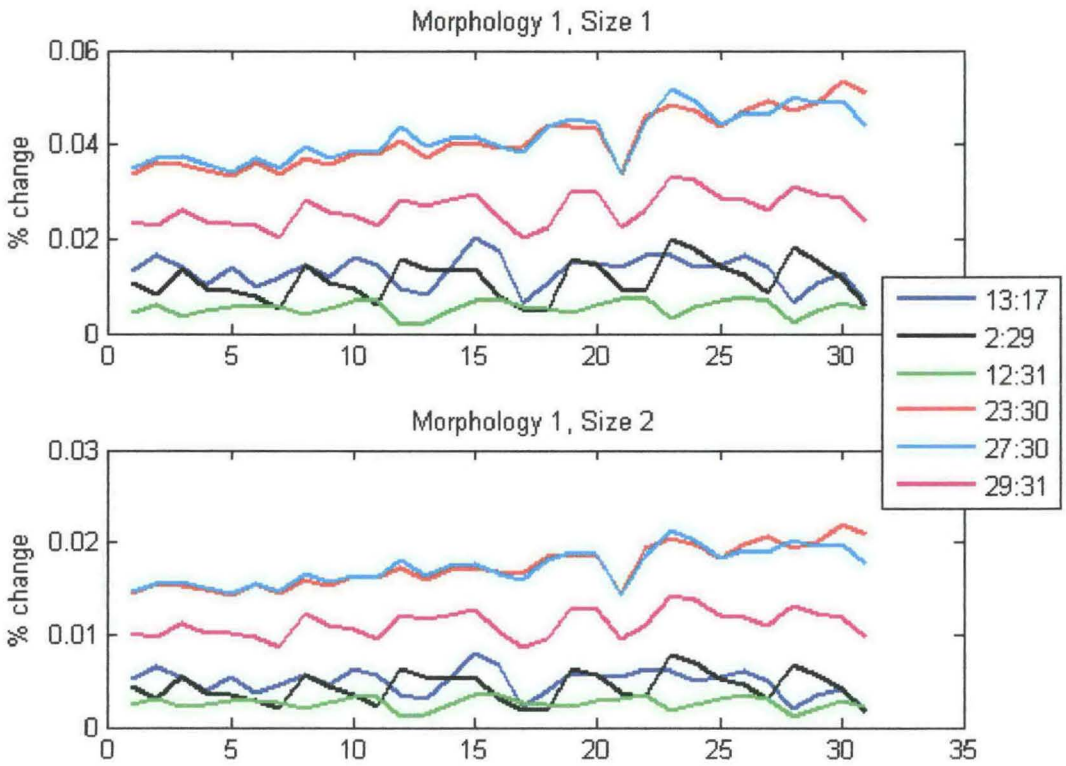

Figure 6.6: Realistic head percentage changes in magnetic field from baseline as a function of position of SQUIDs, for morphology 1 and sizes 1 and 2

For all the sizes, the biggest changes were recorded for current injection through electrode pairs 23:30 and 27:30. The least changes in magnetic field recorded across all SQUID locations were due to current injection through electrode pair 12:31 Figure 6.6 - 6.7).

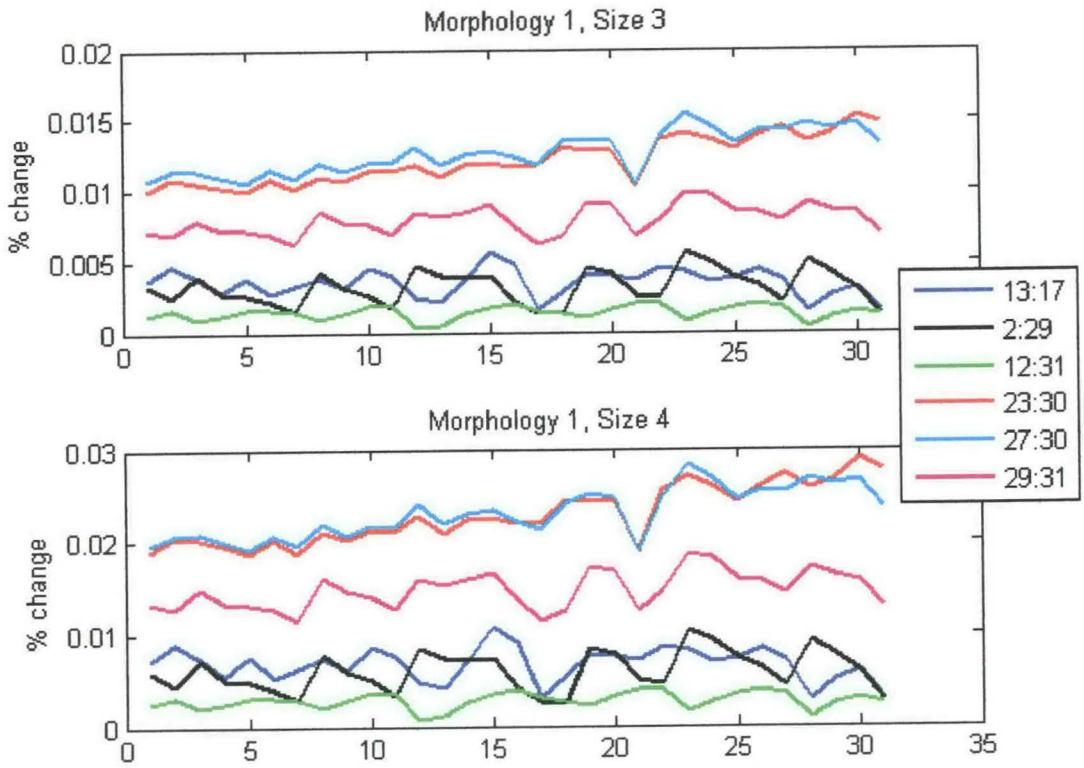

Figure 6.7: Realistic head percentage changes in magnetic field from baseline as a function of position of SQUIDs, for morphology 1 and sizes 3 and 4

6.3.2.2 Morphology 2

Figures 6.8 and 6.9 are plots of variations in magnetic field changes across SQUID locations. The biggest change across all sizes of the primary visual cortex was 0.04% and again this occurred at SQUID locations near the back of the head, and for current injection through electrode pair 23:30. However, the changes in magnetic field across all the SQUID locations for all sizes are similar for current injection through electrode pairs 23:30 and 27:30. The least changes was 0.001%.

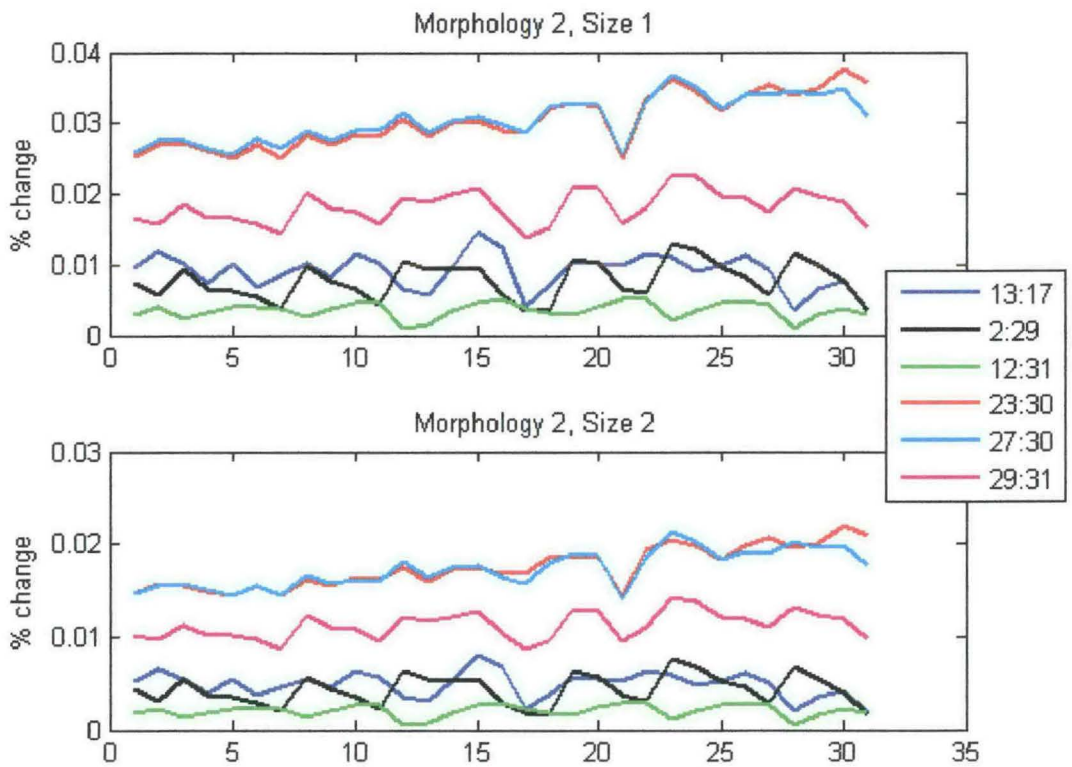

Figure 6.8: Realistic head percentage changes in magnetic field from baseline as a function of position of SQUIDs, for morphology 2 and sizes 1 and 2

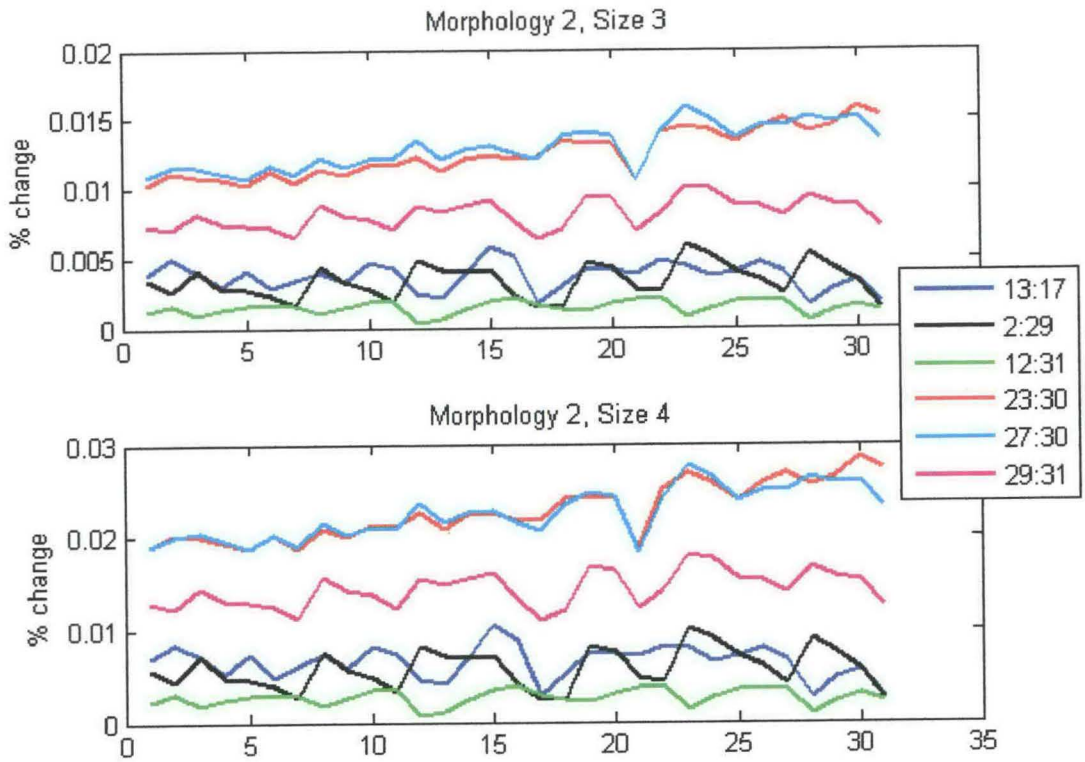

Figure 6.9: Realistic head percentage changes in magnetic field from baseline as a function of position of SQUIDs, for morphology 2 and sizes 3 and 4

6.3.2.3 Morphology 3

The biggest change in magnetic field across all SQUID locations was 0.05%, whereas the least change was 0.001% as in the case of morphologies 1 and 2. Just as in the cases of the last two morphologies, the biggest changes were due to current injections through electrode pairs 23:30 and 27:30, and least was due to current injection through electrode pair 12:31 (Figures 6.10 -11).

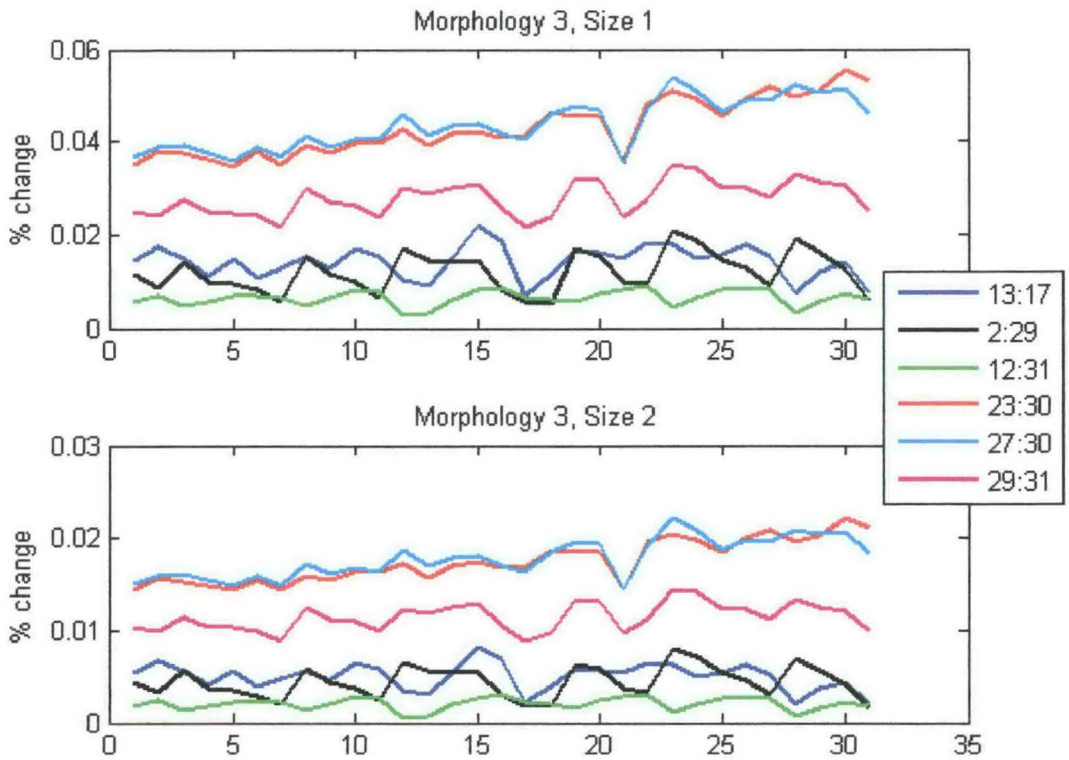

Figure 6.10: Realistic head percentage changes in magnetic field from baseline as a function of position of SQUIDs, for morphology 3 and sizes 1 and 2

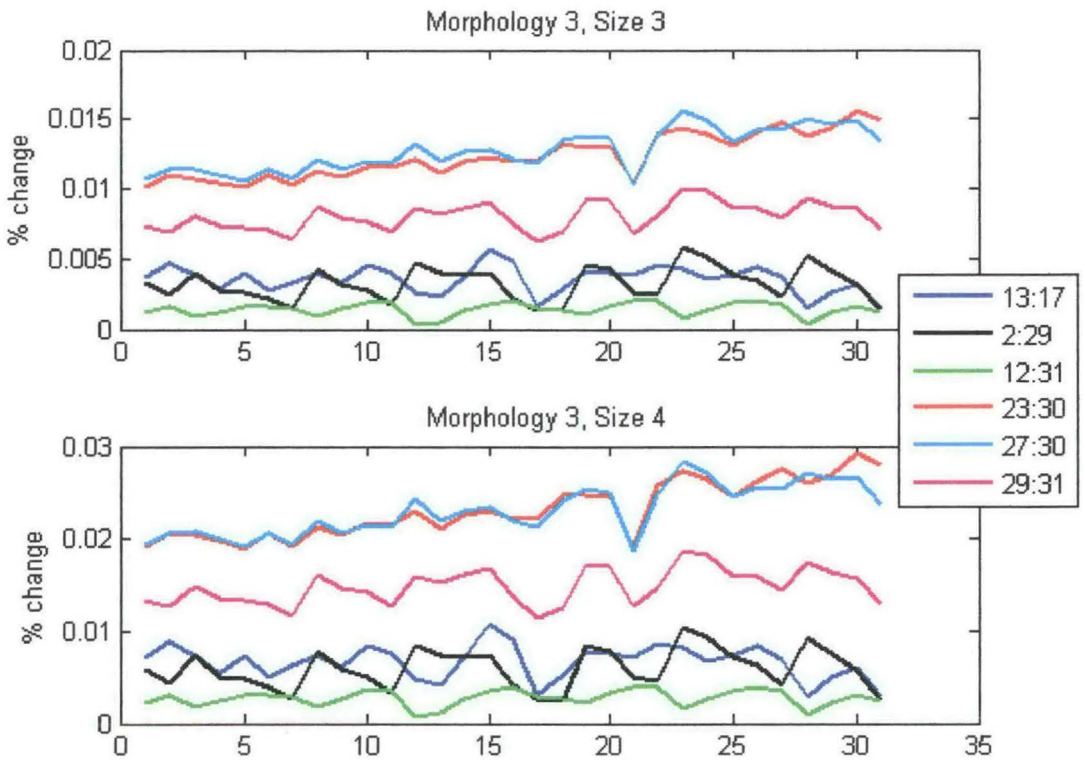

Figure 6.11: Realistic head percentage changes in magnetic field from baseline as a function of position of SQUIDs, for morphology 3 and sizes 3 and 4

6.4 Discussion

The magnitude of the estimated baseline magnetic field associated with the fourshell head model were in the ranges 1 - 74 pT and 3 - 37 pT for current injection through diametrically opposed (DOM) and visual cortex electrodes (VCE) respectively. On the other hand, the baseline magnetic field relating to the realistic head were in the ranges 30-72 pT and 27-47 pT for current injection through the DOMs and VCEs respectively.

As expected, the magnitude of the magnetic field across the head depended upon the point of current injection and the type or model of head used. This was evident, for example, when current was injected through electrode pairs 13:17, the magnetic field across all sensors with respect to the fourshell model was between 1 - 74 pT, whereas it was 39 - 60 pT for the realistic head. Also, the pattern of current injection also played a vital role as expected, since the magnetic field across the head varied according to whether the injection was done through diametrically opposed electrodes or via those at the back of the head. The distribution of the magnetic field across the head was more uniform for injection of current through the diametrically opposed electrodes than those at the back of the head. This uniformity was virtually due to the uniform distribution of current through the head.

The shape and size of the primary visual cortex vary from person to person, and that's why their voltage levels are entirely different in a VEP experiment (Chiappa, 1990). The percentage changes in magnetic field also varied in accordance with variations in the shape and size of and magnitude of local conductivity changes in V1.

Tables 6.5-7 show a summary of the computed percentage changes in magnetic field with respect to percentage local conductivity changes, and how they are related to the different shapes and sizes of the primary visual cortex.

	Volume of Morphology (mm^3)		
Size	**1**	**2**	**3**
1	0.001 - 0.032	0.001 - 0.022	0.001 - 0.034
2	0.001 - 0.013	0.001 - 0.013	0.001 - 0.014
3	0.001 - 0.009	0.002 - 0.010	0.002 - 0.009
4	0.001 - 0.018	0.001 - 0.017	0.001 - 0.017

Table 6.5 Computed percentage change baseline magnetic field for a 0.6% local change inV1 over SQUID locations

	Volume of Morphology (mm^3)		
Size	**1**	**2**	**3**
1	0.001 - 0.053	0.001 - .040	0.002 - 0.056
2	0.001 - 0.022	0.001 - 0.022	0.001 - 0.022
3	0.001 - 0.015	0.001 - 0.015	0.001 - 0.015
4	0.001 - 0.029	0.001 - 0.030	0.001 - 0.030

Table 6.6 Computed percentage change baseline magnetic field for a 1% local change inV1 over SQUID locations

	Volume of Morphology (mm^3)		
Size	**1**	**2**	**3**
1	0.002 - 0.085	0.002 - 0.060	0.001 - 0.080
2	0.001 - 0.035	0.002 - 0.035	0.001 - 0.036
3	0.001 - 0.024	0.001 - 0.025	0.001 - 0.025
4	0.001 - 0.047	0.001 - 0.045	0.001 - 0.046

Table 6.7 Computed percentage change baseline magnetic field for a 1.6% local change inV1 over SQUID locations

For a local conductivity change of 0.6% the best or maximum change from baseline magnetic field was 0.03% whereas, for a 1% local conductivity change, the magnetic field changed up to 0.05%. With a local change in conductivity of 1.6%, the maximum field change was 0.08%. These percentages showed that for local conductivity changes between 0.6% and 1.6% as in the cable theory and mathematical modelling, the surface potential, measured on the scalp reduced by a further 10%. With respect to the maximum changes in magnetic field and local conductivity changes, it was noted here that in the best-case scenario, the magnetic field changed by 5%.

6.5 Is there any advantage

In the electrical recordings in the previous chapter, for 0.6% local conductivity change the potential measured on the scalp was 0.020% whereas the magnetic field changed by 0.03%. With a percentage change of 1% locally, the percentage change in surface potential across all morphologies and sizes was 0.03% whereas the magnetic field change was 0.06%. With a local percentage change if 1.6%, the scalp potential recording changed by 0.05%, whereas the magnetic field recordings changed by 0.085%.

In general, depending on the change in local conductivity and for fixed skull conductivity and irrespective of the shape and size of the V1 (the physiological volume), the maximum percentage change in for the magnetic recordings were much bigger in magnitude than those for the electrical recordings. This suggests that the magnetic recordings have a better potential in EIT measurements. In any case, these values need to be compared with the background in the measurement system that may be used. That is, it depends on the SNR achievable for each element, but not just the magnitudes of the signal.

6.6 Observations

The important observation is whether these magnetic recordings contain enough information for the reconstructive purposes in EIT? It is difficult to tell with the results that were obtained here however, a quantitative analysis "distinguishability" could be employed. Distinguishability is used to provide a quantitative measure of the ability of an impedance imaging systems to distinguish between two conditions from each other by electrical impedance measurements. It is a characteristic of the measurement system, and can be calculated from the data obtained from a system without the need to reconstruct an image from that data. The details of this approach are outlined in section 7.2.2.4. This will involve very fast and memory efficient computing facilities, which at the moment are out of, reach at our research unit. A way of resolving the computing needs to solve this problem will be by using the CONDOR Grid system. Condor is a specialized workload management system for compute-intensive jobs. Like other full-featured batch systems, Condor provides a job queuing mechanism, scheduling policy, priority scheme, resource monitoring, and resource management. The details of this complex but useful procedure are also outlined in section 7.2.2.4.

Summary, Suggestions and Conclusion

Chapter 7

CONCLUSIONS AND SUGGESTIONS FOR FUTURE WORK

7.1 Summary of work done

Electrical Impedance Tomography (EIT), which measures surface potentials, does not uniquely determine impedance changes accompanying neuronal depolarisation, which may be of the order of 1% or less. There has been the interest in imaging small impedance changes in the human head using EIT techniques since I joined the UCLH - EIT group in 2002. This group in the past was able to detect large impedance changes due to cell swelling or blood volume change using the same technique.

It has become necessary for new techniques to be developed in order that these small impedance changes due to neuronal depolarisation are imaged. Undoubtedly, there are many variables that can be controlled in order to improve the spatial and temporal resolution of the EIT images. My PhD work pioneered some of the improvement techniques, which included a multi-modality approach, placement of electrodes on the head, absolute measurement of boundary voltages and current density distributions in the head, and how these are affected by variability of skull and local conductivity changes.

Below is a number of pioneering works done by me for this to study:

1. The first to set up MEG and EIT as multi-modality. The electric current associated with these type of depolarisation are weak but produce magnetic fields though very weak can still be measured by sensitive Superconducting Quantum Interference Device (SQUID) magnetometers. This work describes the first simulated multi-modality sensor system for estimating the ultra weak magnetic field outside the head by injecting a constant current of 100 μA using EIT techniques and determining the magnetic field strength using SQUIDs. The results suggested that with a 1% change in

conductivity in a region enclosed by a 2cm radius volume sphere in the brain, the magnetic fields are of the order of 10^{-12} T and could be measured using SQUIDs.

2. Examined injection of current through all possible pairs of thirty-one (31) electrodes by estimating the changes in boundary voltage as recorded by all other pairs of electrodes not used for the injection. With reference to impedance changes in V1, an EIT electrode protocol for obtaining optimal current density in V1 and maximal changes in boundary voltages was established.

3. Quantitatively measured absolute boundary voltages and changes in boundary voltages accompanying impedance changes in the human head.

4. Estimated absolute current densities in the human head when a current of 100 μA was injected through certain pairs of electrodes.

5. Numerically simulated and determined that to obtain maximal boundary voltage changes due to changes in impedance in V1, at least one of the recording electrodes must be placed near the occipital cortex irrespective of the placement of the injection electrodes. In collaboration with Ori Gilad (member of UCLH - EIT group), it has been validated experimentally on humans and the results would be detailed in his Thesis at a future date.

6. Modelled different sizes and shapes (strawberry, or blob, or an elongated model) of the primary visual cortex, and critically examined their effect on the boundary voltages and current density distributions in the human brain due to changes in their impedance.

7. Performed extensive simulation studies on the effect of variation in human skull conductivity or local conductivity on the changes in boundary voltages and current density distributions due to impedance changes in V1.

8. Performed extensive simulation studies on the effect of variation in human skull conductivity or local conductivity on the changes in magnetic field distributions on the head due to impedance changes in V1.

In conclusion, the results of the multi-modality approach of EIT/SQUID coupled with the modelling work on V1, studies of the effect of variations in skull and local condutivities, and optimal electrode protocol for EIT permitted the first human experiment in MEG/EIT done at Queens Square by UCLH – EIT group. Ori Gilad, my collaborator in the practical experiments, has done enormous studies in this field and would be producing the details in his PhD thesis.

7.1.1 Research question

The focus of my research was on exploring techniques for imaging small and fast impedance changes in the head due to neuronal depolarisation. The major research question was whether magnetic recording of EIT would yield measurable changes in magnetic field as compared to electric field?

7.1.2 Review

A study was done on imaging modalities such as magnetoencephalography (MEG), EIT, functional Magnetic Resonance Imaging (fMRI) among many, in terms of their principles and practical or clinical applications. The merits and demerits of MEG and EIT were carefully considered. The forward problem, which is the relationship between surface potential (V), conductivity (σ) and current density ($\vec{J}$), in relation to this study, has also been formulated. In addition, the application of Finite Element Methods (FEM) in modelling of the human head as a finite and an infinite conductor was considered. These among others have been documented in Chapter one of my thesis as "Review and Introduction".

7.1.3 Multi-modality

The method adopted for this study in order to address the focus, was to set up mathematical models, the forward problem in relation to imaging of fast impedance changes in the human head. The first method was to use a multi-modality approach by integrating EIT and SQUIDs, which is the bedrock MEG. The region of depolarisation in the brain was chosen along the axis joining the left and right temporal lobe. This work constitutes the third chapter of this thesis, which is entitled "Neuromagnetic field strength outside the human head due to impedance changes from neuronal depolarisation". Part of this chapter was presented at the 4th International Conference on Biomedical Applications of EIT held in University of Manchester Institute of Science and Technology, Manchester from 23rd to 25th April 2003. A part of it as well has also been published in IoP Physiological Measurements (Ahadzi *et al.*, 2004c). The proposed model was sensor constrained, that is, current was injected into the head using EIT electrodes and instead of measuring the surface potential, the magnetic field was measured with the aid of SQUID sensors that were not in contact with skin.

The multi-modality approach was based on the fact that the skull does not attenuate magnetic fields as it does to electric field. In MEG, magnetic fields emanating from electrical brain activity are measured outside the human head. These fields are very weak and are of the order fT but could be measured with the help of SQUID gradiometers, which are very sensitive to noise. Since there are no contact electrodes involved in measuring the magnetic field, contact impedance would be eliminated. This approach was proposed in order to be able to record the electrical activity of the brain by measuring the associated magnetic fields.

To validate this new system, a mathematical model was created. This consisted of two head models, homogeneous sphere and four-shell were modelled as the conductor model in 3D using FEM. The four-shell model mimicked the head to consist of scalp, skull, CSF and brain all having different conductivities. For each head model, two different mesh densities were used. One was of a medium density whilst the other was of a higher density. Theoretically, the

higher the mesh density, the more accurate and convergent the estimated potential is. The incorporation of the different head geometries helped in understanding the effect of the skull on the surface potential measured and how current was distributed in the brain.

The bandwidth for the injection current was chosen to be between 1 and 10 Hz and physiological change was 1%. Current was injected using diametrically opposed electrodes for uniform distribution of current to achieve a relatively good sensitivity at the centre of the head. In all, three SQUIDs were positioned 1 cm outside the head at predefined locations to mimic the estimation of magnetic field.

For all the head models and mesh densities, the most realistic approximation of the head was the four-shell model with a higher mesh density. My main interest was to estimate how much the magnetic field changed from baseline when the local conductivity changed by 1%? Analysis of the results suggested that the baseline magnetic field was about 10 pT whereas the change from baseline was 3 fT. By comparing the results with neuromag 122 MEG systems, whose dynamic range was ±200 pT; it meant that it would be fairly practical to detect the baseline signal. But the next question was, what about the change from baseline? To ascertain this, I compared my change in baseline magnetic fields with the spectral noise density in a typical MEG system, which is $7fT/\sqrt{Hz}$ in a frequency band 1 - 100 Hz. The noise level in this MEG system becomes unpredictable at frequencies lower than 1 Hz. The estimated SNR revealed that the magnetic field change due to the simulated physiological changes was very weak as compared to the baseline magnetic fields.

Two issues evolved from this initial study. Firstly by theory, the magnetic field is dependent upon current density. In principle, if the injected current is increased, it would give rise to an increased current density by the same factor and hence the magnetic field. In this physiological measurement, one is limited by two factors: firstly by the allowable current which can be injected into the head, and secondly, the allowable current density in the brain. The simulated injected current was the maximum allowable based on British Standard 101. However, the estimated mean current density in the brain region was about 1×10^{-6} Am^{-2}. Regarding the

second issue, previous research by other authors showed that the current density allowable in the head without stimulating brain tissue is about 100 - 4000 Am^{-2} (100 - 4000 μAmm^{-2}). However, this value was dependent upon the magnitude of the injected current, surface area of the injecting electrodes and duration of the injected current. It was therefore necessary for me to know how much current that could be injected to avoid stimulation of the brain cells. However, to resolve this issue, it was crucial to know how much current density could be obtained in the brain region and whether it was below or above threshold values.

7.1.4 Optimal electrode protocol

The question at hand was, how to increase the current density without stimulating brain cells, hence increasing the SNR? The answer to this question covered the second major part of my work and constituted the fourth chapter of the thesis. It addressed the following research questions: which electrode combinations could be used to obtain optimal current density in a particular region of the brain, and which electrodes may be used to record the change in potential when the conductivity of the region of depolarisation changes by 1%.

To resolve it, 31 electrodes (enhanced 10-20 EEG system) were proposed to be stacked on the head of a subject. Each electrode was paired with all others based on the principle of reciprocity. In all, there were 465 possible pairs of electrodes for current injection. For each pair, at least 10 pairs of electrodes (which are not on the same isopotential line) were defined for recoding of the surface potential. Two realistic FEM head models with different mesh densities were used as the conductor model. The depolarisation region of interest was the primary visual cortex (V1), which elicits during visual stimulation. This was modelled in form of an ellipsoid to approximate the queer shape of V1. By computer simulation, current was injected through all these pairs of electrodes and all the surface potentials were estimated.

The analysis suggested that the highest current density was obtained when at least one of the injecting electrodes was near the region of depolarisation. For a current of 100 μA, the mean current density estimated in the primary visual cortex was about 0.020 ± 0.005 μAmm^{-2}. The

recorded baseline voltage was about 200 ± 50 μV. And for such measurement in relation to V1, for optimal current density or change in surface potential at least one of the recording electrodes should be placed near the occipital cortex.

To validate the results obtained, the measurements were performed experimentally by using a homogenous spherical tank, and then latex tank to measure the baseline voltages. The latter is a three layer realistic tank mimicking scalp, skull, and brain and CSF. Scalp, CSF and brain were all set to the same conductivity of brain, 0.25 mSm^{-1}, and skull's conductivity set to 1.18 mSm^{-1}. A near dc of 100μA was physically injected using some selected electrodes and the surface potential recorded for the two phantoms.

There was a variation of 1 to 10% difference between the baseline voltages simulated and those measured for the homogeneous spherical tank. This was apparent because the skull was not incorporated. On the other hand, there was a significant difference between the simulated results and those measured for the latex tank, as geometry and conductivity values of the tank were completely different from the simulated. This confirmed the fact that geometry of the head together with its varying conductivity limits the accuracy of the baseline voltage and hence signal to noise ratio.

Comparing the mean estimated current density values with theoretical and experimental assertions showed that with this maximum allowable current injected, the current density was 1000 times far below the threshold current density. Again, this suggested that the current density could be increased in the brain region but not exceeding the threshold if we want to increase the magnetic field strength. However, how can this be done as the maximum allowable current had already been injected?

There was a significant difference between the simulated and latex phantom baseline voltages. Incorporated in the simulation program were the different conductivities of the brain, CSF, skull and scalp. The conductivity of skull was the lowest as compared to other tissues in the head. The conductivity of the skull used was 1.18 mSm^{-1}, which in fact, was the lower limit of

skull conductivity as reported by Law and Hoekema. The upper limit was 28 mSm^{-1}, which meant the conductivity value used was almost 28 times less.

Theoretically, an increase in conductivity of an object gives rise to a decrease in the potential drop across it. An interesting question, which arose, was whether by increasing the conductivity by a certain percentage would mean a significant change in the baseline voltage. If so, by how much would that be and how would it improve the signal level in order to increase the SNR. Also, within this range of conductivity, and the usual injection current of 100 μA, are we within the allowable current density in the brain?

7.1.5 Effect of conductivities on surface potential changes

Knowing the positions of electrodes through which current can be injected or be used to collect the surface potentials was just one of several factors that could be addressed in EIT. One of the major drawbacks in EIT has been attributed to the attenuation of the injected current and surface potential by the human skull, whose conductivity varies. For a conclusive model to be arrived at there is the need to study how these variations in skull conductivity and local conductivities affect changes in scalp potential. In this regard, an extensive study was done to analyse these effects and this has been documented in chapter five of the thesis.

In this work, it has been shown that changes in magnitude of the current density in V1 when unperturbed or perturbed depended on the geometry of V1. The mean current density in V1, irrespective of the positions at which current has been injected increased with increasing skull and local conductivity. With a local change of 0.7 - 1.6%, the maximum change in scalp potential was 0.05%. Non-uniformity ratio increased with current injection through non-diametrically opposed electrodes. With multiple current injection through four pairs of electrodes, the total current density increased at most four times.

7.1.6 Effect of conductivities off-scalp magnetic field changes

This chapter aimed at finding whether the magnetic recordings of EIT was any better than the electrical method taking into account the effect of head geometries and variations in conductivities of the head. It was noted in the electrical recordings of EIT that for 0.6% local conductivity change the potential measured on the scalp was 0.020% whereas the magnetic field changed by 0.03%. With a percentage change of 1% locally, the percentage change in surface potential across all morphologies and sizes was 0.03% whereas the magnetic field change was 0.06%. With a local percentage change if 1.6%, the scalp potential recording changed by 0.05%, whereas the magnetic field recordings changed by 0.085%.

In general, depending on the change in local conductivity and for fixed skull conductivity and irrespective of the shape and size of the V1 (the physiological volume), the maximum percentage change in for the magnetic recordings were much bigger in magnitude than those for the electrical recordings. This suggests that the magnetic recordings have a better potential in EIT measurements than the traditional recordings using electrodes.

7.2 Suggestions

7.2.1 Methods of increasing current density in the brain

Three ways by which current density could possibly be increased in the brain region, however taking into consideration the threshold of current density in the brain region are as follows:

a. Using magnetic coils to induce current into the head and then recording the resulting surface potential using electrodes
b. By incorporating in the brain model, ventricles (as they are less conductive and would act as a shunt in the brain region). This would improve the exactness of the head and

hence a better estimation of the surface potentials on and current density distributions in the head

c. By injecting current through suture lines as the conductivity of sutures is 10 times less than that of skull. With this approach, more current can flow into the head, hence a higher current density distribution leading to an improved SNR

7.2.2 Development of accurate forward problem

7.2.2.1. Individual MRIs

With differences in the geometries of the head together with the considerable varying skull and internal conductivities, a logical conclusion of producing more and more accurate models of the head would be to take a diffusion tensor MRI for every subject. Individual MRI's could be segmented, meshed and conductivity tensors defined at each node. It would be trivial then to measure the positions of the scalp electrodes and transfer these directly to the head mesh in order to provide boundary conditions for a full quadratic and anisotropic FEM solution for each subject. At the present time, it is impractical to produce an accurate and unique full head mesh, since the process is not automated, as MRI's would not be available for most normal volunteers taking part in evoked response experiments, for example.. This method may be practicable for patients with focal epilepsy for whom MRI's are available and it would be desirable to use a model with the greatest accuracy possible to locate the epileptic focus. However, given the inconclusive evidence, presented in this thesis, for the improvement gained by inclusion of correct geometry and conductivity distributions, it does not appear that the production of individual sensitivity matrices is of great priority at the present time.

7.2.2.2. Multi-Frequency Imaging

The UCLH group has taken steps towards the application of multi-frequency EIT to imaging haemorrhage and ischaemia. However, this technique may also improve understanding of the complex mechanisms, which cause EIT signals during evoked responses. The changes are

thought to be due to a combination of effects due to blood flow and cell swelling and it would be possible to separate these if multi-frequency measurements were to be made. Images could then be presented with more direct relation to fMRI images, which are reliant on the BOLD response. The new technique could be referred to as BOLD-Related EIT.

7.2.2.3. Improving Computing Power

Condor is a specialized workload management system for compute-intensive jobs. Like other full-featured batch systems, Condor provides a job queuing mechanism, scheduling policy, priority scheme, resource monitoring, and resource management. Users submit their serial or parallel jobs to Condor, Condor places them into a queue, chooses when and where to run the jobs based upon a policy, carefully monitors their progress, and ultimately informs the user upon completion. While providing functionality similar to that of a more traditional batch queuing system, Condor's novel architecture allows it to succeed in areas where traditional scheduling systems fail. Condor can be used to manage a cluster of dedicated compute nodes. In addition, unique mechanisms enable Condor to effectively harness wasted CPU power from otherwise idle desktop workstations. For instance, Condor can be configured to only use desktop machines where the keyboard and mouse are idle. Should Condor detect that a machine is no longer available (such as a key press detected), in many circumstances Condor is able to transparently produce a checkpoint and migrate a job to a different machine, which would otherwise be idle. Condor does not require a shared file system across machines - if no shared file system is available, Condor can transfer the job's data files on behalf of the user, or Condor may be able to transparently redirect all the job's I/O requests back to the submit machine. With these features of Condor, it can be used to resolve the high computing needs that are required in EIT.

7.2.3 Best optimal current pattern using distinguishability approach

7.2.3.1 Qualitative analysis

Distinguishability is used to provide a quantitative measure of the ability of an impedance imaging systems to distinguish between two conditions from each other by electrical impedance measurements. It is a characteristic of the measurement system, and can be calculated from the data obtained from a system without the need to reconstruct an image from that data. Isaacson proposed many ways of measuring the ability of an impedance imaging system to distinguish between different conductivity distributions (Cheney and Isaacson, 1992). Two infinite set of numbers called visibilities and sensitivities were introduced for this purpose (Seager et al., 1984; Seager and Bates, 1985). Two conductivity distributions can be distinguished from one another when an applied current pattern, induces boundary voltages that differ by more than the precision of the voltmeter. These boundary voltages can be made larger by applying more current. However, any practical system will have a limitation on the amount of power that can be applied.

This power limitation or the limit of current density values in the human head must be taken into consideration. This will help in addressing the following problems in EIT: 1) What is the best current pattern to distinguish one conductivity distribution from the other? 2) What electrode size should be used? 3) What are the smallest inhomogeneities detectable with a given measurement precision? Isaacson and Cheney (1992) discussed several ways of taking into account the power limitation, and proved that the answers to the above questions by studying the mathematical idealization, the 'continuum model' in which arbitrary current densities were applied to the entire boundary of an object. They showed how the limiting power applied to the model led to the use of Sobolev norms and spaces. Sobolev spaces are a standard mathematical tool for measuring smoothness of functions.

In another development, Isaacson (Kao et al., 2003) used four methods to investigate breast cancer diagnosis by EIT. These are the single current source (SCS) method (Korjenevsky et

al., 1999), which applied a current to each electrode sequentially, and measured the resulting voltage on all other electrodes. The second method termed the single voltage source (SVS) method used by the T-SCAN system (Kao et al., 2003) which applied a constant voltage to a flat array of electrodes on the body relative to a single electrode held in the hand and measured the resulting currents at each of several electrodes. The Adaptive Current Tomography 3 system (ACT 3) has an independent current source and voltage meter for each electrode. This multiple current source (MCS) system offers a chance to study the effect of the current pattern. They applied the same current to each electrode simultaneously and measured the resulting voltages as the third method. For the fourth method, they applied current pattern given by the adaptive algorithm (Isaacson, 1986) which was optimised to distinguish the difference between saline tank with and without a target. They used these four methods to study distinguishability and explained their results in terms of norm and power distinguishability.

(Demidenko et al., 2005) developed a statistical criterion for optimal patterns in planar circular electrical impedance tomography. These patterns minimise the total variance of the estimation for resistance and conductance. It has been shown that trigonometric patterns (Gisser et al., 1987), originally derived from the concept of distinguishability, are a special case of their optimal statistical patterns.

7.2.3.2 Quantitative measure

Isaacson developed a criterion to distinguish between two conductivities σ_0 and σ_1 inside a body. In this analysis, let $V(\sigma_o, j)$ be the measured voltage when current density j is applied to the homogeneous background with no target, and $V(\sigma_1, j)$ be the measured voltage on the tank with a target. Two conductivities are distinguishable, in the mean square sense, by a measurement precision ε_i if and only if

$$\|V(\sigma_o, j) - V(\sigma_1, j)\| > \varepsilon_i \tag{7.1}$$

for the current density j for which $\|j\| = 1$ where norm $j = \|j\| = \left(\int j^2 dx\right)^{\frac{1}{2}}$.

In the discrete case, the norm distinguishability in the mean square sense, is defined by

$$\partial_l(\sigma_1, \sigma_o, j) = \frac{\|V(\sigma_o, j) - V(\sigma_1, j)\|}{\|j\|} = \sqrt{\frac{\sum_{l=1}^{L} |V(\sigma_o, j) - V(\sigma_1, j)|^2}{\sum_{l=1}^{L} |I_l|^2}} \tag{7.2}$$

where the currents, I_l are simultaneously applied to the electrodes l, $l = 1, 2, 3, \ldots, L$. and this is proportional to a discrete approximation to ∂_l.

Equation 7.2 expresses the distinguishability for the current source system, but does not take into account the power. In order to compare distinguishability between a current source system and a voltage source system, the relative power must be compared (Isaacson, 1986). An inhomogeneity is detectable if the change in power is greater than the measurement precision ε_p with which the system can measure power. That is

$$|P(\sigma_o' j)| - P(\sigma_o' j) > \varepsilon_p \tag{7.3}$$

and the relative power change is defined as

$$p_l(\sigma_1, \sigma_o, j) = \sqrt{\frac{\sum_{l=1}^{L} |V(\sigma_o, j) - V(\sigma_1, j)|^2}{\Re\left(\sum_{l=1}^{L} I_l V(\sigma_o, j)^*\right)}} \tag{7.4}$$

The units of equation 7.2 are in ohms, whereas those of equation 7.4 are the square root of ohms.

The above formulation will provide yet another comprehensive studies in determining whether the signals that are estimated contain enough information reconstruction purposes. This may rather require very heavy computing facilities in terms of speed and memory. An utilisation of CONDOR would be an appropriate means to achieve this interesting task in the future.

Appendix

Appendix A

GESELOWITZ' SENSITIVITY THEOREM

(Geselowitz, 1971) derived an expression for the sensitivity of a four-point impedance measurement, given the position of the four electrodes. He considered a volume conductor on which is placed four electrodes and obtained equation A.1, where ΔZ is the measured impedance change and $\Delta\sigma$ is the actual impedance change in a volume element dV. One pair of electrodes delivers a current I_ϕ and the other pair measures a voltage ψ. By reciprocity, this is equivalent to the second pair delivering a current I_ψ and the first pair measuring a voltage ϕ.

$$\Delta Z = -\Delta\sigma \int_V \frac{\nabla\phi}{I_\phi} \cdot \frac{\nabla\psi}{I_\psi} dV \tag{A.1}$$

When incorporated into an EIT reconstruction algorithm, each pixel has the same volume and the injected current is constant, so a sensitivity coefficient $S_{m,n,x,y,z}$ can be defined for a pixel at (x, y, z) proportional to the measured impedance ΔZ. $S_{m,n,x,y,z}$ is simply proportional to the product of the electric fields (and therefore to the product of the current densities) at that pixel from the two pairs of electrodes ∇V_m and ∇V_n.

$$S_{m,n,x,y,z} = \nabla V_m \cdot \nabla V_n \tag{A.2}$$

Analytical solution

Geselowitz' method (1971) can be used to find the sensitivity coefficients provided the voltage distribution is known. The voltage distribution is given by Poisson's Equation, $\nabla \cdot (\sigma \nabla V) = i$. The potential, V, due to two current electrodes on the boundary of a circle in 2D, whose distances from a point of interest are r_1 and r_2, respectively, is given by equation (A.3).

$$V = \ln\left(\frac{r_1}{r_2}\right) \tag{A.3}$$

Numerical solution

Analytical solutions are only available for simple objects, generally those which are radially symmetric (Pidcock et al., 1994b; Pidcock et al., 1994a). For an arbitrary resistivity distribution in an irregularly shaped object, numerical techniques are required. The object is divided into many elements, small enough for the resistivity to be considered constant in each. In the finite element method (FEM), the voltage distribution is expressed as interpolation functions within each element, which are usually linear or polynomial. This gives a piecewise solution for the entire object. The voltage at each node is found from the interpolation functions, which give the voltage distribution, and hence sensitivity coefficients (Murai and Kagawa, 1985). Increasing the number of elements, and the order of the interpolation functions improves the accuracy and spatial resolution, whilst increasing computation time. Equation (A.4) gives the relationship between the current density at the i^{th} node, electric potential and conductivity σ as:

$$\mathbf{J}_i = -\sigma_i \nabla V_i$$

Appendix B

SPECTRAL NOISE DENSITY

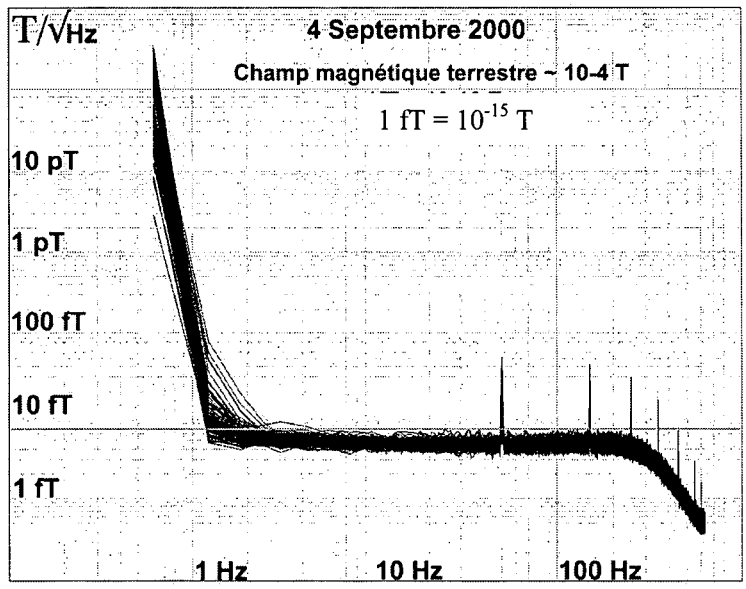

Figure B-1: Spectral noise density for a SQUID as a function of frequency. Source(MEG-EEG Centerat Pitié-Salpêtrière Hospital, 2000)

References

REFERENCES

Ahadzi,G.M., Liston,A.D., Bayford,R.H., and Holder,D.S. (2004a) Neuromagnetic field strength outside the human head due to impedance changes from neuronal depolarization. *Physiol Meas.* **25,** 365-378.

Ahadzi,G., Gilad,O., Horesh,L., Bayford,R., and Holder,D. (2004b) An EIT electrode protocol for obtaining optimal current density in the primary visual cortex. *Proceedings of the XII Intern.Conf.Electrical Bio-Impedance and EIT, Gdansk, Poland* **II,** 621-624.

Ahadzi,G., Liston,A., Bayford,R., and Holder,D. (2003) Would SQUID measurement of magnetic fields be a better way to do EIT imaging of fast electrical brain activity ? *4th International Conference on Biomedical Applications of EIT, University of Manchester Institute of Technology, Manchester.*

Ahadzi,G., Liston,A., Bayford,R., and Holder,D. (2004c) Neuromagnetic field strength outside the human head due to impedance changes from neuronal depolarization. *Physiol Meas.* **25,** 365-378.

Ahlfors,S., Dale,A.M., Belliveau,J.W., Liu,A.K., Korvenoja,A., Virtuanen,J., Houtilainen,M., Tootell,R.B.H., Aronen,J., and Ilmoniemi,R.J. (1999) Spatiotemporal activity of a cortical network for processing visual motion revealed by MEG and fMRI. *J.of Neurophysiology* **82,** 2544-2555.

Andrews et al (1997) Correlated size variations in human cortex, lateral geniculate nucleus, and optic tract. *Int.J.Neurosci* **17,** 2859-2868.

Andrews,T., Halpern, and Purves (1997) Correlated size variations in human cortex, lateral geniculate nucleus, and optic tract. *Int.J.Neurosci* **17,** 2859-2868.

Anling,R. (2000) Electrical impedance tomography of brain activity: studies into its accuracy and physiological mechanisms. PhD Thesis, University College London.

Antal,A., Kincses,T.Z., Nitsche,M.A., Bartfai,O., Demmer,I., Sommer,M., and Paulus,W. (2002) Pulse configuration-dependent effects of repetitive transcranial magnetic stimulation on visual perception. *Neuroreport* **13,** 2229-2233.

Antal,A., Kincses,T.Z., Nitsche,M.A., and Paulus,W. (2003a) Manipulation of phosphene thresholds by transcranial direct current stimulation in man. *Exp.Brain Res.* **150,** 375-378.

Antal,A., Kincses,T.Z., Nitsche,M.A., and Paulus,W. (2003b) Modulation of moving phosphene thresholds by transcranial direct current stimulation of V1 in human. *Neuropsychologia* **41,** 1802-1807.

Antal,A., Nitsche,M.A., and Paulus,W. (2001) External modulation of visual perception in humans. *Neuroreport* **12,** 3553-3555.

Araki,T. and Terzuolo,C. (1962) Membrane currents in spinal motoneurons associated with the action potential. *Journal of Neurobiology* **6,** 772-790.

Arridge,S., Hebden,J., Schweiger,M., Schmidt,F., Fry,M., Hillman,E., Dehghani,H., and Delpy,D. (2000) A method for three-dimensional time-resolved optical tomography. *Int.J.of Imaging Systems Technology* **11,** 2-22.

Ary,J. and Klein,S. (1981) Location of Sources of Evoked Scalp Potentials: Corrections for Skull and Scalp Thickness. *IEEE Trans Biomed.Eng.* **28,** 447-452.

Avis,N. (1993) Image reconstruction in Electrical Impedance Tomography. *Sheffield, University of Sheffield.*

Avis,N. and Barber,D. (1994) Image Reconstruction Using Non-Adjacent Drive Configuration. *Physiol.Meas.* **15,** 153-169.

Bagshaw,A.P., Liston,A.D., Bayford,R.H., Tizzard,A., Gibson,A.P., Tidswell,A.T., Sparkes,M.K., Dehghani,H., Binnie,C.D., and Holder,D.S. (2003) Electrical impedance tomography of human brain function using reconstruction algorithms based on the finite element method. *Neuroimage* **20,** 752-764.

Baillet,S. and Mosher,J. (2001) Electromagnetic Brain Mapping. *IEEE Signal Processing Magazine* **18,** 14-30.

Barber,D.C. and Brown,B.H. (1988) Errors in reconstruction of resistivity images using a linear reconstruction technique. *Clin.Phys.Physiol.Meas.* **9,** 101-104.

Barber,D. and Seagar,A. (1987) Fast reconstruction of resistance images. *Physiol.Meas.* **8,** 47-54.

Bayford,R., Hanquan,Y., Boone,K., and Holder,D.S. (1995) Experimental validation of a novel reconstruction algorithm for electrical impedance tomography based on backprojection of Lagrange multipliers. *Physiol Meas.* **16,** A237-A247.

Bayford,R.H., Gibson,A., Tizzard,A., Tidswell,T., and Holder,D.S. (2001a) Solving the forward problem in electrical impedance tomography for the human head using IDEAS (integrated design engineering analysis software), a finite element modelling tool. *Physiol Meas.* **22,** 55-64.

Bayford,R., Gibson,A., Tizzard,A., Tidswell,A., and Holder,D. (2001b) Solving the forward problem for the human head using IDEAS (Integrated Design Engineering Analysis Software) a finite element modelling tool. *Physiol.Meas.* **22,** 55-63.

Baysal,U. and Eyuboglu,B. (2000) Tissue resistivity estimation in the presence of positional and geometrical uncertainties. *Physiol.Meas.* **45,** 2373-88.

Bindman,L.J., Lippold,O.C., and Redfearn,J.W. (1962) Long-lasting changes in the level of the electrical activity of the cerebral cortex produced bypolarizing currents. *Nature* **196,** 584-585.

Bindman,L.J., Lippold,O.C., and Redfearn,J.W. (1964) The action of brief polarizing currents on the cerebral cortex of the rat (1) during current flow and (2) in the production of long-lasting after-effects. *J.Physiol* **172,** 369-382.

Binnie,C., Copper,C., Mauguiere,F., and Prior,P. (1996) Definitions and introductory remarks - Clinical neurophysiology.

Birgul,O., Eyuboglu,B.M., and Ider,Y.Z. (2003) Current constrained voltage scaled reconstruction (CCVSR) algorithm for MR-EIT and its performance with different probing current patterns. *Phys.Med Biol* **48,** 653-671.

Blumhardt,L., Barrett,G., Halliday,A., and Kriss,A. (1977) The asymmetrical visual evoked potential to pattern reversal in one half field and its significance for the analysis of visual field . *Br.J.Ophthalmol.* **61,** 454-461.

Bodurka,J. and Bandettini,P. (2002) Toward direct mapping of neuronal activity: MRI detection of ultraweak, transient magnetic field changes. *Magn Reson.Med.* **47,** 1052-1058.

Bonovas,P. and Kyriacou,G. (2001) A realistic three-dimensional FEM of the human head. *Physiol.Meas.* **22,** 65-75.

Boone K. (1995) The possible use of applied potential tomography for imaging action potentials in the brain. *Clinical Neurophysiology.*

Boone K. and Holder,D.S. (1994) Imaging of cortical spreading depression using EIT: implecation for localisation of epileptic foci. *Physiol.Meas.* 189-90.

Boone,K. (1995) The possible use of applied potential tomography for imaging action potentials in the brain. *Clinical Neurophysiology.*

Boone,K. and Holder,D. (1994a) Imaging of cortical spreading depression using EIT: implecation for localisation of epileptic foci. *Physiol.Meas.* 189-90.

Boone,K. and Holder,D. (1994b) Imaging of cortical spreading depression using EIT: implications for localisation of epileptic foci. *Physiol.Meas.* **15,** 189-198.

Boone,K. and Holder,D. (1995) Design considerations and performance of a prototype system for imaging neuronal depolarization in the brain using 'direct current' electrical resistance tomography. *Physiol Meas.* **16,** A87-A98.

Boone,K. and Holder,D. (1996a) Current Approaches to Analogue Instrumentation Design in EIT. *Physiological Measurement* **17,** 229-247.

Boone,K. and Holder,D. (1996b) Current Aproaches to Analogue Instrumentation Design in EIT. *Physiological Measurement* **17,** 229-247.

Borsvic,A. and McLeod,C. (2001) Realistic 2D human thorax modelling for EIT. *Physiol.Meas.* **22,** 77-83.

Brenner,D., Williamson,S., and Kaufman,L. (1975) Visually evoked magnetic fields of the human brain. *Science* **190,** 480-482.

Brown,B. and Primhak,R. (2002) Neonatal lungs--can absolute lung resistivity be determined non-invasively? *Med & Biol.Eng & Comp* **40,** 388-394.

Brown,B., Smallwood R.H, Barber,D.C., Lawford,P.V., and Hose,D.R. (1999) *Medical Physics and Biomedical Engineering.* IoP.

Burger,H. and Milaan,J. (1994) Measurements of the specific resistance of the human body to direct current. *Act.Med.Scand.* **11,** 584-607.

Carelli,P., Modena I., and Romani,G. (1983) Detection coils. *Biomagnetism, an interdisciplinary approach.*

Cheney,M. and Isaacson,D. (1992) Distinguishability in impedance imaging. *IEEE Trans Biomed.Eng.* **39,** 852-860.

Chiappa,K. (1990) *Evoked potentials in clinical medicine.* Raven Press, New York.

Clarke,J. (1977) Superconducting quantum interference devices for low frequency measurements. *Super Conductor Applications : Squids and machines.*

Clay,M. and Ferree,T. (2002) Weighted regularization in Electrical Impedance Tomography With Applications to Acute Cerebral Stroke. *IEEE Trans Med Imaging* **21,** 662-667.

Cohen,D. (1968) Magnetoencephalography: evidence of magnetic fields produced by alpha-rhythm currents. *Science* **161,** 784-786.

Cole,K. and Curtis,H. (1939) Electrical Impedance of the squid giant axon during activity. *J.Gen Physiol* 649-670.

Cole,K. and Hodgkin,A. (1939) Membrane and protoplasm resistance in the squid giant axon. *Journal of General Physiology* **22,** 671-687.

Cooper,R., Osselton,J., and Shaw,J. (1969) *EEG Technology.* Butterworths.

Cuffin,B. and Schomer,D. (2001) Experimental Tests of EEG Source Localization Accuracy in Spherical Head Models. *Clin.Neurophysiol.* **112,** 46-51.

Demidenko,E., Hartov,A., Soni,N., and Paulsen,K. (2005) On optimal current patterns for electrical impedance tomography. *IEEE Trans Biomed.Eng.* **52,** 238-248.

Dietzel,I. and Heinemann,U. (1982) Stimulus-induced changes in extracellular Na+ and Cl- concentration in relation to changes in the size of the extracellular space. *Exp.Brain Res.* **46,** 73-84.

Eyuboglu,B.M., Koksal,A., and Demirbilek,M. (2000) Distinguishability analysis of an induced current EIT system using discrete coils. *Phys.Med Biol* **45,** 1997-2009.

Ferree,T., Eriksen,K., and Tucker,D. (2000) Regional Head Tissue Conductivity Estimation for Improved EEG Analysis. *IEEE Trans.in Biomed.Eng.* **47.**

Fox,P. and Raichle,M. (1984) Stimulus rate dependence of regional cerebral blood flow in human striate cortex, demonstrated by positron emission tomography. *J.Neurophysiol.* **51,** 1109-1120.

Freeston,I. and Tozer,R. (1995) Impedance imaging using induced currents. *Physiol.Meas.* **16,** 257-266.

Frerichs,I. (2000) Electrical impedance tomography (EIT) in applications related to lung and ventilation: A review of experimental and clinical activities. *Physiol.Meas.* **21,** R1-21.

Freygang and Laundau (1955) Some relations between resistance and electrical activity in the cerebral cortex of cat. *Journal of Cellular and Comparitive Physiology* **45,** 377-392.

Gabriel,S., Lau,R.W., and Gabriel,C. (1996) The dielectric properties of biological tissues: II. Measurements in the frequency range 10 Hz to 20 GHz. *Phys.Med Biol* **41,** 2251-2269.

Gamache,F., Dold,G.M., and Myres,R.E. (1975) Changes in cortical impedance and EEG activity induced by profound hypotension. *Am.J.Physiology* **228,** 1914-1920.

Ganong,W. Review of Medical Physiology. Appleton and Lange . 1987.

Gisser,D., Isaacson,D., and Newell,J. (1987) Current topics in impedance imaging. *Clin.Phys.Physiol.Meas.* **8,** 39-46.

Goncalves,S. and de Munck,J. (2000) The application of electrical impedance tomography to reduce systematic errors in the EEG inverse problem--a simulation study. *Physiol.Meas.* **21,** 379-393.

Goncalves,S. and de Munck,J. (2002) The application of electrical impedance tomography to reduce systematic errors in the EEG inverse problem--a simulation study. *Physiol.Meas.* **21,** 379-393.

Griffiths,H., Leung,H., and Williams,R. Imaging Permittivity In Electrcal Impedance Tomography. IEEE EMBS [Proceedings of the 13th annual International Conference], 16-17. 1992.
Ref Type: Magazine Article

Hamalainen,M. (1992) Magnetoencephalography: A tool for functional brain imaging. *Brain Topography* **5,** 95-102.

Hamalainen,M., Hari,R., Ilmoniemi,R., Knuutila,J., and Lounasmaa,O. (1993) Magnetoencephalography - theory, instrumentation, and applications to noninvasive studies of working human brain. *Reviews of Modern Physics* **65,** 416-418.

Hansen,J. and Olsen,C. (1980) Brain extracellular space during spreading depression and ischaemia. *Acta Physiol.Scand.* **108,** 355-365.

Harland,C., Clark,T., and Prance,R. (2001) Electric potential probes - new directions in the remote sensing of the human body. *IOP Meas.Sci.Technol.* **13,** 163-169.

Haueisen,J. and Tuch,D. (2002) The Influence of Brain Tissue Anisotropy on Human EEG and MEG. *Journal of Cerebral Blood Flow & Metabolism* **22,** 908-917.

Hemingway,A. and McLendon,J.F. (1932) The high frequency resistance of human tissue. *Am.J.Physiology* **102,** 56-59.

Hoekema,R., Wieneke,G., Leijten,F., van Veelen,C., van Rijen,P., Huiskamp,G., Ansems,J., and van Huffelen,A. (2003) Measurement of the conductivity of skull, temporarily removed during epilepsy surgery. *Brain Topogr.* **16,** 29-38.

Holder,D. (1992) Impedance changes during the compound nerve action potential: implications for impedance imaging of neuronal depolarisation in the brain. *Med Biol Eng Comput* **30,** 140-146.

Holder,D. (2001) *Clinical and Physiological Applications of EIT.*

Holder,D., Rao,A., and Hanquan,Y. (1996a) Imaging of physiologically evoked responses by EIT with cortical electrodes in the anaesthetised rabbit. *Physiol.Meas.* **17,** 178-186.

Holder,D., Rao,A., and Hanquan,Y. (1996b) Imaging of physiologically evoked responses by electrical impedance tomography with cortical electrodes in the anaesthetised rabbit. *Physiol.Meas.* **17,** 179-186.

Horesh,L., Bayford,R., Yerworth,R., Tizzard,A., Ahadzi,G., and Holder,D. (2004) Beyond the linear domain - the way forward in MFEIT image reconstruction of the human head. *Proceedings of the XII Intern.Conf.Electrical Bio-Impedance and EIT, Gdansk, Poland* **II,** 683-686.

Hossman,K. (1971) Cortical steady potential, impedance and excitability changes during and after total ischaemia of cat brain. *Exp.Neurol* **32,** 163-175.

Hua,P., Woo,E.J., Webster,J.G., and Tompkins,W.J. (1993) Using compound electrodes in electrical impedance tomography. *IEEE Trans Biomed.Eng* **40,** 29-34.

Huiskamp,G., Vroeijenstijn,M., van Dijk,R., Wieneke,G., and van Huffelen,A. (1999) The need for correct realistic geometry in the inverse EEG problem. *IEEE Trans Biomed.Eng.* **46,** 1281-1287.

Internet Communication (2002) Specifications of Neuromag 122 dc squids. *http://www.4dneuroimaging.com/external_english/html/n122spec.html.*

Isaacson,D. (1986) Distinguishability of conductivities by electric computed tomography. *IEEE Trans.Med.Imaging* **5,** 92-95.

Isaacson,D., Cheney,M., and Newell,J. (1992) Electrical impedance tomography. Comments on reconstruction algorithms. *Clin.Phys.Physiol Meas.* **13 Suppl A,** 83-89.

Jain,H. and Isaacson,D. (1997) Electrical impedance tomography of complex conductivity distributions with noncircular boundary. *IEEE Trans Biomed.Eng.* **44,** 1051-1060.

Jasper,H. (1958) Report of the committee on methods of clinical examination in electroencephalography. *Electroenceph.Clin.Neurophysiol.* **10,** 370-371.

Jerbi,K. and Lionheart,W. (2000) Sensitivity matrix and reconstruction algorithm for EIT assuming axial uniformity. *Physiol.Meas.* **21,** 61-66.

Jezzard,P. and Turner,R. (1996) Magnetic resonance imaging methods for study of human brain function and their application at high magnetic field. *Computerized Medical Imaging and Graphics* **20,** 467-481.

Jossinet,J. and Trillaud,C. High Frequency Imaging of Capacitive targets. IEEE EMBS [Proceedings of the 13th annual International Conference], 18-19. 1992.
Ref Type: Magazine Article

Joy,M. and Lebedeev,V. (1999) Imaging of current density and current pathways in rabbit brain during transcranial electrostimulation. *IEEE Trans.Biomed.Eng* **46,** 1139-1148.

Jueptner,M. and Weiller,C. (1995) Review: Does Measurement of Regional Cerebral Blood flow Reflect Synaptic Activity? - Implications for PET and fMR. *Neuroimage* **2,** 148-156.

Kao,T., Newell,J., Saulnier,G., and Isaacson,D. (2003) Distinguishability of inhomogeneitites using planar electrode arrays and different patterns of applied excitation. *Physiol.Meas.* **24,** 403-411.

Karp,P., Ernd,S., Hahlbohm,H., and LObbig,H. Cardiomagnetism. Biomagnetism , 219-258. 1981. de Gruyter, Berlin.
Ref Type: Magazine Article

Kerner,T. and Hartov,A. (2001) An improved data acquisition method for electrical impedance tomography. *Physiol.Meas.* **22,** 31-38.

Kerner,T. and Hartov,A. (2002) Imaging the breast with EIS: an initial study of exam consistency. *Physiol.Meas.* **23,** 221-236.

Kerner,T. and Paulsen,K. (2002) Electrical Impedance Spectroscopy of the Breast: Clinical Imaging Results in 26 Subjects. *IEEE Trans Med Imaging* **21,** 638-645.

Kincses,T.Z., Antal,A., Nitsche,M.A., Bartfai,O., and Paulus,W. (2004) Facilitation of probabilistic classification learning by transcranial direct current stimulation of the prefrontal cortex in the human. *Neuropsychologia* **42,** 113-117.

Kleinermann,F. and Avis,N. (2001) Analytical Solution to the three-dimensional electrical forward problem for a circular cylinder. *Inverse Problems* **16,** 461-468.

Kolehmainen,V., Vauhkonen,M., Karjalainen,P., and Kaipio,P. (1997) Assessment errors in static electrical impedance tomography with adjacent and trigonometric current patterns. *Physiol.Meas.* **18,** 289-303.

Korjenevsky,A., Cherepenin,V., and Kornienko,V. (1999) Electric mammograph with 3D visualization. *Ist EPSRC Engineering Network Meeting (London).*

Kosterich,J. and Foster,K. (1983) Dielectric permittivity and electrical conductivity of fluid saturated bone. *EEE Trans Biomed.Eng.* **30,** 81-86.

Kosterich,J., Foster,K., and Pollack,S. (1984) Dielectric properties of fluid saturated bone: The effect of variation in conductivity of immersion fluid. *IEEE Trans.Biomed.Eng* **31,** 369-375.

Krings,T. and Chiappa,K. (1999) Accuracy of EEG dipole source localisation using implanted sources in the human brain. *Clinical Neurophysiology* **110,** 106-114.

Kristeva-Feige,R. and Grimm,C. (1997) Reproducibility and Validity of Electric Source Localisation with High-Resolution Electroencephalography. *Electroencephalography and Clinical Neurophysiology Supplement* **103,** 652-660.

Law,S. (1993a) Thickness and resistivity Variations over the Surface of the Human Skull. *Brain Topography* **6,** 99-109.

Law,S. (1993b) Thickness and resistivity variations over the surface of the human skull. *Brain Topography* **6,** 99-109.

Levy,S., Adam,D., and Bresler,Y. (2002) Electromagnetic impedance tomography (EMIT): A new method for impedance imaging. *IEEE Trans.MedImag.* **21,** 676-687.

Liebetanz,D., Nitsche,M.A., Tergau,F., and Paulus,W. (2002) Pharmacological approach to the mechanisms of transcranial DC-stimulation-induced after-effects of human motor cortex excitability. *Brain* **125,** 2238-2247.

Lionheart,W. (1998) Boundary shape and electrical impedance tomography. *Inverse Problems* **14,** 139-147.

Lionheart,W., Kaipio,J., and McLeod,C. (2001) Generalized optimal current patterns and electrical safety in EIT. *Physiol.Meas.* **22,** 85-90.

Liston,A. (2003) Models and reconstruction in electrical impedance tomography of human brain function. PhD Thesis, School of Health and Social Sciences, Middlesex University: in collaboration with University Collge London.

Liston,A., Bayford,R.H., Tidswell,T., and Holder,D. (2002) A multi-shell algorithm to reconstruct EIT images of brain function. *Physiol Meas.* **23,** 105-119.

Liston,AD., Bayford,R.H., Holder,D., and Enfield,L. A model of resistance change in the human cortex during neuronal depolarization. 157-160. 2001.
Ref Type: Report

Lux,H., Heinemann,U., and et al. (1986) Ionic changes and alterations in the size of the extracellular space during epileptic activity. A. V. Delgado-Escueta, A. A. W. Jr, D. M. Woodbury and R. J. Porter. *Advances in Neurology* **44.**

Malmivuo,J. and Plonsey,R. (1995) *Bioelectromagnetism.* Oxford University Press, New York.

Malmivuo,J., Suihko,V., and Eskola,H. (1997) Sensitivity distributions of EEG and MEG measurements. *IEEE Trans.on Biomed.Eng.* **44,** 196-208.

Matsunaga,K., Nitsche,M.A., Tsuji,S., and Rothwell,J.C. (2004) Effect of transcranial DC sensorimotor cortex stimulation on somatosensory evoked potentials in humans. *Clin.Neurophysiol.* **115,** 456-460.

McArdle,F. and Brown,B. (1993) Imaging cardiosynchronous impedance changes in the aduly head. *Clinical and Physiological Applications of EIT* **Holder, DS, London, UCL Press,** 177-183.

MEG-EEG Centerat Pitié-Salpêtrière Hospital . Noise Levels. http://www.ccr.jussieu.fr/meg-center/public/moyensag.html . 2000.
Ref Type: Internet Communication

Metherall,P. and Barber,D. (1996) Three-dimensional electrical impedance tomography. *Nature* **380,** 509-512.

Morucci,J.P. and Rigaud,B. (1996) Bioelectrical impedance techniques in medicine. Part III: Impedance imaging. Third section: medical applications. *Crit Rev.Biomed.Eng* **24,** 655-677.

Morucci,J. and Granie,M. (1995) 3D reconstruction in electrical impedance tomography using a direct sensitivity matrix approach. *Physiol.Meas.* **16,** 123-128.

Morucci,J. and Granie,M. (2006) 3D reconstruction in electrical impedance tomography using a direct sensitivity matrix approach. *Physiol.Meas.* **16,** 123-128.

Mosher,J., Baillet S., and Leahy RM (1999) EEG source localization and imaging using multiple signal classification approaches. *J.Clin.Neurophysiol.* **16,** 225-238.

Murai,T. and Kagawa,Y. (1985) Electrical impedance computed tomography based on a finite element model. *IEEE Trans.in Biomed.Eng.* **32,** 17784.

Nitsche,M.A., Liebetanz,D., Lang,N., Antal,A., Tergau,F., and Paulus,W. (2003) Safety criteria for transcranial direct current stimulation (tDCS) in humans. *Clin.Neurophysiol.* **114,** 2220-2222.

Nitsche,M.A. and Paulus,W. (2000) Excitability changes induced in the human motor cortex by weak transcranial direct current stimulation. *J.Physiol* **527 Pt 3,** 633-639.

Okada,Y., Lahteenmaki,A., and Xu,C. (1999) Experimental analysis of distortion of magnetoencephalography signals by skull. *Clinical Neurophysiology* **110,** 230-238.

Ollikainen,J.O., Vauhkonen,M., Karjalainen,P.A., and Kaipio,J.P. (1999) Effects of local skull inhomogeneities on EEG source estimation. *Med Eng Phys.* **21,** 143-154.

Oostendorp,T. and Debelke,J. (2000) The conductivity of the human skull: results of in vivo and in vitro measurements. *IEEE Transactions on Biomedical Engineerin* **47,** 1487-1492.

Patterson,R. and Zhang,X. (2001) Variability in the cardiac EIT image as a function of electrode position, lung volume and body position. *Physiol.Meas.* **22,** 159-166.

Pidcock,M., Kuzuoglu,M., and Leblebicioglu,K. (1994a) Analytic and semianalytic solutions in electrical impedance tomography: I Twodimensional problems. *Physiol.Meas.* **16,** 77-90.

Pidcock,M., Kuzuoglu,M., and Leblebicioglu,K. (1994b) Analytic and semianalytic solutions in electrical impedance tomography: II Threedimensional problems. *Physiol.Meas.* **16,** 91-110.

Plonsey,R. (1969) *Biolectric Phenomena.* McGraw-Hill, New York.

Plonsey,R. and Hepper,D. (1967) Considerations of quasistationarity in electrophysiological systems. *Bull.Math.Biophys.* **29,** 657-664.

Pohlmeier,R., Buchner,H., Knoll,G., Rienacker,A., Beckmann,R., and Pesch,J. (1997) The influence of skull conductivity misspecification on inverse source localisation in realistcally shaped finite element head models. *Brain Topogr.* **9,** 157-162.

Polydorides,N. and Lionheart,W.R.B. (2002) A Matlab toolkit for three-dimensional electrical impedance tomography: a contribution to the Electrical Impedance and Diffuse Optical Reconstruction Software project. *Meas.Sci.Technol.* **13,** 1871-1883.

Polydorides,N. and Lionheart,W. (2001) Electrical Imaging of the Brain using a Realistic Head Model. *Biomedical Applications of EIT, University College London.*

Pope,J. (1984) *Medical Physics: Options in Physics.*

Raichle,M. (1998) Behind the scenes of functional brain imaging: a historical and physiological perspective. *Proc Natl.Acad.Sci.U.S.A* **95,** 765-772.

Ranck,J. (1963) Specific impedance of rabbit cerebral cortex. *Exp.Neurol* **7,** 144-152.

Ranck,J. (1966) Electrical Impedance in the Subicular Area of Rats during Paradoxical Sleep. *Exp.Neurol* **16,** 416-437.

Ranck,J. (1975) Which elements are excited in electrical stimulation of mammalian central nervous system: a review. *Brain Res.* **98,** 417-440.

Rao,A., Holder,D., and Hanquan,Y. (1996) Some practical biological phantoms for calibrating multifrequency electrical impedance tomography. *Physiol.Meas.* **17,** 167-177.

Rattay,F. (1998) Analysis of the electrical excitation of CNS neurons. *IEEE Trans.Biomed.Eng* **45,** 766-772.

Rattay,F. (1999) The basic mechanism for the electrical stimulation of the nervous system. *Neuroscience* **89,** 335-346.

Rigaud,B. and Morucci,J.P. (1996) Bioelectrical impedance techniques in medicine. Part III: Impedance imaging. First section: general concepts and hardware. *Crit Rev.Biomed.Eng* **24,** 467-597.

Rosenthal,R. and Tobias,C. (1948) Measurement of the electrical resistance of human blood, use in coagulation studies and cell volume determinations." **33**: 1110-22. *J.Lab.Clin.Med.* **33,** 1110-1122.

Roth,B. and Balish,M. (1993) How well does a three-sphere model predict positions of dipoles in a realistically shaped head? *Electroencephalography and Clinical Neurophysiology Supplement* **87,** 175-184.

Rush,S. and Driscoll,D. (1968) Current distribution in the brain from surface elctrodes. *Anaestheia and Analgesia, Current Researches* **47,** 717-723.

Rush,S. and Driscoll,D. (1969) EEG Electrode Sensitivity - An Application of Reciprocity. *IEEE Transactions on Biomedical Engineering* **16,** 15-22.

Saha,S., Reddy,G., and Albright,J. (1984) Factors affecting the measurement of bone impedance. *Med & Biol.Eng & Comp* **22,** 123-129.

Saha,S. and Williams,P.A. (1992) Electric and dielectric properties of wet human cortical bone as a function of frequency. *IEEE Trans Biomed.Eng.* **39,** 1298-1304.

Sarvas,J. (1987) Basic mathematical and electromagnetic concepts of the biomagnetic inverse problem. *Phys.Med.Biol.* **32,** 11-22.

Saulnier,G. and Blue,R. (2001) Electrical Impedance Tomography. *IEEE Signal Processing Magazine* **18,** 31-43.

Schlappa,J., Annese,E., and Griffiths,H. (2000) Systematic errors in multi-frequency EIT. *Physiol.Meas.* **21,** 111-118.

Schwan,H. and Kay,C. (1956) Specific resistance of body tissues. *Circ.Res.* **4,** 664-670.

Seager,A. and Bates,R. (1985) Full-wave computed tomography, Part 4: Low frequency electric current CT. *IEEProc.* **132A,** 455-466.

Seager,A., Yeo,T., and Bates,R. (1984) Full-wave computed tomography, Part 2: Resolution limits. *IEEProc.* **132A,** 616-622.

Smyth,W. (1968) *Static and Dynamic Electricity.* McGraw-Hill, New York.

Stinstra,J.G. and Peters,M.J. (1998) The volume conductor may act as a temporal filter on the ECG and EEG. *Med Biol Eng Comput* **36,** 711-716.

Stratton,J. (1941) *Electromagnetic Theory.* McGraw-Hill, New York.

Swithenby SJ . Squids and their application in the measurement of weak magnetic fields. J.Phys E:Sci.Instrum 13, 801-813. 1980.
Ref Type: Magazine Article

Tesche,C. and Clarke,J. dc SQUID: Noise and optimalization. Journal of Low temperature Physics 29[3/4], 301-331. 1977.
Ref Type: Magazine Article

Tidswell,A., Gibson A, Bayford RH, and Holder DS (2001) Electrical impedance tomography of human brain activity with a two-dimensional ring of scalp electrodes. *Physiol.Meas.* **22,** 167-175.

Tidswell,A. and Gibson,A. (2001) Validation of a 3D reconstruction algorithm for EIT of human brain function in a realistic head-shaped tank. *Physiol.Meas.* **23,** 177-185.

Towers,C. and McCann,S. (2000) 3D simulation of EIT for monitoring impedance variations within the human head. *Physiol.Meas.* **21,** 119-124.

Tozer,R. (1992) A low capacitance sense amplifier for impedance imaging applications. *Meas.Sci.Technol.* **3,** 508-514.

Tozer,R., Simpson,J., Freeston,I., and Mathiias,J. (1992) Non contact induced current impedance imaging. *Elctron.Lett.* **28,** 773-774.

VanHarreveld,S. and Murphy,D. (1963) Specific Impedance of Rabbit's Cortical Tissue. *Am.J.Physiology* **205,** 203-207.

VanHarreveld,S. and Ochs,A. (1956) Cerebral Impedance Changes After Circulatory Arrest. *Am.J.Physiology* **187,** 180-192.

Vauhkonen,P. and Vauhkonen,M. (2000) Errors due to truncation of the computational domain in static three-dimensional electrical impedance tomography. *Physiol.Meas.* **21,** 125-135.

Walter,H., Kristeva,R., Knorr,U., Schlaug,G., Huang,Y., Steinmetz,H., Nebeling,B., Herzog,H., and Seitz,R.J. (1992) Individual somatotopy of primary sensorimotor cortex revealed by intermodal matching of MEG, PET, and MRI. *Brain Topogr.* **5,** 183-187.

Webster,J. (1990) *Electrical Impedance Tomography.* Adam Higler, Bristol and New York.

Wieringa H.J. (1993) MEG, EEG and the Integration with Magnetic Resonance Images. PhD.

Wikswo,J., Gevins,A., and Williamson,S. (1993) The future of the EEG and MEG. *Electroenceph.Clin.Neurophysiol.* **87,** 1-9.

Wilson,A.J., Milnes,P., Waterworth,A.R., Smallwood,R.H., and Brown,B.H. (2001) Mk3.5: a modular, multi-frequency successor to the Mk3a EIS/EIT system. *Physiol Meas.* **22,** 49-54.

Wirestam,R., Ryding,E., Lindgren,A., Geijer,B., Holtas,S., and Stahlberg,F. (2000) Absolute cerebral blood flow measured by dynamic susceptibility contrast MRI: a direct comparison with Xe-133 SPECT. *MAGMA.* **11,** 96-103.

Woo,E., Hua,P., Webster,J., and Tomkins,W. (1993) A robust image reconstruction algorithm and parallel implementation in electrical impedance tomography. *IEEE Trans.Med.Imag.* **12,** 137-146.

Yerworth,R., Bayford RH, Cusick G, Conway M, and Holder DS (2002) Design and performance of the UCLH mark 1b 64 channel electrical impedance tomography (EIT) system, optimized for imaging brain function. *Physiol Meas.* **23,** 149-158.

Yorkey,T.J., Webster,J.G., and Tompkins,W.J. (1987) Comparing reconstruction algorithms for electrical impedance tomography. *IEEE Trans Biomed.Eng* **34,** 843-852.

Yvert,B. and Bertrand,O. (1997) A systematic evaluation of the spherical model accuracy in EEG dipole localization. *Electroenceph.Clin.Neurophysiol.* **102,** 452-459.

Zida Ider,Y., Onart,S., and Lionheart,W.R.B. (2003) Uniqueness and reconstruction in magnetic resonance–electrical impedance tomography (MR–EIT). *Physiol.Meas.* **24,** 591-604.